

Generating Secure and Gentle Grip on Soft Substrates

van Assenbergh, S.P.

DOI

[10.4233/uuid:d2ed28b3-b003-4ac7-b9d4-dfd3ac273732](https://doi.org/10.4233/uuid:d2ed28b3-b003-4ac7-b9d4-dfd3ac273732)

Publication date

2022

Document Version

Final published version

Citation (APA)

van Assenbergh, S. P. (2022). *Generating Secure and Gentle Grip on Soft Substrates*. [Dissertation (TU Delft), Delft University of Technology]. <https://doi.org/10.4233/uuid:d2ed28b3-b003-4ac7-b9d4-dfd3ac273732>

Important note

To cite this publication, please use the final published version (if applicable). Please check the document version above.

Copyright

Other than for strictly personal use, it is not permitted to download, forward or distribute the text or part of it, without the consent of the author(s) and/or copyright holder(s), unless the work is under an open content license such as Creative Commons.

Takedown policy

Please contact us and provide details if you believe this document breaches copyrights. We will remove access to the work immediately and investigate your claim.

Generating Secure and Gentle Grip on Soft Substrates

Peter van Assenbergh



Generating Secure and Gentle Grip on Soft Substrates

Peter van Assenbergh

Generating Secure and Gentle Grip on Soft Substrates

PROEFSCHRIFT

Ter verkrijging van de graad van doctor
aan de Technische Universiteit Delft,
op gezag van de Rector Magnificus, prof.dr.ir. T.H.J.J. van der Hagen,
voorzitter van het College voor Promoties,
in het openbaar te verdedigen op

maandag 17 januari 2022 om 12:30 uur

door

Simon Petrus VAN ASSENBERGH

Master of Science in Molecular Life Sciences,
Wageningen University & Research, Nederland
geboren te Tricht, Nederland

Printed by: proefschriftenprinten.nl

Cover and Layout: Reproserve

Artwork Cover: Peter van Assenbergh, Rachel van Maaswaal

ISBN: 978-94-6366-495-0

This research is supported by the Netherlands Organization for Scientific Research (NWO), Domain Applied and Engineering Sciences (TTW), Open Technology Program, project 13353 "Secure and gentle grip of delicate biological tissues".

Table of Contents

Summary	XI
Samenvatting	XIV
Zusammenfassung	XVII

1. Introduction	1
1.1 Grasping in minimally invasive surgery	2
1.2 Generation of grip	2
1.3 Optimizing grip for surgical applications	6
Geckos	6
Tree frogs	7
1.4 Aim and approach	8
1.5 Outline of this thesis	11
References	13

2. NANO- AND MICROSTRUCTURE FABRICATION: FROM DESIRED PROPERTIES TO SUITABLE PROCESSES

15

Abstract

15

2.1 Introduction

16

2.2 Fabrication methods for two-dimensional structures extruded in the third dimension with a fixed extrusion height or depth (geometric complexity level 1)

25

Scanning probe lithography (SPL) 25

Photolithography 27

Scanning beam lithography 31

Directed self-assembly of planar two-dimensional structures 34

2.3 Fabrication methods for three-dimensional structures with areas of various heights and no overhanging parts or cavities (geometric complexity level 2)

39

Droplet deposition methods 39

Imprinting with hard molds 41

Dit proefschrift is goedgekeurd door de promotoren.

Samenstelling promotiecommissie bestaat uit:

Rector Magnificus,	voorzitter
Dr. D. Dodou	TU Delft, promotor
Prof.dr.ir. P. Breedveld	TU Delft, promotor
Prof.dr. J. H. van Esch	TU Delft, promotor

Onafhankelijke commissieleden:

Prof.dr.ir. J. L. van Leeuwen	Wageningen University & Research
Prof.dr. E. J. Stamhuis	University of Groningen
Prof.dr. M. van der Elst	TU Delft, Delft
Prof.dr. S. J. Picken	TU Delft, Delft
Prof.dr.ir. J. Harlaar	TU Delft, Delft, reservelid

Shaping and printing with soft molds	44
Shaping methods with soft molds	45
Printing and pattern transfer methods with soft molds	47
2.4 Fabrication methods for three-dimensional structures with overhanging features and/or cavities (geometric complexity level 3)	51
Vat photopolymerization	51
Focused ion or electron beam-induced deposition	53
Directed self-assembly of three-dimensional structures	54
2.5 Discussion	57
Choosing between fabrication methods: a multivariate problem	57
Attainable geometric complexity versus processing characteristics	62
Additive manufacturing	63
Increasing geometric complexity by post-processing	64
Future directions	64
2.6 Conclusion	65
References	67
3. ADHESION AND FRICTION OF MICROPATTERNED ELASTOMERS ON SOFT SUBSTRATES: THE EFFECTS OF PATTERN LENGTH SCALE AND STIFFNESS	75
Abstract	75
3.1 Introduction	76
Adhesion and friction of micropatterned adhesives as a function of geometry, feature size, and stiffness	76
Fabrication of micropatterned adhesives with various geometries, feature sizes, and stiffness degrees	79
3.2 Results	80
Characterization of particles, dimple micropatterns with and without terminal layer, and PVA substrates	80
Adhesion of micropatterns on PVA and glass	83
Friction of micropatterns on PVA and glass	86

3.3 Discussion	89
Adhesion	89
Friction	93
Limitations and recommendations for future work	94
3.4 Conclusion/Outlook	97
3.5 Experimental	97
Materials	97
Synthesis and characterization of particles	98
Fabrication of micropatterns	98
Characterization of micropatterns	100
Fabrication and characterization of polyvinyl alcohol substrates	100
Measurement of adhesion and friction	101
Statistical analyses	103
Acknowledgements	103
References	104
4. EFFECT OF LATERAL REINFORCEMENTS ON THE ADHESION AND FRICTION OF MICROPILLAR ADHESIVES	107
Abstract	107
4.1 Introduction	108
4.2 Experimental	110
Fabrication	110
Friction and adhesion measurements	113
4.3 Results	114
Fabrication of adhesives	114
Friction and adhesion measurements	116
4.4 Discussion	119
Fabrication	119
Friction measurements	120
Adhesion measurements	122
Durability tests	122

Limitations and future work	123
4.5 Conclusion	123
References	125
5. ANISOTROPIC STIFFNESS ADHESIVES FOR HIGH SHEAR FORCES ON SOFT SUBSTRATES	127
Abstract	127
5.1 Introduction	128
Patterned adhesives	128
Internal geometry	129
5.2 Results	131
Fabricated adhesives	131
Shear forces on a glass substrate	134
Shear forces on PDMS substrates	135
5.3 Discussion	137
Anisotropic adhesives	137
5.4 Mechanical characterization	138
Shear forces	138
Outlook	143
5.5 Conclusion	144
5.6 Experimental Section	144
References	148
6. IMPLEMENTATION OF ANISOTROPIC SOFT PADS IN A SURGICAL GRIPPER FOR SECURE AND GENTLE GRIP ON VULNERABLE TISSUES	151
Abstract	151
6.1 Introduction	152
6.2 Design	154
Soft pads	154

3D printed gripper	156
6.3 Experimental methods	158
Pinch force measurements	158
Gripping force measurements	159
6.4 Results	160
Pinch force measurements	160
Gripping force measurements	161
6.5 Discussion	162
6.6 Conclusion	166
References	167
7. Discussion	169
7.1 Main findings of this thesis	170
7.2 Fabrication methods for adhesives	172
Fabricating microscale features	172
Fabricating macroscale features	173
7.3 Form vs. function	173
Internal walls (normal or lateral reinforcement)	176
Bridging (Lateral reinforcement)	176
Internal fibres (Lateral reinforcement)	176
7.4 From experimental to real-world conditions	177
7.5 Future work/Challenges ahead	178
Controlling the thickness, stiffness, and length of the terminal layer	178
Drainage properties of micropillar adhesives on wet substrates	181
From the biological model to designs for artificial adhesives	184
Toward a technical application	185
References	187

Supporting Information Chapter 3	188
SI3.1: Rheological characterization of polyvinyl alcohol (PVA) substrates (PVA-12 and PVA-18)	188
Supporting Information Chapter 5	195
SI5.1 Measuring setup	195
SI5.2. Shear force measurements: Additional results	196
Acknowledgements	198
Personalia	202
Curriculum Vitae	202
Publications	202

SUMMARIES

Summary

Generation of grip on soft tissue in the surgical field is most commonly done with forceps that generate friction grip, that is, the translation of normal (pinch) forces into shear forces. Errors made with these surgical grippers are often force-related: applying too low pinch forces results in slipping of the tissue out of the gripper, and too high pinch forces may lead to tissue damage. One possible solution for generating tissue grip that is secure yet gentle is the adhesive grip. In this case, contact between tissue and gripper is maintained by attracting gripper-tissue interactions, and gripping strength does not depend on the applied pinch forces. Inspiration for the design of such a gripper can be derived from the tree frog, an animal that uses adhesive grip to grip on a range of substrates in its habitat. The main aim of this thesis is to translate grip-generating principles used by tree frogs into designs of artificial adhesives that can generate firm yet gentle grip on soft substrates. The designs of the artificial adhesives in this thesis are inspired by two important characteristics of the tree frog's attachment apparatus: the hierarchical surface pattern on the tree-frog toe-pad and reinforcing fibrillar structures located inside the pad. Specifically, the aim of this thesis is to mimic function rather than form, and focuses on mechanisms underlying the tree-frog attachment apparatus to satisfy two main requirements for strong grip: (1) contact formation and (2) preservation of the formed contact.

In Chapter 2, we explain that, when fabricating a functional nano- or micro-structure, in order to realize the envisioned functionality (for example, grip generation), it is important to choose the fabrication method that is most suitable to fabricate the required architecture. Therefore, we organize common fabrication methods for functional nano- and microstructures based on moderators that affect functionality, such as obtainable architectural complexity or compatible material types. We find that the highest resolutions are obtained with electron beam lithography, but this technique is costly and has low throughput. Vat photopolymerization can be used to obtain high architectural complexity, but its throughput is low, and making architectures larger than a few mm's is not possible (yet). High throughput can be obtained with parallel methods such as photolithography, although this method has limitations in terms of the achievable architectural complexity.

In Chapter 3, adhesives were fabricated where the surface was patterned with densely packed dimples. Dimples had either a diameter of about 1 μm or 10 μm . In a third geometry, 10- μm -sized dimple arrays were topped with a covering terminal layer, resulting in a thin adhesive surface, internally supported by the dimple walls. Adhesion and friction of fabricated adhesives were measured on hard glass substrates and two soft poly-vinylalcohol (PVA) substrates of 12 and 18 kPa. We found that on soft substrates, microscale dimples generate higher adhesion and friction than sub-microscale dimples. The positive effects of sub-microscale features on adhesion and friction, such as defect control and crack trapping, as reported in the literature for hard substrates, seem to disappear on soft substrates. In the presence of a terminal layer, adhesion was higher compared to unpatterned reference adhesives on PVA of 12 kPa, presumably because the soft substrate got interlocked into micro-holes present on the terminal layer. The highest friction was generated by adhesives with microscale dimples without a terminal layer, likely thanks to indentation of the dimple walls into the substrate, resulting in interlocking.

In Chapter 4, micropillar adhesives laterally reinforced with bridging structures between neighbouring micropillars were fabricated. The micropillar arrays were fabricated using a soft lithographic approach, and bridges were subsequently integrated by spin-coating a liquid precursor, forming bridges via capillary action, followed by curing. Results showed that in the presence of bridging structures, higher shear forces were generated compared to adhesives without bridging. Bridging is expected to prevent buckling and irreversible aggregation of micropillars, resulting in higher shear forces. Furthermore, bridging had a positive effect on the durability of adhesives, an effect that increased with increasing bridging thickness.

In Chapter 5, we investigated the use of internal reinforcing walls on millimetre length scales. This relatively large scale allows for the use of commercially available 3D printing techniques to fabricate the adhesives. Adhesives with sub-surface cylindrical pores, separated by pore walls, were fabricated. Pore walls were either aligned with the shearing direction or perpendicular to the shearing direction. Pores were topped with a thin terminal layer with high deformability in the normal direction. The distribution, thickness, and direction of internal pore walls all affected the stiffness of adhesives in shearing or normal direction. It was found that on soft substrates, the highest friction forces were generated by adhesives with the

most flexible terminal layer, combined with the pore walls aligned in the shearing direction. The low normal stiffness yielded high contact formation prior to sliding, whereas a high shear stiffness prevents loss of contact from the soft substrate when lateral loads are applied.

In Chapter 6, we integrated some of the findings of previous chapters, and implemented soft adhesive pads, internally reinforced with a stiff carbon fibre fabric, in a prototype of a novel soft surgical gripper. Two types of adhesive pads were implemented, with either an unpatterned (smooth) surface or a surface with arrays of sub-microscale dimples as presented in Chapter 3. We find that grippers equipped with soft pads generate significantly lower pinch forces on tissue phantoms while generating gripping forces similar to reference metal grippers. Generated gripping forces with this gripper are in the order of 1-2 N, making this gripper interesting for grasping delicate vulnerable tissues such as veins.

This thesis used nature as inspiration for new technology and mimicked the function of the biological paradigm rather than its form. As a result, although based on looks, the developed adhesives do not resemble any natural adhesive system, basic functionalities, such as the presence of reinforcing components, are present in each of them, by means of either internal walls, bridges, or internal fibers.

Samenvatting

Het genereren van grip op zacht weefsel bij chirurgische ingrepen gebeurt meestal met grijpinstrumenten door middel van frictiegrip, dat wil zeggen, de omzetting van normale (knijp)krachten in afschuifkrachten. Fouten die met deze chirurgische grijpers worden gemaakt zijn vaak gerelateerd aan de toegepaste knijpkracht: te lage knijpkrachten resulteren in het slippen van het weefsel uit de gripper, en te hoge knijpkrachten kunnen leiden tot beschadiging van het weefsel. Een mogelijke oplossing voor het genereren van stevige grip op zacht en glibberig weefsel, die desondanks toch veilig en zacht is, is het gebruik van adhesieve grip. In dat geval wordt het contact tussen weefsel en gripper in stand gehouden door de interactie tussen gripper en weefsel, onafhankelijk van de toegepaste knijpkrachten. Inspiratie voor het ontwerp van zo'n gripper kan worden ontleend aan de boomkikker, een dier dat door het gebruik van adhesieve grip, zich stevig kan hechten op zeer uiteenlopende oppervlaktes in zijn leefomgeving.

Het hoofddoel van dit proefschrift is om mechanismes die de boomkikker gebruikt om aan oppervlaktes te hechten, te implementeren in kunstmatige adhesieven, om zo grip te kunnen genereren op zachte substraten. Bij het ontwerpen van de kunstmatige adhesieven in dit proefschrift heb ik me gebaseerd op twee belangrijke kenmerken van de boomkikker: het typische, hiërarchische patroon op de teentop van de boomkikker, en de vezelachtige versterkende structuren die zich binnen in de tenen bevinden. Daarbij richt het werk in dit proefschrift zich veel meer op het nabootsen van de op de functie van deze dan op de structuren zelf, waarbij de functionaliteit voornamelijk bestaat uit twee kern-mechanismen nodig voor stevige hechting, namelijk (1) het vormen van zoveel mogelijk contact en (2) het behouden van het gevormde contact.

In hoofdstuk 2 leggen we uit dat bij het fabriceren van een functionele nano- of microstructuur, om de beoogde functionaliteit (bijvoorbeeld het genereren van grip) te realiseren, het belangrijk is om de meest geschikte methode te kiezen om de structuur te fabriceren teneinde de benodigde architectuur te realiseren. Daarom bespreken we fabricagemethoden- en processen die gangbaar zijn voor het maken van dergelijke nano- en microstructuren, en ordenen die op basis van factoren die invloed hebben op de uiteindelijke functionaliteit, zoals de architectonische complexiteit, of materiaalsoorten. De hoogste resoluties worden verkregen met elek-

tronenbundel-lithografie, maar deze techniek is kostbaar en fabricage is langzaam. Fotopolymerisatie kan worden gebruikt om een hoge architectonische complexiteit te verkrijgen, maar fabricagesnelheid is weer laag, en het maken van structuren groter dan enkele mm's is (nog) niet mogelijk. Een hoge fabricagesnelheid kan worden verkregen met parallelle methoden zoals fotolithografie, hoewel deze methode dan weer beperkingen heeft ten aanzien van de haalbare architectonische complexiteit.

In hoofdstuk 3 heb ik adhesieven gefabriceerd waarbij het oppervlak was voorzien van een patroon van dicht opeengepakte ronde kuiltjes. De patronen bestonden uit kuiltjes van ongeveer 1 μm of 10 μm . In een derde geometrie, werd het patroon met kuiltjes 10 μm in doorsnede bedekt met een dunne toplaag, resulterend in een adhesief met een zeer dun, glad oppervlakte, intern ondersteund door de kuilranden. We hebben de adhesie en wrijvingskrachten van de gefabriceerde structuren gemeten op harde glazen substraten en twee zachte poly-vinylalcohol (PVA) substraten, van 12 en 18 kPa. Op zachte substraten genereren de patronen van 10 μm -kuiltjes meer adhesie en wrijvingskracht dan patronen de kleinere kuiltjes van 1 μm . De voordelige eigenschappen van dergelijke microschaal kuiltjes, zoals het afremmen van scheurvorming of inperken van defecten, zoals in de literatuur gerapporteerd bij testen op harde oppervlaktes, lijken tenietgedaan te worden zodra het oppervlakte zacht en vervormbaar is. In aanwezigheid van een dunne toplaag was de adhesie hoger dan met adhesieven zonder een patroon, vermoedelijk omdat het zachte substraat kleine uitstulpingen maakt in de microgaatjes die aanwezig in de toplaag. De hoogste wrijving werd gegenereerd door adhesieven met 10 μm -kuiltjes, zonder toplaag, vermoedelijk omdat het kuiltjespatroon in het zachte PVA oppervlakte drukt, en licht blijft haken in het oppervlakte bij afschuiving.

In hoofdstuk 4 werden adhesieven met een oppervlak van microschaal pilaartjes lateraal versterkt door bruggetjes aan te brengen tussen aangrenzende pilaartjes. De pilaarpatronen werden vervaardigd met behulp van lithografie, en bruggen werden vervolgens geïntegreerd door het spincoaten van het materiaal in vloeibare vorm, die bijgevolg via capillaire werking brug-vormende druppels vormen en vervolgens uitgehard worden. Metingen toonden aan dat in de aanwezigheid van deze overbruggende structuren, hogere wrijvingskrachten werden gegenereerd in vergelijking met adhesieven zonder bruggetjes. Dat komt vermoedelijk omdat in de aanwezigheid van bruggetjes knikken en samenklonteren van pilaartjes

voorkomen wordt, wat resulteert in hogere wrijving. Verder had de aanwezigheid van bruggetjes tussen pillartjes een positief effect op de herbruikbaarheid van de adhesieven, een effect dat toenam met toenemende dikte van de bruggetjes.

In hoofdstuk 5 hebben we het gebruik van interne versterkende wanden op millimeter lengteschalen onderzocht. Deze relatief grote lengteschaal van structuren maakt het mogelijk om commercieel beschikbare 3D-printtechnieken te gebruiken om de adhesieven te fabriceren. Gemaakte adhesieven hadden cilindrische poriën, gescheiden door wanden. Deze poriewanden waren stonden in richting van of haaks op de afschuifrichting. Poriën werden bedekt met een dunne toplaag met hoge vervormbaarheid in de normaalrichting. De verdeling, dikte en richting van de interne poriewanden beïnvloedden de stijfheid van het adhesief in afschuif- of normaal richting. Het bleek dat op zachte substraten de hoogste wrijvingskrachten werden gegenereerd door adhesieven met de meest vervormbare eindlaag, indien uitgelijnd met de afschuifrichting. De lage normale stijfheid zorgde voor een hoge contactvorming voorafgaand aan het schuiven, terwijl een hoge stijfheid in de schuifrichting voorkomt dat het gevormde contact met het zachte substraat verloren gaat wanneer belastingen in de afschuifrichting worden uitgeoefend.

In hoofdstuk 6 heb ik enkele van de bevindingen uit de vorige hoofdstukken geïntegreerd, en heb ik zachte adhesieven, inwendig versterkt met een stijf koolstofvezelweefsel, geïmplementeerd in een prototype voor een nieuwe chirurgische grijper. Twee soorten adhesieven werden geïmplementeerd, met ofwel een glad oppervlak (zonder patroon) of een oppervlak met het fijnste kuiltjespatroon zoals gepresenteerd in hoofdstuk 3. We vonden dat grijpinstrumenten uitgerust met zachte adhesieve oppervlaktes aanzienlijk lagere knijpkracht genereren op fantoomweefsel, terwijl de sterkte van de gegenereerde grip vergelijkbaar was met metalen referentiegrijpers. Gegenereerde krachten met deze grijper zijn in de orde van 1-2 N, waardoor deze grijper interessant is voor het grijpen van kwetsbare weefsels zoals aderen.

In dit proefschrift is de natuur gebruikt als inspiratie voor nieuwe technologie en bootsten we de functionaliteit na van een biologisch systeem. Bij gevolg, hoewel gefabriceerde adhesieven uiterlijke weinig weg hebben van de boomkikker, basale functionaliteiten zoals de aanwezigheid van interne versterkende structuren, zijn aanwezig in de vorm van interne wanden, bruggen of interne vezelstructuren.

Zusammenfassung

In der Chirurgie wird Weichgewebe meist mit Zangen gegriffen, die Reibungskraft erzeugen, also Normal- in Scherkräfte umsetzen. Häufig entstehen Probleme in der Nutzung dieser Greifzangen durch Fehler in dieser Kräfteerzeugung. Eine zu geringe Normalkraft lässt das Gewebe aus der Greifzange herausrutschen, während eine zu hohe Normalkraft zu Gewebeschäden führen kann. Eine mögliche Lösung zur Erzeugung eines gleichzeitig sicheren und schonenden Gewebegriffs ist die Nutzung von Adhesion. Hierbei wird der Kontakt zwischen Gewebe und Zange durch adhäsive Greifer-Gewebe-Wechselwirkungen aufrechterhalten, und ist somit nicht von der Normalkraft abhängig. Als Vorbild für die Entwicklung eines solchen Greifers kann der Baumfrosch dienen, welcher sich mit Hilfe des Klebegriffs an einer Vielzahl von natürlichen Oberflächen festhalten kann. Das Hauptziel dieser Dissertation besteht darin, die von Baumfröschen genutzten Prinzipien zur Haftkräfteerzeugung in das Design synthetischer Haftsysteme zu übertragen, um so einen sicheren und dennoch sanften Griff auf weichen Substraten zu erzeugen. Die Entwürfe der synthetischen Haftmaterialien in dieser Arbeit sind von zwei wichtigen Merkmalen der Zehen des Laubfrosches inspiriert: dem auffälligen, hierarchischen Muster der Zehenoberfläche und der inneren faserverstärkten Struktur des Zehs. Ziel dieser Arbeit ist vor allem das Imitieren der Funktion und weniger der Form. Sie konzentriert sich hierbei auf Mechanismen, die dem Haftapparat des Baumfrosches zugrunde liegen, um so zwei der Bedingungen starker Haftung zu erfüllen: (1) Erzeugung von Kontakt und (2) fortdauernde Erhaltung des erzeugten Kontakts.

In Kapitel 2 erläutern wir, dass es bei der Herstellung eines nano- oder mikrostrukturierten Haftsystems mit definierter Funktionalität wichtig ist diejenige Methode zu wählen, die am besten geeignet ist um die hierfür erforderliche Geometrie zu erschaffen. Darum führen wir gängige Herstellungsmethoden zur Erzeugung von Nano- und Mikrostrukturen auf und klassifizieren diese basierend auf funktionalitätsbedingten Faktoren, beispielsweise der geometrischen Komplexität oder dem Materialtyp. Wir zeigen, dass Elektronenstrahlolithographie die höchsten Auflösungen erreicht, dass diese Technik aber auch kostspielig und langsam ist. Mittels Photopolymerisation kann eine hohe geometrische Komplexität erreicht werden, jedoch ist die Fertigungsgeschwindigkeit gering und die erreichbare Strukturgröße auf wenige Millimeter begrenzt. Hohe Fertigungsgeschwindigkeiten können mit parallelen Methoden wie der Photolithographie erreicht werden, aller-

dings sind diese hinsichtlich der erreichbaren geometrischen Komplexität beschränkt.

Kapitel 3 beschreibt die Herstellung von Haftsystemen, deren Oberfläche ein Muster von dicht aneinander liegenden, kreisrunden Vertiefungen mit Durchmessern von entweder etwa 1 μm oder 10 μm aufweist. In einer dritten Variante wurde das Lochmuster mit Vertiefungen von 10 μm Durchmesser mit einer < 1 μm dünnen Schicht bedeckt. Diese Modifikation resultierte in einem Haftsystem mit dünner, glatter Oberfläche, welche im Inneren durch die Trennungsränder der Vertiefungen unterstützt wird. Adhäsion und Reibung der hergestellten Haftmaterialien wurden auf harten Glassubstraten und zwei weichen Polyvinylalkohol-(PVA)-Substraten mit ein Young's Modul von 12 und 18 kPa gemessen. Wir fanden heraus, dass auf weichen Substraten mikroskopische Vertiefungen eine höhere Haftung und Reibung erzeugen als submikroskopische Vertiefungen. In der Literatur beschriebene positive Auswirkungen von submikroskopischen Merkmalen auf Haftung und Reibung auf harten Substraten, wie beispielsweise Defektkontrolle und das Ablösekontrolle, scheinen auf weichen Substraten nicht aufzutreten. Eine Endsicht erhöhte die Adhäsion im Vergleich zu unstrukturierten Haftsystemen auf PVA um 12 kPa, vermutlich weil das weiche Substrat in die Mikrolöcher der Endsicht eingeklemmt wurde. Die höchste Reibung wurde von Haftsystemen mit mikroskopischen Vertiefungen ohne Endsicht erzeugt, was wahrscheinlich auf die Verzahnung der Vertiefungswände mit dem Substrat zurückzuführen ist.

In Kapitel 4 wurden Haftmaterialien mit Mikrosäulen hergestellt, die mit Brückenstrukturen zwischen benachbarten Mikrosäulen verstärkt waren. Die Mikrosäulen-Arrays wurden mit einem wechlithografischen Verfahren hergestellt. Anschließend wurden die Brücken durch Schleuderbeschichtung eines flüssigen Polymersiations-Vorprodukt verbunden, wobei sich die Brücken durch Kapillarwirkung bildeten und aushärteten. Die Messergebnisse zeigen, dass bei Vorhandensein von Brückenstrukturen höhere Scherkräfte erzeugt werden als bei Haftsystemen ohne Brückenbildung. Vermutlich verhindert die Brückenbildung das Umknicken und die irreversible Aggregation der Mikrosäulen, was zu höheren Scherkräften führt. Außerdem wirkte sich die Verbrückung positiv auf die Haltbarkeit der Haftsystemen aus, ein Effekt, der mit zunehmender Dicke der Verbrückung zunahm.

In Kapitel 5 untersuchten wir die Verwendung von inneren ~ 1 mm dicken/

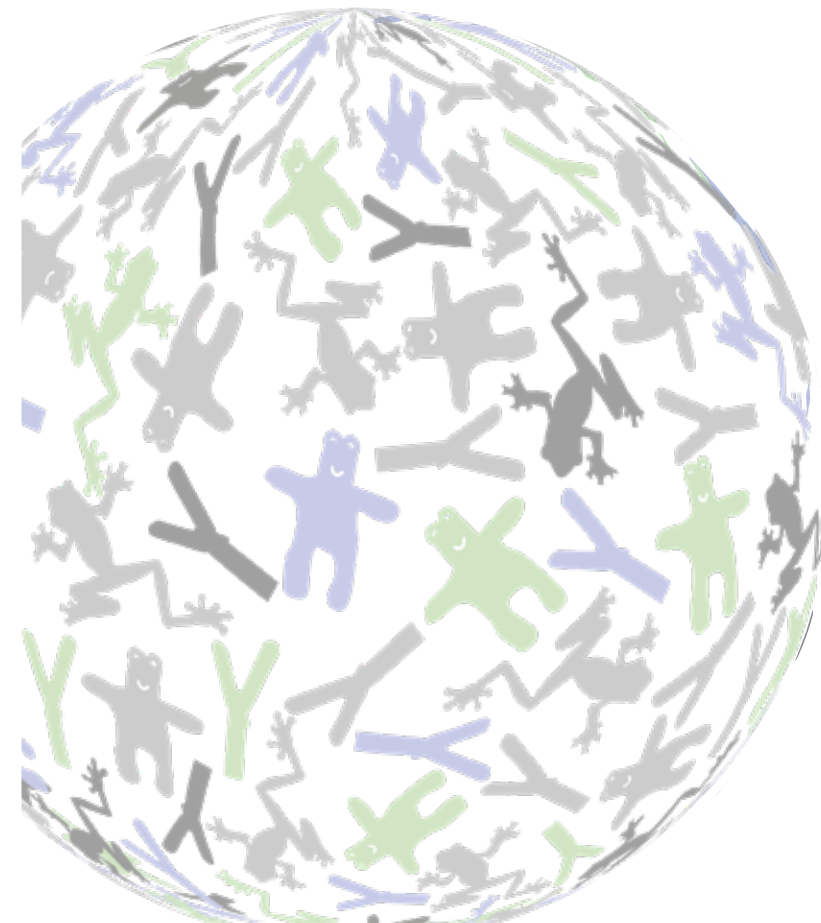
hohen Verstärkungswänden in Heftsystemen. Dieser relativ große Maßstab ermöglicht die Verwendung kommerziell verfügbarer 3D-Drucktechniken zur Herstellung der Haftsystemen. Es wurden Systemen mit unter der Oberfläche liegenden zylindrischen Poren hergestellt, die durch Porenwände getrennt sind. Die Porenwände waren entweder entlang oder senkrecht zur Scherrichtung ausgerichtet. Die Poren waren mit einer dünnen Deckschicht mit hoher Verformbarkeit in Normalrichtung bedeckt. Die Dichtheit, Dicke und Richtung der inneren Porenwände beeinflussten die Steifigkeit der Haftsystemen in Scher- und/oder Normalrichtung. Auf weichen Substraten wurden die höchsten Reibungskräfte durch Haftsystemen mit der flexibelsten Endsicht in Kombination mit den in Scherrichtung ausgerichteten Porenwänden erzeugt. Die geringe Normalsteifigkeit führte zu einer hohen Kontaktbildung vor dem Gleiten, während eine hohe Schersteifigkeit den Kontaktverlust mit dem weichen Substrat bei Scherbelastung verhindert.

In Kapitel 6 haben wir einige der Erkenntnisse aus den vorangegangenen Kapiteln integriert und weiche, im Inneren mit steifen Kohlefasern verstärkte Klebekissen in den Prototyp eines neuartigen weichen chirurgischen Greifers eingebaut. Es wurden zwei Arten von Klebepads implementiert, entweder mit einer unstrukturierten (glatten) Oberfläche oder mit einer Oberfläche mit Anordnungen von submikroskopischen Grübchen, wie in Kapitel 3 vorgestellt. Wir haben festgestellt, dass Greifer mit weichen Pads deutlich geringere Normalkräfte auf Gewebemodellen erzeugen, während sie ähnliche Greifkräfte wie Referenzgreifer aus Metall erzeugen. Die mit diesem Greifer erzeugten Greifkräfte liegen in der Größenordnung von 1-2 N, was dieses Design für die Handhabung von empfindlichem, verletzlichem Gewebe wie Venen interessant macht.

Diese Arbeit nutzte die Natur als Inspiration für eine neue Technologie und ahmte die Funktion des biologischen Vorbildes nach, nicht seine Form. Daher ähneln die entwickelten Haftsystemen zwar äußerlich keinem natürlichen Haftsystem, aber grundlegende Funktionen, wie das Verteilen von Kräften durch Verstärkungskomponenten, sind in jedem von ihnen vorhanden, entweder in Form von Innenwänden, Brücken oder internen Fasern.

Chapter 1

Introduction



1.1 Grasping in minimally invasive surgery

Laparoscopy is a surgical procedure for interventions in the abdomen or the pelvis region. Laparoscopy is a Minimal Invasive Surgery (MIS) procedure, performed through incisions of 1.5 cm in diameter at the most. The use of such small-sized incisions leads to reduced trauma compared to open surgery. In the Netherlands, thousands of operations are annually performed in a laparoscopic manner.^[1]

Grasping soft tissue is an important task during surgical procedures. In laparoscopic procedures, grasping forceps are used to pick and place soft tissues, expose or get access to the region of interest, or make space. The functionality of these grasping forceps relies on the translation of pinch forces into friction forces that prevent slipping of the tissue out of the forceps jaws.^[2] As laparoscopic procedures are performed through small incisions, surgeons experience distorted haptic feedback and sub-optimal ergonomics when using grasping instruments.^[3,4]

Due to the reduced haptic feedback and sub-optimal ergonomics, laparoscopic grasping forceps are associated with surgical errors. Specifically, because tissues are wet and soft, high pinch forces are required to generate sufficient grip. Errors occur when applying insufficient pinch forces, leading to tissue slipping out of the grasping forces, the need to repeat the grasping action, and thus prolonged operation times.^[5] Grasping errors also occur when applying excessive pinch forces.^[2] At the edges and ridges of the forceps jaws, stresses as high as 800 kPa have been measured.^[6] Considering that the safety threshold for cell apoptosis in abdominal organs is estimated at 200 kPa,^[7] subjecting the tissue to pressures four times higher than that might lead to complications, including bleeding, perforation, infection, or postoperative adhesions.^[8]

1.2 Generation of grip

Generating grip on an object is indispensable in various application fields, from lifting car parts in an assembly line to picking and placing fruits in horticulture or picking and placing microparts in electrical engineering. Gripping mechanisms strongly vary, depending on, among others, the size, stiffness, and vulnerability of the gripped object. Grip, for any application, requires the optimization of three main parameters: strength, reversibility, and load dependence.

- Strength

The required strength of the generated grip depends on the size and/or weight of the gripped object. When lifting heavy or large objects, mechanical gripping is typically used. For smaller or lighter objects, suction or adhesion could be used instead.

- Reversibility

Grip can be permanent or temporary. When glueing objects together, attachment needs to be permanent, whereas for pick-and-place procedures, the object needs to be gripped and released on demand.

- Load-dependence

When the gripped object is not vulnerable, applying some normal load on the object is not a problem. Oppositely, when grasping and placing soft tissues or soft fruits, grip needs to function with a minimum normal load to prevent damaging the gripped object.



Figure 1.1. Different applications in which generation of grip is required. Left: A gripper arm for picking up cars at a junkyard. High gripping strength is required, and a high load on the grasped car is allowed. From www.canva.com. Middle: An air-actuated gripper for gently grasping fruits. Gripping is based on embedding and releasing, and only a gentle load is applied. From: www.dutchsoftrobotics.nl. Right: Surgical instrument grasping a bowel. In this case, grip relies on pinch forces. From De et al.^[7]

The functionality of gripping solutions can be summarized by a combination of the above mentioned main parameters. Three fundamentally different gripping mechanisms can be distinguished.

Mechanical grip: Grip generation via clamping/interlocking. The length scale of gripped objects generally varies from meters^[9] to a few millimetres^[10] in size (see Yi for some exceptions).^[11] Mechanical solutions are preferred when strong and reversible grip is required. The gripping strength relies on applying high normal loads, embedding or interlocking.

Chemical grip: Areas are attached via chemical binding of two objects (e.g., curing a third binder component). The length scale of the attached objects is typically from centimetres^[12] to a few millimetres.^[13] Chemical binding is useful when grip needs to be permanent and independent of applied loads. For some chemical interactions, such as binding two substrates with a curing glue, the formation of close contact is required before binding or curing, which is achieved by applying pre-loading. Once the attachment is established, its strength is independent of the applied load and can even withstand negative loads.

Physical grip: Objects can be attached via physical interactions such as capillary effects^[14] or Van der Waals forces.^[15] The length scale of the attached objects is, depending on the type of physical interaction typically in the order of centimetres to millimetres, but can also occur at (macro) molecular scale. Some physical interactions, including Van der Waals interactions, require the formation of close contact by applying pre-loads for the interaction to occur. Once the attachment is established, it is independent of the applied load and can even withstand negative loading. Physical grip is reversible but typically not as strong as chemical or mechanical grip.

In these three gripping mechanism, two important stages can be recognized when grip is generated: contact formation and contact preservation. Depending on the application, the important of both stages differs. When gripping a car on a junkyard, the formation of contact is not challenging, but the high weight of the car makes the preservation of the formed contact during lifting challenging. This is solved by applying high pinch forces. When grasping slippery tissue with a surgical gripper, its functionality relies on applying high pinch forces order to preserve the formed contact. However, when grasping a vulnerable fruit, the formation of contact is maximized in order to lower the peak forces on the fruit. A glue in its liquid state efficiently conforms to surface roughness to maximize the contact formation. By curing of the glue, the formed contacts are fixated, and when loads are applied, the high area of contact prevents peak forces at the interface of attached surfaces.

Figure 2 shows the three fundamental gripping mechanisms related to how they do in terms of gripping strength, reversibility, and load independence.

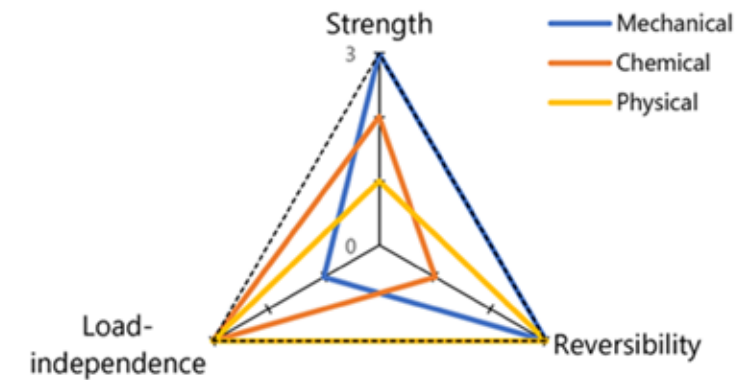


Figure 1.2. Performance of mechanical, chemical, and physical grip in terms of strength, reversibility, and load independence. Performance of gripping mechanisms is rated as 1 (low), 2 (medium), or 3 (high) on each of the three functional parameters. Physical grip has high load independence and reversibility. Improving the strength of physical grip has the potential to render a powerful gripping mechanism.

Figure 2 shows that none of the three gripping mechanisms scores high on all three functional parameters. The high strength of mechanical grip relies on applying loads on the gripped object. This load dependence makes it challenging to use mechanical grip for vulnerable objects. The strength of chemical grip depends on the binding or hardening of two objects or an in-between binder—processes intrinsically irreversible. Physical grip has a relatively low gripping strength compared to mechanical and chemical grip. While high loads are inherent to mechanical grip, and irreversibility is inherent to chemical grip, a low gripping strength is not per se inherent to physical grip. Therefore, improving the gripping strength of physical grip could lead to a powerful gripping mechanism for a range of applications requiring secure and gentle grip of deformable and vulnerable objects, including surgical applications.

1.3 Optimizing grip for surgical applications

For laparoscopic applications, grip needs to be strong enough to lift (parts of) tissue in the order of grams. Load independence is required to prevent damaging the vulnerable soft tissue. Additionally, grip needs to be reversible on a timescale of seconds in order to allow pick-and-place actions. In other words, the generated grip needs to be secure yet gentle on a soft, wet and slippery object. While engineered solutions that satisfy all these three requirements are lacking, nature offers a range of examples on how to generate strong grip on soft and vulnerable substrates. In these examples, we recognize structures with a function of contact *formation*, and structures with a function of *preservation* of the formed contact.

Geckos

Geckos' hairy toe pads generate reversible grip without using high normal loads. Toe pads of geckos are covered with ridges perpendicular to the shearing direction, so-called scansors, which are covered with hierarchical microscale hairs, ultimately branching into sub-micrometre sized setae.^[16, 17] These setae play an important role in forming multiple close contacts with the substrate to enable Van der Waals forces.^[18]

Researchers have successfully developed adhesive pads with fibrillar geometries, the attachment of which is based on Van der Waals interactions between fibrillar tips and the substrate.^[19-23] On the one hand, these fibrillar geometries rely on maximizing the formation of contact through their high adaptability to rough substrates to maximize Van der Waals interactions.^[24] On the other hand, these geometries efficiently preserve the contact that is formed. A contact split up into multiple smaller contact points has efficient stress-distributing and defect controlling properties on the length scale of the fibrils, hence higher resistance to applied stresses.^[24] With gecko-inspired adhesives, pull-off forces up to six times higher have been generated compared to unpatterned adhesive pads of similar sizes.^[25]

In geckos, the array of microscale seta is the main component responsible for maximizing the contact formation. The setae tips also have contact preservation properties, albeit mainly on the the microscale setae. The contact preservation of geckos on millimetre or centimetre length scales relies on the overall toe morphology.^[26] Loads on the toe pad surface are effectively transmitted from the scansors to internal stiff tendons aligned

in the shearing direction of the toe pad. These tendons are attached to the skeleton joints in the toe, which are connected to muscles. It is presumed that these internal reinforcing structures play an important role in load sharing, necessary to preserve the contact that has been formed.^[27, 28] Kim et al. showed that with lower deformability of the supporting layer, the generated adhesion of fibrillar structures increased. The authors contributed this observation to load sharing, leading to more efficient preservation of contact.^[28]

One disadvantage of gecko-inspired grip for surgical procedures is that contact formation with fibrillar geometries relies on Van der Waals-based interactions, which are inhibited when the two surfaces are separated by only a thin film of environmental water.^[29-31] Moreover, contact preservation in gecko-inspired adhesives relies on the global re-distribution of stresses over remaining contact points when one fibril detaches.^[32] However, on deformable substrates, neighbouring fibrils are coupled during detachment, which causes the growth of defects at the adhesive-substrate interface.^[32]

Tree frogs

Tree frogs are a fascinating example of how to adhere to wet and slippery substrates. Tree frogs can adhere to most substrates occurring in nature, including wet or even flooded substrates, with only a limited contact area available.^[33] Generated grip by tree frogs is reversible, and, as frogs are lightweight, applied normal loads are in the order of grams. The gripping apparatus of tree frogs can inspire adhesives that generate gentle grip on challenging substrates.^[34, 35]

Figure 3 shows the morphology of a tree frog toe pad. The toe pads are covered with a specific epidermal surface pattern, consisting of arrays of closely packed, polygonal (predominantly hexagonal) epithelial cells (Figure 3B).^[36] The diameter of these epithelial cells is 8-15 μm , depending on the species. The epithelial cells are separated by narrow grooves of 1-5 μm in width, resulting in a grid of channels covering each toe pad. Epithelial cells are covered with closely-packed peg-like protrusions, 15-800 nm in diameter, depending on the species (figure 3 C, D). These nanoscale pegs are again separated by a network of grooves, the width of which is much smaller than the nanoscale peg diameter. Tree frog toe pads are covered with a mucus layer (as is the rest of the body, which is the case for all amphibians).

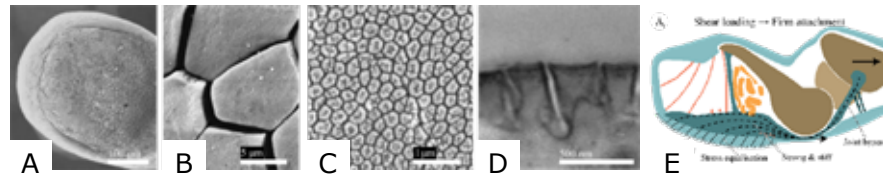


Figure 1.3. The toe pad of a tree frog on different length scales. A: The toe pad is covered with an array of predominantly hexagonal-shaped epidermal cells. B: These epidermal cells are separated by narrow grooves, forming a channel network covering the pad. C: Each epidermal cell is covered with closely packed peg-like protrusions. D: These protrusions are again separated by narrow grooves. E: A schematic representation of the internal geometry of a tree frog toe pad. Underneath the epidermis, collagen filaments are present, connected to the skeleton joint via collagen ligaments. A-D: Adapted from Federle et al.^[36] E: Adapted from Langowski et al.^[37]

The surface structure of tree frog toe pads has been hypothesized to contribute to the generation of capillary interactions via the formed mucus meniscus.^[38] The hierarchical groove network has been hypothesized to play a role in generating hydrodynamic forces.^[39] Moreover, these grooves might lead to efficient drainage of environmental water, maximizing dry contact formation.^[40, 41] At dry regions, Van der Waals interactions between toe pad and substrate occur. The grooves at the toe pad surface might also lead to interlocking, in which substrate protrusions enter the grooves.^[38,42]

The contribution of the internal structure of the toe pad to grip generation is much less well understood. Recently, Langowski et al. characterized the internal toe-pad morphology and presumed that a relatively stiff collagen layer is involved in transmitting shear forces from the contact interface into the stiff regions of the toe pad such as the skeleton.^[37] This collagen layer exists of long, stiff fibrils positioned across the toe pad, loaded in the tensile direction during shearing of the toe pad. Similar to geckos, this reinforcing internal component presumably plays an important role in transmitting shear forces and load-sharing to preserve the formed contact at the toe pad surface.^[37]

1.4 Aim and approach

Commonly, grip on tissue is generated with friction-based pinching instruments, the functionality of which relies on the transition of normal load to

friction.^[43] Tree frog attachment potentially offers missing links in the design and fabrication of artificial adhesives that can generate secure yet gentle grip on biological tissues. Existing tree frog inspired adhesives are usually tested on hard substrates, primarily glass and polystyrene.^[41,44,45]

While sophisticated fibrillary structures are required to maximize contact formation on a hard substrate, on a soft substrate, contact formation is facilitated by the deformability of the substrate. Therefore, *external* patterning of the adhesive might not be particularly contributing to the gripping strength on soft substrates. Furthermore, the contact preservation properties of fibrillar structures, as reported for hard substrates, are mostly lost on soft substrates, as detachment of neighbouring fibrils is coupled via substrate deformations, and defect control properties are largely lost.^[32] For grip on soft substrates, the challenge is not so much the formation of contact but rather the preservation of the formed contact.

The biological examples of geckos and tree frogs show that internal, sub-surface structures play a reinforcing role, resulting in load sharing and thus preservation of the formed contact. The *internal* structure of artificial adhesives, i.e., internal reinforcing components involved in grip by preventing stress concentrations at the adhesive-substrate interface, has not been extensively investigated yet.

The aim of this thesis is to develop nature-inspired artificial adhesives suitable for generating firm yet gentle grip on deformable and slippery substrates. Thereto, the internal directional reinforcing components as present in the tree frog toe pads are translated into technological analogues and implemented into artificial adhesives as a means of preserving the contact that has been formed. When abstracting the internal morphology of the tree frog toepad into artificial adhesives, we aim to abstract the *functionality* of this internal morphology (i.e., reinforcing components) rather than the *structure* (i.e., the literal mimicking of the internal collagen fibrillar geometry).

An important consideration when designing artificial adhesives with internal geometries is to find the most suitable fabrication method, taking into account the envisioned length scale, material properties, and internal and geometry of fabricated adhesives. In this thesis, both additive and subtractive approaches are used to fabricate adhesives with directional reinforcements.

Another design parameter that is explored in this thesis is the length scale of internal reinforcements. Where in nature internal reinforcements are present on hierarchical length scales by means of branching, we explore the functionality of internal reinforcements varying from micro- to mesoscale, including the combination of different length scales in one design.

Another perspective, not completely independent from the previous aspect of the length scale, is the strength and stiffness of the reinforcements. In this thesis, when the fabrication methods allowed for, we vary the strength and/or stiffness of reinforcements and investigate their effects on the generated gripping strength of artificial adhesives.

This thesis is part of a research project titled "Secure and gentle grip of delicate biological tissues", a collaboration between the Department of BioMechanical Engineering, Delft University of Technology and the Experimental Zoology Group (EZ), Wageningen University & Research. Figure 1.4 shows the outline of this collaborative research project. Where EZ has been focussing on the biological model of the tree frog, this thesis focuses on the design of artificial adhesives, in which principles of tree frog attachment are abstracted and used.

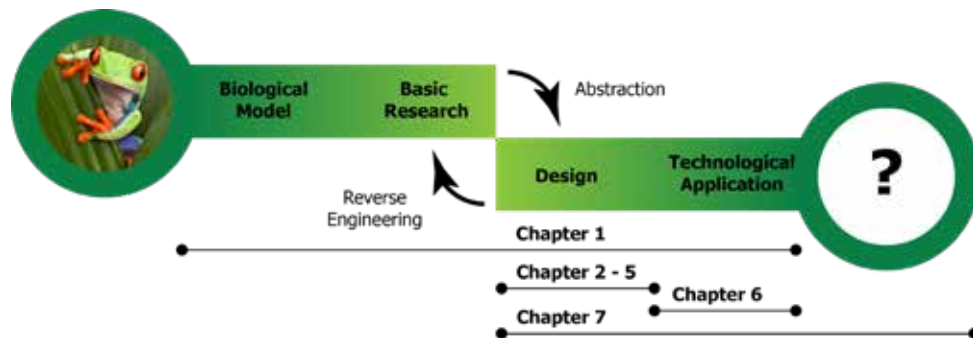


Figure 1.4. Placement of the thesis chapters in the research project "Secure and gentle grip of delicate biological tissues." The work of the Experimental Zoology Group at Wageningen University & Research focuses mainly on the biological model and basic research to the attachment of tree frogs. This thesis is about abstracting the obtained biological knowledge into designing artificial adhesives, and applying these designs in a technical application.

1.5 Outline of this thesis

In Chapter 2, we point out that the functionality of structures with microscale features, such as the envisioned adhesives in this thesis, strongly depends on parameters such as obtainable feature size, total dimensions, variety of materials, and the use of more than one type of materials in one structure. The obtainability of these architecture-related parameters strongly depends on the method that is used to fabricate an adhesive. This chapter outlines commonly used **fabrication methods**, organized by the architectural complexity and thus the functionality that can be realized with them.

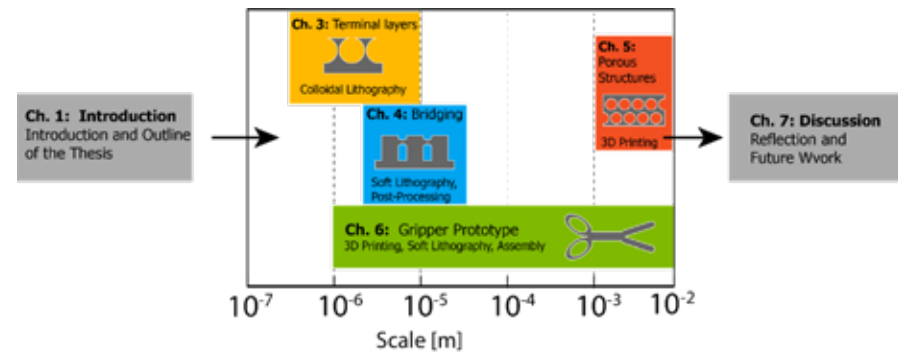


Figure 1.5. Outline of this thesis, with the different chapters projected on the length scale on which reinforcements are applied. For each design chapter, the used fabrication approach is also depicted.

In Chapter 3, we use colloidal lithography to fabricate **arrays of dimples with and without a terminal layer**. Dimples are fabricated on both sub-microscale and microscale, and the effects of length scale and geometry on adhesion and friction are investigated on slippery and deformable substrates of PVA. We find that a thin terminal layer facilitates the generation of grip on such substrates, possibly due to a thin-film peeling mechanism. Furthermore, given the presence of microscale holes in the terminal layer, an interlocking mechanism could not be ruled out.

In Chapter 4, we fabricated micropillar adhesives, and laterally reinforced these by introducing bridging in between micropillars. We use standard molding techniques to fabricate micropillar arrays, and use a spincoating method to introduce bridging in these arrays. We test adhesion and friction

of such **bridged micropillar adhesives** on slippery and deformable substrates as a function of feature size and soft-coating thickness.

Chapter 5 discusses adhesives with optimized internal geometries for grip on rigid and soft substrates. Architecturally complex **porous internal structures** are fabricated using 3D printing. We investigate the performance of adhesives that contain cylindrical voids with various packing and diameters. We combine these porous adhesives with fibrillar surface structures and measure adhesion and friction on slippery and deformable substrates as a function of geometry and pulling direction.

In Chapter 6, we integrate some results of earlier chapters in a **technical solution** for grip generation on slippery and deformable substrates. We investigate how the design and operation of grasping instruments are affected when the functionality is based on adhesion. Furthermore, we implement some of our tested adhesives in this prototype to demonstrate that load-independent grip is a promising approach toward secure and gentle grip of slippery and deformable substrates.

At the end of this thesis, we interpret the results we found, present some work that did not make it into this thesis, and reflect on the process of developing technology inspired by biological systems.

References

- [1] *Operaties in het ziekenhuis; soort opname, leeftijd en geslacht, 1995-2010*, **2014**, CBS
- [2] E. A. M Heijnsdijk, A. Padeloup, J. Dankelman, & D. J. Gouma, *Surgical Endoscopy*, **2004**, *18*(12), 1766–1770
- [3] P. Breedveld, H. G. Stassen, D. W. Meijer, & J. J. Jakimowicz, *Journal of Laparoendoscopic & Advanced Surgical Techniques* **1999** *9*(6): 469–80.
- [4] G. Tholey, J. P. Desai, J. P. & A. E. Castellanos, *Annals of Surgery*, **2005** *241*(1), 102–9.
- [5] T. R. Eubanks, R. H. Clements, R. H., D. Pohl, N. Williams, D. C. Schaad, S. Horgan, C. Pellegrini, C, *Journal of the American College of Surgeons* **1999**, *189*(6), 566–74.
- [6] J. A. Cartmill, A. J. Shakeshaft, W. R. Walsh, & C. J. Martin, *Australian and New Zealand Journal of Surgery*, **1999**, *69*, 127–130
- [7] S. De, **2008**, *The grasper-tissue interface in minimally invasive surgery: Stress and acute indicators of injury*, Doctoral Thesis, University of Washington, Washington
- [8] L. P. Stassen, W. A. Bemelman, J. Meijerink, *Surg Endosc.* **2010**, *24*(3), 495–498.
- [9] R. Wagner, *International Conference on Robotics and Automation*, **2008**, Presentation to the Orbital Robotics Workshop, Pasadena, CA.
- [10] C. Wang et al., *Journal of nanoscience and nanotechnology*, **2020**, *20*(3), 1401-1408.
- [11] Y. Qin, *Micromanufacturing engineering and technology*. William Andrew, **2010**, p. 176-183
- [12] S. Bhattacharya, A. Datta, J. M. Bert & S. Gangopadhyay, *Journal of Microelectromechanical Systems*, **2005**, *14*(3), 590-597.
- [13] R. J. Stewart, et al. *Advances in colloid and interface science* **2017**, *239*, 88-96.
- [14] G. Fantoni, H. N. Hansen, M. Santochi, *CIRP Annals - Manufacturing Technology*, **2013**, *62*(1), 17–20.
- [15] A. Del Campo, C. Greiner, E. Arzt, *Langmuir* **2007**, *23*(20), 10235–10243.
- [16] A. P. Russell, *J. Morphol.* **1981**, *169*, 293–323.
- [17] A. P. Russell, *J. Zool.* **1986**, *64*, 948–55.
- [18] K. Autumn, M. Sitti, Y. A. Liang, A. M. Peattie, W. R. Hansen, S. Sponberg, T. W. Kenny R. Fearing, J. N. Israelachvili, R. J. Full, *Proc. Natl Acad. Sci. USA* **2002**, *99*, 12252–6.
- [19] A. K. Geim, S. V. Dubonos, I. V. Grigorieva, K. S. Novoselov, A. A. Zhukov, A. A., & S. Y. Shapoval, *Nature Materials* **2003**, *2*, 461–463.
- [20] M. Sitti & R. S. Fearing, *Journal of Adhesion Science and Technology* **2003**, *17*, 1055–1073.
- [21] A. J. Crosby, M. Hageman, & A. Duncan, *Langmuir* **2005**, *21*, 11738–11743.
- [22] B. Yurdumakan, N. R. Raravikar, P. M. Ajayan & A. Dhinojwala, *Chemical Communications*, **2005**, 3799–3801.
- [23] N. Gravish, M. Wilkinson, S. Sponberg, A. Parness, A., N. Esparza, D. Soto, T. Yamaguchi, M. Broide, M. R. Cutkosky, C. Creton & K. Autumn, K., *Journal of the Royal Society Interface* **2010**, *7*, 259–269.
- [24] M. Kamperman, E. Kroner, A. Del Campo, R. M. McMeeking, E. Arzt, *Adv. Eng. Mater.* **2010**, *12* (5), 335–348.
- [25] A. Del Campo, C. Greiner, E. Arzt, *Langmuir* **2007**, *23*(20), 10235–10243.

Chapter 2

NANO- AND MICROSTRUCTURE FABRICATION: FROM DESIRED PROPERTIES TO SUITABLE PROCESSES

This chapter has been published as:

Peter van Assenbergh, Erwin Meinders, Jo Geraedts, Dimitra Dodou, Small **2018**, 14(20), 1703401. doi: 10.1002/sml.201703401

2

- [26] E. V. Eason, E. W. Hawkes, M. Windheim, D. L. Christensen, T. Libby, M. R. Cutkosky, *Bioinspir. Biomim.* **2015**, 10, 016013.
- [27] B. Chen, P. Wu & H. Gao *Proc. R. Soc.* 2008, A464, 1639–52.
- [28] S. Kim, M. Sitti, C.-Y. Hui, r. Long, A. Jagota, *Appl. Phys. Lett.* **2007**, 91, 161905.
- [29] G. Huber, S. N. Gorb, R. Spolenak, & E. Arzt, *Biology Letters* **2005**, 1, 2–4.
- [30] W. Sun, P. Neuzil, T. S. Kustandi, S. Oh & V. D. Samper, *Biophysical Journal* **2005**, 89, L14–L17.
- [31] A. Y. Stark, T. W. Sullivan, & P. H. Niewiarowski, *The Journal of Experimental Biology* **2012**, 215, 3080–3086.
- [32] E. Cheung and M. Sitti, *Langmuir* **2009**, 25, 6613.
- [33] J. Langowski, D. Dodou, M. Kamperman, J.L. van Leeuwen, *Frontiers in Zoology* **2020**, 15, 1-21.
- [34] L. Xue, B. Sanz, A. Luo, K. T. Turner, X. Wang, D. Tan, R. Zhang, H. Du, M. Steinhart, C. Mijangos et al. *ACS Nano* **2017**, 11 (10), 9711–9719 11 (10).
- [35] D. M. Drotlef, L. Stepien, M. Kappl, W.J.P. Barnes, H. J. Butt, A. Del Campo, *Adv. Funct. Mater.* **2013**, 23 (9), 1137–1146.
- [36] W. Federle, W. J. P. Barnes, W. Baumgartner, et al., *J. R. Soc. Interface* **2006**, 3, 689.
- [37] J. K. A. Langowski, H. Schipper, A. Blij, F. T. van den Berg, S. W. S. Gussekloo, J. J. van Leeuwen, *J Anat.* **2018**, 233(4), 478-495.
- [38] S. B. Emerson, D. Diehl, *Biological Journal of the Linnean Society* **1980**, 13(3), 199-216.
- [39] F. Kaveh, J. Ally, M. Kappl & H. J. Butt, *Langmuir* **2014**, 30(39), 11619-11624.
- [40] C. Dhong, J. Frechette, *Soft Matter* **2015**, 11(10), 1901-1910.
- [41] R. Gupta, J. Frechette, *Langmuir* **2012**, 28(41), 14703-17412.
- [42] N. Crawford, T. Endlein, J. T. Pham, M. Riehle, W. J. P. Barnes, *Beilstein journal of nanotechnology* **2016**, 7(1), 2116-2131.
- [43] H. De Visser, , *Grasping Safely: Instruments for bowel manipulation investigated*, **2003**, Doctoral Thesis, Delft University of Technology, Delft.
- [44] D. M. Drotlef, L. Stepien, M. Kappl, W. J. P. Barnes, W. J. P.; H. J. Butt, A. Del Campo, *Adv. Funct. Mater.* **2013**, 23(9), 1137–1146.
- [45] B. Murarash, Y. Itovich, M. Varenberg, *Soft Matter* **2011**, 7(12), 5553-5557

Abstract

When designing a new nano- or microstructure, one can follow a processing-based manufacturing pathway, in which the structure properties are defined based on the processing capabilities of the fabrication method at hand. Alternatively, a performance-based pathway can be followed, where the envisioned performance is first defined, and then suitable fabrication methods are sought.

To support the latter pathway, fabrication methods are here reviewed based on the geometric and material complexity, resolution, total size, geometric and material diversity, and throughput they can achieve, independently from processing capabilities. Ten groups of fabrication methods were identified and compared in terms of these seven moderators. We found that the highest resolution is obtained with electron beam lithography, with feature sizes below 5 nm. The highest geometric complexity is attained with vat photopolymerization. For high throughput parallel methods, such as photolithography ($\sim 10^1$ m²/h), are needed. This review offers a decision-making tool for identifying which method to use for fabricating a structure with predefined properties.



2.1 Introduction

Nano- and microstructures are used in several research and application fields. Advancements in nano- and microfabrication technologies over the last decades include increasingly smaller feature sizes, enhanced functionality, and improved economic viability either for large-scale production in industry or for small-scale production in laboratory research. For example, in the information-technology industry, feature sizes of Integrated Circuits (ICs) are continuously scaled down, consistent with Moore's law of biennial doubling of the number of transistors on a microprocessor chip.^[1,2] In polymer sciences, researchers emulate biological structures with feature sizes down to 10 nm and with self-cleaning,^[3] adhesive,^[4-6] anti-reflective,^[7] and sensing^[8] properties. In the biomedical field, nano- and microstructures are fabricated as antibacterial and antiadhesive coatings for implantable prostheses^[9,10] and as scaffolds for enhanced tissue regeneration.^[11] Nano- and microfabrication methods are also used to make nano- and micro-electro-mechanical systems (NEMS and MEMS), for example for trapping biomolecules or biostructures,^[12] for facilitating diagnostic purposes,^[13,14] and for carrying out chemical reactions in a configurable and scalable fashion.^[15,16] MEMS and NEMS can also be paper-based, making fabricated structures disposable, or fully recyclable at low cost.^[17]

The wide array of applications for nano- and microstructures is accompanied by a variety of fabrication methods. Lithographic methods, such as photolithography, electron beam lithography, and ion beam lithography, are the fabrication methods of choice in the field of microelectronics,^[18] likely due to the high resolutions and throughput that these methods can achieve. Additive manufacturing (AM) of micro- and nanostructures is gaining attention for fabrication of photonic crystals,^[19] bio-inspired adhesives,^[20] and optical data storage,^[21] probably because the digital nature of the AM process allows on-demand manufacturing and thus wide diversity in structural design.^[19,22] Pattern transfer methods, such as stamping and molding, are greatly used for research purposes, as they are simple and low-cost, providing a fast and effective tool toward structures with nano- or micrometer-sized features^[23] and compatible with a range of materials, including biomaterials,^[24] polymeric materials,^[25] and paper.^[26]

The diversity of nano- and microfabrication methods, their rapid progress in terms of resolution and geometric complexity, and the emergence of new

fabrication methods create a need for systematic comparisons between these methods, in order to depict what is currently possible in terms of manufacturability and to identify trends in the development of fabrication methods and their applications. Several classifications of nano- and microfabrication methods have been presented in the literature. Gates et al.^[23] distinguished between conventional (i.e., commercialized) and unconventional (i.e., emerging) nano- and microfabrication methods, and between top-down (e.g., lithographic) and bottom-up (e.g., molecular or particle interaction and assembly) methods. These authors predicted that one of the main future trends will be the development of fabrication techniques that enable resolutions under 20 nm at low cost. Brinksmeier et al.^[27] classified nano- and microfabrication methods based on two large application fields: microsystem technologies (including micro-electro-mechanical systems [MEMS] and micro-opto-electro-mechanical system [MOEMS]) and micro-engineering technologies (including mechanical components, molds, and micro-structured surfaces). These authors observed that while each of these two fields employs a different set of preferred fabrication techniques (e.g., photolithography primarily being used in microsystem technologies and micro-engraving being used in microengineering technologies), (electron, ion, and laser) beam lithographic methods are used in both fields. Qin et al.^[28] divided micro-manufacturing methods in traditional MEMS-based manufacturing methods, and emerging non-MEMS-based manufacturing methods. A few years later, Razali and Qin^[29] presented an alternative classification based on the nature of the process used, distinguishing between additive, subtractive, deforming, joining, and hybrid processes, and argued that deforming processes, such as stamping, are highly promising for industrial applications, but that achieving high throughput in combination with precise positioning of the material in an industrial environment is a critical bottleneck. A similar classification was made earlier by Dimov et al.,^[30] based on whether a fabrication method relies on removal or addition of material, and on the number of dimensions in which processing occurs (e.g., milling being a one-dimensional material-removal process and injection molding being a three-dimensional material-adding process). Dimov et al.^[30] acknowledged that it is unlikely that a sole type of fabrication technology becomes dominant and highlighted the importance of integrating multiple technologies and of developing hybrid technologies. Vaezi et al.^[31] argued that MEMS technology will improve with the availability of more complex 3D microstructures and accordingly reviewed 3D micro-additive manufacturing methods, classified in scalable additive manufacturing methods (with which

both macro- and microscale structures can be fabricated), 3D direct writing methods (suitable for microscale structures only), and hybrid processes (in which additive and subtractive processes are combined).

A common feature of the aforementioned classifications is that nano- and microfabrication methods are categorized based on their processing characteristics. This is certainly meaningful, resonating field-dependent developments in fabrication methods. A consequence thereof might be, however, that researchers and designers could miss opportunities that are becoming available outside their fields of expertise. When designing a new nano- or microstructure, it may be more fruitful to choose a fabrication method based on the properties of the envisioned structure rather than deciding on the properties of the structure based on the processing capabilities of the fabrication methods at hand.

The difference between a processing-based and a performance-based decision-making can be illustrated by the three-link chain model proposed by Olson,^[32] which integrates relations between processing, structure, property, and performance, in a manufacturing roadmap. Olson distinguished between a processing-based (deductive) and a performance-based (inductive) pathway through the chain (**Figure 2.1**).^[32] While the deductive approach follows the path from processing towards performance, an inductive approach is also possible, according to which the structure needed for the envisioned performance and properties is defined first, and then the most suitable processing methods are sought. Such a pathway shift is ongoing in the rapidly evolving field of AM, in which “depending on the needed structure, a suitable AM process for manufacturing can be selected that is able to create the needed structure.”^[22] (see also Bourell et al.,^[33] in which such an inductive design methodology is identified as a way to assist understanding the relationships between processing, structure, properties, and performance).

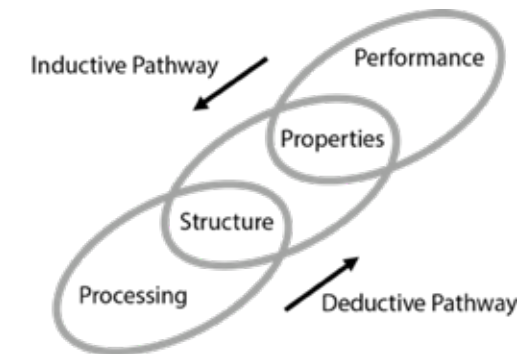


Figure 2.1. Three-link chain model integrating the relations between processing, structure, property, and performance of an engineered structure. Adapted from Olson et al.^[32]

To support a performance-based pathway of designing and fabricating nano- and microstructures, in this paper we review nano- and microfabrication methods based on the geometric characteristics and the materials the structure is made of, independently from the processing characteristics of the fabrication methods (e.g., subtractive vs. additive, top-down vs. bottom-up) and their current application fields (e.g., nano- or microelectronics, bioengineering, etc.). Accordingly, in this review, we review nano- and microfabrication methods based on the following four moderators:

- **Geometric complexity:** Geometric complexity refers to the architectural design of a functional nano- or microstructure, the complexity of which we consider increasing with the presence of geometric features such as curvatures, cavities, and overhangs. We define three levels of increasing geometric complexity, ranging from 1 to 3, which will be introduced later in this section.
- **Material complexity:** With material complexity we refer to the number of materials that can be used in one structure, resulting in integration of materials with different values of the same material property (e.g., variable degrees of stiffness) or integration of materials serving different properties (e.g., one material for low stiffness and another material allowing for conducting regions in the structure). We define two levels of material complexity, single (one material in the structure) and multiple (two or more materials in the structure).

- **Resolution:** Resolution is defined as the smallest volume that can be added to or removed from a structure. This volume is determined by both the size of the smallest piece of matter that can be added or removed (which is sometimes referred to as the smallest feature size) and the minimal spatial separation between two added or removed pieces of matter.^[34] The minimal spatial separation is determined by the attainable placement accuracy and/or by the properties of the material that is added or removed. Here, we use a 4-point scale to quantify resolution, ranging between ≤ 10 nm, 11–100 nm, 101 nm–1 μ m, and > 1 μ m.
- **Total size:** Total size refers to the maximum attainable total area of the structure. We use a 4-point scale to quantify the total size of nano- or microstructures, ranging between < 1 mm², 1–99 mm², 1–10 cm², and > 10 cm².

The contribution of each of these four moderators to the performance of a nano- or microstructure varies between applications. For example, performance of patterned adhesives is predominantly determined by their geometric complexity (e.g., mushroom-shaped pillars,^[35] hierarchical structures^[36]), but high resolution (i.e., small size of features^[37]) and the use of more than one material in the structure^[38] can also be employed for enhancing adhesion. Another example is MEMS, the performance of which is assumed to improve with miniaturization of these systems, leading to higher processing speeds, energy conservation, and cost reduction.^[39] Application of nanoscale components (as is done in NEMS) introduces even more functionalities, including space-efficient and light-weight structures or high mechanical resonance frequencies^[39,40]. However, next to resolution, material complexity (i.e., integration of different materials^[41]) and geometric complexity (e.g., stacked architectures^[41,42]) also contribute to the performance of MEMS.

Next to the four above-mentioned moderators of a single nano- or microstructure, an important criterion in deciding which fabrication method to use is the flexibility of methods, that is, the extent of the output, both in terms of diversity and in terms of size. Accordingly, in this review we also include the following three moderators:

- **Geometric diversity:** With geometric diversity we refer to the variety of shapes that can be fabricated with the same instrumental setup. For

example, with one three-dimensional mold only one geometry can be made, whereas with a scanning beam lithography setup multiple geometries can be made. We define geometric diversity based on the number of dimensions (between zero and three) in which a structure can be independently tuned. For example, for imprinting methods, this number would be zero, whereas for a scanning-beam lithographic method, the structure is freely tunable in two dimensions (with the possibility of linearly extruding a two-dimensional pattern in the third dimension by varying etch depth).

- **Material diversity:** With material diversity we refer to the variety of material types of which a nano- or microstructure can be made. A fabrication method that allows for higher material diversity can be used to attain structures with a greater variety in material properties (e.g., structures with various degrees of stiffness or refractive indexes). We define two levels of material diversity, in which level 1 implies that the fabrication methods can accommodate only one group of materials (e.g., only metallic materials, or photosensitive materials, or biomaterials), and levels 2 implies compatibility with more than one group of materials.
- **Throughput:** Throughput refers to fabrication speed. Depending on the type of fabrication method, throughput is expressed in 'writing length per second',^[19,43] 'area or volume per hour',^[19] or 'wafers per hour'.^[44–46] Here we use a 4-point scale to characterize throughput, ranging between low, medium, high, and very high. A low throughput means fabrication speed in the order of a few mm² per hour, a very high throughput is in the order of tens of mm² per hour.

In recent years, the quest for functional structures inspired by nature raised great interest in the relation between function (e.g., light harvesting,^[47] impact-resistance,^[48] adhesion^[49,50]) and properties (e.g., strength, toughness, stiffness) by means of varying structural rather than material properties.^[51,52] Indeed, to meet the natural equilibrium between material formation and degradation,^[51] biological materials are limited in both number and performance (e.g., natural materials are typically soft or brittle^[52,53]), and exceptional properties originate from geometric complexity, rather than from the used materials. An example thereof is the impact-resistant club of smashing stomatopods, which is used to hammer the shells of prey. The high strength of the club originates from a specific architecture, namely a

helical arrangement of mineralized chitin fibres, resulting in a so-called Bouligand geometry.^[54]

Following this rationale, we chose to classify the fabrication methods based on the geometric complexity that can be attained with them. We operationalize geometric complexity based on the number of isolines, also referred to as contour lines,^[55] required to describe the topology of the structure (or of one module of the structure, in the case of a periodic structure, that is, a structure consisting of repetitive modules) and define accordingly three levels of geometric complexity (**Table 2.1**). We borrowed the concept of isolines from physical geography (among other fields), where isolines are commonly used as an effective two-dimensional representation of three-dimensional landscapes and surfaces. We defined the three levels of geometric complexity.

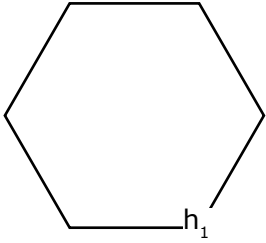
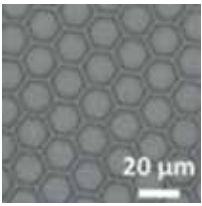
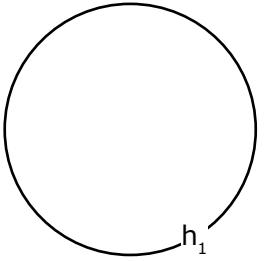
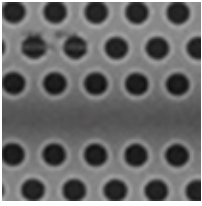
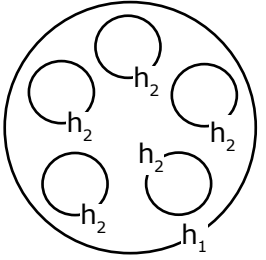
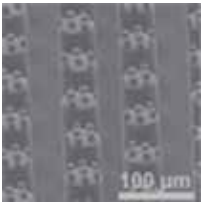
Level 1. Two-dimensional structures, extruded in the third dimension with a fixed extrusion height or depth. When a three-dimensional structure is an extrusion of a planar pattern with a fixed extrusion height or depth, one isoline, with a nonzero height or depth, is required to describe the structure.

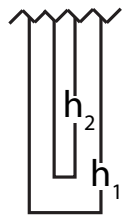
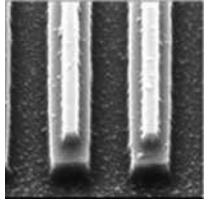
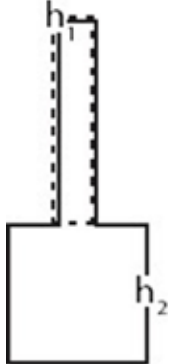
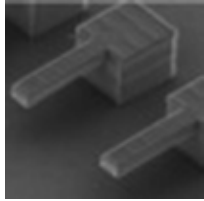
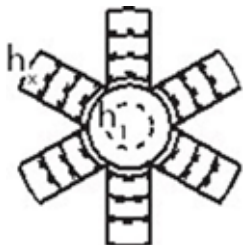
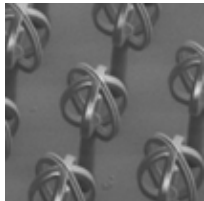
Level 2. Three-dimensional structures with areas of various heights and no overhanging parts or cavities. Two or more isolines are required to describe such structures, and for *all* pairs of isolines it holds that if $h_2 > h_1$, then $l_2 \leq l_1$, where h is the height of the isoline and l is the length of the isoline. The larger the variability in heights (cf. structures with curved surfaces), the larger the number of isolines required to describe the structure.

Level 3. Three-dimensional structures with overhanging parts and/or cavities. The contour map either contains crossing isolines or there is *at least* one pair of isolines for which it holds that if $h_2 > h_1$, then $l_2 > l_1$.

These levels of geometric complexity are comparable to three shape categories for particles in a dispersion, as presented in Reuter et al.,^[56] who distinguished between “quasi 2D” (shaped in plane), “hemi 3D” (shaped in half space), and “fully 3D” (shaped in the entire space).

Table 2.1. Levels of geometric complexity.

Geometric complexity level	Contour map	Examples and applications
<p>Level 1. Two-dimensional structures, extruded in the third dimension with a fixed extrusion height or depth. The structure is an extrusion of a planar structure with a fixed height or depth. One isoline, with a nonzero height (or depth) h_1, is required to describe the structure.</p>		 <p>Patterned adhesive consisting of hexagonal pillar arrays, fabricated using molds made with photolithography. Adapted with permission.^[6] Copyright 2015, John Wiley and Sons.</p>
		 <p>Two-dimensional photonic crystals, deposited and self-assembled on a silicon substrate. Adapted with permission.^[57] Copyright 2017, The Japan Society of Applied Physics.</p>
<p>Level 2. Three-dimensional structures with areas of various heights and no overhanging parts or cavities. Two or more isolines are required to describe the structure, and for <i>all</i> pairs of isolines it holds that if $h_2 > h_1$, then $l_2 \leq l_1$, where l is the isoline length and h is the isoline height.</p>		 <p>Hierarchical adhesive, fabricated with a two-step molding process. Adapted with permission.^[58] Copyright 2009, John Wiley and Sons.</p>

		 <p>Two-level lines on a substrate, to be cut into T-shaped particles. Made with imprinting lithography. Adapted with permission.^[56] Copyright 2017, Springer Nature.</p>
<p>Level 3. Three-dimensional structures with overhanging parts and/or cavities. The contour map either contains <i>at least</i> one pair of isolines for which it holds that if $h_2 > h_1$, then $l_2 > l_1$ (top picture; the isoline with height h_1 is located partially under the isoline with height h_2), or contains overlapping (i.e., crossing) isolines (bottom picture). The dashed lines are located below the solid lines and are slightly shifted (laterally at the top picture and radially at the bottom picture) for the sake of visibility.</p>		 <p>Micro-cantilevers to be used for quantifiably evaluating the mechanical properties of the material the structure is made of. Adapted with permission.^[59] Copyright 2012, AIP Publishing LLC.</p>
		 <p>An air-trapping surface to be used underwater. Fabricated with stereolithography. Adapted with permission.^[60] Copyright 2015, American Chemical Society.</p>

In the remainder of the paper, nano- and microfabrication methods are presented in order of ascending geometric complexity; for each fabrication method, we briefly describe the working principle and assess the method in terms of the aforementioned moderators. In the discussion section, a

decision tool is presented, in which all seven moderators are taken into consideration simultaneously.

2.2 Fabrication methods for two-dimensional structures extruded in the third dimension with a fixed extrusion height or depth (geometric complexity level 1)

Nano- and microstructures the third dimension of which is an extrusion of a two-dimensional pattern can be manufactured by means of scanning probe lithography, photolithography, scanning (ion or electron) beam lithography, colloidal lithography, and block-copolymer lithography.

Scanning probe lithography (SPL)

In SPL, a scanning probe tip is used to pattern substrates in either an additive (so-called additive SPL) or a subtractive (called subtractive SPL) fashion by transferring molecules toward or from a substrate mechanically, diffusively, electrically, or thermally.^[61] SPL can be realized with a standard atomic force microscope (AFM), making SPL an accessible, versatile, and appealing method for nanoscale engineering.^[61,62] The main advantage of SPL is that, with piezoelectric positioning of the scanning probe tip, resolutions of 10 nm can be achieved in a direct-writing step.^[63] Structures are freely written in or on a substrate, and are thus tunable in two dimensions. Due to their serial character, a limitation of SPL methods is that throughput is typically low: writing speeds are in the order of micrometers per second, and higher writing speeds typically go at the expense of resolution. One approach to increase the throughput with SPL is to use multiple tips simultaneously.

Processing conditions are generally mild in terms of temperature and stress on the sample, and a wide range of materials and substrates can be used, including biomaterials and soft matter.^[61] Furthermore, some SPL techniques allow for patterning with different materials either simultaneously^[64] or consecutively.^[65,66]

For a review on SPL techniques and their applications, see Garcia et al.^[61]

Additive SPL methods

Additive SPL methods are based on deposition of material on a substrate to form a pattern. Here, we discuss dip pen nanolithography (DPN) and bias-induced SPL. In DPN, an AFM tip is used to transfer molecules or a liquid ink to a substrate by molecular diffusion or fluid flow, respectively.^[63,67] DPN is a fitting tool for patterning biomaterials, because of the absence of harsh post-treatments such as ultraviolet, ion-, or electron-beam irradiation, and due to its high compatibility with soft matter.^[67] The thickness of the deposited layer depends on the used material that is deposited, and is fixed throughout the whole structure. DPN has been used to pattern self-assembled monolayers of molecules for trapping oligonucleotides, viruses, or proteins.^[23] Another example of patterning self-assembled monolayers with DPN was presented by Wang et al.,^[68] who used DPN to pattern a gold substrate with circular 16-mercaptohexadecanoic acid arrays, on which self-assembly of single-walled nanotubes (SWNTs) was then directed (**Figure 2.2**).

To increase throughput, Chen et al.^[69] used 55,000 tips simultaneously to write a pattern of initiator molecule on a gold substrate, on which a resist layer was grown. In a subsequent etching step, the written pattern was transferred into the underlying gold substrate.

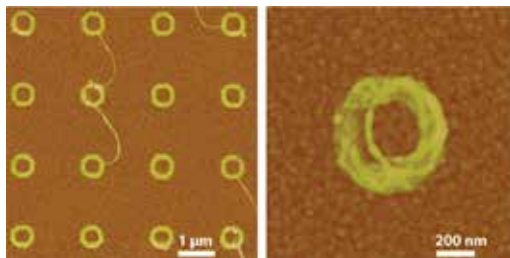


Figure 2.2. Left: Single-walled carbon nanotubes on a gold substrate, arranged in circles. Right: Close-up of one nanotube. Self-assembly of the nanotubes was directed on circular 16-mercaptohexadecanoic acid arrays created on a gold substrate by means of dip pen nanolithography (DPN). Reproduced with permission.^[68] Copyright 2006, National Academy of Sciences.

Bias-induced SPL is another additive SPL method, in which a voltage is applied over the AFM probe and the substrate, to induce local deposition or transformation^[61] For example, Ferris et al.^[70] coated a substrate with a polymer brush and then used bias-induced SPL to electrochemically pattern

the surface of the polymer brush. Such electrochemical patterns can act as templates for self-assembly or for local deposition of inorganic molecules.

Subtractive Scanning Probe Lithography methods

Subtractive SPL methods include thermal SPL and some forms of bias-induced SPL. Thermal SPL is an SPL method in which the substrate is altered by means of evaporation induced via a heated tip. By varying the tip temperature, the writing depth can be controlled with an accuracy down to 10 nm.^[71,72] Bias-induced SPL is also used in a subtractive fashion, inducing electrochemical processes to remove matter. For example, by locally inducing oxidation, nanopatterns can be written.^[61,73] Because of the time needed for the tip-substrate interaction to take place, most types of electrical SPL (whether additive or subtractive) come with low writing speeds.^[19] In subtractive SPL, substrate-tip interactions can also be of mechanical nature, such as scratching.^[74]

With SPL, typically single-layer structures are fabricated. A recent paper on SPL has shown that it is possible to use SPL to print structures in a layer-by-layer fashion, resulting in structures with various heights throughout the structure.^[75] If SPL turns out to be an established method for such structures, SPL will be upgraded to a complexity level 2-method.

Photolithography

In photolithography, a photoresist layer is applied on a substrate. Then, the photoresist layer is exposed to light through a photomask, that is, a planar array with transparent and opaque regions that form a pattern. Upon light exposure, the chemical stability of the photoresist changes, and depending on the type of the photoresist, either the exposed (in the case of a so-called positive resist) or unexposed (negative resist) areas of the photoresist become soluble. In a subsequent etching step, the chemically altered areas of the photoresist are removed, resulting in a patterned photoresist layer. Next, the photoresist is hardened to obtain the final structure.^[23]

Besides photosensitivity, photoresist materials need to have specific requirements, such as etch resistance, adhesion to the underlying substrate, or ability to form defect-free thin films.^[76] Commonly used photoresists are SU-8, polyimide, and Parylene C.^[77] When photolithography is used for the fabrication of ICs, the patterned photoresist acts as template for patterning the underlying semiconducting silicon layer in a subsequent etching step,

and the resist is removed after pattern transfer.^[76] Due to the parallel nature of photolithography, complete layers are patterned in a single-step exposure or etch. Therefore, multi-layer or multi-material structures can only be made with post-processing or repeating exposing and etching cycles.

The attainable geometric diversity with photolithography is low, since a two-dimensional pattern (the mask) acts as template to fabricate an extruded structure. The only freely tunable dimension is the height or depth of the structure, which can be controlled by choosing the resist layer thickness. Photolithography has a parallel nature, meaning that two-dimensional arrays can be fabricated in a single exposure step, and feature sizes in the μm -range were obtained already in the 1970s.^[78] The method was therefore rapidly adopted by the industry, particularly for the fabrication of ICs and printed circuit boards (PCBs).

In both industrial and laboratory settings, the basic principle of photolithography is the same, but moderators such as throughput and resolution can be very different. Industrial photolithographic instruments have been drastically evolved in terms of throughput and resolution by means of automatization and optimization of the instrumentation. The required instrumentation is costly,^[79] but with such optimized setups, structures can be fabricated at throughputs of more than 100 wafers per hour (equivalent to over 28 m² per hour),^[80] making the costs per patterned area relatively low.

On laboratory level, photolithography is used for fabrication of, among other applications, bio-inspired adhesive microstructures^[4,6] and microfluidic chips,^[81,82] because great geometric diversity (with the use of a different photomask for each structure) and reasonable resolutions (in the order of micrometers) are possible with lab-scale photolithographic setups. Expensive optics and automatization machinery are not required for such research purposes, and therefore the costs of a photolithographic lab instrument can be two orders of magnitude lower as compared to industrial setups.

Depending on the distance between the photomask and the substrate, three types of photolithography can be distinguished: projection photolithography, proximity photolithography, and contact photolithography. Another parallel lithographic method is plasmonic lithography. Finally, lithography with light can be also used without masks. Such maskless optical lithographic methods will be discussed in section 2.3.

Projection photolithography

Projection photolithography is sometimes referred to as far-field (optical) lithography,^[83] because a distance between the mask and the substrate has to be maintained. An optical lens (or a series of mirrors and lenses) is located between the mask and the substrate, focusing the light after it passes the mask and allowing pattern-size reduction of 2–10 times with respect to the mask.^[83] The high resolutions that can be attained (down to 37 nm)^[83] in combination with the high throughput make projection photolithography the most common method for fabricating ICs.^[84]

The main challenge of projection photolithography is that at high resolutions, the mask acts like a diffraction grating.^[85] To cancel out diffraction effects, expensive phase-shifting optics and high-sensitive photoresists are required.^[86] With the introduction of Deep UV lasers, the wavelength was reduced from 365 nm to 248 nm in 1995 and to 193 nm in 2000,^[87] minimizing these diffraction effects. Resolutions down to 37 nm with a 193 nm-wavelength excimer laser have been demonstrated.^[83] With an expected wavelength of 13.5 nm, the use of extreme ultraviolet lithography (EUV) has resulted in resolutions below 10 nm.^[88] With the use of double-patterning (or multiple-patterning), in which a pattern is split in two (or more) masks that are subsequently projected into the resist layer, patterns with a higher density and resolution than the used masks can be obtained.^[87]

Besides photons, also ions can be used with masks to transfer patterns into resist layers, as is done in ion projection lithography.^[89,90] With ion projection lithography, thanks to lower diffraction effects than with photon projection lithography, a high accuracy can be obtained, although obtainable resolutions are lower.^[90]

Proximity photolithography

In proximity photolithography, the distance between photomask and photoresist is much smaller than in projection photolithography, and no optics are used to downsize the projection, significantly suppressing the costs as compared to projection photolithography.^[83] The attainable resolution with proximity (photo)lithography can improve by decreasing the laser wavelength λ and the proximity length x between the mask and the substrate according to $\sqrt{\lambda \cdot x}$.^[91] To obtain resolutions below 30 nm, the proximity length has to be at the sub-micrometer level, which is challenging.^[92] At the beginning of the 21st century, methods were developed to correct for or even

exploit Fresnel diffraction at the photomask, allowing larger mask-substrate distances.^[91]

Due to the absence of expensive optics, proximity photolithography is a cost-effective technique, considering the resolutions (2–3 μm) and throughput that can be obtained with it.^[83] Recently, extreme ultraviolet (EUV) proximity lithography has been used for the fast fabrication of arrays of infrared antennas with feature sizes in the μm -range.^[92]

Contact photolithography

In contact photolithography, the proximity length x is brought to zero, that is, the mask and the resist layer are in contact.^[93] Linewidths of around 16 nm have been fabricated using gratings in contact with the resist.^[94] The downside of this method is that the contact can cause defects on the mask or resist layer, which is the main reason why contact photolithography is not the photolithographic method of choice for industry.^[95]

Plasmonic lithography

In plasmonic lithography, a thin metal plate is mounted on a prism of (typically) glass prism. When a light beam hits the metal plate through the prism at a certain incident angle, the normal component of the light wave vector couples with the wave vector of surface plasmon polaritons (SPPs) in the metal. Because of the permittivity difference between the metal and the supporting glass, this photon-SPP coupling induces SPPs propagating along the metal surface with frequencies much higher than the photons used to induce them. In plasmonic lithography, this phenomenon is used to pattern a resist layer with SPPs.

A challenge with plasmonic lithography is that SPPs decay faster than photons (in the order of 5–20 nm), only allowing for proximity lengths that are much shorter than those achieved with proximity photolithography.^[96] Feature sizes down to 22 nm have been demonstrated, by projecting a ring-shaped interference pattern of plasmonic oscillations on a resist layer.^[97] By giving the metal surface a typical curvature, high intensities of SPPs can be generated very locally, resulting in even smaller writing beams. A recent example of this is the incorporation of bowtie-shaped apertures in a metal layer. SPPs were collected at the narrowest part of the bowtie, resulting in a writing spot with diameters down to 16 nm.^[94]

Scanning beam lithography

Direct-writing lithographic methods are referred to as scanning beam lithography (SBL). In SBL, a pattern is written on a resist layer by one or more scanning beams of photons, electrons, or ions. Note that the 'resist' layer does not necessarily act as an etch-resistant layer, but rather as the layer that is manipulated. SBL methods are often used for the production of lithographic masks.^[83]

Similar to masked lithographic methods, with scanning-beam fabrication methods a pattern is freely written on or in a planar substrate. The extrusion depth of the two-dimensional pattern is determined by the resist thickness or the beam intensity. The attainable resolution of SBL methods improves with lower beam intensities, which reduce the beam spot size. As a consequence, the search for resists with higher sensitivities (i.e., reacting at exposure to low-intensity beams) is a critical element in SBL.^[98] Due to the serial character of SBL, manufacturing speed is slow: it can take 24 hours to pattern a 1-cm² array with 20-nm features.^[23] SBL-fabricated structures are geometrically complex and diverse, and therefore, SBL-fabricated structures are commonly used as templates (molds or masks). Materials for resists that are compatible with SBL are limited, because they need to be photon-, electron-, or ion sensitive. Here, we discuss optical beam lithography, interference lithography, electron beam lithography, and ion beam lithography.

Optical beam lithography

In optical beam lithography (OBL), also referred to as maskless photolithography, two-dimensional structures with a defined height or depth are written in or on a planar substrate using UV light. Photons react with the substrate atoms by means of the photoelectric effect or by initiating photopolymerization to reduce or increase the etch resistance of a resist layer. Depending on the used resist, resolutions of about 50 nm can be achieved with OBL.^[34] Similar to masked photolithography, using light with shorter wavelengths (e.g., EUV: 13.5 nm) reduces diffraction effects. With OBL, where the photoresist is cured by means of photopolymerization, the depth of polymerization can be defined by tuning the photon intensity at the focal point of the beam. Therefore, OBL is used to write nanometer-sized lines with a defined height on a substrate.^[99] Due to this tunable polymerization depth, OBL is also suitable for the fabrication of stacked two-dimensional projected structures, resulting in level-2-complexity structures.^[34]

Interference lithography

Interference lithography (also referred to as holographic lithography) is a variant of OBL, in which the interference pattern of two coherent beams is projected on a resist layer.^[100] Alternatively, beams (or one wide beam) are diffracted with gratings to generate interference patterns.^[84] When using the second order intersect of two interfering beams, the pathway between light source and substrate is elongated, resulting in further pattern size reduction (sub-10-nm linewidths with EUV lasers).^[101] Interference lithography has the limitation that the resist layer can only be patterned with periodical structures.^[84]

Electron beam lithography

In electron beam lithography (EBL), electrons are accelerated toward a resist layer on a substrate. The dominant mechanism of EBL is electron-electron collision, resulting in either crosslinking (in case of a negative resist) or scissoring (in case of a positive resist) of the polymeric resist layer.^[102] Subsequently, a developing step (e.g., etching) is required to obtain a pattern. The resist layer can be made of hydrogen silsesquioxane (HSQ), poly(methyl methacrylate) (PMMA), NaCl, SiO₂, or LiF.^[103] The use of a high-sensitive resist such as HSQ improves the resolution of EBL, but this comes with the disadvantage that HSQ has a high susceptibility for beam scattering and back-scattering at the resist;^[102] by defining and predicting the back-scattering, however, structures with sub-5-nm feature sizes have been fabricated (**Figure 2.3**).^[104] This resolution limit is not determined by the electron beam diameter, but by the mechanical strength of the resist during the subsequent developing step. In EBL, high resolution comes with a low electron dose, and therefore goes at the expense of throughput.^[104]

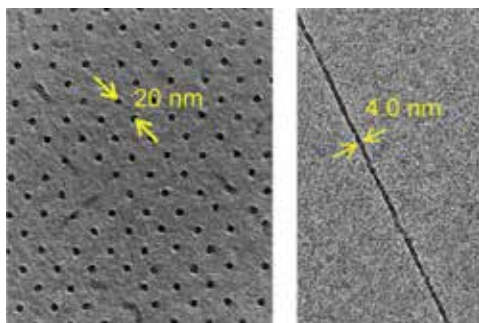


Figure 2.3. Left: A dot array in hydrogen silsesquioxane (HSQ), fabricated with electron beam

lithography. The center-to-center distance between two dots is 10 nm, and the diameter of one dot is 5.1 nm. Right: An isolated line in HSQ, with 4-nm width. This is the smallest obtainable width at which the line did not collapse during development. Adapted with permission.^[104] Copyright 2013, American Chemical Society.

Ion beam lithography

Ion beam lithography (IBL) is a collective name for techniques in which a focused beam of ions is used to modify a surface by altering its structure or chemical properties, or by atom removal.^[105] An advantage of IBL as compared to EBL is that ions scatter less than electrons upon collision with the resist layer, minimizing collateral modifications of the resist.^[105] Moreover, ion beams have a higher impact on the substrate, meaning that a lower dose suffices to leave a pattern.^[105]

Focused ion beam lithography (FIB) is an IBL method in which heavy ions (typically Ga⁺ ions, around 30 keV) are used. The heavy ions alter the substrate upon colliding. Depending on the resist, the substrate is milled, ions are implanted, or the substrate is sputtered.^[90,105] FIB was invented in the 1970s and became commercially available 10 years later.^[90] A beam spot size of 8 nm has been reported and used to write 10-nm-sized features in a 30-nm thick layer of PMMA.^[106] In **Figure 2.4**, 8-nm wide lines, written in a 50-nm thick resist layer of AlF₃/GaAs are depicted. Such small features were obtained thanks to vaporization of the resist upon etching, which filters the edges of the ion beam and leads to a peak intensity in the center of the ion beam.^[107]

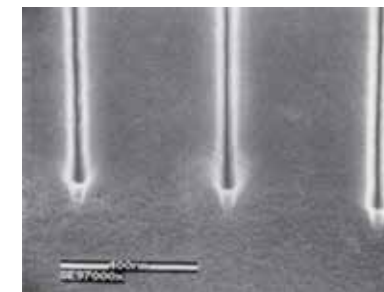


Figure 2.4. Lines with a width of 8 nm in a AlF₃/GaAs resist, fabricated with focused ion beam lithography. Reproduced with permission.^[107] Copyright 1999, Elsevier.

p-beam writing is another IBL method, in which protons are used to write

directly and deeply in a resist layer.^[90] Protons are light and fast ions, with energies typically in the MeV range, which interact with substrate ions and undergo thousands of collisions before they are adsorbed. Contrary to the heavy ions used in FIB, light-ion beams show minimal internal scattering. Moreover, light ion beams have well-defined penetration depths, which is useful for manipulating one (thick) resist layer at several depths to create multi-layered structures.^[90]

Directed self-assembly of planar two-dimensional structures

By directing the self-assembly of macromolecules on a substrate, a variety of planar patterns can be made. These patterns act as templates that are transferred into or onto underlying layers by means of etching, deposition, or stamping in parallel high-throughput processes.^[108,109] As such, two-dimensional patterns, which are extruded in the third dimension with a fixed extrusion height or depth, can be generated.

Self-assembled templates can be fabricated by tuning the physical or chemical properties of self-assembling (macro)molecules such as block-copolymer (BCPs) or colloids upon deposition on a substrate.^[110] DNA has also been used as building block for nanoscale structures. Folding and self-organization of DNA molecules can be directed by, for example, using pre-defined base pair sequences obtained from enzymatic synthesis.^[111] In this section, we discuss block-copolymer lithography, colloidal lithography, and nanoporous anodic aluminum oxide.

Block-copolymer lithography

In block-copolymer (BCP) lithography, a thin film of self-assembled block-copolymers on a substrate is used as a lithographic mask after selective removal of one block by dissolving or etching. Self-assembly of BCPs can be driven by phase separation of the two (or more) blocks, induced by, for example, dissolving the polymer in a solvent, temperature modification, or acidity modification. Self-assembly of BCPs on a substrate can also be induced by modifying the supporting substrate to create initiation point of self-assembly, for example by applying defects using IBL^[105] or pattern high-affinity regions using SPL.^[112] By incorporating etch-resistant blocks in the BCP, the BCP pattern is transferred to an underlying functional layer through etching.^[108,113,114] Alternatively, a metallic layer can be evaporated

on top of the self-assembled pattern; subsequent lift-off of the polymer layer leaves the desired pattern on the underlying substrate.^[115] Onses et al.^[116] integrated self-assembly of block-copolymers with electro-hydrodynamic jet printing (EHD; see section 23) by printing microdroplets of BCPs dissolved in an organic solvent (**Figure 2.5**).

The resolution of BCP lithography can be tuned with the BCP block sizes and chemical properties, and is typically in the order of 10 nm.^[108] Line widths of 6 nm have been also reported.^[117] Materials used as BCP include polystyrene (PS), polymethyl methacrylate (PMMA), poly(ethylene-alt-propylene) (PEP), and poly(vinylpyridine) (PVP).^[114] Because of its relatively low costs and high attainable resolutions, BCP lithography is used for the fabrication of nano-patterns for IC fabrication, photonics, and membrane fabrication.^[113,118] With photolithography being pushed to its resolution limits at the expense of high costs, BCP lithography is a very promising method for semi-conductor manufacturers in their search for ever smaller feature sizes.^[108] Fundamental geometries required in IC fabrication, including lines, dots, t-junctions, bends, and jogs can be obtained using directed self-assembly.^[119] Next to being used as templates, self-assembled layers are used as functional thin films or ordered nanoparticle arrays,^[19] photonic structures,^[120] and antireflective coatings.^[121]

BCPs can also self-assemble into three-dimensional structures. We will discuss these structures under section 24.

Colloidal lithography

Colloidal lithography, also referred to as nanosphere lithography, is a special type of contact photolithography, in which, instead of a patterned photoresist layer, colloids are used as a two-dimensional template. The colloidal pattern can be transferred by means of etching (in which, similar to BCP lithography, etch-resistant colloids act as a positive resist), deposition or evaporation (with subsequent lift-off of the colloids), or imprinting.^[122,123] Colloidal lithography is a cost-effective nanofabrication method, and has been used to fabricate nanohole arrays, often used in nanophotonic devices.^[124] Lithographic masks from colloids can be further used to create triangular patterns, nanorings, and pillars.^[125] In colloidal lithography, polymeric colloids (made of e.g., polystyrene (PS),^[126]) and metallic colloids are most commonly used. When a colloidal crystal is used as an etch-resistant mask, the underlying layer consists of, for example, a polymeric layer,^[127]

Table 2.2. Fabrication methods for two-dimensional structures extruded in the third dimension with a fixed extrusion height or depth (geometric complexity level 1).

Fabrication method	Material complexity	Resolution	Total size	Geometric diversity	Materials diversity	Throughput
<p>Substrate Scanning probe Ink Resist layer (e.g., thermo-responsive polymer) Heated scanning probe Subtractive SPL (thermal SPL)</p>	Multiple materials possible	10 nm ⁽⁶³⁾	Up to 500 μm ² (61)	Two tunable dimensions	Multiple materials possible: Biomaterials, soft matter, nanoparticles, graphene, silicon, ceramics, etc.	Low
<p>Photo-UV Light Photoresist layer Etching 1. Photoresist layer 2. Etching 3. Substrate Photoresist selectively removed Etching Photoresist and exposed regions in metallic layer removed</p>	Multiple materials possible	Down to 37 nm; (83) potentially sub-10 nm ⁽⁸⁷⁾	15-cm diameter circular substrates	Two tunable dimensions	Only photosensitive materials	Very high
<p>Substrate Resist layer Laser beam Subtractive OBL: excitation Photoresist Additive OBL: photopolymerization</p>	Single material structures	52 nm ⁽⁹⁴⁾	2x2 cm ² substrates ⁽⁴⁵⁾	Three tunable dimensions	Only photosensitive materials	Low
<p>Substrate Resist layer FIB Sputtered atoms Resist layer Milling/Sputtering/Writing Resist layer FIB Implanted atoms Chemical modification/implantation</p>	Single material structures	8 nm ⁽¹⁰⁷⁾	12.5x12.5 mm ² pillar arrays; [90] centimeter-sized patterns [105]	Two tunable dimensions	Polymeric or metallic materials	Low

glass,^[128] or silica.^[129] Deposition with colloidal templates is typically done with metallic materials.^[130] The attainable material complexity with colloidal lithography is low, since the colloidal pattern is transferred or deposited into a single-material layer.

Nanoporous anodic aluminum oxide

When carried out in an acid electrolyte, the anodic oxidation of aluminum results in a nanoporous layer of aluminum oxide.^[131] In a method referred to as nanoporous anodic aluminum oxide (AAO), size and distance between pores is controlled in a two-step anodization process. Before anodization, a substrate of aluminum is electropolished to obtain a nanoscale flat substrate. Subsequently, in the first anodization step, pores are grown with various inter-distances and at various angles. Upon the removal of the oxide layer, a homogeneous array of nanoscale dimples is revealed, covering the aluminum substrate. These dimples form the onset for pore growth during a second anodization step, resulting in a homogeneous pore array in an aluminum oxide layer. By varying the applied voltage during oxidation, the viscosity of the electrolyte, or the temperature, the pore size and center-to-center distance between the pores can be varied.^[132,133] With AAO, Buijnsters et al.^[134] developed a range of structures with tunable wettability by tuning the pore array. AAO surfaces can also be used as templates to shape polymer layers by imprinting, or for fabricating pillars by molding.^[135]

Table 2 illustrates the basic working principles and specifications of fabrication methods for two-dimensional structures, extruded in the third dimension with a fixed extrusion height or depth (geometric complexity level 1).

2.3 Fabrication methods for three-dimensional structures with areas of various heights and no overhanging parts or cavities (geometric complexity level 2)

Three-dimensional structures with areas of various heights but without overhanging parts or cavities can be fabricated with droplet deposition methods and molding techniques. In this section, droplet deposition methods (electrohydrodynamic jet printing and laser-induced forward transfer), hard molding (nanoimprint lithography and step-and-flash imprint lithography), and soft molding (replica molding, microtransfer molding, micromolding in capillaries, solvent-assisted micromolding, microcontact printing, and nanotransfer patterning) techniques are reviewed.

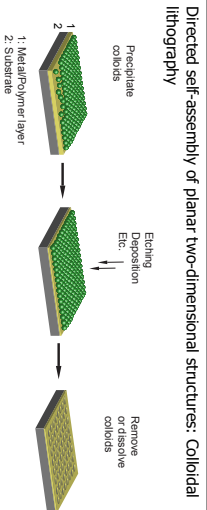
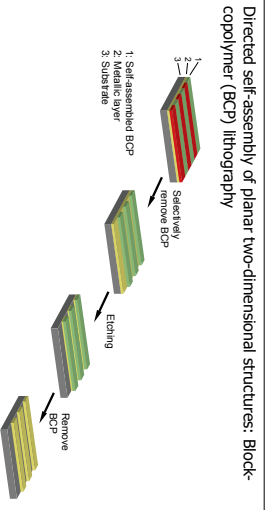
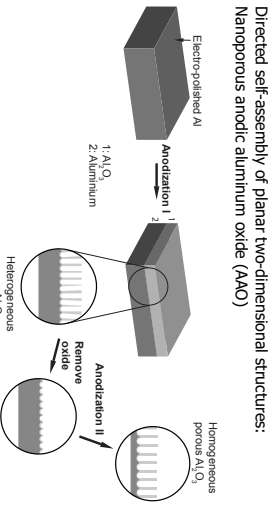
Droplet deposition methods

Droplet deposition methods are methods in which structures are formed out of liquid droplets of, for example, metals or particle solutions. Structures are built from fusion of droplets by melting or flowing upon deposition. Droplet deposition methods are mainly used for depositing two-dimensional patterns, resulting in structures of level-2 geometric complexity. Three-dimensional structures can be fabricated in a layer-by-layer fashion, or in a sequential fashion to create, for example, wire-like structures.^[138] The attainable resolution of droplet-printing methods is limited by the droplet size, which is typically in the order of 100 nm.^[138] Droplet printing methods have a serial character in all three dimensions, as opposed to scanning beam methods, where the pattern height or depth is developed simultaneously with the two-dimensional patterning. Therefore, droplet-printing methods are relatively slow. Here, we discuss electro-hydrodynamic jet printing and laser-induced forward transfer.

Electro-hydrodynamic jet printing

In electro-hydrodynamic jet printing (EHD), microdroplets of nanoparticles, polymers, and proteins are used to print patterns on a substrate. The ink microdroplets are created by applying an electric potential over a larger ink droplet ejected through a nozzle, causing mobile ions to accumulate at the nozzle tip and to form a pulsating droplet, which is called a Taylor cone.^[19] By controlling the electric field strength, streams of droplets much smaller than the nozzle diameter can be formed. The resolution of EHD improves with a decreasing size of the jetted microdroplets, for example by opti-

Table 2.2. (continued)

Fabrication method	Material complexity	Resolution	Total size	Geometric diversity	Materials diversity	Throughput
 <p>Scanning beam lithography: Electron beam lithography (EBL)</p>	Single material structures	4 nm ^[109]	Wafers and photomasks up to around 30 cm diameter ^[78]	Two tunable dimensions	Polymeric or metallic materials	Low
 <p>Directed self-assembly of planar two-dimensional structures: Colloidal lithography</p>	Single material structures	Down to tens of nm	Up to 15 cm (6-inch) diameter substrates ^[138]	Two tunable dimensions	Polymeric or metallic materials	Medium
 <p>Directed self-assembly of planar two-dimensional structures: Block-copolymer (BCP) lithography</p>	Single material-structures	6 nm ^[117]	300 nm diameter wafers ^[127]	Two tunable dimensions	Polymeric or metallic materials	Medium
 <p>Directed self-assembly of planar two-dimensional structures: Nanoporous anodic aluminum oxide (AAO)</p>	Single material structures	10–450 nm ^[134]	1 cm ²	Two tunable dimensions	Only aluminum oxide	Low

mizing the Taylor cone using viscoelastic inks,^[139] and with increasing microdroplet placement accuracy. Accuracy of microdroplet placement can be increased by lowering the distance between the nozzle and the substrate^[19] or by surface functionalization, in which case the positioning of the microdroplets is controlled by regions of varying wettability or by relief on the surface.^[140] A maximum positioning accuracy around 10 μm has been reported.^[140] Feature sizes down to 240 nm with a nozzle diameter of 300 nm were achieved by Park et al.^[140] by dissolving 3-nm sized nanoparticles in microdroplets. Upon evaporation of the microdroplet, nanoparticle deposits were obtained. With EHD, it is possible to print more than one material in one structure. For example, Sutanto et al.^[141] used organic silver ink to print conductive lines, with photo-curable polymer prints as an isolator between the conductive lines.



Figure 2.5. Electro-hydrodynamic jet printing of a butterfly from microdroplets of BCP solution. The light and dark colors originate from the use of two PS-*b*-PMMA, with different block sizes. The images left and right show magnifications of dark and light regions. The fingerprint-like patterns at the bottom two images are the result of BCP self-assembly. Reproduced with permission.^[116] Copyright 2013, Springer Nature.

Laser-induced forward transfer

In laser-induced forward transfer (LIFT), metal droplets are transferred to a substrate from a so-called donor layer. This layer has a thickness of about 100 nm and is positioned at about 100 μm from the substrate. The donor layer is supported by a transparent carrying layer, and upon selective exposure to a pulsed laser, local evaporation of the donor layer results in ejection of microdroplets, which are captured by the substrate.^[142] Metals that are used in LIFT include chromium, tungsten, gold, nickel, and aluminum; also pastes, hydrogels, and liquids can be used in LIFT methods.^[142] Because the droplets melt together upon deposition, structures fabricated with LIFT are relative inhomogeneous. The droplet size depends on the size of the

focal point of the laser, and thus the exposed area on the donor layer.^[143] Layers with a thickness of 3.5 μm have been fabricated.^[143] Moreover, high aspect-ratio pillars (5 μm in diameter, 860 μm in height) have been fabricated by stacking of droplets (**Figure 2.6**).^[142] Since droplets are deposited in vertical direction, overhanging structures cannot be printed in principle, although some metallic droplets, when molten together, do provide sufficient mechanical strength to realize overhanging structures.^[144]

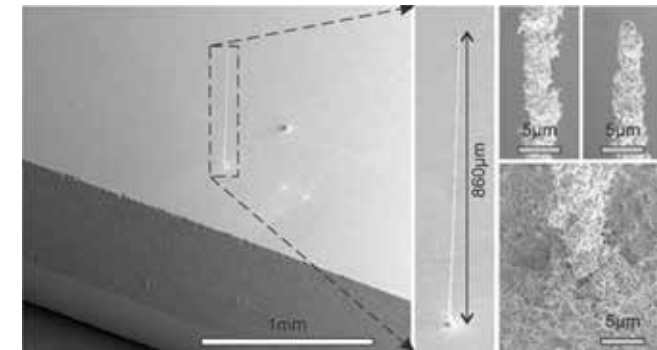


Figure 2.6. Left: A high-aspect ratio pillar fabricated with laser-induced forward transfer. Middle: A close-up of the same pillar. Top right: The thickness of the pillar at its center and top is about 4 μm . Bottom right: The thickness of the pillar at its base is 6 μm , because of multiple droplets being deposited close to the pillar. Adapted with permission.^[142] Copyright 2015, John Wiley and Sons.

Imprinting with hard molds

In imprinting methods, a three-dimensional template (referred to as mold) is used to press a pattern into a layer located on a substrate. The shaped layer is commonly referred to as the resist layer. If the resist layer is heated before imprinting, these methods are sometimes called hot embossing.^[145] Hard molds are usually fabricated by means of SBL and typically made of quartz or silica, because these materials are chemically inert to most monomers and (pre-) polymers.^[23] Moreover, because of the low thermal expansion coefficients of quartz and silica, hard molds are compatible with manufacturing processes that require high temperatures.^[146]

Forming nano- or microstructures in a resist layer with the use of a hard mold is a contact process and therefore comes with specific challenges. The pressure on the resist needs to be uniformly distributed during molding, which is facilitated by the residual layer, the compressed layer of resist that

prevents the mold from making contact with the underlying substrate. Removing the residual layer after molding requires a subsequent etching step of the molded structure.^[147] Defect control during release of the mold is also a challenge, commonly tackled by pre-coating the mold with a release layer.^[148,149]

With imprinting methods, the fabricated structure is freely tunable in one dimension, because the imprint depth or the thickness of the deposited layer can be freely tuned. Because a full two-dimensional pattern is imprinted in a parallel fashion, the throughput of imprinting methods is in the order of 10^{-4} m²/hour, which is typically higher than most serial methods.^[19] Hard molding methods can be divided in nanoimprint lithography (NIL) and step-and-flash imprint lithography (SFIL), which both will be discussed here.

Nanoimprint lithography

In nanoimprint lithography (NIL), a mold is used to shape a polymer glass when above the transition temperature T_g of the polymer. Upon cooling down, the polymer hardens, and the template is removed, leaving the patterned resist.^[46] The patterned layer can be the final nanostructure or can act as an etch-resistant layer in a subsequent etching step. NIL, sometimes referred to as thermal NIL, was introduced in 1995,^[46,150] and exceptionally low feature sizes (about 10 nm) were demonstrated soon after that.^[25] Therefore, and because of limited instrumental requirements and a high-throughput, NIL quickly became a serious contender of conventional nanofabrication methods such as photolithography and EBL.^[149] To increase the throughput of NIL, the use of a rolling pin-like mold was suggested in 2008,^[151] in which a flexible oblong substrate is guided over a rotating cylindrical mold. NIL has been used to make soft molds or stamps,^[152] high aspect ratio parallel lines on a substrate,^[149] nanopillars,^[153] and microfluidic devices.^[154] A silica mold with 10 nm wide pillars, separated by 40 nm spacing, was fabricated to imprint a polydimethylsiloxane (PDMS) layer (**Figure 7**), resulting in similar sized holes.^[25] High aspect ratios of about 20 have been also reported.^[155] NIL is often used as part of a fabrication toolbox set, for example for fabricating the master structure in a replication molding process.^[148]

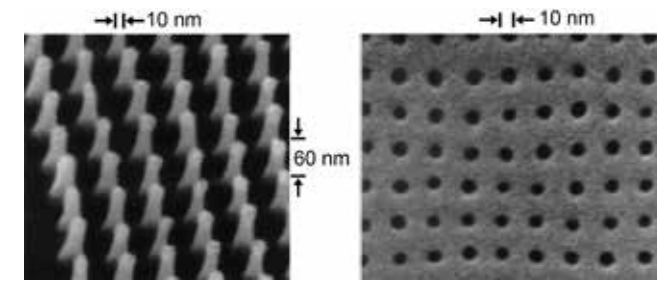


Figure 2.7. A silica mold (left), used to imprint a polydimethylsiloxane layer (right). The holes are 10 nm wide; the spacing is 40 nm. Reproduced with permission.^[25] Copyright 1997, AIP Publishing.

Step-and-flash imprint lithography

In step-and-flash imprint lithography (SFIL; sometimes referred to as UV-NIL),^[149] UV light is used to polymerize a photosensitive pre-polymer during molding. The mold has thus to be transparent, made of, for example, quartz or silica.^[146] SFIL is more suitable than NIL for fabricating structures consisting of multiple stacked layers, because, due to the transparency of the mold, layer alignment is easier with SFIL. Furthermore, because of the milder molding conditions of SFIL, the shaped layers do not need to undergo large temperature changes for each subsequent layer, as is the case with NIL.^[23,156] Photocurable low-viscous acrylate-based precursors^[157] and biomaterials^[24] can be used as resists. SFIL has also been used in a two-step imprinting processes to replicate complex structures (**Figure 8**).^[158] With SFIL, lines of 20-nm width have been fabricated, as well as multi-layered structures.^[159] Even 4-nm line widths were demonstrated by imprinting an ion-beam fabricated pattern of HSQ into a PDMS-based UV resist.^[160] A method similar to SFIL is jet-and-flash imprint lithography (JFIL), in which the resist layer is jetted on a substrate.^[24]

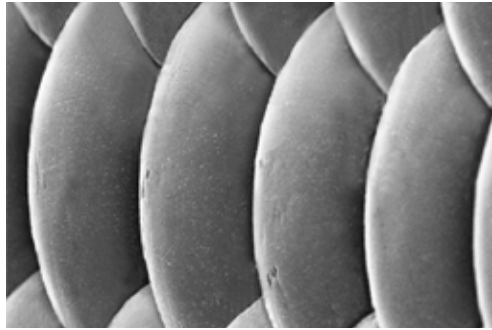


Figure 2.8. Replicated microlenses, fabricated by a two-step SFIL process. A negative replica of the master mold was obtained by imprinting a UV-curable resist. Upon application of a release layer, this negative replica was used in a second imprinting step to obtain the replicated microlenses. Scale bar is 10 μm . Adapted with permission.^[158] Copyright 2018, Springer Berlin Heidelberg.

Shaping and printing with soft molds

Fabrication methods in which soft molds are used for shaping, printing, or pattern transfer are generally referred to as soft lithography. Soft molding methods were introduced in the late 1990s^[161–164] and rapidly became popular for research purposes, because, contrary to hard molds, soft molds are inexpensive to make. Soft molds are often made of PDMS, a polymer that is deformable, inexpensive, inert to most chemical solvents, and easy to process.^[23] A wide range of materials can be used as resist, varying from amorphous, thermoplastic, and crystalline polymers to gels, ceramics, lithographic resists, and even paper, creating bio-based microstructures. Some resists need subsequent curing, for example by inducing crosslinking or by changing the temperature.^[23] Mechanical properties, friction between mold and resist, transparency, chemical inertness, and costs are some of the main criteria for choosing the resist material.^[165]

Contrary to hard molds, which can only be used on planar substrates, soft molds can be also used on non-planar substrates. When shaping a deformable layer with a three-dimensional mold, the geometric diversity is low (i.e., no tunable dimensions), because only the specific geometry of the used mold can be fabricated. When a (soft) mold is used for stamping, imprinting, or printing, the thickness (or depth) of the deposited (or imprinted) pattern is tunable, so the geometric diversity that can be attained with these methods is higher compared to using mold for shaping a resist layer.

Here, we discuss shaping methods (including micro-transfer molding, micro-molding in capillaries, solvent-assisted micromolding, and replica molding) and printing methods (including micro-contact printing and nano-transfer printing methods).

Shaping methods with soft molds

Soft molds are commonly used to shape or pattern deformable polymeric layers. This is done either by filling the mold or by pressing the mold into the layer. Micro-transfer molding (μTM) is a method in which a soft mold is used to first fabricate a pattern from curing a shaped liquid pre-cursor, and then transfer it to a substrate. With μTM , the smallest attainable feature sizes are about 100 nm, a limit caused by the fact that smaller (negative) features in the mold are too small for the liquid to fill them. In principle, with μTM (and molding methods in general) only level-2 complexity structures can be fabricated, as overhanging structures cannot be de-casted from a three dimensional mold. However, LaFratta et al.^[166] used μTM to fabricate acrylic replicas of masters with overhanging features (**Figure 2.9**), by exploiting the deformability of the mold, which allowed mold removal by means of stretching after transfer to a glass substrate. In a method similar to μTM , Hamedi et al.^[17] used 3D-printed PU molds to shape paper, which was subsequently assembled to form disposable paper-based microchannel structures.

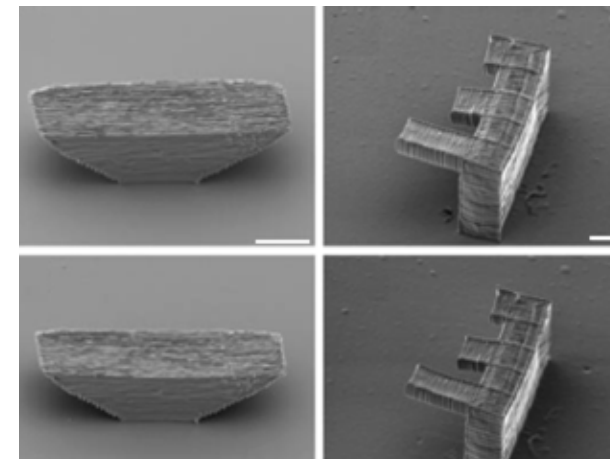


Figure 2.9. Master structures (top), on which PDMS is casted to create an elastomeric mold. This mold is then filled with an acrylic resin, which is subsequently transferred to a glass substrate. These structures have an overhang of around 10 μm , but still replicas can be fabricated

Nano- and microstructure fabrication

because the molds are stretchable (bottom). The scale bars are 10 μm . Adapted with permission.^[166] Copyright 2004, American Chemical Society.

To fill nano- and microscale features of a soft mold with a liquid prepolymer resist, capillary action can be used. This method is referred to as micro-molding in capillaries (MIMIC). After a droplet of pre-polymer is dragged into the mold, (sometimes facilitated by a pressure difference over the capillaries,^[167] by heating the pre-polymer,^[168] or by an electric field^[23]) the polymer resist is hardened by means of solvent evaporation. Due to flow resistance, the smallest attainable feature size is around 100 nm.^[23]

Another way to facilitate mold filling is by wetting the mold with a good solvent for the polymeric resist. Upon contact with the mold, the polymer softens and conforms to the mold. Hardening of the polymer is achieved by letting the solvent dissipate and evaporate into the PDMS mold. This strategy of mold filling is referred to as solvent-assisted micromolding (SAMIM).^[23] Because no high temperature is required during the SAMIM process, disadvantageous effects such as shrinkage after cooling, polymer degradation at high temperatures, and incompatibility with high- T_g materials do not play a role in SAMIM.^[169] Parallel lines with a width of around 60 nm have been achieved with this method,^[162] although resolutions are typically in the order of micrometers.^[170,171]

Replica molding (RM) is a technique in which a hard mold or pattern (the so-called master) is replicated using soft molds.^[163,172] In RM, first PDMS is casted on the master, which is then cured to obtain a negative pattern. This negative pattern is subsequently used as a template for the replica by means of shaping a PDMS resist layer on a substrate. The negative PDMS patterns are inexpensive to fabricate and reusable. RM has been used to replicate SWNTs on a substrate, down to feature sizes of 1 nm (**Figure 2.10**).^[172] A bilayer of PDMS (one soft and one hard layer) was needed to protect the SWNTs from getting damaged and still get a robust PDMS imprint. Also nanorods with a diameter of 30–150 nm have been successfully replicated.^[173] RM has been further used to fabricate biomimetic adhering surfaces, consisting of pillar arrays, to study the interlocking of two approaching surfaces.^[174]

Three-dimensional structures with various heights

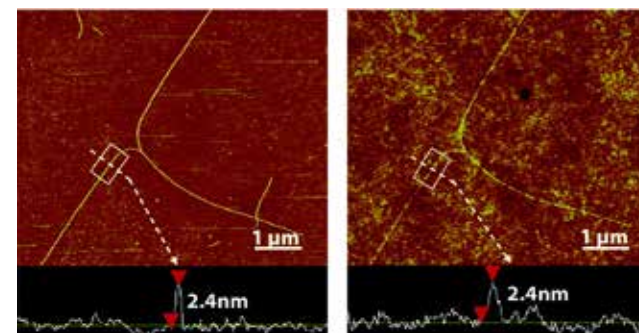
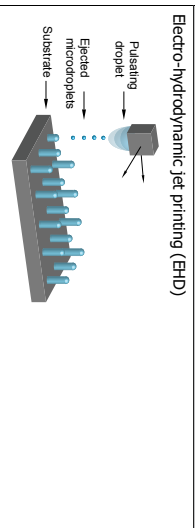
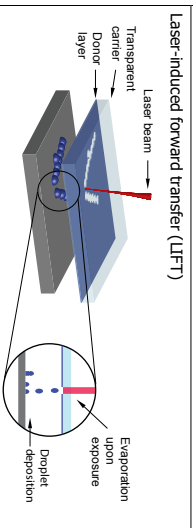
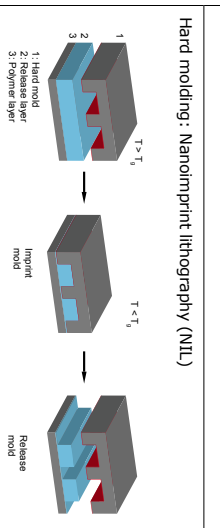
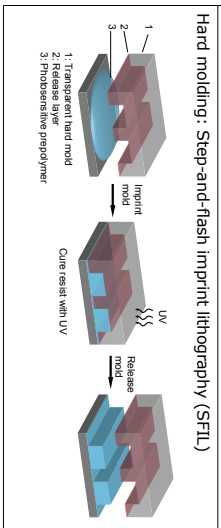


Figure 2.10. Left: Carbon single-walled nanotubes on a silica substrate. By casting and curing polydimethylsiloxane on the substrate, a mold is obtained with feature sizes below 1 nm. Right: Replicated single-walled nanotubes, fabricated by shaping a polyurethane layer using the obtained PDMS mold. The scale bars are 1 μm . Adapted with permission.^[172] Copyright 2004, American Chemical Society.

Printing and pattern transfer methods with soft molds

Soft molds are also used to transfer an ink to a substrate, a method referred to as printing. In micro-contact printing (μCP), a coating (e.g., alkanethiols)^[175] is selectively transferred from an elastomeric stamp to a substrate. The transferred coating thus acts as an ink and is only transferred upon contact with the substrate, because it is functionalized with a thin layer of a noble metal. The ink is transferred by diffusion and covalent-bond formation with the metal layer, requiring molecular-scale contact between the stamp and the substrate. The transferred ink then self-assembles into a monolayer.^[176] With μCP , printed features can be as small as the stamp allows, and feature sizes down to 50 nm have been reported.^[177] Besides printing self-assembling monolayers, also biomolecules^[178] and nanoparticles^[179] can be selectively deposited on substrates, which is useful in cell patterning. Deposited ink can also act as a positive or negative resist in a subsequent etching step.^[180] Choi et al. ^[181] demonstrated multiple-layer transfer printing to create arrays of micrometer-sized light-emitting diodes (LEDs). To increase the material diversity of inks compatible with μCP , Li et al.^[182] suggested the use of molds the surface energy of which can be controlled. By chemically modifying polyurethane acrylate based molds, the release and transfer of printed materials is optimized.

Table 2.3. Fabrication methods for three-dimensional structures with areas of various heights and no overhanging parts or cavities (geometric complexity level 2).

Fabrication method	Material complexity	Resolution	Total size	Geometric diversity	Materials diversity	Throughput
 <p>Electro-hydrodynamic jet printing (EHD)</p>	Multiple materials possible	240 nm (using evaporation or deposited droplets)[140]	15x15 μm ² with BCPs-[116] several mm ² with polymeric particles[140]	Two tunable dimensions (extrusion in third dimension possible)	Multiple materials possible: polymers, biomaterials	Low
 <p>Laser-induced forward transfer (LIFT)</p>	Single material structures	Down to 3.5 μm ^[153]	Not reported	Two tunable dimensions	Only metallic materials	Low
 <p>Hard molding: Nanoinkprint lithography (NIL)</p>	Single material structures	30 nm ^[153]	300 × 400 mm ² [184]	One tunable dimension	Only polymeric materials	High
 <p>Hard molding: Step-and-flash Imprint Lithography (SFI)</p>	Single material structures	5 nm ^[24]	Up to 250 × 250 mm wafers ^[185]	One tunable dimension	Only polymeric materials	High

Similar to μCP is nano-transfer patterning (nTP), in which a thin film of, for example, polymers^[183] is transferred from a hard or soft stamp to a substrate. This thin film has the 3D shape of the used stamp. Pattern transfer takes place by covalent or noncovalent interactions between substrate and pattern. The resolution of nTP is limited by the resolution of the elastomeric stamp and by the materials used for the mold and resist. Lines of 8-nm width have been shown when a soft stamp (made of directed self-assembled BCPs on a substrate) was inked with gold and this ink was transferred to a PDMS substrate by covalent bond formation.^[183]

Table 2.3 illustrates the basic working principles and specifications of fabrication methods for three-dimensional structures with areas of various heights and no overhanging parts or cavities (geometric complexity level 2).

2.4 Fabrication methods for three-dimensional structures with overhanging features and/or cavities (geometric complexity level 3)

In this section, we discuss nano- and microfabrication methods in which structures can be fabricated in a three-dimensional direct-writing fashion: vat photopolymerization (stereolithography and direct laser writing), focused ion or electron beam-induced deposition, and directed self-assembly. These fabrication methods are all serial, additive methods, meaning that the structure is fabricated voxel by voxel, and complex structures with overhanging features and cavities can be fabricated.

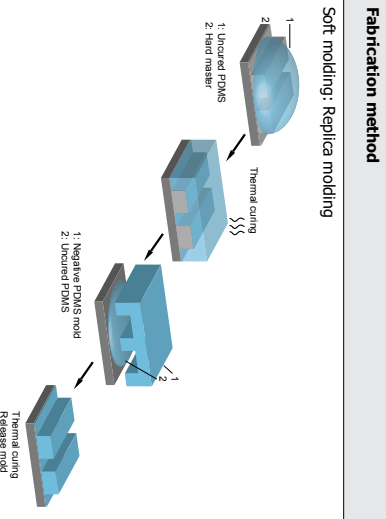
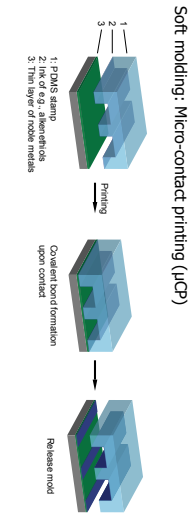
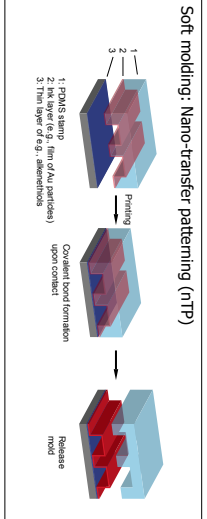
Vat photopolymerization

Vat photopolymerization is a collective name for fabrication methods in which nano- or microstructures are formed by curing a liquid photoresist (also referred to as a resin) in a vat. Curing of the resin takes place at the focal point of a laser beam, and by controlling the position of this focal point (including the depth), three-dimensional structures can be fabricated. Resins compatible with vat photopolymerization include photopolymers, but also collagen- hydrogel has been used.^[187] No multi-material structures can be fabricated, as the vat can be filled only with one type of resin. The photosensitivity of the resin needs to be high, such that polymerization only takes place locally, and not in neighboring regions.^[85] The resolution is determined by the size of the focal point. To reduce the focal point size, stimulated emission depletion (STED) methods are used in vat photopolymerization,^[188,189] where a second beam acts as an inhibitor of the writing beam by creating destructive interference pattern at the peripheral regions of the focal point. Another approach to obtain high resolutions with optical-beam fabrication methods for three-dimensional structures is the use of a spatial light modulator, in which the focal point shape is spatially tuned by electronic modulation, varying wave front, intensity, or polarization of the laser beam.^[189,190] With vat photopolymerization methods, high geometric diversity can be obtained, because fabricated structures are tunable in all three dimensions. Because of its serial character, vat photopolymerization is not a very fast technique, with scanning speeds in the order of micrometers per second.^[19]

Stereolithography

Stereolithography (SL) is a vat photopolymerization method in which a

Table 2.3. (continued)

Fabrication method	Material complexity	Resolution	Total size	Geometric diversity	Materials diversity	Throughput
 <p>Soft molding: Replica molding</p>	Single material structures	3 μm ^[172]	100 mm ²	Zero tunable dimensions	Multiple materials possible: biomaterials, elastomers, paper	Soft mod.: 100 mm ² per cycle ^[186]
 <p>Soft molding: Micro-contact printing (μCP)</p>	Multiple materials possible	50 nm ^[177]	A few cm ² ^[177]	Zero tunable dimensions (one tunable dimension in a layer-by-layer fashion)	Multiple materials possible: biomaterials, elastomers, etc.	High
 <p>Soft molding: Nano-transfer patterning (nTP)</p>	Multiple materials possible	8 nm ^[183]	100-nm diameter substrates ^[183]	Zero tunable dimensions	Multiple materials: Biomaterials, elastomers, etc.	High

laser beam serially solidifies the resin by means of photopolymerization. The resin consists of liquid photopolymer, sometimes with a photoinitiator, which starts the polymerization upon light exposure. The vat with the resin is moved around a stable focal point of a laser. By means of polymerization, the structure is formed point-by-point and layer-by-layer.^[31] The minimal layer thickness in SL is determined by the volume of the focal point (and thus by the polymerization volume), the resin viscosity, and the surface tension of the resin. Resolutions in the μm -range were obtained soon after the introduction of SL as a fabrication method.^[191] SL is used in various fields, including the fabrication of micromachines^[192], microfluidic systems,^[193] tissue engineering,^[187] and bio-analysis.^[31]

Direct laser writing

Direct laser writing (DLW) is a vat photopolymerization technique in which the process of two-photon-polymerization (TPP, also abbreviated as 2PP) or multiphoton-polymerization (MPP) is applied to obtain smaller polymerization volumes within the laser beam focal point compared to SL. TPP and MPP rely on the fact that the resin polymerizes only when two or more photons are absorbed simultaneously. Polymerization therefore only takes place in the center of the focal point, where the photon intensity is sufficiently high for this simultaneous absorption to occur, thereby reducing the polymerization volume.^[194] TPP was introduced in resin-based AM in 1990,^[195] and with the ongoing progress of optics and resists, diverse structures have been fabricated with it. In **Figure 2.11**, three examples of structures with feature sizes below $1\ \mu\text{m}$ are shown, fabricated with a commercial instrument and resist, using a 405-nm diode laser.^[196] With this setup, linewidths down to 78 nm and point diameters down to 50–70 nm have been demonstrated.^[196] With STED-based DLW, resolutions down to 100 nm have been reported.^[197] DLW has also been used to fabricate biocompatible porous scaffolds to grow cells in.^[198] Also for bioinspired adhesive or (de)wetting surfaces, which are commonly fabricated with lithographic methods,^[4,199] DLW methods have been used, because of the attainable high resolutions in combination with geometric diversity. An example of a bioinspired surface with variable wetting properties to water was fabricated by Tricinci et al.,^[60] who used DLW with an epoxy-based resist to write an array of tree-like structures, similar to the pattern on the leaves of *Salvinia molesta* (see **Figure 2.12**).

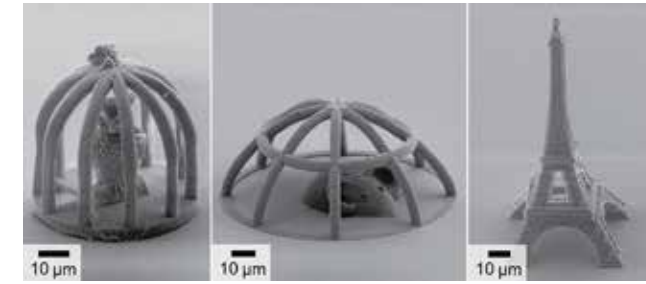


Figure 2.11. Microstructures fabricated by DLW in a commercially available photoresist. Reproduced with permission.^[196] Copyright 2014, Optical Society of America.

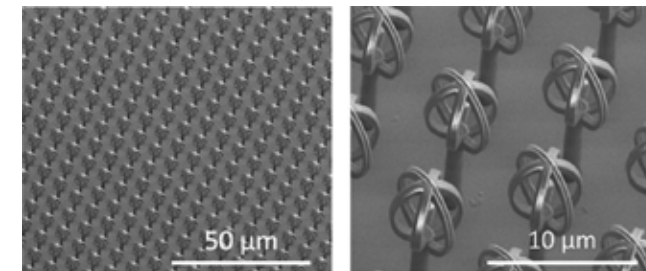


Figure 2.12. Inspired by the *Salvinia molesta* leaf, patterns were fabricated that, when submerged in water, trap a layer of air. One module of this repetitive microstructure consists of a $7\text{-}\mu\text{m}$ tall hair (diameter of $1.5\ \mu\text{m}$), with three intersecting circles (diameter of $6\ \mu\text{m}$) as a head. The structures were written in an epoxy-based resist, using DLW. Reproduced with permission.^[60] Copyright 2015, American Chemical Society.

The terminology of resin-based AM methods varies in the literature. DLW methods are also referred to as three-dimensional OBL,^[34] laser 3D printing,^[198] and direct laser lithography.^[60] DLW is also called TPP, 2PP, MPP, non-linear lithography (NNL), and multi-photon lithography (MPL).^[194] Sometimes, TPP methods are considered as a special stereolithography technique, and referred to as micro-SL^[31] or TPP-SL.^[200]

Focused ion or electron beam-induced deposition

Focused ion beam-induced deposition (FIBID) and focused electron beam-induced deposition (FEBID) are nanolithographic direct-writing fabrication methods in which a beam of ions or electrons is used to induce molecular decomposition of a gas (commonly metal-organic molecules), resulting in local chemical vapor deposition on a substrate.^[201,202] Deposi-

Nano- and microstructure fabrication

tion of materials is limited to one material at a time. FIBID and FEBID are suitable for fabrication of three-dimensional structures, because deposition can be controlled precisely by tuning the beam diameter and its focal point. With FIBID, spirals with a wire thickness of about 80 nm have been fabricated by means of platinum deposition (**Figure 2.13**).^[203] FEBID is used for lithographic mask repair, probe preparation in SPL methods, and fabrication of nanotubes.^[202,204]

Deposition of particles from a gas can also be induced by a laser beam. This technique is referred to as laser chemical vapor deposition (LCVD).^[31] The focal point has a diameter of about 1 μm , meaning that attainable resolutions are lower than those attained with FIBID and FEBID.

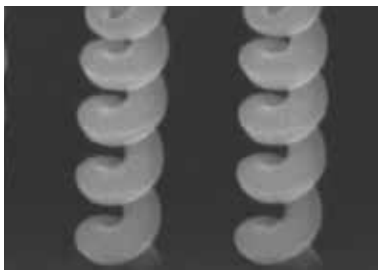


Figure 2.13. Platinum nanospirals fabricated with focussed ion beam-induced deposition on a Si substrate. Because the presence of the first nanospiral changes the particle scattering behavior, the second and next nanospirals have a different growth rate during fabrication compared to the first one. Adapted with permission.^[203] Copyright 2014, John Wiley and Sons.

Directed self-assembly of three-dimensional structures

Besides using macromolecules as building blocks for single-layer patterns on planar substrates, as is done with BCP lithography and colloidal lithography, self-assembling macromolecules can also be used to fabricate three-dimensional structures.^[205] The self-assembling properties can be tailored by tuning the dissolvability, the functional groups, or the molecular size of the macromolecules.

Inspired by cells and their organelles, a range of vesicles and nanospheres have been fabricated by exploiting the physical properties of macromolecules. These nanospheres can be used as microreactors^[206] or drug carriers.^[207] Amphiphilic polymers have been applied as building blocks for functional membranes, which can be used for separation processes (e.g., osmosis,

Three-dimensional structures with overhanging features

filtration) or catalysis.^[208] Macromolecules have been also used as building blocks for stimuli-responsive structures, like spheres or surfaces.^[209] Akkerboom et al.^[210] fabricated surfaces with controllable wettability using an array of self-assembled carboxylated polystyrene colloids as templates. By dissolving the colloid array after casting polypyrrole on the top of the array, air-filled cavities in a polypyrrole surface were fabricated (see **Figure 2.14**).

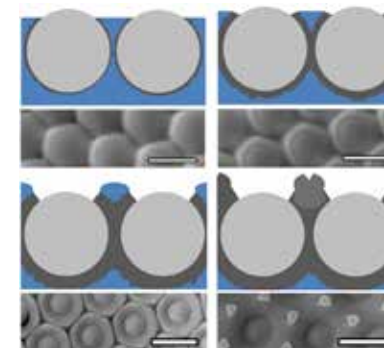
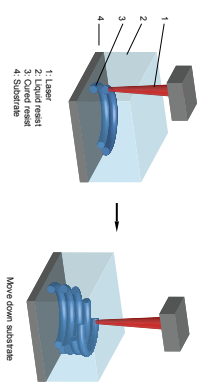
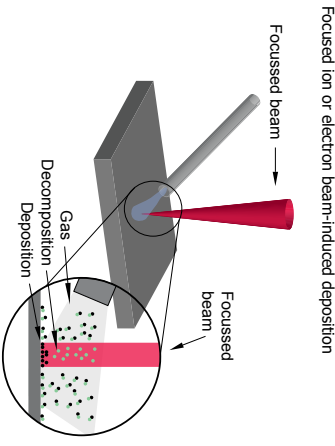


Figure 2.14. Overhanging features fabricated by polymerizing pyrrole monomers around a monolayer of carboxylated polystyrene colloids (grey spheres) at the air-water interface. Subsequent dissolving of the colloidal template resulted in a polypyrrole crystalline structure. Adapted with permission.^[210] Copyright 2015, American Chemical Society.

Table 2.4 illustrates the basic working principles and specifications of fabrication methods for three-dimensional structures containing cavities and/or overhanging features (geometric complexity level 3)

Table 2.4. Fabrication methods for three-dimensional structures containing cavities and/or overhanging features (geometric complexity level 3).

Fabrication method	Material complexity	Resolution	Total size	Geometric diversity	Materials diversity	Throughput
 <p>Vat photopolymerization</p>	Single material structures	0.1–10 μm^3 [201,203]	100 μm^2 [89]	Three tunable dimensions	Only photosensitive materials	Low
 <p>Focused ion or electron beam-induced deposition</p>	Single material materials	100 nm [201,203]	300 nm-sized wafers	Three tunable dimensions	Limited to metal- or-ganic gasses	Low

2.5 Discussion

In this paper, we reviewed nano- and microfabrication methods using seven moderators related to the characteristics of the envisioned structures, namely geometric complexity, material complexity, resolution, total size, geometric diversity, material diversity, and throughput. Ten groups of fabrication methods were identified, and their working mechanisms and specifications were reviewed.

Choosing between fabrication methods: a multivariate problem

When fabricating a nano- or microstructure, choosing the most suitable fabrication method to realize the envisioned performance is a multivariate problem. To facilitate this decision-making process, **Figure 2.15** and **Table 2.5** can be used. **Figure 2.15** illustrates the aforementioned seven moderators in a radar plot for the ten groups of nano- and microfabrication methods discussed in this paper. For each of the moderators in the radar plot, we show typical values, rather than absolute limits. For example, we classify the resolution of self-assembly methods in the 11–100 nm range, although resolutions of 6 nm have been also reported.^[117]

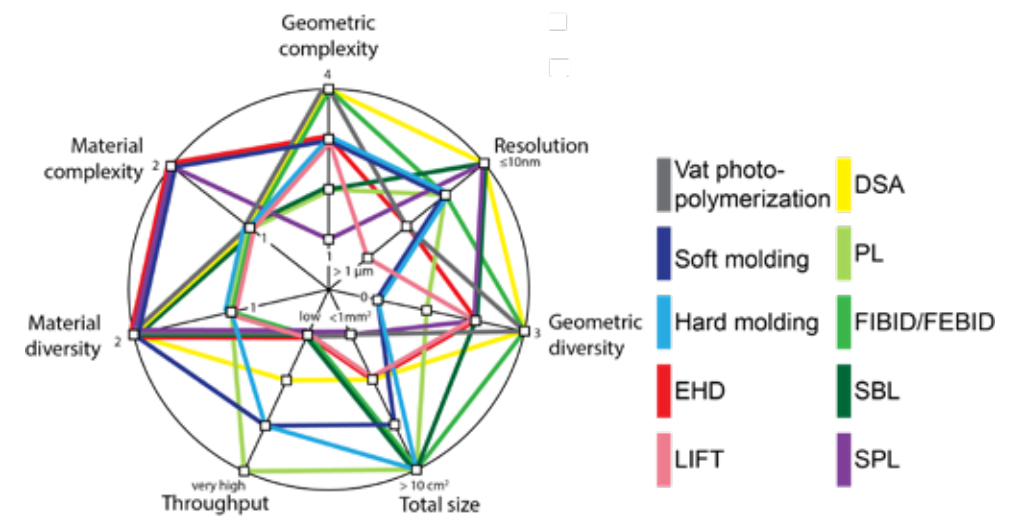
The radar plot lends itself to several observations and trends:

- 1) Photolithography is characterized by relatively high resolution and throughputs. While with other serial lithographic methods (SBL and FIBID/FEBID) high resolutions can be also obtained, the throughput of these methods is lower than that of photolithography, which may explain why photolithography rather than other serial lithographic methods is a preferred method in industrial-scale applications.
- 2) Hard molding achieves structures of larger total size than soft molding. With relatively high throughput, hard molding can be useful for industrial purposes, whereas soft molding is popular in research, as it is quite fast and relatively high resolutions can be obtained with it.
- 3) SPL has low throughputs and attainable complexity, but the method is compatible with a wide range of materials due to its mild processing conditions. Furthermore, with SPL the highest resolutions can be obtained, down to features on single-molecule length scales.

- 4) Nano- and microdroplet deposition methods such as LIFT or EHD exhibit advantages from a structural perspective, as they can be used to fabricate structures with a large total size with high complexity and diversity. Due to the serial character of fabricating, however, throughput is low, and resolutions are limited at the micrometer range.
- 5) The highest geometric complexity can be obtained with vat photopolymerization. On the other hand, the resin in vat photopolymerization needs to be a photocurable material, which limits the range of compatible materials. With vat photopolymerization, also high resolutions can be obtained, although this comes at the cost of writing speed.
- 6) With fabrication methods that use self-assembly of molecules, high complexity, resolutions, and diversity can be achieved. Using self-assembled patterns as templates during etching processes results in a high-throughput process, making self-assembly particularly interesting for industry.

2

The radar plot may be used as a decision-making tool for choosing the most suitable fabrication method(s), based on the most relevant moderators to realize the envisioned performance of a nano- or microstructure. For example, suppose a researcher wants to make structures with a resolution down to 100 nm. In this case, the researcher could choose between scanning beam lithography, hard or soft molding, FIBID/FEBID, and directed self-assembly. If the envisioned structure contains overhanging features and geometric diversity is required, self-assembly methods and FIBID/FEBID are preferred. On the other hand, if relatively large structures are required at a high throughput, hard molding may be the method of preference.



2

Figure 2.15. Performance of ten groups of nano- and microfabrication methods in terms of geometric complexity (levels 1–3), resolution ($> 1 \mu\text{m}$, $101 \text{ nm} - 1 \mu\text{m}$, $11 - 100 \text{ nm}$, and $\leq 10 \text{ nm}$), geometric diversity (0–3 tunable dimensions), total size of the structure ($< 1 \text{ mm}^2$, $1 - 99 \text{ mm}^2$, $1 - 10 \text{ cm}^2$, and $> 10 \text{ cm}^2$), throughput (low, medium, high, and very high), material diversity (one group of materials or multiple groups of materials), and material complexity (one group of materials or multiple groups of materials). All ranges are described from the origin to the outer circle.

Table 2.5 provides a comparative overview of the identified ten groups of nano- and microfabrication methods in terms of the aforementioned seven moderators.

Table 2.5. Performance of ten groups of nano- and microfabrication methods in terms of seven moderators.

Geometric complexity	Level 1	Level 2	Level 3	Level 4
	Scanning probe lithography (SPL)	Photolithography Scanning beam lithography (SBL)	Soft molding Hard molding Electrohydrodynamic jet printing (EHD) Laser-induced forward transfer (LIFT)	Directed self-assembly (DSA) Vat photopolymerization
Material complexity	Single			
	Vat photopolymerization Hard molding Laser-induced forward transfer (LIFT) FIBID/FEBID	Directed self-assembly (DSA) Photolithography Scanning beam lithography (SBL)	Electrohydrodynamic jet printing (EHD) Soft molding Scanning probe lithography (SPL)	Electrohydrodynamic jet printing (EHD) Soft molding Scanning probe lithography (SPL)
Resolution	≤ 10 nm	11 – 100 nm,	101 nm – 1 μm	> 1 μm
	Directed self-assembly (DSA) Scanning beam lithography (SBL) Scanning probe lithography (SPL)	Soft molding Hard molding Focus ion/electron beam-induced deposition (FIBID/FEBID) Photolithography	Electrohydrodynamic jet printing (EHD) Vat photopolymerization	Laser-induced forward transfer (LIFT) Scanning probe lithography (SPL)
Total size	< 1 mm ²	1–99 mm ²	1–10 cm ²	> 10 cm ²
	Vat photopolymerization Scanning probe lithography (SPL)	Electrohydrodynamic jet printing (EHD) Laser-induced forward transfer (LIFT) Directed self-assembly (DSA)	Soft molding	Photolithography Scanning beam lithography (SBL) Hard molding Focus ion/electron beam-induced deposition (FIBID/FEBID)

Geometric diversity	0 dimensions			1 dimensions			2 dimensions			3 dimensions		
	Soft molding Hard molding	Photolithography	Scanning beam lithography Electrohydrodynamic jet printing (EHD) Laser-induced forward transfer (LIFT) Scanning probe lithography (SPL)	Focus ion/electron beam-induced deposition (FIBID/FEBID)	Directed self-assembly (DSA) Vat photopolymerization	Electrohydrodynamic jet printing (EHD) Soft molding Hard molding	Photolithography					
Material diversity	Single											
	Laser-induced forward transfer (LIFT) Hard molding	Photolithography Focus ion/electron beam-induced deposition (FIBID/FEBID)	Electrohydrodynamic jet printing (EHD) Scanning probe lithography (SPL) Vat photopolymerization	Directed self-assembly (DSA) Scanning beam lithography (SBL) Soft molding								
Throughput	Low			Medium			High			Very high		
	Scanning beam lithography (SBL) Scanning probe lithography (SPL) Laser-induced forward transfer (LIFT) Electrohydrodynamic jet printing (EHD) Focus ion/electron beam-induced deposition (FIBID/FEBID) Vat photopolymerization	Directed self-assembly (DSA)	Soft molding Hard molding	Photolithography								

Attainable geometric complexity versus processing characteristics

By categorizing fabrication methods based on a structure-related moderator (e.g., geometric complexity as we did in this review), fabrication methods can be assessed independently from processing characteristics such as being of additive or subtractive nature, parallel or serial (i.e., based on single-step and multi-step manufacturing, respectively), etc. However, identifying the relationship between processing characteristics and the structural characteristics of the envisioned structures can provide useful insights regarding the evolvement of existing fabrication methods as well as the emergence of new fabrication methods. Accordingly, in **Table 6**, we relate geometric complexity and processing characteristics for the reviewed methods. It can be seen that for level-1 geometric complexity in nano- or microstructures (e.g., extruded two-dimensional structures), both additive and subtractive fabrication methods, and both serial and parallel methods, can be used, whereas structures of the highest level of complexity can only be fabricated with serial, additive methods. This also means that high geometric complexity currently can only be achieved at low throughputs. Besides, for additive, serial methods, a higher resolution is only possible with even lower writing speeds, meaning that the attainable resolution depends on the geometric complexity of a structure. Similar associations can be made between processing characteristics and other structure-related moderators.

Table 2.6. Fabrication methods categorized based on the geometric complexity that can be achieved with them, versus their processing characteristics (additive or subtractive and parallel or serial).

Processing characteristics		Geometric complexity		
		Level 1	Level 2	Level 3
Additive	Serial	Laser-induced forward transfer (LIFT) Electrohydro-dynamic jet printing (EHD)		Vat photopolymerization Focus ion/electron beam-induced deposition (FIBID/FEBID)
	Parallel	Directed self-assembly (DSA)		
Subtractive/ Additive	Serial	Scanning beam lithography (SBL) Scanning probe lithography (SPL)		
	Parallel	Photolithography	Hard molding Soft molding	

Additive manufacturing

One could not avoid noticing that additive manufacturing (AM, commonly referred to as 3D printing) occupies a relatively small part of our review, which may not seem in hand with the attention that this group of techniques is gaining both in academia and in industry. The reason why we did not present a more extensive overview of AM methods is that, except for vat photopolymerization methods, EHD, and LIFT, AM methods are not yet suitable for fabricating nano- or microstructures. Specifically, most AM methods are solid-, ink- and powder-based and use deposition mechanisms such as sintering, melting, and gluing.^[211,212] For these deposition mechanisms, a high pixel volume is required and thus true micrometer-sized features are currently not possible. Increasing the attainable resolution of such AM methods would directly add to the number of nano- and microfabrication methods that can achieve microstructures with high geometric complexity.

Increasing geometric complexity by post-processing

When determining the attainable complexity of fabrication methods, we did not take into consideration post-processing steps. It is, however, common to use fabrication methods as part of a toolbox set, together with operations such as post-process melting, grinding, and stacking of two-dimensional layers to obtain a three-dimensional structure. As an example of post-processing resulting in increased geometric complexity, Del Campo et al.^[213] fabricated pillar arrays with lithographic methods, after which overhanging parts were incorporated by pressing the pillars against a surface. Alternatively, geometric complexity can be increased by doing multiple cycles of one fabrication method, to create multilayered structures. For example, Varghese et al.^[214] fabricated woodpile-like structures by means of EBL by writing in added layers on top of fabricated patterns.

Future directions

In this review an inductive pathway of designing nano- and microstructures is supported by focusing on making the step from the geometric and material properties of an envisioned structure toward a fabrication method suitable for fabricating this structure (see **Figure 2.1**). To further support an inductive design pathway, the step from the desired *performance* toward the required geometric and material properties should be also better understood. To achieve that, a comprehensive assessment of the (attainable) performance of functional nano- and microstructures is needed. Here, the seven identified performance-determining moderators were used in a qualitative/conceptual fashion to organize fabrication methods based on the attainable nano- and microstructures. Studying the quantitative effect of these, and possibly other, moderators on the performance of nano- and microstructures would provide useful insights into how performance can be improved.

In order to assess which characteristics of a fabrication method have the potential to improve in the future, it is important to first consider the intrinsic limitations of each methods. For example, the low geometric diversity of hard and soft molding is an intrinsic limitation of these methods, as with one mold, only one structure with defined size and shape can be fabricated. As another example, the low throughput of SPL is caused by the fact that a probe can only modify single nanoscale objects or molecules. Accelerating the SPL process would be only possible at the expense of a lower resolution. (An exception is thermal SPL, in which high writing speeds, up to 20 mm/s

at 15 nm resolution,^[215] can be obtained, making thermal SPL comparable with electron beam lithography in terms of throughput.)

When it comes to processing characteristics of fabrication methods, next to intrinsic limitations, it is also important to note that the characteristics of a fabrication method may be interdependent. For example, the resolution of photolithography can be improved by using shorter wavelength light, combined with more precise, expensive optics. In other words, increased resolution in photolithography is possible, but for increased costs.^[87] In the future, it is likely that the resolution of vat photopolymerization methods will increase by reducing the laser focal point size.^[200] A resolution increase will come at the expense of throughput, however, since more writing steps will be required to pattern a certain area or volume. A similar trade-off between feature size and throughput applies to serial deposition methods, namely EHD and LIFT. Engstrom et al.^[19] noted that with EHD, thinner lines can be written faster than thicker lines, because the required amount of ink is lower for smaller features, given a fixed ink flow rate. While this is true for single objects like lines or pillars, throughput will decrease for smaller feature sizes, considering that smaller features also result in a higher number of features per area.

From the radar plot we can deduce that molecular-scale methods such as DSA and SPL can be improved when it comes to throughput and total size, without going at the expense of resolution or complexity. The fundamental resolution limit of more conventional nanofabrication methods (such as photolithography) is still an order of magnitude above the molecular-scale resolutions that DSA and SPL attain, showing their promise for nanofabrication.

2.6 Conclusion

In this paper, we reviewed nano- and microfabrication methods based on the geometric complexity that they can achieve, independently from processing characteristics, and with material complexity, resolution, total size of the structure, geometric diversity, material diversity, and throughput as moderators. A geometric complexity-based categorization of nano- and microfabrication methods facilitates the decision-making for identifying the most suitable method for fabricating functional nano- or microstructures with predefined properties. Furthermore, such a categorization provides a

framework for systematically organizing fabrication methods across application fields. This allows designers of nano- and microstructures to include a wide range of fabrication methods in their design considerations.

Acknowledgements

This research is supported by the Netherlands Organization for Scientific Research (NWO) Domain Applied and Engineering Sciences (TTW), (Open Technology Program, project 13353 "Secure and gentle grip of delicate biological tissues").

References

- [1] G. E. Moore, IEEE Solid-State Circuits Soc. Newsl. **2006**, 11, 37.
- [2] G. E. Moore, *Proc. IEEE* **1998**, 86, 82.
- [3] S. Nishimoto, B. Bhushan, *RSC Adv.* **2013**, 3, 671.
- [4] D. M. Drotlef, L. Stepien, M. Kappl, W. J. P. Barnes, H. J. Butt, A. del Campo, *Adv. Funct. Mater.* **2013**, 23, 1137.
- [5] H. Lee, B. P. Lee, P. B. Messersmith, *Nature* **2007**, 448, 338.
- [6] J. Iturri, L. Xue, M. Kappl, L. García-Fernández, W. J. P. Barnes, H.-J. Butt, A. del Campo, *Adv. Funct. Mater.* **2015**, 25, 1499.
- [7] W. L. Min, B. Jiang, P. Jiang, *Adv. Mater.* **2008**, 20, 3914.
- [8] C. Lucarotti, C. M. Oddo, N. Vitiello, M. C. Carrozza, *Sensors* **2013**, 13, 1435.
- [9] F. de Gaetano, P. Bagnoli, A. Zaffora, A. Pandolfi, M. Serrani, J. Brubert, J. Stasiak, G. D. Moggridge, M. L. Costantino, *J. Mech. Med. Biol.* **2015**, 15, 1540009.
- [10] S. L. Lin, C. C. Lin, D. Y. Lin, C. S. Chuang, *8th Annu. IEEE Int. Conf. Nano/Micro Eng. Mol. Syst.*, IEEE, Piscataway, NJ, USA **2013**, pp. 594–597.
- [11] M. López-Álvarez, C. Rodríguez-Valencia, J. Serra, P. González, *Procedia Eng.* **2013**, 59, 51.
- [12] J. F. Swennenhuis, A. G. J. Tibbe, M. Stevens, M. R. Katika, J. van Dalum, H. Duy Tong, C. J. M. van Rijn, L. W. M. M. Terstappen, *Lab Chip* **2015**, 15, 3039.
- [13] J. Swennenhuis, A. G. J. Tibbe, C. J. M. van Rijn, L. W. M. M. Terstappen, *Lab Chip* **2015**, 15, 3039.
- [14] E. K. Sackmann, A. L. Fulton, D. J. Beebe, *Nature* **2014**, 507, 181.
- [15] P. J. Kitson, M. H. Rosnes, V. Sans, V. Dragone, L. Cronin, *Lab Chip* **2012**, 12, 3267.
- [16] D. Rochette, B. Kent, A. Habicht, S. Seiffert, *Colloid Polym. Sci.* **2017**, 295, 507.
- [17] M. M. Hamedi, B. Ünal, E. Kerr, A. C. Glavan, M. T. Fernandez-Abedul, G. M. Whitesides, *Lab Chip* **2016**, 16, 3885.
- [18] M. M. Waldrop, *Nature* **2016**, 530, 145.
- [19] D. S. Engstrom, B. Porter, M. Pacios, H. Bhaskaran, *J. Mater. Res.* **2014**, 29, 1792.
- [20] M. Röhrig, M. Thiel, M. Worgull, H. Hölscher, *Small* **2012**, 8, 3009.
- [21] X. Li, Y. Cao, M. Gu, *Opt. Lett.* **2011**, 36, 2510.
- [22] Z. Doubrovski, J. C. Verlinden, J. M. P. Geraedts, *Proc. ASME Des. Eng. Tech. Conf.* **2011**, 9, 635.
- [23] B. D. Gates, Q. Xu, M. Stewart, D. Ryan, C. G. Willson, G. M. Whitesides, *Chem. Rev.* **2005**, 105, 1171.
- [24] M. C. Traub, W. Longsine, V. N. Truskett, *Annu. Rev. Chem. Biomol. Eng.* **2016**, 7, 1.
- [25] S. Y. Chou, P. R. Krauss, W. Zhang, L. Guo, L. Zhuang, *J. Vac. Sci. Technol.* **1997**, 15, 2897.
- [26] M. N. Costa, B. Veigas, J. M. Jacob, D. S. Santos, J. Gomes, P. V. Baptista, R. Martins, J. Inácio, E. Fortunato, *Nanotechnology* **2014**, 25, 94006.
- [27] E. Brinksmeier, O. Riemer, R. Stern, in *Initiatives of Precision Engineering at the Beginning of a Millennium* (Ed: I. Inasaki), Kluwer Academic Publishers, Boston, USA **2001**, pp. 3–11.

Nano- and microstructure fabrication

- [28] Y. Qin, A. Brockett, Y. Ma, A. Razali, J. Zhao, C. Harrison, W. Pan, X. Dai, D. Loziak, *Int. J. Adv. Manuf. Technol.* **2010**, *47*, 821.
- [29] A. R. Razali, Y. Qin, *Procedia Eng.* **2013**, *53*, 665.
- [30] S. S. Dimov, C. W. Matthews, A. Glanfield, P. Dorrington, in *4M 2006 - Second Int. Conf. Multi-Material Micro Manuf.*, Elsevier, Amsterdam, the Netherlands **2006**, pp. xi–xxv.
- [31] M. Vaezi, H. Seitz, S. Yang, *Int. J. Adv. Manuf. Technol.* **2013**, *67*, 1721.
- [32] G. B. Olson, *Science* (80-.). **1997**, *277*, 1237.
- [33] D. L. D. Bourell, J. J. Beaman, M. C. Leu, D. W. Rosen, *US-Turkey workshop on rapid technologies*, (Eds: ...), Wohlers Associates, Fort Collins, Colorado, USA **2009**, p. 5.
- [34] Z. Gan, Y. Cao, R. A. Evans, M. Gu, *Nat. Commun.* **2013**, *4*, 2061.
- [35] L. Heepe, S. N. Gorb, *Annu. Rev. Mater. Res.* **2014**, *41*, 110301100446097.
- [36] D. Brodoceanu, C. T. Bauer, E. Kroner, E. Arzt, T. Kraus, *Bioinspiration & Biomimetics* **2016**, *11*, 5, 051001.
- [37] C. Greiner, A. del Campo, E. Arzt, *Langmuir* **2007**, *23*, 3495.
- [38] L. Xue, B. Sanz, A. Luo, K. T. Turner, X. Wang, D. Tan, R. Zhang, H. Du, M. Steinhart, C. Mijangos, M. Guttman, M. Kappl, A. del Campo, *ACS Nano* **2017**, *11*, 9711-9719
- [39] A. Ghosh, B. Corves, *Introduction to Micromechanisms and Microactuators*, Springer, New York, NY, USA **2015**, *28*, 35-36
- [40] M. Li, H. X. Tang, M. L. Roukes, *Nat. Nanotechnol.* **2007**, *2*, 114.
- [41] M. Esashi, S. Tanaka, *Micromachines* **2016**, *7*, 8.
- [42] T. Brecht, W. Pfaff, C. Wang, Y. Chu, L. Frunzio, M. H. Devoret, R. J. Schoelkopf, *npj Quantum Inf.* **2016**, *2*, 16002.
- [43] Q. Liu, X. Duan, C. Peng, *Novel Optical Technologies for Nanofabrication*, **2014**.
- [44] N. Khusnatdinov, Z. Ye, K. Luo, T. Stachowiak, X. Lu, J. W. Irving, M. Shafran, W. Longsine, M. Traub, V. Truskett, B. Fletcher, W. Liu, F. Xu, D. LaBrake, S. V. Sreenivasan, *Altern. Lithogr. Technol. VI* **2014**, *9049*, 904910.
- [45] S. R. J. Brueck, *Proc. IEEE* **2005**, *93*, 1704.
- [46] S. Chou, *Nanoimprint Lithography*, Woodhead Publishing Limited, **1996**.
- [47] Q. Yang, J. Liu, H. Li, Y. Li, J. Hou, M. Li, Y. Song, *RSC Adv.* **2015**, *5*, 11096.
- [48] L. K. Grunenfelder, S. Herrera, D. Kisailus, *Small* **2014**, *10*, 3207.
- [49] W. Federle, W. J. P. Barnes, W. Baumgartner, P. Drechsler, J. M. Smith, *J. R. Soc. Interface* **2006**, *3*, 689.
- [50] A. Tulchinsky, A. D. Gat, *Journal of Fluid Mechanics*, **2015**, *775*, 188-303
- [51] A. Chworos, W. Smitthipong, in *Bio-Based Compos. High-Performance Mater.*, CRC Press, Boca Raton, FL, USA **2014**, pp. 43–58.
- [52] U. G. K. Wegst, H. Bai, E. Saiz, A. P. Tomsia, R. O. Ritchie, *Nat. Mater.* **2014**, *14*, 23.
- [53] R. O. Ritchie, *Nat. Mater.* **2011**, *10*, 817.
- [54] L. K. Grunenfelder, N. Suksangpanya, C. Salinas, G. Milliron, N. Yaraghi, S. Herrera, K. Evans-Lutterodt, S. R. Nutt, P. Zavattieri, D. Kisailus, *Acta Biomater.*, **2014**, 3997–4008.
- [55] R. Courant, H. Robbins, I. Stewart, *What Is Mathematics? An Elementary Approach to Ideas and Methods*, OUP Us, **1996**.
- [56] S. Reuter, M. A. Smolarczyk, A. Istock, U. M. Ha, O. Schneider, N. Worapattarakul, S. Nazemroaya, H. Hoang, L. Gomer, F. Pilger, M. Maniak, H. Hillmer, *J. Nanoparticle Res.* **2017**, *19*, 184
- [57] S. Uchida, N. Ozaki, T. Nakahama, H. Oda, N. Ikeda, Y. Sugimoto, *Jpn. J. Appl. Phys.* **2017**, *56*, 050303
- [58] C. Greiner, E. Arzt, A. del Campo, *Adv. Mater.* **2009**, *21*, 479.
- [59] K. Cicha, T. Koch, J. Torgersen, Z. Li, R. Liska, J. Stampfl, *J. Appl. Phys.* **2012**, *112*, 9, 094906
- [60] O. Tricinci, T. Terencio, B. Mazzolai, N. M. Pugno, F. Greco, V. Mattoli, *ACS Appl. Mater. Interfaces* **2015**, *7*, 25560.
- [61] R. Garcia, A. W. Knoll, E. Riedo, *Nat Nano* **2014**, *9*, 577.
- [62] A. W. Knoll, D. Pires, O. Coulembier, P. Dubois, J. L. Hedrick, J. Frommer, U. Duerig, *Adv. Mater.* **2010**, *22*, 3361.
- [63] K. Brown, D. J. Eichelsdoerfer, X. Liao, S. He, C. A. Mirkin, *Front. Phys.* **2014**, *9*, 385.
- [64] K. M. Carroll, X. Lu, S. Kim, Y. Gao, H.-J. Kim, S. Somnath, L. Polloni, R. Sordan, W. P. King, J. E. Curtis, *Nanoscale* **2014**, *6*, 1299.
- [65] S. Hong, *Science*, **1999**, *286*, 523.
- [66] O. A. Nafday, J. R. Haaheim, F. Villagran, *Scanning* **2009**, *31*, 122.
- [67] K. Salaita, Y. Wang, C. A. Mirkin, *Nature Nanotechnology*, **2007**, *2*, 145-155.
- [68] Y. Wang, D. Maspoch, S. Zou, G. C. Schatz, R. E. Smalley, C. A. Mirkin, *Proc. Natl. Acad. Sci. U. S. A.* **2006**, *103*, 2026.
- [69] L. Chen, X. Wei, X. Zhou, Z. Xie, K. Li, Q. Ruan, C. Chen, J. Wang, C. A. Mirkin, Z. Zheng, *Small* **2017**, *13*, 1702003
- [70] R. Ferris, A. Hucknall, B. S. Kwon, T. Chen, A. Chilkoti, S. Zauscher, *Small* **2011**, *7*, 3032.
- [71] F. Holzner, P. Paul, M. Despont, L. L. Cheong, J. Hedrick, U. Dürig, A. Knoll, *Proceedings of the SPIE* **2013**, *8886*, 888605.
- [72] Y. K. Ryu Cho, C. D. Rawlings, H. Wolf, M. Spieser, S. Bisig, S. Reidt, M. Sousa, S. R. Khanal, T. D. B. Jacobs, A. W. Knoll, *ACS Nano* **2017**, *11*(12), 11890-11897
- [73] J. A. Dagata, J. Schneir, H. H. Harary, C. J. Evans, M. T. Postek, J. Bennett, *Appl. Phys. Lett.* **1990**, *56*, 2001.
- [74] A. A. O. Elkaseh, W. J. Perold, V. V. Srinivasu, *J. Appl. Phys.* **2010**, *108*, 53914.
- [75] J. Zhao, L. A. Swartz, W. Lin, P. S. Schlenoff, J. Frommer, J. B. Schlenoff, G. Liu, *ACS Nano* **2016**, *10*, 5656-5662.
- [76] H. Ito, *Adv. Polym. Sci.* **2005**, *172*, 37.
- [77] B. J. Kim, E. Meng, *J. Micromechanics Microengineering* **2016**, *26*, 13001.
- [78] S. Okazaki, *Microelectron. Eng.* **2014**, *133*, 23.
- [79] P. Clarke, "Intel Orders 15 EUV Lithography Systems," **2015**.
- [80] TWINSKAN NXE : 3400B. Technical Specifications, **2017**.
- [81] A. R. Abate, P. Mary, V. van Steijn, D. A. Weitz, *Lab Chip* **2012**, *12*, 1516.
- [82] P. Zhu, L. Wang, *Lab Chip* **2017**, *17*, 34.
- [83] A. Pimpin, W. Srituravanich, *Eng. J.* **2012**, *16*, 37.

Nano- and microstructure fabrication

- [84] N. Mojarad, J. Gobrecht, Y. Ekinici, *Microelectron. Eng.* **2015**, *143*, 55.
- [85] J. Fischer, M. Wegener, *Laser Photonics Rev.* **2013**, *7*, 22.
- [86] E. Buitrago, R. Fallica, D. Fan, T. S. Kulmala, M. Vockenhuber, Y. Ekinici, *Microelectron. Eng.* **2016**, *155*, 44.
- [87] C. Wagner, N. Harned, *Nat. Photonics* **2010**, *4*, 24.
- [88] N. Mojarad, M. Hojeij, L. Wang, J. Gobrecht, Y. Ekinici, *Nanoscale* **2015**, *7*, 4031.
- [89] J. Melngailis, *J. Vac. Sci. Technol. B Microelectron. Nanom. Struct.* **1998**, *16*, 927.
- [90] F. Watt, A. A. Bettiol, J. A. van Kan, E. J. Teo, M. B. H. Breese, *Int. J. Nanosci.* **2005**, *4*, 269.
- [91] S. Danylyuk, H. Kim, S. Brose, C. Dittberner, P. Loosen, T. Taubner, K. Bergmann, L. Juschkina, *J. Vac. Sci. Technol. B Microelectron. Nanom. Struct.* **2013**, *31*, 21602.
- [92] G. Kunkemöller, T. W. W. Maß, A.-K. U. Michel, H.-S. Kim, S. Brose, S. Danylyuk, T. Taubner, L. Juschkina, *Opt. Express* **2015**, *23*, 25487.
- [93] L. Markey, F. Zacharatos, J.-C. Weeber, A. Prinzen, M. Waldow, M. G. Nielsen, T. Tekin, A. Dereux, *Microelectron. Eng.* **2015**, *141*, 129.
- [94] Y. Chen, J. Qin, J. Chen, L. Zhang, C. Ma, J. Chu, X. Xu, L. Wang, *Nanotechnology* **2017**, *28*, 55302.
- [95] A. Doolittle, *Lithography and Pattern Transfer*, **2008**.
- [96] J. Dong, J. Liu, G. Kang, J. Xie, Y. Wang, *Sci. Rep.* **2014**, *4*, 5618.
- [97] L. Pan, Y. Park, Y. Xiong, E. Ulin-Avila, Y. Wang, L. Zeng, S. Xiong, J. Rho, C. Sun, D. B. Bogy, X. Zhang, *Sci. Rep.* **2011**, *1*, 1.
- [98] L. Bruchhaus, S. Bauerdick, L. Peto, U. Barth, A. Rudzinski, J. Mussmann, J. Klingfus, J. Gierak, H. Hövel, *Microelectron. Eng.* **2012**, *97*, 48.
- [99] Z. Gan, Y. Cao, R. A. Evans, M. Gu, *Nat. Commun.* **2013**, *4*, 2061.
- [100] J.-H. Jang, C. K. Ullal, M. Maldovan, T. Gorishnyy, S. Kooi, C. Koh, E. L. Thomas, *Adv. Funct. Mater.* **2007**, *17*, 3027.
- [101] B. Päivänranta, A. Langner, E. Kirk, C. David, Y. Ekinici, *Nanotechnology* **2011**, *22*, 375302.
- [102] A. A. Tseng, K. Chen, C. D. Chen, K. J. Ma, *IEEE Trans. Electron. Packag. Manuf.* **2003**, *26*, 141.
- [103] N. Arjmandi, L. Lagae, G. Borghs, *J. Vac. Sci. Technol. B* **2009**, *27*, 1915.
- [104] V. R. Manfrinato, L. Zhang, D. Su, H. Duan, R. G. Hobbs, E. A. Stach, K. K. Berggren, *Nano Lett.* **2013**, *13*, 1555.
- [105] A. Joshi-Imre, S. Bauerdick, *Journal of Nanotechnology* **2014**, 2014.
- [106] R. L. Kubena, *J. Vac. Sci. Technol. B Microelectron. Nanom. Struct.* **1991**, *9*, 3079.
- [107] J. Gierak, A. Septier, C. Vieu, *Nucl. Instruments Methods Phys. Res. Sect. A Accel. Spectrometers, Detect. Assoc. Equip.* **1999**, *427*, 91.
- [108] C. M. Bates, M. J. Maher, D. W. Janes, C. J. Ellison, C. G. Willson, *Macromolecules* **2014**, *47*, 2.
- [109] S. Ji, L. Wan, C. C. Liu, P. F. Nealey, *Prog. Polym. Sci.* **2016**, *54–55*, 76.
- [110] S. B. Darling, *Prog. Polym. Sci.* **2007**, *32*, 1152.
- [111] S. M. Douglas, H. Dietz, T. Liedl, B. Hogberg, F. Graf, W. M. Shih, *Nature* **2009**, *459*, 414.
- [112] V. K. Khanna, *Integrated Nanoelectronics Nanoscale CMOS, Post-CMOS and Allied Nanotechnologies*, Springer India, **2016**.
- [113] Y. C. Tseng, Q. Peng, L. E. Ocola, J. W. Elam, S. B. Darling, *J. Phys. Chem. C* **2011**, *115*, 17725.
- [114] C. J. Hawker, T. P. Russell, *MRS Bull.* **2005**, *30*, 952.
- [115] C.-C. Chang, D. Botez, Lei Wan, P. F. Nealey, S. Ruder, T. F. Kuech, *J. Vac. Sci. Technol. B* **2013**, *31*, 031801.
- [116] M. S. Onses, C. Song, L. Williamson, E. Sutanto, P. M. Ferreira, A. G. Alleyne, P. F. Nealey, H. Ahn, J. A. Rogers, *Nat. Nanotechnol.* **2013**, *8*, 667.
- [117] J. W. Jeong, W. I. Park, M. J. Kim, C. A. Ross, Y. S. Jung, *Nano Lett.* **2011**, *11*, 4095.
- [118] B. H. Kim, J. Y. Kim, S. O. Kim, *Soft Matter* **2013**, *9*, 2780.
- [119] M. P. Stoykovich, H. Kang, K. C. Daoulas, G. Liu, C. C. Liu, J. J. de Pablo, M. Müller, P. F. Nealey, *ACS Nano* **2007**, *1*, 168.
- [120] M. Stefiik, S. Guldin, S. Vignolini, U. Wiesner, U. Steiner, *Chem. Soc. Rev.* **2015**, *44*, 5076.
- [121] K. Askar, B. M. Phillips, Y. Fang, B. Choi, N. Gozubenli, P. Jiang, B. Jiang, *Colloids Surfaces A Physicochem. Eng. Asp.* **2013**, *439*, 84.
- [122] H. J. Nam, J. H. Kim, D. Y. Jung, J. B. Park, H. S. Lee, *Appl. Surf. Sci.* **2008**, *254*, 5134.
- [123] J. Zhang, Y. Li, X. Zhang, B. Yang, *Adv. Mater.* **2010**, *22*, 4249.
- [124] K. A. Willets, R. P. van Duyne, *Annu. Rev. Phys. Chem.* **2007**, *58*, 267.
- [125] J. Zhang, B. Yang, *Adv. Funct. Mater.* **2010**, *20*, 3411.
- [126] S. Akerboom, J. Appel, D. Labonte, W. Federle, J. Sprakel, M. Kamperman, *J. R. Soc. Interface* **2015**, *12*, 20141061.
- [127] H. M. Powell, J. J. Lannutti, *Langmuir* **2003**, *19*, 9071.
- [128] D. G. Choi, H. K. Yu, S. G. Jang, S. M. Yang, *J. Am. Chem. Soc.* **2004**, *126*, 7019.
- [129] C. Cong, W. Junus, Z. Shen, T. Yu, *Nanoscale Res. Lett.* **2009**, *4*, 1324.
- [130] G. Zhang, D. Wang, H. Möhwald, *Nano Lett.* **2005**, *5*, 143.
- [131] H. H. Masuda, K. Fukuda, P. M. Chaikin, et. al, *Science* **1995**, *268*, 1466.
- [132] A. Belwalkar, E. Grasing, W. van Geertruyden, Z. Huang, W. Z. Misiolek, *J. Memb. Sci.* **2008**, *319*, 192.
- [133] W. J. Stępniewski, D. Forbot, M. Norek, M. Michalska-Domańska, A. Król, *Electrochim. Acta* **2014**, *133*, 57.
- [134] J. G. Buijnsters, R. Zhong, N. Tsyntsar, J.-P. Celis, *ACS Appl. Mater. Interfaces* **2013**, *5*, 3224.
- [135] A. Y. Y. Ho, L. P. Yeo, Y. C. Lam, I. Rodríguez, *ACS Nano* **2011**, *5*, 1897.
- [136] N. Vogel, L. de Viguerie, U. Jonas, C. K. Weiss, K. Landfester, *Adv. Funct. Mater.* **2011**, *21*, 3064.
- [137] S. J. Jeong, J. Y. Kim, B. H. Kim, H. S. Moon, S. O. Kim, *Mater. Today* **2013**, *16*, 468.
- [138] L. Hirt, A. Reiser, R. Spolenak, T. Zambelli, *Adv. Mater.* **2017**, *201604211*, 1604211.
- [139] M. Yu, K. H. Ahn, S. J. Lee, *Mater. Des.* **2016**, *89*, 109.

Nano- and microstructure fabrication

- [140] J.-U. Park, M. Hardy, S. J. Kang, K. Barton, K. Adair, D. K. Mukhopadhyay, C. Y. Lee, M. S. Strano, A. G. Alleyne, J. G. Georgiadis, P. M. Ferreira, J. A. Rogers, *Nat. Mater.* **2007**, *6*, 782.
- [141] E. Sutanto, K. Shigeta, Y. K. Kim, P. G. Graf, D. J. Hoelzle, K. L. Barton, A. G. Alleyne, P. M. Ferreira, J. A. Rogers, *J. Micromechanics Microengineering* **2012**, *22*, 45008.
- [142] C. W. Visser, R. Pohl, C. Sun, G. W. Römer, B. Huis in 't Veld, D. Lohse, *Adv. Mater.* **2015**, *27*, 4087.
- [143] M. Zenou, Z. Kotler, *Opt. Express* **2016**, *24*, 1431.
- [144] B. W. An, K. Kim, H. Lee, S. Y. Kim, Y. Shim, D. Y. Lee, J. Y. Song, J. U. Park, *Adv. Mater.* **2015**, *27*, 4322.
- [145] L. Peng, Y. Deng, P. Yi, X. Lai, *J. Micromechanics Microengineering* **2013**, *24*, 13001.
- [146] L. J. Guo, *Adv. Mater.* **2007**, *19*, 495.
- [147] Q. Xia, R. F. Pease, *Nanotechnology* **n.d.**, *26*, 182501.
- [148] H. Schiff, *Appl. Phys. A* **2015**, *121*, 415.
- [149] M. D. Stewart, S. C. Johnson, S. V. Sreenivasan, D. J. Resnick, C. G. Willson, *J. Microolithogr., Microfabr., Microsyst.* **2005**, *4*, 011002-11006
- [150] S. Y. Chou, P. R. Krauss, P. J. Renstrom, *Appl. Phys. Lett.* **1995**, *67*, 3114.
- [151] S. H. Ahn, L. J. Guo, *Adv. Mater.* **2008**, *20*, 2044.
- [152] G. Calafiore, A. Koshelev, F. I. Allen, S. Dhuey, S. Sassolini, E. Wong, P. Lum, K. Munechika, S. Cabrini, *Nanotechnology* **2016**, *27*, 375301.
- [153] H. Küpers, A. Tahraoui, R. B. Lewis, S. Rauwerdink, M. Matalla, O. Krüger, F. Bastiman, H. Riechert, L. Geelhaar, *Semicond. Sci. Technol.* **2017**, *32*, 115003.
- [154] I. Fernandez-Cuesta, A. Laura Palmarelli, X. Liang, J. Zhang, S. Dhuey, D. Olynick, S. Cabrini, *J. Vac. Sci. Technol. B Microelectron. Nanom. Struct.* **2011**, *29*, 06F801.
- [155] K. Ansari, J. A. van Kan, A. A. Bettiol, F. Watt, *Appl. Phys. Lett.* **2004**, *85*, 476.
- [156] D. J. Resnick, W. J. Dauksher, D. Mancini, K. J. Nordquist, E. Ainley, K. Gehoski, J. H. Baker, T. C. Bailey, B. J. Choi, S. Johnson, S. V. Sreenivasan, J. G. Ekerdt, C. G. Willson, *J. Microolithogr. Microfabr. Microsystems* **2002**, *1*, 284.
- [157] M. Nakagawa, A. Nakaya, Y. Hoshikawa, S. Ito, N. Hiroshiba, T. Kyotani, *ACS Appl. Mater. Interfaces* **2016**, *8*, 30628.
- [158] D. Jucius, A. Lazauskas, V. Grigaliūnas, B. Abakevičienė, S. Smetona, S. Tamulevičius, *Microsyst. Technol.* **2018**, *24(2)*, 1115-1125.
- [159] M. D. Stewart, S. C. Johnson, S. V. Sreenivasan, D. J. Resnick, C. G. Willson, *J. Microolithogr. Microfabr. Microsystems* **2005**, *4*, 11002.
- [160] W.-D. Li, W. Wu, R. Stanley Williams, *J. Vac. Sci. Technol. B Microelectron. Nanom. Struct.* **2012**, *30*, 06F304.
- [161] Y. Xia, J. J. McClelland, R. Gupta, D. Qin, X. M. Zhao, L. L. Sohn, R. J. Celotta, G. M. Whitesides, *Adv. Mater.* **1997**, *9*, 147.
- [162] E. King, Y. Xia, X. M. Zhao, G. M. Whitesides, *Adv. Mater.* **1997**, *9*, 651.
- [163] Y. Xia, G. M. Whitesides, *Annu. Rev. Mater. Sci.* **1998**, *28*, 153.
- [164] N. L. Jeon, R. G. Nuzzo, Y. Xia, M. Mrksich, G. M. Whitesides, *Langmuir* **1995**, *11*, 3024.
- [165] M. Hecke, W. K. Schomburg, *J. Micromechanics Microengineering* **2003**, *14*, R1.
- [166] C. N. LaFratta, T. Baldacchini, R. A. Farrer, J. T. Fourkas, M. C. Teich, B. E. A. Saleh, M. J. Naughton, *J. Phys. Chem. B* **2004**, *108*, 11256.
- [167] H.-H. Jeong, J.-H. Lee, Y.-M. Noh, Y.-G. Kim, C.-S. Lee, *Macromol. Res.* **2013**, *21*, 534.
- [168] D. Pisignano, E. Sariconi, M. Mazzeo, G. Gigli, R. Cingolani, *Adv. Mater.* **2002**, *14*, 1565.
- [169] L. Han, J. Zhou, X. Gong, C. Gao, *Chinese Sci. Bull.* **2009**, *54*, 2193.
- [170] D. Liyu, S. H. Nemat, A. E. Vasdekis, *J. Polym. Sci. Part B Polym. Phys.* **2016**, *54*, 1681.
- [171] E. Müller, T. Pompe, U. Freudenberg, C. Werner, *Adv. Mater.* **2017**, *29*, 1703489.
- [172] F. Hua, Y. Sun, A. Gaur, M. A. Meitl, L. Bilhaut, L. Rotkina, J. Wang, P. Geil, M. Shim, J. A. Rogers, A. Shim, *Nano Lett.* **2004**, *4*, 2467.
- [173] Z. X. Deng, C. D. Mao, *Langmuir* **2004**, *20*, 8078.
- [174] C. Pang, T. Kim, W. G. Bae, D. Kang, S. M. Kim, K.-Y. Suh, *Adv. Mater.* **2012**, *24*, 475.
- [175] J. A. Helmuth, H. Schmid, R. Stutz, A. Stemmer, H. Wolf, *J. Am. Chem. Soc.* **2006**, *128*, 9296.
- [176] J. C. Love, L. A. Estroff, J. K. Kriebel, R. G. Nuzzo, G. M. Whitesides, *Chemical Reviews* **2005**, *105*, 1103-1170.
- [177] S. Alom Ruiz, C. S. Chen, *Soft Matter* **2007**, *3*, 168.
- [178] S. A. Lange, V. Benes, D. P. Kern, *J. K. H. Ho*, **2004**, *76*, 1641.
- [179] S. T. Han, Y. Zhou, Z. X. Xu, L. B. Huang, X. B. Yang, V. A. L. Roy, *Adv. Mater.* **2012**, *24*, 3556.
- [180] Y. Xia, G. M. Whitesides, *Langmuir* **1997**, *13*, 2059.
- [181] M. K. Choi, J. Yang, K. Kang, D. C. Kim, C. Choi, C. Park, S. J. Kim, S. I. Chae, T.-H. Kim, J. H. Kim, T. Hyeon, D.-H. Kim, *Nat. Commun.* **2015**, *6*, 7149.
- [182] J. Li, L. Xu, S. Kim, A. A. Shestopalov, *J. Mater. Chem. C* **2016**, *4*, 4155.
- [183] J. W. Jeong, S. R. Yang, Y. H. Hur, S. W. Kim, K. M. Baek, S. Yim, H.-I. Jang, J. H. Park, S. Y. Lee, C.-O. Park, Y. S. Jung, *Nat. Commun.* **2014**, *5*, 5387.
- [184] J.-G. Kim, Y. Sim, Y. Cho, J.-W. Seo, S. Kwon, J.-W. Park, H. G. Choi, H. Kim, S. Lee, *Microelectron. Eng.* **2009**, *86*, 2427.
- [185] D. J. Resnick, S. V. Sreenivasan, C. G. Willson, *Mater. Today* **2005**, *8*, 34.
- [186] M. B. Chan-Park, J. Zhang, Y. Yan, C. Y. Yue, *Sensors Actuators, B Chem.* **2004**, *101*, 175.
- [187] R. Gauvin, Y. C. Chen, J. W. Lee, P. Soman, P. Zorlutuna, J. W. Nichol, H. Bae, S. Chen, A. Khademhosseini, *Biomaterials* **2012**, *33*, 3824.
- [188] C. Maurer, A. Jesacher, S. Bernet, M. Ritsch-Marte, *Laser Photon. Rev.* **2011**, *5*, 81.
- [189] J. K. Hohmann, M. Renner, E. H. Waller, G. von Freymann, *Adv. Opt. Mater.* **2015**, *3*, 1488.
- [190] G. Vizsnyczai, L. Kelemen, P. Ormos, *Opt. Express* **2014**, *22*, 24217.
- [191] C. W. Hull, S. T. Spence, D. J. Albert, D. R. Smalley, R. A. Harlow, P. Stinebaugh, H. L. Tarnoff, H. D. Nguyen, C. W. Lewis, T. J. Vorgitch, , D. Z. Remba, U.S. Patent No 5, **1993**, *184*, 307.
- [192] Q. Chen, R. Xu, Z. He, K. Zhao, L. Pan, *J. Electrochem. Soc.* **2017**, *164*, A1852.

- [193] A. A. Yazdi, A. Popma, W. Wong, T. Nguyen, Y. Pan, J. Xu, *Microfluid. Nanofluidics* **2016**, *20*, 1.
- [194] M. Malinauskas, M. Farsari, A. Piskarskas, S. Juodkazis, *Phys. Rep.* **2013**, *533*, 1.
- [195] E. S. Wu, J. H. Strickler, W. R. Harrell, W. W. Webb, *Optical/Laser Microlithography V* **1992**, *1674*, 776.
- [196] P. Mueller, M. Thiel, M. Wegener, *Opt. Lett.* **2014**, *39*, 6847.
- [197] J. Fischer, M. Wegener, **2011**, *1*, 2363.
- [198] P. E. Petrochenko, J. Torgersen, P. Gruber, L. A. Hicks, J. Zheng, G. Kumar, R. J. Narayan, P. L. Goering, R. Liska, J. Stampfl, A. Ovsianikov, *Adv. Healthc. Mater.* **2015**, *4*, 739.
- [199] R. Gupta, J. Fréchet, *Langmuir* **2012**, *28*, 14703.
- [200] K. S. Lee, D.-Y. Yang, S. H. Park, T. W. Lim, Ran Hee Kim, in *2006 Int. Symp. Biophotonics, Nanophotonics Metamaterials*, IEEE, Piscataway, NJ, USA **2006**, 8-14.
- [201] A. Fernández-Pacheco, L. Serrano-Ramón, J. M. Michalik, M. R. Ibarra, J. M. de Teresa, L. O'Brien, D. Petit, J. Lee, R. P. Cowburn, *Sci. Rep.* **2013**, *3*, 1492.
- [202] W. F. van Dorp, C. W. Hagen, *J. Appl. Phys.* **2008**, *104*, 1.
- [203] M. Esposito, V. Tasco, F. Todisco, A. Benedetti, D. Sanvitto, A. Passaseo, *Adv. Opt. Mater.* **2014**, *2*, 154.
- [204] A. J. M. Mackus, N. F. W. Thissen, J. J. L. Mulders, P. H. F. Trompenaars, Z. Chen, W. M. M. Kessels, A. A. Bol, *Appl. Phys. Lett.* **2017**, *110*, 013101.
- [205] H. Cölfen, S. Mann, *Angew. Chemie - Int. Ed.* **2003**, *42*, 2350.
- [206] R. Gramage-Doria, J. Hessels, S. H. A. M. Leenders, O. Tröppner, M. Dürr, I. Ivanović-Burmazović, J. N. H. Reek, *Angew. Chemie - Int. Ed.* **2014**, *53*, 13380.
- [207] S. Mura, J. Nicolas, P. Couvreur, *Nat Mater* **2013**, *12*, 991.
- [208] M. Ulbricht, *Polymer (Guildf)*. **2006**, *47*, 2217.
- [209] M. A. Cohen Stuart, W. T. S. Huck, J. Genzer, M. Müller, C. Ober, M. Stamm, G. B. Sukhorukov, I. Szleifer, V. V. Tsukruk, M. Urban, F. Winnik, S. Zauscher, I. Luzinov, S. Minko, *Nat. Mater.* **2010**, *9*, 101.
- [210] S. Akerboom, S. P. Pujari, A. Turak, M. Kamperman, *ACS Appl. Mater. Interfaces* **2015**, *7*, 16507.
- [211] K. V. Wong, A. Hernandez, *ISRN Mech. Eng.* **2012**, *2012*, 1.
- [212] N. Guo, M. C. Leu, *Front. Mech. Eng.* **2013**, *8*, 215.
- [213] A. del Campo, C. Greiner, E. Arzt, *Langmuir* **2007**, *23*, 10235.
- [214] L. T. Varghese, L. Fan, J. Wang, Y. Xuan, M. Qi, *Small* **2013**, *9*, 4237.
- [215] A. W. Knoll, M. Zientek, L. L. Cheong, C. Rawlings, P. Paul, F. Holzner, J. L. Hedrick, D. J. Coady, R. Allen, U. Dürrig, *SPIE Adv. Lithogr.* **2014**, *11*, 90490B.

Chapter 3

ADHESION AND FRICTION OF MICROPATTERNED ELASTOMERS ON SOFT SUBSTRATES: THE EFFECTS OF PATTERN LENGTH SCALE AND STIFFNESS

This chapter has been published as:

Peter van Assenbergh, Marike Fokker, Julian Langowski, Jan van Esch, Marleen Kamperman and Dimitra Dodou, *Beilstein J. Nanotechnol.* **2019**, *10*(1), 79-94, doi: 10.3762/bjnano.10.8

Abstract

Background: *In nature, impressive examples of micropatterned adhesives can be found. The adhesiveness of biological micropatterned adhesives primarily relies on their geometry (e.g., feature size, architecture) and material properties (e.g., stiffness). Over the last few decades, researchers have been developing adhesives mimicking the geometry and material properties of biological micropatterned adhesives. The performance of these biomimetic micropatterned adhesives is usually tested on hard substrates. Much less is known about the effect of geometry, feature size, and material properties on the performance of micropatterned adhesives when the substrate is deformable.*

Results: *Micropatterned adhesives of two stiffness degrees (Young's moduli of 280 and 580 kPa) were fabricated from polydimethylsiloxane (PDMS) and tested on soft polyvinyl alcohol (PVA) substrates of two stiffness degrees (12 and 18 kPa), and on hard glass substrates as a reference. An out-of-the-cleanroom colloidal lithographic approach was successfully expanded to fabricate adhesives with two geometries, namely dimples with and without a terminal layer. Geometries of dimples without a terminal layer were fabricated on two length scales, namely with sub-microscale and microscale dimple di-*

ameters. We found that the presence of a terminal layer has a positive effect on adhesion on soft substrates compared to flat reference samples. Friction was the highest for the microscale dimple geometry without a terminal layer.

Conclusion: Based on our measurements we found that, on soft substrates, microscale dimples generate higher adhesion and friction than sub-microscale dimples. The positive effects of sub-microscale features on adhesion and friction, such as defect control and crack trapping, as reported in the literature for hard substrates, seem to disappear on soft substrates. Adhesion on soft substrates increased with the substrate stiffness for all tested geometries. On the softer PVA substrate, the dimple geometry with a terminal layer generated significantly higher adhesion compared to the other geometries.

3

3.1 Introduction

Adhesion and friction of micropatterned adhesives as a function of geometry, feature size, and stiffness

Over the last few decades, several researchers have developed micropatterned adhesives mimicking the geometry and material properties of biological dry adhesives.^[1-5] Adhesion and friction of these biomimetic adhesives rely on the formation of intimate contact with the substrates,^[6] enabling physical interactions between adhesive and substrate, in the form of intermolecular forces, capillary forces, and suction forces. To achieve intimate contact between the adhesive and the substrate, researchers have been designing micropatterned adhesives with a low effective elastic modulus E_{eff} .^[6] For example, micro- and/or nanoscale fibrillar geometries have been reported,^[7] where the flexibility of the individual fibrils leads to a low E_{eff} .^[8] In micropatterns with a fibrillar geometry, the formed contact area is divided into multiple smaller contacts. This so-called contact splitting has been shown to result in higher pull off forces than a non-fibrillar contact of the same area, due to a better defect control,^[9] better stress distribution.^[10] The decreased E_{eff} of such a geometry also leads to a decreased contact stiffness,^[11] and higher conformability to substrate roughness.^[12]

The abovementioned effects of contact splitting can be further enhanced with variations of the pillar geometry. For example, Gorb et al. fabricated micropillars of 100 μm height and a stem diameter of 60 μm , terminated with a thin (2 μm) disc of 40 μm in diameter.^[11] These so-called mushroom-shaped micropillars generated higher adhesion than flat-punch micropillars, a phenomenon attributed to a higher adaptability to substrate roughness due to the presence of the terminal thin disc.^[11] Varenberg et al. found that detachment of the terminal disc happens from the inside out, with a peeling line moving from the center of the disc toward its outer edge.^[13] In later work, Varenberg et al. reasoned that, as the terminal disc of mushroom-shaped micropillars detaches via a local thin-film peeling mechanism, multiple peeling fronts are present throughout the micropattern.^[14] This splitting up of the peeling front in multiple smaller fronts results in a drastic increase in peeling line length, and therefore in high adhesion and friction forces.^[14,15] Heepe et al. investigated the significance of suction forces during detachment of mushroom-shaped micropillars.^[16] Considering that the inside-towards-outside detachment mechanism gives rise to a low-pressure enclosed space in the center of the terminal disc during detachment. These authors empirically showed that suction forces are responsible for about 10 percent of the pull off force mushroom micropatterns.^[16]

The presence of a terminal layer connecting neighboring micropillars at their tips has also shown to have a favorable effect on adhesive and friction forces on hard substrates. Glassmaker et al., for example, fabricated arrays of micropillars of 14 μm in diameter and 50 μm in height, where neighboring micropillars were connected at their tips with a continuous terminal layer of 4 μm in thickness.^[17] These authors found that adhesion increased with increasing spacing between micropillars, and 9 times higher adhesion was found compared to flat control samples at a spacing of 87 μm . The authors suggested that the increase in adhesion was caused by a crack-trapping mechanism during pulling off.^[17] Bae et al. argued that the presence of a terminal layer leads to an increase of contact area with increasing preloads, resulting in higher adhesion under compression as compared to geometries without a terminal layer.^[18] The friction of micropatterned adhesives with a terminal layer has been also investigated. He et al., for example, reported that, for a film-terminated ridge-channel structure, friction forces increased when channel width increased.^[19] It was suggested that the terminal layer stretches during sliding, causing loss of elastic energy, thereby contributing to friction.

3

Besides geometry (i.e., shape), also the size of micropattern features has an effect on the E_{eff} of micropatterned adhesives. Varenberg et al. reasoned that feature size has an effect on the contact stiffness of individual micropillars.^[14] More specifically, smaller micropillars have a lower elastic resistance when making contact with the substrate, leading to an increased pull-off force.^[14] Greiner et al. found that with increasing aspect ratio of micropattern features, their compliance increases, resulting in a better conformability to substrate roughness.^[20]

Hierarchical geometries, that is, architectures with features on different length scales, conform to substrate roughness on different length scales, increasing adhesion and friction.^[21]

Besides geometry and feature size, the E_{eff} of adhesive micropatterns also relates to the stiffness of the material the micropattern is made of.^[6] When a soft material is used for the micropattern, the E_{eff} is low, and effects of contact splitting such as defect control, stress distribution, and contact stiffness are enhanced compared to micropatterns made of stiffer materials.^[22] Also the strength of the contacts formed between adhesive and substrate is affected by the material stiffness of the micropatterned adhesive, as this strength depends on the area of contact that is formed, which in turn is determined by the indentation depth of the adhesive into the substrate.^[23]

The performance of biomimetic micropatterned adhesives is usually tested on hard substrates, primarily glass and polystyrene. Much less is known about the performance of micropatterned adhesives when the substrate is deformable. Secure grip on soft, deformable substrates can be useful in a range of applications, including soft-tissue manipulation during surgical procedures and pick-and-place of soft biological objects such as grapes and poultry in food processing industries. The role of the geometry, feature size, and material stiffness of a micropattern in its adhesion and friction on a soft, deformable substrate can be expected to be different than when approaching a hard substrate, as soft substrates deform under load and may conform to the geometry of the adhesive. For a simplified representation of a beetle's discoidal adhesive element, Heepe et al., showed that if the substrate is stiffer than the adhesive apparatus, a detachment mechanism similar to that observed for mushroom-shapes micropillars is present, with detachment starting from the center of the disc and moving toward its outer edge. However, if the substrate was softer than the adhesive apparatus,

the latter potentially behaved like a flat punch, and detachment started at the outer edge. Cheung et al. showed that during pulling off a micropattern from a soft substrate, the substrate deforms, and the detachment of neighboring pillars is no longer independent.^[24]

Accordingly, the adhesion of mushroom-pillar micropatterns on a soft elastic substrate (Young's modulus $E = 200$ kPa) has been found to be lower than on a rigid glass substrate.^[24]

On very soft substrates (Young's modulus $E = \sim 10$ kPa), the indentation depth of microscale features is determined by a balance between the elastic properties of the substrate and the substrate-micropattern adhesion effects.^[25] The length scale at which these adhesion effects are present is referred to as the elastocapillary length l , which is defined as $l = \gamma/\mu$, where γ is the surface tension of the substrate and μ is the elastic shear modulus of the substrate.^[26] If the length scale of the microscale features is in the order of the elastocapillary length, indentation is dominated by surface tension effects, whereas for larger features, surface tension effects are balanced by elasticity.^[25]

Summarizing, whereas for rigid substrates, adhesive micropatterns have been designed to gain a low E_{eff} , it remains to be investigated whether this design approach should also be followed for generating adhesive micropatterns for soft substrates. In order to gain insight into this question, we investigated the adhesion and friction of adhesive micropatterns on soft substrates as a function of the geometry and feature size of the micropattern, and the stiffness of both the substrate and the adhesive.

Fabrication of micropatterned adhesives with various geometries, feature sizes, and stiffness degrees

Fabrication of micropatterned adhesives is most commonly done with molding techniques, in which a curable resin is shaped using a photolithographically fabricated three-dimensional hard template.^[3,24,27] This fabrication method allows fabrication of a wide range of architectures and of features sizes at both nano- and microscale.^[28] A limitation of this molding method is that demolding becomes challenging when the shaped material is soft. Another challenge of this method is that it requires complex instrumentation.^[28]

Akerboom et al. recently demonstrated a fast and cost-effective alternative method to fabricate micropatterns, in which a colloidal monolayer acts as a three-dimensional template to shape a curable resin,^[29,30] resulting in arrays of sub-microscale dimples.^[30] This fabrication method allows demolding of resins even if, due to soft properties, they adhere to the template, as demolding is done by chemically dissolving the colloidal template.

In this work, we used the abovementioned colloidal lithographic approach to fabricate adhesive micropatterns with various stiffness degrees. Moreover, we expanded the fabrication method in order to fabricate two dimple sizes: sub-microscale and microscale. Finally, considering the positive effect of a terminal layer on the adhesion of micropatterns, we expanded the fabrication process in order to also fabricate dimple arrays topped with a thin terminal layer.

The adhesion and friction of these micropatterns were tested on soft substrates made of polyvinyl alcohol (PVA) with two stiffness degrees and compared with the corresponding performance on glass as reference.

3.2 Results

Characterization of particles, dimple micropatterns with and without terminal layer, and PVA substrates

The sub-microscale particles we used had an average diameter of 691 nm (SD = 14 nm), and a polydispersity index of 1.23. The average diameter of the microscale particles was 8.7 μm (SD = 1.4 μm), with a polydispersity index of 1.10.

Micropatterned adhesives were fabricated from colloidal templates, as shown in **Figure 3.1** and explained in the experimental section. For the micropatterns of dimples from sub-microscale particles, the packing and size of the obtained dimples was homogeneous, as confirmed by AFM and SEM (**Figure 3.2**). AFM measurements further showed a dimple diameter of about 500 nm and a depth of about 200 nm (see Supporting Information 2, **Figure SI3.3**). For micropatterns with dimples from microscale particles with and without a terminal layer, top view SEM images showed an average dimple diameter of 8.1 μm (SD = 1.17 μm, n = 100) (**Figure 3.3**, left). The depth of dimples from microscale particles could not be accurately de-

termined from microscopic cross-section images, as it is unknown whether a dimple was sectioned through its center, where the diameter is largest. From the cross-section shown at **Figure 3.3** (left, onset), the dimple depth was equal to half of the dimple diameter. The cross-section of samples with a terminal layer showed voids with a spherical shape, separated by hour-glass-shaped walls (**Figure 3.3**, right, onset). These voids penetrate the terminal layer, resulting in an array of holes at the surface (**Figure 3.3**, right).

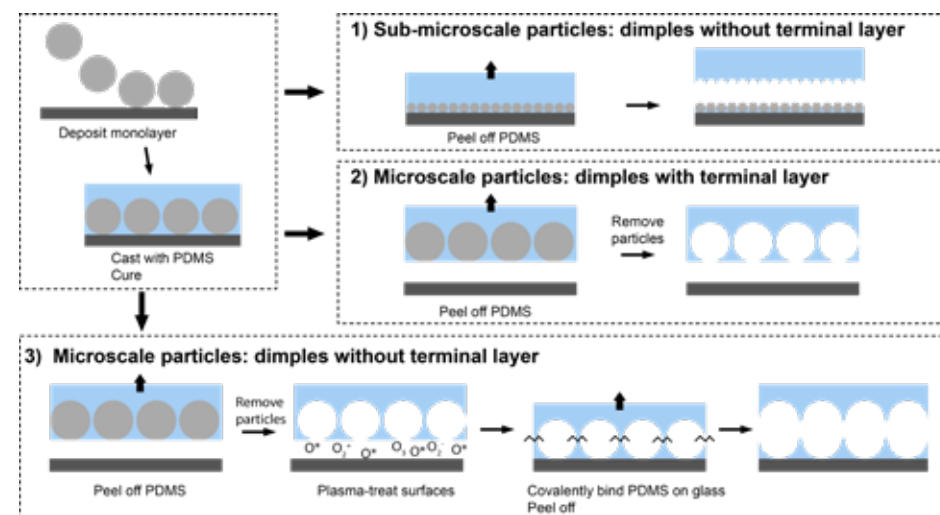


Figure 3.1. Pathway to fabricate dimple arrays with and without terminal layers. Starting from the left: Deposition of a colloidal monolayer with a dip-coating cycle, followed by casting the monolayer with PDMS and subsequent curing. Depending on the particle size, the PDMS either comes off without the terminal layer (pathway 1), and the particles remain attached to the glass, or with the terminal layer (pathways 2 and 3), and the particles remain embedded in the PDMS. In the latter case, particles are subsequently removed by washing them in N-methylpyrrolidone. To obtain dimples without a terminal layer from microscale particles (pathway 3), dimples with a terminal layer from microscale particles are first fabricated, after which the terminal layer is removed by covalently binding it to glass, and subsequently peeling off.

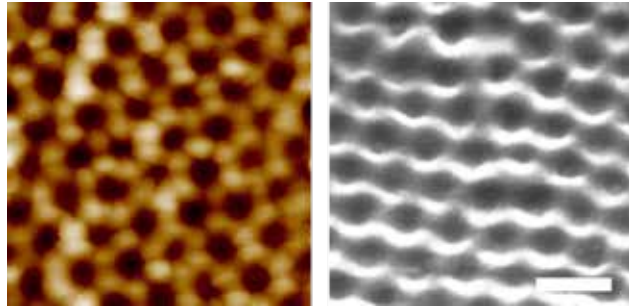


Figure 3.2. SEM and AFM images of micropatterns from sub-microscale particles. Left: Top view of the dimple micropattern after peeling off from untreated glass and removing the particles. A regular array of dimples is visible. Right: SEM picture of sub-microscale dimples. Charging of the edges of the micropattern impeded high-quality surface imaging. SEM data, however, confirmed a homogeneous distribution of dimple packing and dimple size. The image is taken from an angle of 30°. The scale bar is 1 μm .

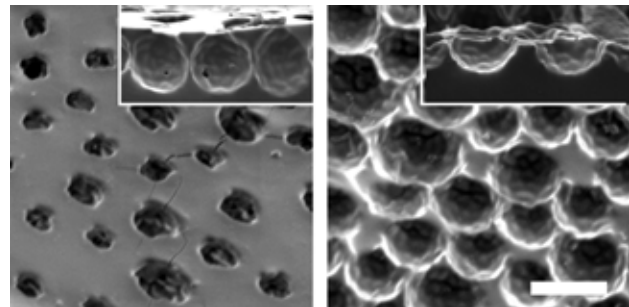


Figure 3.3. SEM images of micropatterns from microscale particles. Left: Array of dimples. Inset: Cross section of a dimple array showing a dimple depth of about 5 μm . Right: Micropattern with a terminal layer. The image is taken from a 45° angle. Subsurface voids are visible through the holes. Inset: Cross-section of a micropattern with terminal layer showing spherical voids, separated by hourglass-shaped walls. The scale bar is 10 μm .

PDMS in 1:10 and 1:20 crosslinker:pre-polymer weight ratios was prepared, resulting in samples with Young's moduli of 580 kPa (henceforth referred to as PDMS-580) and 280 kPa (PDMS-280), respectively.^[31]

The stiffness of the PVA substrates was adjusted by varying the number of freeze-thaw cycles of the PVA. PVA subjected to two and three freeze-thaw cy-

cles had storage moduli of 12 kPa (referred to as PVA-12) and 18 kPa (referred to as PVA-18), respectively, as measured using a rheometer (see SI1). The dissipation factor $\tan \delta$ was 0.05 and 0.07 for PVA-12 and PVA-18, respectively. The elastocapillary length l of PVA is defined as $l = \gamma_{PVA} / \mu_{PVA}$ ^[26] (surface tension $\gamma_{PVA} = \sim 50$ kPa,^[32] elastic shear modulus $\mu_{PVA} = \sim 12$ kPa for PVA-12), and is in the order of 400 nm.

Adhesion of micropatterns on PVA and glass

Figure 3.4 shows representative force-time plots of adhesion measurements of microscale dimples without a terminal layer on PVA-18 and glass. It can be seen that detachment during pull-off (phase II) was slower on PVA than on glass.

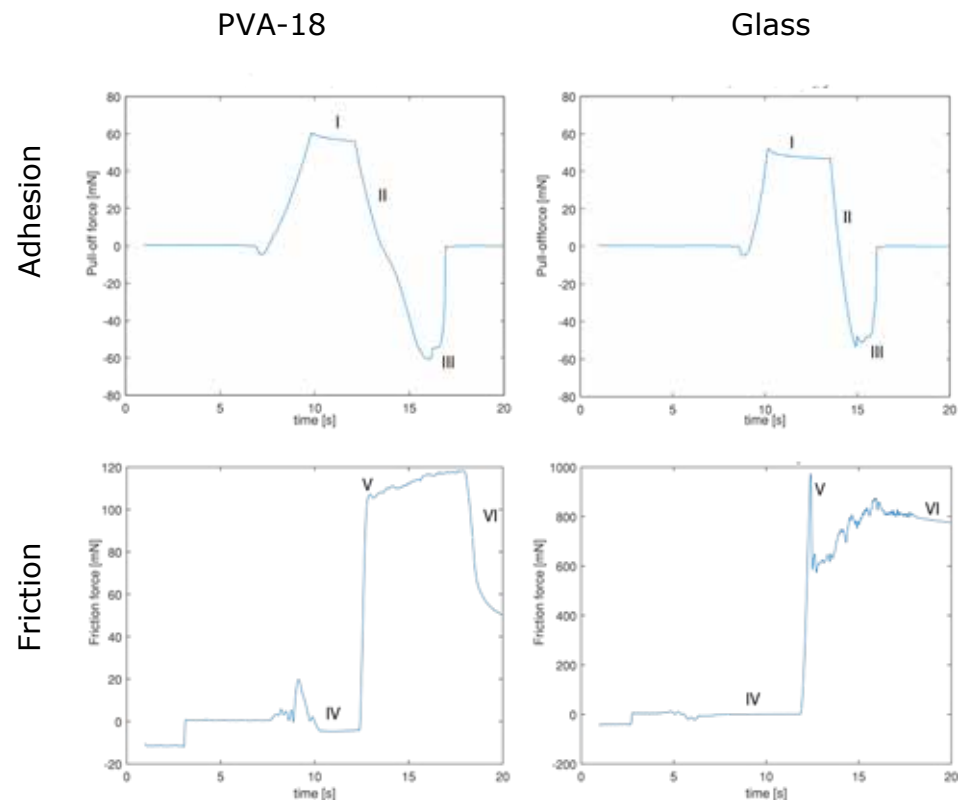


Figure 3.4. Representative force-time plots of adhesion (top row) and friction (bottom row) measurements of microscale dimples without a terminal layer on PVA-18 (left column) and

glass (right column). Adhesion measurements: I) A normal preload of 55 mN is applied. II) The substrate is pulled off from the sample at 100 $\mu\text{m/s}$. III) The sample detaches from the substrate. The local minimum is reported as the pull-off force. Friction: IV) A normal (pre)load of 55 mN is applied. V) The substrate starts sliding at 500 $\mu\text{m/s}$. The first peak is reported as the static friction force. VI) After 6 seconds, sliding is stopped, and the forces in lateral direction decrease.

Figure 3.5 shows the adhesion force on PVA-12 and PVA-18 for samples of PDMS-580 with various geometries and feature sizes. The results for the samples made of PDMS-280 are not shown here, as these exhibited similar trends to the PDMS-580 samples. Measurement data of PDMS-280 micropatterns, as well as descriptive statistics of the adhesion and friction forces for all measured conditions are reported in SI3.5.

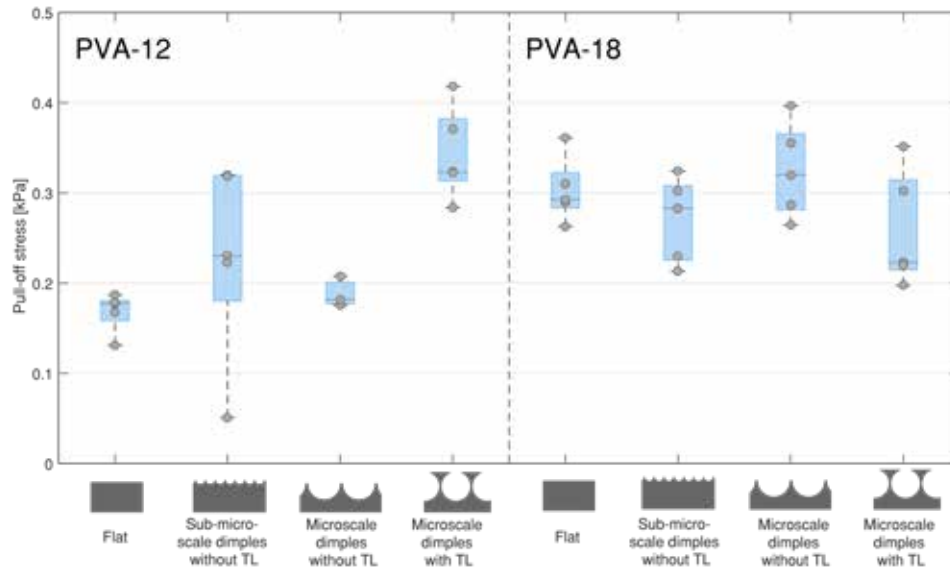


Figure 3.5. Adhesion stress (adhesion force divided by the sample area) for flat samples, sub-microscale dimples without terminal layer and microscale dimples with and without terminal layer, on PVA-12 (left) and PVA-18 (right). Only the results for PDMS-580 samples are shown. Each data point represents the average of five consecutive measurements of one sample, and each boxplot consists of five different samples of the same geometry.

A three-way ANOVA for sample geometry (flat, microscale dimples with terminal layer, and microscale dimples without terminal layer), sample stiff-

ness (580 vs. 280 kPa), and substrate stiffness (18 vs. 12 kPa) showed significant main effects for the sample geometry ($F(2,46) = 18.31, p < 0.001$) and substrate stiffness ($F(1,46) = 19.29, p < 0.001$); the main effect of sample stiffness was not significant ($F(1,46) = 2.32, p = 0.135$). An interaction effect between sample geometry and substrate stiffness was also observed ($F(2,46) = 29.61, p < 0.001$). Post-hoc analysis showed that, on the softer PVA (i.e., PVA-12) and for both sample stiffness degrees, adhesion of microscale dimples with a terminal layer was significantly higher than the adhesion on flat samples as well as microscale dimples without a terminal layer (all $p < 0.001$, after Bonferroni correction). Flat samples and microscale dimples without a terminal layer did not exhibit significant difference in adhesion (PDMS-580 samples: $p = 1$; PDMS-280 samples: $p = 0.486$). On the stiffer PVA (i.e., PVA-18), no significant effects of either sample geometry or sample stiffness were observed. Flat samples and microscale dimples without a terminal layer generated higher adhesion on PVA-18 than on PVA-12 (PDMS-580 samples: both $p < 0.001$; PDMS-280 samples: both $p = 0.003$).

A three-way ANOVA for feature size (flat, sub-microscale dimples without terminal layer, and microscale dimples without terminal layer), sample stiffness (580 vs. 280 kPa), and substrate stiffness (18 vs. 12 kPa) showed a significant effect for substrate stiffness ($F(1,47) = 32.63, p < 0.001$); the main effects for feature size ($F(2,47) = 2.78, p = 0.072$) and sample stiffness ($F(1,47) = 0.86, p = 0.358$) were not significant. An interaction effect between feature size and substrate stiffness ($F(2,47) = 10.2, p < 0.001$) was also observed. Post-hoc analysis showed that adhesion was significantly higher on PVA-18 than on PVA-12 for flat PDMS-580 samples and microscale PDMS-580 samples ($p < 0.001$). On PVA-18, microscale PDMS-280 samples exhibited significantly higher adhesion than sub-microscale PDMS-280 samples ($p < 0.001$).

Figure 3.6 shows the adhesion forces on glass for samples of PDMS-580 with various geometries and feature sizes. The results for the samples made of PDMS-280 are not shown, as these exhibited similar trends to the PDMS-580 samples. It can be seen that sub-microscale samples and microscale samples with a terminal layer tend to generate higher adhesion than flat samples and microscale samples without a terminal layer. For these two conditions, one of the five measurements could not be completed because the sensor reached its maximum capacity. Because of the small sample

size, we refrained from presenting boxplots with median and interquartile range, and present only raw data instead.

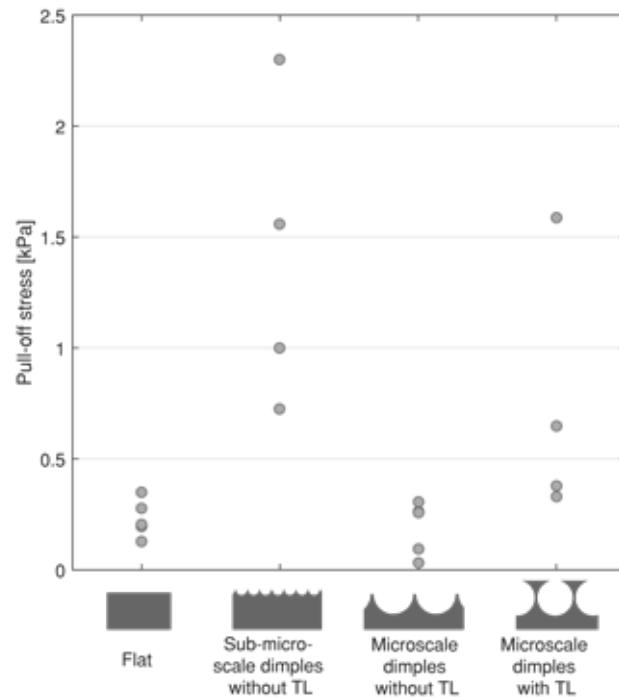


Figure 3.6. Adhesion stress for flat samples, sub-microscale samples without terminal layer and microscale samples with and without terminal layer on glass. Only the results for PDMS-580 samples are shown. Each data point represents the average of five consecutive measurements of one sample, and for each geometry, four or five samples have been tested. For sub-microscale samples without terminal layer and microscale samples with terminal layer (i.e., second and fourth geometry) one data point for each is missing because the measurement exceeded the maximum capacity of the sensor.

Friction of micropatterns on PVA and glass

In Figure 3.4, time-force plots of friction measurements are depicted. Friction plots show that a static friction peak right before sliding (phase V) was observed only on glass but not on PVA. **Figure 3.7** shows the friction forces on PVA-12 and PVA-18 for samples of PDMS-580 with various geometries and feature sizes. The results for the samples made of PDMS-280 are not shown, as these exhibited similar trends to the PDMS-580 samples. The results of friction measurements of all conditions are reported in SI5.

A three-way ANOVA for sample geometry (flat, microscale with, and sub-microscale without terminal layer), sample stiffness (580 vs. 280 kPa), and substrate stiffness (18 vs. 12 kPa) showed significant main effects for the sample geometry ($F(2,50) = 34.33, p < 0.001$) and substrate stiffness ($F(1,50) = 18.3, p < 0.001$); the main effect of sample stiffness was not significant ($F(1,50) = 0.09, p = 0.763$). A small interaction effect between sample geometry and substrate stiffness was also observed ($F(2,50) = 4.17, p = 0.021$). Post-hoc analysis showed that on the harder PVA-18 substrate and for both PDMS-580 and PDMS-280, microscale samples without terminal layer generated higher friction than both flat samples ($p < 0.001$) and microscale samples with a terminal layer (PDMS-580: $p < 0.001$, PDMS-280: $p = 0.031$). The friction of the microscale samples with a terminal layer was not significantly different from the flat samples for either substrate and either sample stiffness.

A three-way ANOVA for feature size (flat, sub-microscale samples without terminal layer, and microscale without terminal layer), sample stiffness (580 vs. 280 kPa), and substrate stiffness (18 vs. 12 kPa) showed a significant effect for feature size ($F(2,50) = 45.35, p < 0.001$); the main effects for sample stiffness ($F(1,50) = 2.43, p = 0.125$) and substrate stiffness ($F(1,50) = 3.00, p = 0.090$) were not significant. A small interaction effect between feature size and sample stiffness was also observed ($F(2,50) = 7.39, p = 0.002$). Post-hoc analysis showed that friction was significantly higher for microscale samples than for flat samples for both sample stiffness degrees and both substrate stiffness degrees, with the effect being stronger for the softer substrate (PVA-12: PDMS-580, $p = 0.001$, PDMS-280, $p = 0.003$; PVA-18: both $p < 0.001$). Microscale samples also generated higher friction than sub-microscale samples for PDMS-580 (PVA-12: $p < 0.001$, PVA-18: $p = 0.002$), whereas for PDMS-280 both sub-microscale and microscale samples generated equally high friction.

Figure 3.8 shows the friction forces on glass for samples of PDMS-580 with various geometries and feature sizes. Sub-microscale samples without terminal layer seem to generate higher friction than the remainder of the samples, but we refrain from drawing any conclusions, as for 6 out of the 35 measurements the sensor reached its maximum capacity (for PDMS-580: 1 measurement for each of the four samples; for PDMS-280: 2 measurements for micrometer samples with terminal layer).

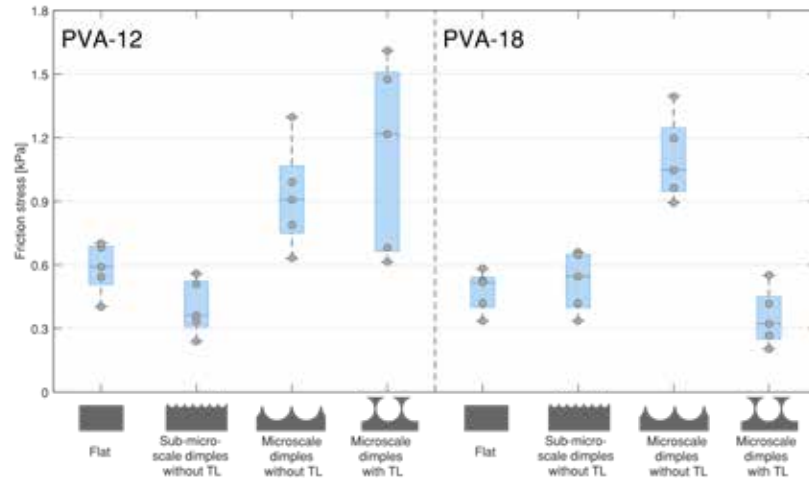


Figure 3.7. Friction stress (friction force divided by the sample area) for flat samples, sub-microscale samples without terminal layer, and microscale samples with and without terminal layer, on PVA-12 (left) and PVA-18 (right). Only the results for PDMS-580 samples are shown.

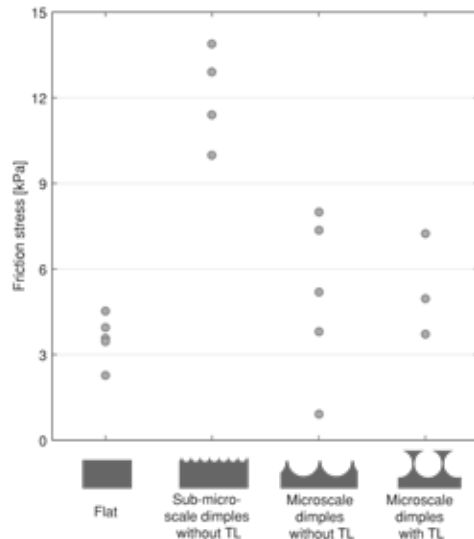


Figure 3.8. Friction stress for flat samples, sub-microscale samples without terminal layer, and microscale samples with and without terminal layer, on glass. Only the results for PDMS-580 samples are shown. One data point for each geometry is missing because these measurements exceeded the maximum capacity of the sensor.

3.3 Discussion

In this work, we expanded a recently introduced colloidal lithographic approach and showed that it is possible to fabricate micropatterns with microscale dimples, which are about one-order larger than the (sub-)micrometer sized dimples reported in the literature,^[28,30,33,34] and with stiffness down to 280 kPa, which is lower than the typical stiffness in the MPa range achieved by soft molding.^[35] This fabrication method showed to be highly repeatable, and provided consistent results in terms of geometrical properties. With this fabrication method, we also demonstrated how to fabricate dimple arrays with and without a terminal layer. The adhesion and friction of the fabricated micropatterns was measured on soft substrates as a function of feature size, stiffness degree of the micropattern and of the substrate, and the presence or absence of a terminal layer.

Adhesion

Effect of geometry and stiffness on pull-off forces on soft substrates

Adhesion measurements on soft substrates show that micropatterns of sub-microscale and microscale dimples without a terminal layer do not generate significantly higher adhesion than flat samples. We assume that, for both dimple sizes, the soft substrate fully conforms to the dimples, and splitting up of contacts does not happen. Sub-microscale dimples have a depth of around 250 nm. As the elastocapillary length of PVA substrates is in the order of 400 nm, the PVA substrates fully conform to the micropattern based on surface tension effects, without elastic penalty. Microscale dimples have a dimple depth of around 5 μm, which is well above the elastocapillary length of PVA, and conformation to the micropattern is expected to be elastically dominated. As a result of the conformation properties of the substrate, a single larger contact area is formed, and advantageous effects of contact splitting, such as defect control and crack trapping mechanisms, as reported for rigid substrates,^[30] are not present.

A microscale dimple geometry with a terminal layer generated higher adhesive forces compared to other tested geometries and flat control samples on the softer PVA substrate (PVA-12). A possible underlying mechanism explaining the positive effect of the terminal layer on adhesion is that the soft PVA substrate interlocks with the holes of the terminal layer. Deformation of the PVA substrate, resulting in protrusions perforating the terminal layer, is elastically dominated, as the terminal layer thickness is well above the

elastocapillary length of PVA of 400 nm. Formation of protrusions is a trade-off between, on the one hand, elastic stresses and, on the other hand, the compressive load on the bulk. On the stiffer PVA-18 substrate, this positive effect of a terminal layer on adhesion was not observed. PVA-18 has a higher elasticity, likely resulting in a higher elastic penalty for protrusion formation than in the case of the PVA-12 substrate. Therefore, during pulling off, formed protrusions jump back, and interlocking is lost faster on the PVA-18 substrate compared to the softer PVA-12 substrate. We expect that crack trapping mechanisms, as reported for terminal-layer geometries on hard substrates, are not involved on the tested PDMS-PVA configurations. As Heepe et al. already reasoned for a (simplified) representation of a discoidal adhesive element,^[6] the advantageous effect of a thin film micropattern on adhesion is lost when the substrate is soft compared to the adhesive.

3 Suction forces might also play a role in generating adhesion with arrays of dimples, both with and without a terminal layer. Air in dimples or, in the presence of a terminal layer, in the sub-surface cavities, will be squeezed out during loading, resulting in an under-pressure during detachment. However, we do not expect that suction is a dominant mechanism in the tested micropatterned adhesives, as there was no significant difference in adhesion between sub-microscale and microscale dimples without a terminal layer on soft substrates, despite the fact that sub-microscale dimples have a much lower suction cup volume compared to microscale dimples. Besides, Spolenak et al. found that at contact radii smaller than 10 μm , as is the case for our geometries, suction cups rapidly lose their effectiveness.^[36]

Force-time plots of adhesive force on soft substrates (**Figure 3.4**) show that during pull off (phase II in **Figure 3.4**), the drop in force was took a few seconds longer compared to pulling off from glass substrates, indicating that contact is lost less abruptly on soft substrates. This gradual contact loss is probably caused by deformation of the soft substrate during pull off, as was observed by Cheung et al.^[24] We did not test whether this deformation has a dissipative or an elastic nature, a question that could be investigated in future works by varying the pull-off speed. Force-time plots on soft substrates also show that the adhesion peak at phase III is wider compared to measurements on glass, indicating that detachment from PVA was slower than from glass.

On soft substrates, we did not find a consistent effect of the theoretical con-

tact area of the measured geometries on adhesion. For example, while microscale dimples without a terminal layer have a higher contact area compared to sub-microscale dimples without a terminal layer, the former did not generate higher adhesion compared to the latter on soft substrates. This observation might indicate that the contact formed between micropattern and substrate is not a strong contact. A low strength of the formed contact might be explained by PVA having a low surface energy ($\sim 50 \text{ mN/m}$),^[32] and because of the presence of water at the PVA-micropattern interface, which might be squeezed out of the PVA gel during loading.

Whereas geometry did not show consistent effects on adhesion, the substrate stiffness did exhibit a systematic effect on pull-off forces for geometries without a terminal layer and for flat control samples, generating higher adhesion on the stiffer PVA-18 substrate compared to the softer PVA-12. This result is logical, because, given that the PVA substrates are much softer than the used microstructures ($G'_{\text{PVA}} \sim 10^1 \text{ kPa}$; $E_{\text{PDMS}} \sim 10^2 \text{ kPa}$), the substrate is expected to be the main component to deform when stress is applied.

Geometry effects, if present, are unlikely to significantly contribute to the generated adhesion and friction forces, because the soft substrates likely fully conform to the micropattern, thereby eliminating contact splitting effects. The PVA substrates have some dissipative properties (dissipation factors of PVA-12: $\tan \delta = 0.05$; PVA-18: $\tan \delta = 0.07$), which might contribute to the resultant adhesion as well. Given the low value of these dissipation factors, we doubt whether damping plays a significant role in generating adhesion.

Our measurement data suggest that, when the substrate is softer than the adhesive, the substrate conforms to the features of the adhesive when load is applied, enabling intimate contact.^[37,38] The intimate contact has a positive effect on adhesion and friction, as long as the elastic penalty of the substrate deformation does not dominate over surface energy effects. Because the formed intimate contact between a micropatterned adhesive and a conformed soft substrate is a singular contact, the positive effects of contact splitting on adhesion and friction, such as defect control and stress distribution, are not expected to be present on a soft substrate when the adhesive micropattern is stiff compared to the substrate.

Effect of geometry on pull-off forces on hard substrates

Measurements on glass showed that sub-microscale samples tend to generate higher adhesion than flat samples and microscale samples without a terminal layer and flat samples. Crack trapping, as proposed for similar microscale dimple arrays by Akerboom et al.,^[30] is likely more dominant in the smaller (sub-microscale) features than in the microscale micropatterns. Furthermore, sub-microscale dimples might form complete contact with the substrate,^[30] generating a higher contact area compared to other geometries. Because of the high surface energy of glass (about 1000 mJ/m² ^[39]), the formed contact points between the micropattern and the substrate are stronger than the contact points between micropattern and PVA substrates, which may partially explain the higher adhesion on glass compared to soft substrates.

3 Microscale dimples without a terminal layer did not generate higher adhesion compared to flat control samples. We expect that, under the applied load, the elastic penalty for making full contact dominates over the gained adhesion as a result of formed contact for this geometry.

Similar to the results on the soft substrates, microscale dimples with a terminal layer tended to generate higher adhesive forces on glass compared to the same dimples without a terminal layer and flat samples. In line with Glassmaker et al.,^[17] we assume that a crack trapping mechanism plays a role in our terminal-layer geometries. Additionally, crack trapping may be promoted by the presence of microscale voids in the terminal layer, similar to the observations by Hwang et al., who found enhanced adhesion by using cuts in the applied materials, thereby introducing compliant regions in stiff adhesive films.^[40] The presence of a terminal layer further enhances adhesion because of the deformability of the former, resulting in a higher effective contact area than micropatterns without a terminal layer.^[17] This deformation effect of the terminal layer on adhesion is supported by the findings by Shahsavan et al., who reported that with thin film-terminated micropillars higher compliance and pull-off forces can be realized when the terminal layer has viscoelastic material properties.^[41] For microstructures of dimples with a terminal layer, deformation of the terminal layer is likely to happen, given that the elastic modulus of PDMS is in the kPa range, and thus elastic and the thickness of the terminal layer is limited (i.e., conformation to substrate roughness requires only a small volume of material to elastically deform, resulting in a minor elastic penalty for conformation).

The result that higher pull-off forces are generated with the softer PDMS-280 microstructures compared to PDMS-580 microstructures supports a deformation effect of the terminal layer. Besides elastic stretching of the terminal layer, the effective modulus of the dimples with terminal layer is likely lower compared to other geometries, because of the presence of sub-surface voids.

A suction mechanism, if present, is expected to play a more dominant role on the rigid and impermeable substrate of glass than on PVA substrates.^[33] However, we do not expect that suction forces are the main mechanism generating adhesion in the tested geometries, as sub-microscale dimples, despite having much smaller suction cups compared to microscale dimples, outperformed microscale dimples on glass.

Friction*Effect of geometry and stiffness on friction forces on soft substrates*

On soft substrates, force-time plots of friction force (**Figure 3.4**) show that the static friction force (phase V in **Figure 3.4**) is comparable to the dynamic friction. A minor increase in friction force during sliding was typically observed, presumably caused by the PVA substrate 'piling up' at the front line during sliding of the micropattern. On the stiffer PVA (PVA-18) substrate, large dimples without a terminal layer outperformed all other geometries. A similar, albeit less pronounced, effect was also observed on the softer PVA-12 substrate. We assume that with large dimples indent deeply into the PVA substrates, generating mechanical interlocking and a relatively high contact area. The microstructure starts moving when this interlocking is lost due to deformation of the substrate. A low indentation depth, as is expected for flat samples, sub-microscale dimples and dimples with a terminal layer, requires a smaller volume of substrate to elastically deform to start sliding, resulting in lower friction forces. On the softer substrate of PVA-12, the elastic penalty for deforming is lower compared to PVA-18, which can explain why the superior performance of microscale dimples without a terminal layer on PVA-18 was less pronounced on the softer PVA-12.

Dimples with a terminal layer generated higher friction on the softer substrate of PVA-12 compared to the stiffer PVA-18, in line with the findings for adhesion. It is possible that the same protrusion formation as described

for adhesion also holds for friction, with the substrate protruding into the sub-surface voids of the microstructure. Similar to adhesion experiments, suction forces cannot be ruled out either.

Effect of geometry on friction forces on glass

On the glass substrate, force-time plots of friction force (Figure 6) show that static friction (peak at phase V in Figure 6) is dominant over dynamic friction. Some sort of zigzag was typically visible in the dynamic friction regime, indicating stick-slip-like behavior during sliding for both flat and micropatterned samples.

Our results suggest that sub-microscale dimples led to higher friction forces compared to flat samples and to large dimples with or without terminal layer. We expect that under the applied preload, sub-microscale dimples flatten, and a contact area similar to flat samples is formed. Due to stored elastic energy in the micropattern, the formed contact might be better preserved during sliding compared to a flat geometry, resulting in higher friction forces.

For a microscale dimple geometry without a terminal layer, friction forces are similar to or even lower than the friction forces of flat control samples on glass. Similar to the adhesion measurements, we assume that the applied load during sliding is not sufficient to bring the bottom of the dimples into contact with glass, leading to a small contact area and thus low friction forces.

Microscale dimples with a terminal layer generate higher friction forces compared to flat control samples. This might be related to the compliance of the terminal layer, due to which the contact during sliding is more efficiently conserved compared to flat samples. Elastic storage by means of stretching of the terminal layer, as suggested by He et al.^[19] might also occur, leading to an increase in friction. Besides, as already noted earlier, because of the presence of spherical voids below the surface, the effective modulus of the terminal-layer micropatterns is likely lower compared to other geometries and flat control samples.

Limitations and recommendations for future work

In our experimental setup, we performed adhesion and friction measurements in a plate-to-plate configuration. We took extensive measures to assure proper alignment of the sample on the substrate, including visual in-

spection of the sample-substrate interface prior and during measurements using a magnifying camera, and real-time inspection of the recorded time-force curves. Moreover, the platform on which the substrate was placed was positioned between three sets of springs (flexures), which gave the platform some self-aligning properties. Despite these measures, we suspect that the high variation of the measurement data on glass was caused by misalignment.

To counterbalance such issues of misalignment, our experimental design and statistical analysis were conservative: each data point was the average of 5 consecutive repeats and the measurements of independent samples were done in a randomized order. We also opted for a low alpha value of 0.001. It should be further noted that the increase in random variance because of misalignment and other side effects was not too large to dilute the strongly significant non-random effects we observed. On soft substrates, the variation of the measurement data was lower, which is logical, because the flexibility of the soft substrate ensures that the sample establishes good contact with the substrate.

For follow-up experiments, the use of a (hemi-)spherical probe instead of a plate-to-plate configuration can be considered, to avoid misalignment issues.

Due to the limited force range of our measuring setup, some samples could not be measured on glass. Considering the limited amount of data, we refrained from drawing conclusions on the effect of microscale samples with and without a terminal layer on friction.

The fabricated sub-microscale dimples had a lower depth than the particle radius. Considering that the time between casting the monolayer with PDMS, degassing and subsequent curing at 68 °C was in the order of 15 minutes, the uncured PDMS does not fully flow through the colloidal monolayer on this timescale, resulting in a limited dimple depth. A strategy to increase the PDMS penetration into the monolayer would be to cure the PDMS at room temperature for 48 hours, in which case PDMS remains in a liquid state for much longer. Indeed, we did observe larger dimples and thinner walls between dimples when curing the sample at room temperature in a post-hoc synthesis, as can be seen in SI3.3.

Given the high adhesion and friction of microscale dimples with a terminal

layer on both hard and soft substrates, it would be interesting to test the performance of sub-microscale dimples with a terminal layer. However, we were not able to fabricate sub-microscale dimples with a terminal layer, presumably because the walls between dimples are so thin that they break during peeling off from the template, or because the uncured PDMS did not fully penetrate the monolayer. The latter problem could be solved by creating colloidal monolayers with a larger spacing, for example by optimizing the surface chemistry of particles.

The mechanism of generating grip on tested substrates is likely indentation-based, creating mechanical interlocking, and therefore strongly depends on the stiffness of both substrate and adhesive. Consequently, it is not surprising that our results pointed towards higher friction on soft substrates when using large dimples compared to small dimples. This result suggests that with even larger dimples the friction performance of micropatterns on soft substrates can be improved, even under low (pre)loads, a hypothesis that deems further investigation.

In our work, the stiffness of the substrate was much lower than the stiffens of the sample. Future work could be directed towards testing configurations in which the stiffness of adhesive and substrate are of the same order. Our hypothesis is that in this case, contact loss due to substrate deformations is prevented, and effects of geometry, such as increased contact area with a dimples-with-terminal-layer geometry, become visible. Although the use of a much softer micropattern might give rise to geometry effects, it remains to be investigated whether the loss in contact strength accumulatively leads to an increase in pull-off force.

While we found significant effects of geometry on adhesion and friction on soft substrates, it was difficult to clarify the underlying mechanisms that cause these effects, both qualitatively and quantitatively. The hypothesized interlocking effects could be investigated in future studies by quickly freezing microstructure-substrate complexes when under load and studying their cross-sectional image with optical microscopy. The importance of deformation mechanisms of the substrate in the pull-off and sliding of our adhesives could be further investigated by varying the pull-off or sliding speed, since the strain rates of both substrate and adhesives are time dependent.

3.4 Conclusion/Outlook

We used a facile, out-of-the-cleanroom method to fabricate structures with microscale and sub-microscale features, and expanded it to fabricate microscale features. We fabricated geometries of moderate architectural complexity (extruded patterns with curved surfaces) and of high architectural complexity (overhanging features), at different length scales and different degrees of stiffness.

We found that higher adhesion and friction on soft substrates were generated with larger feature sizes. On soft substrates, the positive effects of sub-microscale features on adhesion and friction, such as defect control and crack trapping, are not present, because the substrate conforms to the micropattern. Instead, interlocking is likely the dominant mechanism of adhesion and friction on soft substrates.

The effect of the microstructure stiffness was not pronounced, which is not surprising, considering that the microstructures were one order stiffer than the soft substrate, meaning that the latter was the main component to deform. We expect that the effect of the microstructure stiffness becomes larger when it is in the same order as the substrate stiffness, in which case both the microstructure and the substrate compete to deform.

In conclusion, we found that, on soft substrates, microscale dimples generate higher adhesion and friction than sub-microscale dimples. Generation of grip on soft substrate seems to be dominated by different underlying mechanisms than those holding for hard substrates.

3.5 Experimental

Materials

Sylgard-184 pre-polymer (base) and crosslinker (curing agent) were purchased from Dow Corning, polyvinyl alcohol (PVA) (Selvol PVOH 165; hydrolysis rate: $99.65\% \pm 0.35\%$; degree of polymerization: about 2000, as reported by the manufacturer) was purchased from Sekisui Chemical Group. N-methyl-2-pyrrolidone (NMP) was purchased from Sigma Aldrich. DVB/Sulfate latex particles with a reported diameter of $10 \mu\text{m}$ were purchased from ThermoFisher Scientific as a 4 w/v% dispersion in water and

were dispersed in ethanol to get an 8% w/v dispersion before use.

Synthesis and characterization of particles

Sub-microscale particles

Carboxylated polystyrene (PS) particles with a sub-microscale diameter were synthesized in a single-step surfactant-free emulsion polymerization, according to Appel et al.^[42] The particles were washed by centrifugation three times in ethanol and three times in water. The particles were dispersed in ethanol to get a 20% w/v dispersion before use.

Particle size and polydispersity index were determined with a Malvern Nano ZS 3600 Zetasizer. The laser had a wavelength of 633 nm and a scattering angle of 173°.

Microscale particles

The purchased microscale particles were characterized by assessing microscopic images of dispersion droplets of particles in water. Diameters of 100 particles were determined using ImageJ,^[43] and the average diameter and polydispersity index were determined using equations 1-3 from Nematollahzadeh et al.^[44]

Fabrication of micropatterns

Deposition of colloidal monolayers on glass using dip coating

Colloidal monolayers from sub-microscale and microscale particles were obtained by deposition of particles on an untreated microscopic slide of glass (75×26 mm²) (Corning®) using a dip coating process.^[45] Specifically, a Langmuir-Blodgett trough (KSV Nima KN2002, medium-sized) was filled with demineralized water, and the microscopic glass slide was partially immersed for 20 mm in the bath in vertical direction. A plasma-treated glass cover slip was placed in the filled trough against one of the barriers in a diagonal orientation. The particle dispersion was added dropwise via the glass cover slip. Particles were added until a nearly-packed monolayer was observed. Surface pressure was measured using a Wilhelmy plate.

After complete evaporation of the ethanol was achieved, as confirmed by stabilization of the surface pressure, the monolayer was compressed by moving the barriers toward each other until a sharp increase in surface

pressure was observed, indicating close packing of the colloidal monolayer. A single dip-coating cycle was done by pulling out the glass slide vertically at a speed of 0.5 mm/s while keeping the surface pressure constant.

Dimples without a terminal layer from sub-microscale particles

Samples with dimples from sub-microscale particles were fabricated according to pathway 1 shown in **Figure 3.1**. Uncured pre-polymer-crosslinker mixture (henceforth referred to as uncured PDMS) was degassed in a desiccator, and casted on a 14×14 mm² area of the monolayer, obtaining a thickness of 4 mm (see also SI3.4). The monolayer with casted PDMS was placed in an oven for 2 hours at 68.3 °C to cure the PDMS. The cured PDMS was peeled off from the glass slide, leaving the monolayer attached to the glass together with a terminal PDMS layer. Following Akerboom et al.,^[30] residue particles were removed from the sample by cleaning it with Scotch Magic Tape, and by immersing it in NMP for 1 hour under stirring. Subsequently, while still immersed in NMP, the sample was placed in an ultrasonic bath for 1 minute.

Dimples with a terminal layer from microscale particles

Samples with dimples from microscale particles and with a terminal layer were fabricated by casting uncured PDMS on a 14×14 mm² area of the monolayer, with a thickness of 4 mm, and by subsequently curing it in an oven for 2 hours at 68 °C (see also SI4). Opposite to the case of sub-microscale particles described in the previous paragraph, in which peeling off the cured PDMS left both the monolayer and a terminal PDMS layer attached to the glass, upon peeling off the cured PDMS from the glass slide with microscale particles, the monolayer remained embedded in the PDMS and the terminal PDMS layer came off from the glass surface (see pathway 2 in **Figure 3.1**). The sample was washed to dissolve the monolayer by immersing it in NMP for 1 hour under stirring. Subsequently, while still immersed in NMP, the sample was placed in an ultrasonic bath for 1 minute.

Dimples without a terminal layer from microscale particles

Dimple arrays without a terminal layer from microscale particles were fabricated according to pathway 3 in **Figure 3.1**. Dimple arrays with a terminal layer were first fabricated as described in the previous paragraph. Then, the samples were covalently attached to a glass slide by plasma-treating both the glass and the sample surfaces, and bringing the treated surfaces together. After applying some load, the sample-on-glass was placed in an

oven for 20 minutes at 68 °C to form covalent bonds between the two. After binding, the sample was peeled off from the glass slide. Upon peeling off, the terminal layer remained attached to the glass slide. The peeled-off sample separated from the terminal layer, resulting in a micropattern with dimples.

All three types of samples (1: dimples without a terminal layer from sub-microscale particles; 2: dimples with a terminal layer from microscale particles; and 3: dimples without a terminal layer from microscale particles) were prepared using two crosslinker:pre-polymer weight ratios, namely 1:10 and 1:20.

Flat samples were also fabricated as controls. To do so, we degassed uncured PDMS of 1:10 and 1:20 crosslinker:pre-polymer weight ratios in a desiccator. Uncured PDMS was casted on a 14×14 mm² area of an untreated microscopic glass to obtain a layer of 4 mm thickness, and subsequently cured in an oven for two hours at 68 °C.

Characterization of micropatterns

Monolayers and samples from sub-microscale particles were characterized with atomic force microscopy (AFM), optical microscopy, and scanning electron microscopy (SEM). Monolayers and samples from microscale particles were characterized with optical microscopy and SEM. The elastic modulus of the fabricated micropatterns was measured with a TA Instruments AG-2R rheometer. A parallel plate geometry with diameter of 25 mm was used. Storage and loss moduli were determined at a strain of 0.05%, for a frequency range of 1*10⁻¹ – 1*10² rad/s, as can be seen in the Supporting Information (Figure SI3.1-2). We use the storage moduli G' as measured at an angular velocity of 0.1 rad/s, since the adhesion and friction measurements are done at similar velocities.

Fabrication and characterization of polyvinyl alcohol substrates

Polyvinyl alcohol (PVA) substrates were fabricated by filling 3D-printed molds with 10% w/v PVA hydrogel. In a PVA gel, crosslinks between chains are formed by hydrogen bonding between hydroxyl side groups. We used hydrolyzed PVA, because by additional hydrolysis, acetate side groups in the polymer are turned into hydroxyl groups, and crosslink formation is

promoted. Subjecting PVA to freeze-thaw cycles further stiffens the hydrogel by growing local crystalline regions that act as network junctions.^[46] We prepared substrates of two stiffness degrees, by subjecting PVA to two or three freeze-thaw cycles, respectively.

Measurement of adhesion and friction

Adhesion and friction of the samples were measured with a custom-built force transducer (see **Figure 3.9** for a schematic representation of the setup). The force transducer consisted of a sample holder suspended via three sets of serially arranged parallelogram-flexures which allowed translation of the sample in three orthogonal directions. The displacement of the sample holder in the three directions was measured with confocal chromatic aberration sensors (CL1 MG210; Stil S.A.S) controlled with Prima controllers (Stil) via the CCS Manager software (Version 1.5.2.404; Stil). The setup has a resolution of 0.09 mN, a measurement range of 2550 mN in the friction direction, and a resolution of 0.05 mN and a range of 4800 mN in adhesion direction. The measurement frequency was 1000 Hz.

The substrate (red in **Figure 3.9**) was mounted on a digitally controlled 2D translation stage (Thorlabs PT1/M-Z8, with additional KDC101 controllers, green in Figure 2), allowing the controlled positioning of the substrate with respect to the sample mounted on the force transducer.

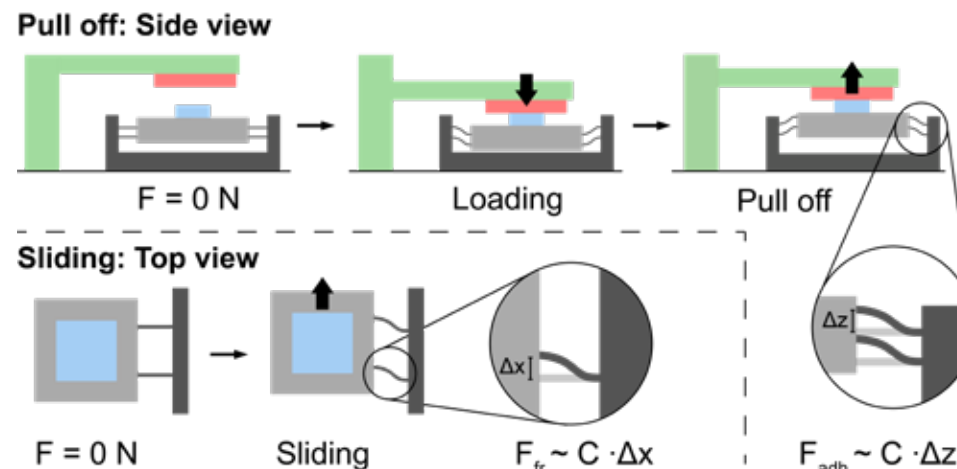


Figure 3.9. Schematic representation of the customized measuring setup in the configuration of an adhesion measurement (top line) and a friction measurement (bottom line). Adhesion:

The micropatterned adhesive (blue) is mounted on a holder (grey) suspended via three sets of parallelogram-flexures. The substrate (red) is brought in contact with the sample using a translation stage (green). When the substrate is pulled off, adhesive forces are exerted on the sample holder, which gets displaced vertically. The adhesive force is calculated from the holder displacement Δz via the flexure stiffness C . Friction: The substrate (transparent, red) is brought in contact with the micropattern, and the substrate is displaced laterally. Before the micropattern starts sliding, the force platform is displaced in lateral direction. The holder displacement Δx at the moment the micropattern starts sliding is recorded, and the friction force is calculated from the holder displacement Δx via the flexure stiffness C .

To assure proper alignment, the measuring platform (which had a size of 2×2 cm) was recorded with a Photron Fastcam SA-X2 camera (maximum resolution of 2000×2000 px), fitted with a Nikon Micro-Nikkor AF-S VR 105 mm F/2.8G lens and a 27.5 mm distance collar (Nikon PK-13), prior and during measuring, and real-time projected full-screen on a 22" display.

We measured adhesion and friction of the three types of micropatterns described above (1: dimples without a terminal layer from sub-microscale particles; 2: dimples with a terminal layer from microscale particles; and 3: dimples without a terminal layer from microscale particles) and of flat samples, fabricated from two crosslinker:pre-polymer weight ratios (1:10 and 1:20), on three substrates (PVA-12, PVA-18, and glass). An overview of the tested conditions is given in **Figure 3.10**.

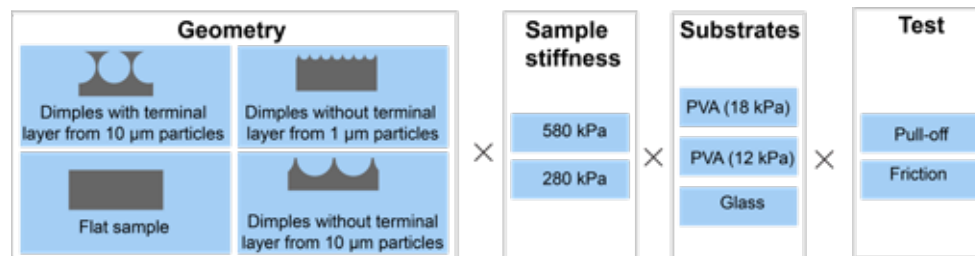


Figure 3.10: Overview of the tested conditions.

Adhesion was measured after preloading the sample with 55 mN for 10 seconds. The pull-off speed was 100 µm/s. Friction was measured using a load of 55 mN and a sliding speed of 500 µm/s. The peak adhesion and friction forces were derived from the recorded force curves.

The sample size was 5. For each sample, both adhesion and friction were measured five consecutive times. Adhesion and friction were measured consecutively for each sample and in counterbalanced order across the samples. The conditions (4 geometries x 2 stiffness degrees of the sample x 3 substrates) were tested in randomized order. When measuring on PVA substrates, the substrate was left for 2 minutes between consecutive measurements to elastically recover. Humidity and temperature were kept constant during all measurements.

Statistical analyses

All statistical analyses were conducted between samples, using the first of the five consecutively recorded peak (adhesion or friction) forces measured for each sample. We used the first of the five consecutively recorded peak forces instead of their mean, because a consistent decreasing trend was observed from the first to the fifth measurement (likely due to time-dependent stiffness and relaxation of the sample and the substrate), pointing towards a dependency between the consecutive measurements. Because the adhesion and friction measurement data may have unequal variances and/or be non-normally distributed, these data were rank-transformed (cf. Conover and Iman^[47]) prior to being subjected to a three-way analysis of variance (ANOVA) with a post hoc Tukey-Kramer test to test the effects of geometry, sample stiffness, and substrate stiffness on adhesion and friction.

Acknowledgements

This research is supported by the Netherlands Organization for Scientific Research (NWO) Domain Applied and Engineering Sciences (TTW), (Open Technology Program, project 13353 "Secure and gentle grip of delicate biological tissues").

We kindly acknowledge Ties van der Laar (Laboratory of Physical Chemistry and Colloid Science, Wageningen University) for synthesizing the sub-microscale particles for us. We also kindly acknowledge Menno Lageweg, Henry van der Ster, David Jager, and Remi van Starckenburg from the Electronic and Mechanical Support Division (DEMO) of the Delft University of Technology the design and fabrication of the measurement setup and sample- and fabrication holders.

References

- [1] P. Y. Isla, E. Kroner, *Adv. Funct. Mater.* **2015**, *25* (16), 2444–2450.
- [2] L. Xue, B. Sanz, A. Luo, K. T. Turner, X. Wang, D. Tan, R. Zhang, H. Du, M. Steinhart, C. Mijangos, et al. *ACS Nano* **2017**, *11* (10), 9711–9719 *11* (10).
- [3] D.M. Drotlef, L. Stepien, M. Kappl; W.J.P. Barnes, H. J. Butt, A. Del Campo, *Adv. Funct. Mater.* **2013**, *23*(9), 1137–1146.
- [4] A. Del Campo, E. Arzt, *Macromolecular Bioscience*. 2007, pp 118–127.
- [5] D. Brodoceanu, C.T. Bauer, E. Kroner, N.A. Fleck, E.V. Eason, E.W. Hawkes, M. Windheim, M. Röhrig, M. Schneider, G. Etienne, *Bioinspiration&biomimetics*, **2016**, *11* (5), 051001.
- [6] L. Heepe, L. Xue, S. Gorb, *Bio-inspired Structured Adhesives; Biologically-Inspired Systems*, Vol. 9; Springer International Publishing: Cham, Switzerland, **2017**.
- [7] R. D. O'Rorke, T.W.J. Steele, H. K. Taylor, *J. Adhes. Sci. Technol.* **2016**.
- [8] A. Jagota, *Integr. Comp. Biol.* **2002**, *42*(6), 1140–1145.
- [9] M. Kamperman, E. Kroner, A. Del Campo, R. M. McMeeking, R. M.; E. Arzt, *Adv. Eng. Mater.* **2010**, *12* (5), 335–348.
- [10] C.-Y. Hui, N. J. Glassmaker, T. Tang, A. Jagota, *J. R. Soc. Interface* **2004**, *1*(1), 35–48.
- [11] S. Gorb, M. Varenberg, A. Peressadko, J. Tuma, *J. R. Soc. Interface* **2007**, *4*(13), 271–275.
- [12] N. J. Glassmaker, A. Jagota, C.-Y. Hui, J. Kim, *J. R. Soc. Interface* **2004**, *1*(1), 23–33.
- [13] M. Varenberg, S. Gorb, *J. R. Soc. Interface* **2008**, *5*, 383–385.
- [14] M. Varenberg, B. Murarash, Y. Kligerman, S. Gorb, *Appl. Phys. A Mater. Sci. Process.* **2011**, *103*(4), 933–938.
- [15] K. Kendall, *J. Phys. D. Appl. Phys.* **1975**, *8*, 1449–1452.
- [16] L. Heepe, M. Varenberg, Y. Itovich, S. Gorb, *J. R. Soc. Interface* **2011**, *8*(57), 585–589.
- [17] N. J. Glassmaker, A. Jagota, C.-Y. Hui, W. L. Noderer, M. K. Chaudhury, *Proc. Natl. Acad. Sci.* **2007**, *104*(26), 10786–10791.
- [18] W.-G. Bae, D. Kim, D. K.-Y. Suh, *Nanoscale* **2013**, *5*(23), 11876.
- [19] Z. He, C. -Y. Hui, B. Levrard, Y. Bai, A. Jagota, *Sci. Rep.* **2016**, *6*.
- [20] C. Greiner, A. Del Campo, E. Arzt, *Langmuir* **2007**, *23*(7), 3495–3502.
- [21] T. W. Kim, B. Bhushan, *J. Adhes. Sci. Technol.* **2007**, *21*(1), 1–20.
- [22] R. Spolenak, S. Gorb, E. Arzt, *Acta Biomater.* **2005**, *1*(1), 5–13.
- [23] K. L. Johnson, K. Kendall, A. D. Roberts, *Proc. R. Soc. A Math. Phys. Eng. Sci.* **1971**, *324*(1558), 301–313.
- [24] E. Cheung, M. Sitti, *Langmuir* **2009**, *25*(12), 6613–6616.
- [25] R. W. Style, C. Hyland, R. Boltyanskiy, J.S. Wettlaufer, E.R. Dufresne, *Nat. Commun.* **2013**.
- [26] S. Mora, T. Phou, T. J. M. Fromental, L. M. Pismen, Y. Pomeau, *Y. Phys. Rev. Lett.* **2010**, *105*, 214301
- [27] A. Del Campo, C. Greiner, E. Arzt, *Langmuir* **2007**, *23*(20), 10235–10243.
- [28] P. van Assenbergh, E. Meinders, J. Geraedts, D. Dodou *Small* **2018**, *14*(20), 1703401.
- [29] S. Akerboom, S. P. Pujari, A. Turak, M. Kamperman *ACS Appl. Mater. Interfaces* **2015**, *7*(30), 16507–16517.
- [30] S. Akerboom, J. Appel, D. Labonte, W. Federle, J. Sprakel, M. Kamperman, M. J. R. Soc. *Interface* **2015**, *12*(102), 20141061.
- [31] J. Y. Park, S. J. Yoo, E. J. Lee, D.H. Lee, J.Y. Kim, S. H. Lee, S. H. *Biochip J.* **2010**, *4*(3), 230–236.
- [32] A. Bhattacharya, P. Ray, *J. Appl. Polym. Sci.* **2004**, *93*, 122–130.
- [33] L. Wang, S. Qiao, N. Lu, *Extrem. Mech. Lett.* **2017**, *15*, 130–138.
- [34] X. Ye, L. Qi, L. *Sci. China Chem.* **2014**, *57*(1), 58–69.
- [35] D. J. Lipomi, R. V. Martinez, L. Cademartiri, G.M. Whitesides *Elsevier B.V.*, **2012**; Vol. 7.
- [36] R. Spolenak, S. Gorb, H. Gao, E. Arzt, *Proc. R. Soc. A Math. Phys. Eng. Sci.* **2005**, *461*(2054), 305–319.
- [37] J. S. Kaiser, M. Kamperman, E. J. de Souza, B. Schick, E. Arzt *Int. J. Artif. Organs* **2011**, *34*(2), 180–184.
- [38] M. D. Kern, R. Long, M.E. Rentschler *Mech. Mater.* **2018**, *119*, 65–73.
- [39] E. M. Petrie, McGraw-Hill, *Handbook of Adhesives and Sealants*; ed., McGraw-Hill, New York, 2000.
- [40] D. G. Hwang, K. Trent, M. D. Bartlett *ACS Appl. Mater. Interfaces* **2018**, *10*(7), 6747–6754.
- [41] H. Shahsavan, B. Zhao *Macromolecules* **2014**, *47*(1), 353–364.
- [42] J. Appel, S. Akerboom, R. G. Fokkink, J. Sprakel, *Macromol. Rapid Commun.* **2013**, *34*(16), 1284–1288.
- [43] M. D. Abramoff, P. J. Magalhães, S. J. Ram, *Biophotonics Int.* **2004**, *11*(7), 36–42.
- [44] A. Nematollahzadeh, M. J. Abdekhodaie, A. Shojaei, *A. J. Appl. Polym. Sci.* **2012**, *125*(1), 189–199.
- [45] Blodgett, K. B. *J. Am. Chem. Soc.* **1935**, *57* (6), 1007–1022.
- [46] P. J. Willcox, D. W. Howie, K. Schmidt-Rohr, D. A. Hoagland, S. P. Gido, S. Pudjianto, L. W. Kleiner, S. Venkatraman *J. Polym. Sci. Part B Polym. Phys.* **1999**, *37*, 3438–3454.
- [47] W. J. Conover, R. L. Iman, *Am. Stat.* **1981**, *35*(3), 124–128.

Chapter 4

EFFECT OF LATERAL REINFORCEMENTS ON THE ADHESION AND FRICTION OF MICROPILLAR ADHESIVES

This chapter has been published as:

Peter van Assenbergh*, Kai Zhang*, Ivan Buijnsters and Dimitra Dodou, *Appl. Phys. A* **2020**, 126, 790. doi: 10.1007/s00339-020-03947-y

*Both authors contributed equally to this chapter.

Abstract

Micropillar adhesives have gained increasing attention because they generate high pull-off forces. The generation of high friction, however, has been proven difficult with such geometries, because micropillars tend to buckle under shear loading. Here, we fabricated orthogonal arrays of composite poly-dimethoxysiloxane (PDMS) micropillars with a stiff core and spincoated them with PDMS solutions to form a soft coating, as well as bridges between neighboring micropillars. We used 10 wt.% and 5 wt.% PDMS solution to obtain thick or thin bridges, respectively. The micropillars had an average height of about 60 μm and a diameter of 40 μm . Adhesion and friction measurements were performed with three types of adhesives (i.e., without bridges and with either thin or thick bridges) as well as unpatterned samples as reference, on stiff glass substrates and on deformable PDMS substrates. We found that, on PDMS substrates, bridging resulted in increased friction, compared to non-bridged micropillars. Friction increased with increasing bridge thickness, presumably due to buckling prevention. The adhesives were also subjected to 99 repeating friction cycles to test the effect of micropillar bridging on the durability of the adhesives. Results showed that adhesives with thick micropillar bridges preserved their friction performance over the cycles, whereas adhesives with no bridges or thin bridges exhibited a gradual decay of friction.

4.1 Introduction

Pressure-sensitive adhesives can be detached and reattached only a limited number of times because they tend to be gradually fouled with dust and other particles. Over the last years, gecko-inspired adhesives have been developed as an attractive alternative of pressure-sensitive adhesives that can detach and reattach multiple times without deterioration of their adhesive performance. Opposite to pressure-sensitive adhesives that employ some type of glue, gecko adhesion is 'dry', relying on Van der Waals forces.^[1] Specifically, gecko adhesion relies on the fine-structure on the gecko toepads, which consists of arrays of microscale fibrils, each of which branches into nanoscale spatulas.^[1,2] This fibrillary structure makes the gecko toepads soft and deformable at various scales,^[3] resulting in the formation of a large contact area.^[4,5] Additionally, as the formed contact is split up into multiple fibrils, when an individual fibril detaches, the load is redistributed over the remaining attached fibrils, inhibiting the growth of defects.^[6] Importantly, when attached to a tilted or vertical substrate, the fibrils are loaded in their stiff tensile direction, preventing deformations that could lead to loss of the formed contact.^[3]

Inspired by the gecko toepads, over the last decades, researchers have been fabricating artificial adhesives consisting of arrays of microscale high-aspect-ratio cylindrical micropillars. Similar to the gecko, the functionality of these man-made adhesives relies on the deformability of the micropillars, which facilitates large contact formation, and the splitting-up of the formed contact, which inhibits the propagation of defects.^[6] Detachment of cylindrical micropillars in the normal (pull-off) direction is caused by peak stresses developing at the edge of the contact when loads are applied, followed by the initiation of a crack that propagates from the edge towards the center of the contact.^[7] The pull-off strength of individual micropillars can be increased by topping them with a thin terminal disc, resulting in so-called mushroom-shaped micropillars.^[8] Pulling off mushroom-shaped pillars occurs via a thin-film peeling mechanism of the disc, directed from the center to the edge of the contact, which leads to higher pull-off forces than adhesives with straight micropillars.^[9]

Under shear loading, due to their high aspect ratio, micropillars tend to buckle, which drastically reduces contact area, leading to loss of grip.^[10,11] Moreover, buckling causes pillars to attach to one another, which limits the

reusability of the adhesive.^[10,12] The presence of thin terminal disk, as in mushroom-shaped micropillars, cannot prevent this buckling and subsequent loss of contact.^[13] Higher friction forces have been reported for adhesives topped with a thin terminal film, thanks to the high peeling strength of the terminal layer, which results in a crack trapping mechanism^[14,15] and adhesion hysteresis of the terminal layer^[16] Additionally, it has been hypothesized that internal sliding of micropillars underneath the terminal layer contributes to friction.^[16] Tian et al. found that embedding microparticles in micropillars led to an increase in the stiffness of the micropillars, and consequently higher friction when particles were distributed homogeneously.^[17] Another approach to increase friction in micropillar adhesives was reported by Bae et al., who fabricated composite mushroom-shaped micropillars with a stiff core and a soft shell.^[10] The soft shell and a terminal disc allowed for firm grip, while the stiff core prevented irreversible buckling of the micropillars.^[10] Durability testing of these adhesives showed that the friction performance of the reinforced adhesives over 100 of friction cycles did not decline, opposite to micropillars without reinforcement, the friction of which reduced significantly after about 15 cycles of testing.^[10] Similarly, Xue et al. fabricated composite soft micropillars reinforced with bundles of stiff nanopillars and found that these reinforcements had a positive effect on the generated (dynamic) friction.^[18] Minsky and Turner^[19] fabricated and experimentally tested single pillars with a hard core and soft shell and reported that these composite pillars generated 9 times higher adhesion and 7 times higher friction than homogeneous pillars. A different reinforcement method has been proposed by Fischer et al.^[20] and Gorumlu and Aksak,^[21] who fabricated micropillars with a stiff stem and a soft tip and showed that the adhesion of these composites deteriorated less with an increasing substrate roughness as compared to homogeneous micropillars of the same dimensions.

The studies described above on pull-off and friction forces of bio-inspired micropillar adhesives has all been done on hard substrates. Limited research has been conducted on investigating how to achieve high friction on deformable substrates by micropillar adhesives. Friction depends on the stiffness of the substrate, with a lower Young's modulus leading to better contact formation.^[22] On the other hand, mechanical interlocking of patterned adhesives with substrate asperities, a mechanism that increases with increasing substrate stiffness, has been shown to be an important contributor to friction.^[23] The above studies on hard substrates all indicate

that the generation of firm, repetitive grip requires anisotropic mechanical properties of adhesives, that is, high deformability in the normal direction to maximize contact formation, and high stiffness in the loading (either shear or pull-off direction) to preserve the formed contact when loads are applied. In this paper, we aimed to investigate whether such stiffness anisotropy is also beneficial for generating high friction on deformable substrates.

We explored an approach of generating adhesives with high deformability in the normal direction and high stiffness in the shearing direction by combining two strategies: reinforcement of soft individual micropillars with a hard core and incorporation of bridges between neighboring micropillars. We measured pull-off and friction stresses (i.e., forces divided by the effective contact area) of the reinforced adhesives on rigid glass substrates and elastomeric poly-dimethoxysiloxane (PDMS) substrates, and compared these with the corresponding stresses generated by reference micropillar arrays without a soft shell and without inter-pillar bridges.

4.2 Experimental

Fabrication

Adhesives

Adhesives with bridged micropillars were fabricated in a three-step process: fabrication of a soft mold, fabrication of micropillar arrays by soft molding, and bridging of the micropillars via a spin coating process.

First, a soft mold was fabricated by replicating a patterned silicon wafer via a double-molding process. Thereto, a silanized silicon wafer with 1.0×1.0 cm² orthogonal patterns, consisting of circular pits with a diameter of 40 μ m, a depth of 55 μ m, and a spacing of 10 μ m, was casted with a degassed mixture of polydimethylsiloxane base and curing agent (10:1 ratio; PDMS, Sylgard 184, Dow Corning) and cured at 70°C for 24 hours. The as-formed PDMS micropillar array was then treated with oxygen plasma for 3 minutes and silanized with trichloro(1H,1H,2H,2H-perfluorooctyl)silane (Sigma-Aldrich) in an evacuated desiccator for 2 hours. Subsequently, a degassed mixture of PDMS base and curing agent (10:1 ratio; Young's modulus: 580 kPa)^[24] was poured onto the modified PDMS micropillar array and cured at 70°C for 24 hours to obtain the wafer replica that acted as a soft mold.

In the second step, the soft mold was used to fabricate adhesives with micropillars. To facilitate demolding, the obtained soft mold was silanized with trichloro(1H,1H,2H,2H-perfluorooctyl)silane (Sigma-Aldrich) in an evacuated desiccator for 2 hours. Afterwards, a custom-made aluminum frame with a square hole of 7.5×7.5 mm² and a depth of 2 mm was placed on the soft mold. PDMS mixtures with a 5:1 ratio of base and curing agent (Young's modulus: 1000 kPa)^[24] were degassed and cured in this frame, resulting in adhesives with micropillars with a backing layer thickness of 2 mm, corresponding to the depth of the frame. The curing temperature and time were 70°C and 24 hours, respectively.

In the third step, an elastomeric coating and bridges were introduced to the micropillar arrays via a spin coating procedure (Figure 1). Specifically, PDMS with a 20:1 ratio of base and curing agent (Young's modulus: 280 kPa)^[24] was first dissolved in 45°C tert-butyl alcohol (TBA, Sigma-Aldrich) to control the concentration of PDMS in the solution. TBA was used as a solvent here, because it provides not only a good solubility for uncured PDMS, but also negligible swelling for cross-linked PDMS,^[25] preventing unwanted expansion or deformation of the micropillars. We used 5 wt.% and 10 wt.% of uncured PDMS in TBA as polymer solution to spincoat micropillar arrays. A drop of the according polymer solution ($\sim 80 \mu$ L) was spin coated on the micropillars at 2000 rpm for 3 minutes, resulting in coating of the micropillars and formation of microdroplets in between neighboring micropillars. Subsequently heating of spincoated micropillar arrays in the oven at 70°C for 24 hours rendered elastomeric bridges between neighboring micropillars. A polymer solution of 5 wt.% PDMS in TBA rendered bridges with small thickness (referred henceforth to as B1), and spincoating with 10 wt.% PDMS in TBA resulted in bridges with large thickness (referred henceforth to as B2).

Adhesives of non-bridged micropillars, referred henceforth to as B0, were fabricated using the same method, but without the third step of spin coating. Unpatterned adhesives (UNP) were fabricated by placing the aluminum frame on a silanized glass slide, filling the frame with PDMS, and subsequent curing.

The fabricated adhesives were inspected with scanning electron microscopy (SEM, JEOL 6010) and optical microscopy (Nikon E400POL). The pillar heights and diameters before and after spin coating were determined from

SEM images, using ImageJ software. Twelve micropillars were measured for each sample. The number of bridges that single micropillars were connected to was counted in a 15×15 pillar area. Three specimens, namely 675 pillars in total, were investigated for both B1 and B2.

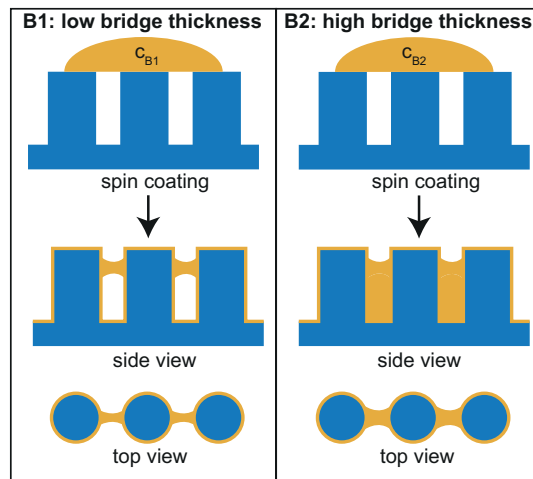


Figure 4.1. Schematic of bridge fabrication. Bridges and coatings of different thickness were obtained by using spin coating precursors (yellow in the figure) with different concentration (c_{B1} and c_{B2}). Capillary action determines the shape and thickness of the bridges and thickness of the coating, and curing fixates the shapes of the bridges.

Substrates

Adhesion and friction were measured on two types of spherical probes: from glass and from PDMS. The glass probe was a UV Fused Silica Plano-Convex Lense with a curvature radius of 46.0 mm and a center thickness of 3.8 mm (Thorlabs Inc., Newton, NJ, USA, LA4380) and was used to replicate the PDMS probe via a double-molding process. In short, the glass probe was placed in a plastic Petri dish and casted with uncured and degassed PDMS (10:1 base and curing agent mixing ratio). After curing, the formed PDMS mold was silanized and filled with uncured PDMS (10:1 base and curing agent mixing ratio), followed by degassing and curing to obtain a spherical PDMS probe.

Friction and adhesion measurements

Measurement setup

Friction and adhesion measurements were performed by placing the adhesive sample on a force platform, with its surface facing upwards. The spherical probe of glass or PDMS was brought from above in contact with the adhesive using a 2D translation stage PT1/M-Z8 (Thorlabs), controlled with KDC101 controllers (Thorlabs), via Kinesis software (Thorlabs). The force platform was an adapted version of a custom-made force transducer presented in earlier work.^[26] The force platform was connected to its immobile environment via flat plate springs. Loading the sample normally or laterally resulted in displacements of the force platform, which were recorded with two confocal chromatic aberration sensors (CL1 MG210; Stil S.A.S.), controlled with Prima controllers (Stil) via the appurtenant CCS Manager software (Version 1.5.2.404; Stil). Observed displacements of the platform were translated to forces using the effective stiffness of the force platform. In an earlier calibration procedure, the stiffness of the force platform was estimated by separately loading it in the lateral and normal direction with 0, 6, 11, 16, 21, and 26 gram, and measuring the displacements in both directions as a result of loading. Displacements of the platform were recorded at 1000 Hz. Here, we adapted the setup by limiting the displacement of the force platform from three to two directions: the normal direction and the lateral direction of sliding.

Adhesion and friction measurements

When the substrate was brought in contact with the adhesive, the moment of contact formation could accurately be determined from measuring minor displacements of the force platform. When in contact, the substrate was moved downwards $3 \mu\text{m}$ more, corresponding to a loading force of 60-90 mN. In adhesion measurements, this preload was maintained for 5 s, after which the measurement started. In friction measurements, this normal load was maintained during the entire measurement. In adhesion measurements, the pull-off speed was $100 \mu\text{m/s}$. In friction measurements, the sliding speed was $500 \mu\text{m/s}$ and the travel distance was 3 mm.

Per substrate (glass or PDMS), adhesion and friction were measured on each of the three types of fabricated adhesives, B0, B1 and B2, as well as unpatterned adhesives UNP. Two copies of each type of adhesive were used, each tested five times (resulting in a total of 10 repetitions for each type

of adhesive), in a randomized order. In each measurement, adhesion and friction were measured successively, where the order (adhesion-friction or friction-adhesion) was randomized. Before each measurement, the sample was cleaned with Scotch tape. The spherical probe was cleaned every 20 measurements with Scotch tape.

We also did a durability test, consisting of 99 successive friction measurements on glass. One sample of each type of adhesive was used in this so-called cycle measurements, using the same loads, sliding speed, and travel distance as in the friction measurements described above. The displacement data of every third measurement were recorded and used in further analysis.

Data analysis

Displacement data were analyzed in MATLAB R2018b. Displacement data were filtered and converted into forces using the obtained calibration data. From the obtained force-time plots, the maximum adhesive force and the static friction peak were acquired. These forces were divided by the effective area of each adhesive type (56.25 mm² for UNP, and 28.27 mm² for micropillar adhesives [i.e., B0, B1, B2]) to convert them into stresses. The resulted adhesion and friction stresses were used as measures of adhesion and friction performance, respectively.

Adhesion and friction stresses were compared between the different types of adhesives using a multiway analysis of variance (ANOVA) to test the effects of adhesive type and substrate type on the generated adhesion and friction performance. An alpha level of 0.001 was used for all statistical comparisons.

4.3 Results

Fabrication of adhesives

Table 4.1 shows the micropillar thickness and Figure 2 shows representative SEM and optical microscopy images of the three micropillar adhesives.

Table 4.1. Mean (standard deviation in parentheses) of micropillar thickness of the three micropillar adhesives. Coating thickness on top of micropillars corresponds to the increase in height, whereas the coating thickness at the vertical sides of micropillars is half of the diameter increase.

	Height (μm)	Height increase (μm)	Diameter (μm)	Diameter increase (μm)
B0	55.9 (0.4)	--	41.0 (0.6)	--
B1	58.6 (0.7)	2.7	42.8 (0.7)	1.8
B2	60.3 (0.9)	4.4	42.3 (0.5)	1.3

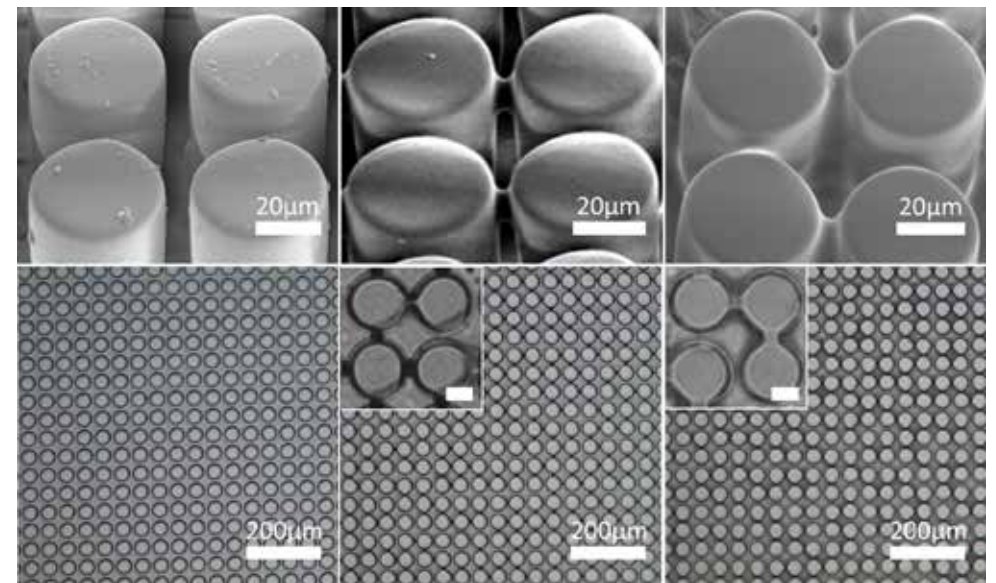


Figure 4.2. SEM images (top row) and optical microscopy images (bottom row) of adhesives without bridging (B0; first column), thin bridges (B1; second column), and thick bridges (B2; third column). Scale bars of insets are 20 μm.

Figure 4.3 shows that the number of bridges which single micropillars were connected to varied between zero and four. In B1, micropillars with different number of bridges were more or less equally present, whereas in B2, most micropillars had two bridges connected to them.

Friction and adhesion measurements

Friction on glass and PDMS

Table 4.2 and **Figure 4.4** show the friction and adhesion stresses of the four types of adhesives (UNP, B0, B1, and B2) on glass and PDMS substrates. A two-way ANOVA showed a significant effect of adhesive type ($F(3,156) = 5.25, p = 0.002$) and substrate ($F(1,156) = 89.0, p < 0.001$). The interaction effect between adhesive type and substrate was also significant ($F(3,156) = 7.51, p < 0.001$). Post-hoc analysis showed that, on glass substrates, UNP generated significantly higher friction than B0 and B1 ($p < 0.001$), whereas the difference between UNP and B2 was not statistically significant. Between the three adhesives with micropillars, no statistically significant differences were found in generated friction on glass substrates. Post-hoc analysis also showed that, on PDMS, B2 outperformed B0 and UNP ($p < 0.001$). The difference between the two adhesives with bridged micropillars, B1 and B2, was not statistically significant. Adhesives with micropillars (B0, B1, and B2) generated statistically significantly higher friction forces on PDMS than on glass ($p < 0.001$).

Table 4.2. Mean (standard deviation in parentheses) of friction and adhesion stresses of adhesives without micropillars (UNP), and adhesives with micropillars with no bridges (B0), thin bridges (B1), or thick bridges (B2), on glass and PDMS substrates.

	Friction [kPa]		Adhesion [kPa]	
	Glass	PDMS	Glass	PDMS
UNP	6.07 (1.37)	5.96 (0.75)	3.03 (0.31)	7.03 (0.86)
B0	3.12 (0.49)	5.36 (0.76)	4.52 (0.97)	7.17 (0.74)
B1	3.31 (0.31)	5.96 (0.98)	3.46 (0.67)	5.52 (0.39)
B2	3.52 (0.32)	7.06 (0.75)	2.74 (0.91)	6.36 (0.44)

4

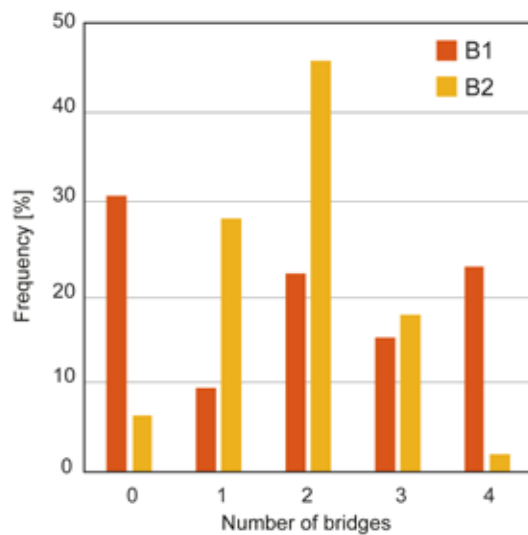


Figure 4.3. Frequency of micropillars with different numbers of bridges for B1 (red) and B2 (yellow).

4

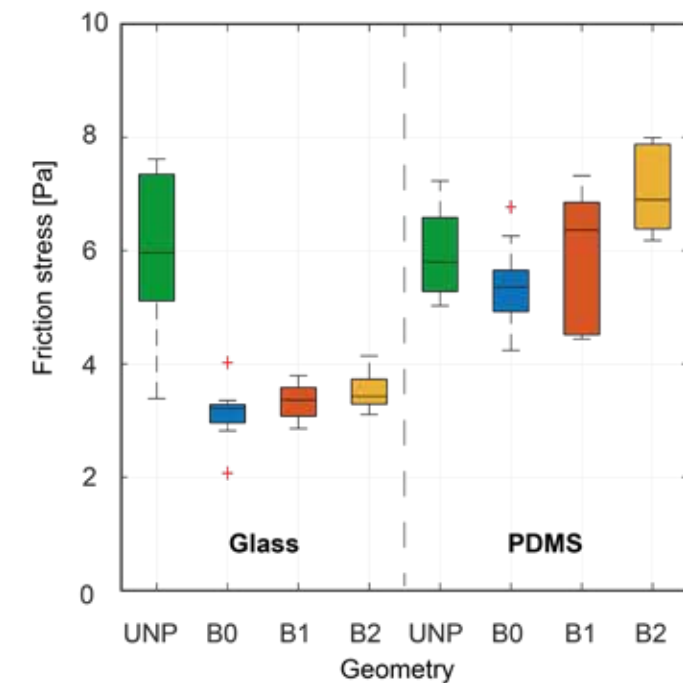


Figure 4.4. Friction stress of unpatterned reference samples UNP, and the three micropillar adhesives B0, B1, and B2, on glass and PDMS substrates.

Micropillar adhesives with lateral reinforcements

Adhesion on glass and PDMS

Figure 4.5 shows the adhesion stress of the four types of adhesives (UNP, B1, B2, and B3) on glass and PDMS substrates. A two-way ANOVA showed a significant effect of adhesive type ($F(3,159) = 20.5$, $p < 0.001$) and substrate ($F(1,159) = 284$, $p < 0.001$). An interaction effect between adhesive geometry and substrate was not observed ($F(3,159) = 2.65$, $p = 0.051$). Post-hoc analysis showed that, on glass substrates, B0 generated statistically significantly higher adhesive stresses than B1, B2, and UNP ($p < 0.001$). On PDMS, adhesives with non-bridged micropillars (B0) generated significantly higher adhesion stress than both adhesives with bridged micropillars (B1 and B2) ($p < 0.001$). All adhesive types generated significantly higher adhesive stresses on PDMS than on glass ($p < 0.001$).

Durability of friction

Figure 4.6 shows the generated peak friction forces of adhesives subjected to 99 subsequent friction force measurements on glass. The decrease of friction was the strongest during the first 3–10 cycles for all three adhesive types. In B2, friction properties were better preserved than in B0 (fitting slope -0.002 vs. -0.012 , respectively) and B1 (fitting slope -0.010).

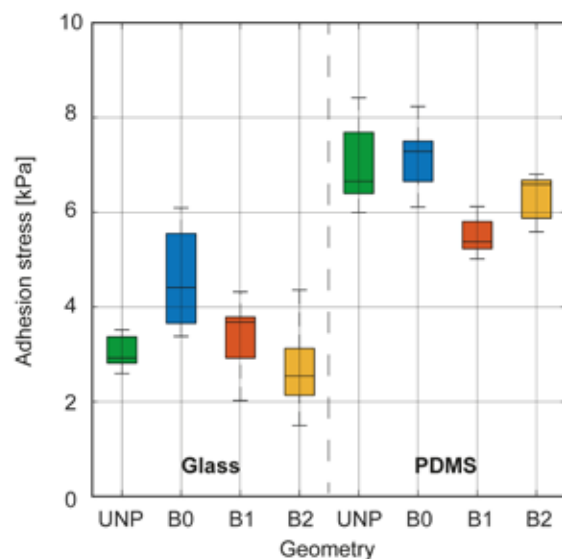


Figure 4.5. Adhesion force of unpatterned reference samples UNP, and the three micropillar adhesives B0, B1, and B2, on glass and PDMS substrates.

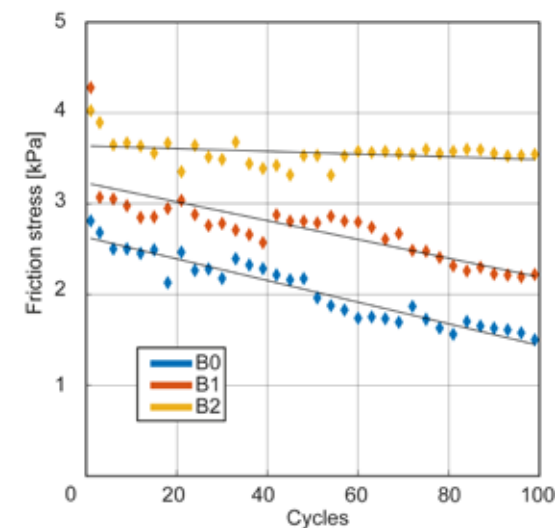


Figure 4.6. Friction durability of the three micropillar adhesives (B0, B1, and B2) on a glass substrate. All three adhesive types show a steep decay in the first 9 cycles.

4.4 Discussion

Fabrication

We showed that a relatively simple fabrication method can be used to introduce bridges in micropillar arrays, acting as lateral reinforcements. A higher concentration of PDMS in the spincoated solution led to thicker bridges. The formation of bridges is dominated by the competition between capillary force, similar for 5% and 10% concentrations of PDMS in TBA, and structural cohesive force of the liquid bridge, increasing with increasing PDMS concentration in TBA.^[27] We assume that, due to spincoating, the polymer solution forms a film on the micropattern, and that, additionally, due to excess of polymer solution, microscale droplets are present as menisci in between neighboring micropillars. The relatively high-cohesive bridging microdroplets obtained from spincoating with 10% PDMS solution are larger compared to microdroplets obtained from spincoating with 5% DMS solution, leading to, respectively, thicker (B2) and thinner (B1) bridges after curing. Furthermore, microdroplets from a 10% PDMS solution are presumably large enough to form two bridging microdroplets connected to a single micropillar, whereas microdroplets formed after spincoating a 5% PDMS solution are mostly only large enough to form a single bridge in between

neighboring micropillars. Consequently, the distribution of bridges (Figure 3) is mostly clusters of two in B2 adhesives around a single micropillar, and one by one in B1 adhesives, with a random orientation. The observation that, with higher PDMS concentrations, a thicker coating is present on the top and sides of micropillars can be explained by a mechanism shown by Roy et al., who found that, when spincoating a polymer film such as PDMS on patterned surfaces, the thickness of the polymer film increases with increasing polymer concentration.^[28]

Friction measurements

Results of friction measurements showed that, for micropillar adhesives B0, B1, and B2, significantly higher friction stresses were generated on PDMS than on glass substrates. The increased friction stresses on PDMS compared to glass substrates are partially because of substrate effects. Deformability of the PDMS substrate might introduce indentation of micropillars into the substrate, leading to interlocking.^[23] Also, elastic deformations of the substrate under applied normal and lateral loads during shearing might lead to an enhanced adhesive contribution to friction, a mechanism that is not present on rigid glass substrates.^[22]

When assessing friction on each substrate, an effect of bridging is visible on PDMS, with friction stresses generated by adhesives with thick bridges (B2) being higher compared to adhesives without bridges (B0). It is likely that the increased lateral stiffness of adhesives with micropillars as a result of bridging has a positive effect on interlocking on PDMS. On glass substrates, interlocking is not present, so this effect of bridging on interlocking is not observed.

Another effect of bridging is that collapsing of pillars is prevented, with preservation of contact as a result, rendering an advantage of bridged pillars (B2) over non-bridged pillars (B0) on PDMS substrates. We used force-time data of friction measurements to assess the transition from static friction, corresponding to region *s* in the force-time plot from **Figure 4.7**, to dynamic friction (region *d*). **Table 4.3** shows the average duration of the static friction regime *s* for B0, B1, and B2 on glass and PDMS substrates. On glass, we found no statistically significant differences in the length of *s* for adhesives with micropillars with or without bridging. Region *s* was significantly longer for PDMS than for glass ($F(2,58) = 359, p < 0.001$), illustrating that deformation of the substrate plays an important role in

preservation of the contact. The length of the static friction region was not statistically significantly different between B1 and B2 on PDMS.

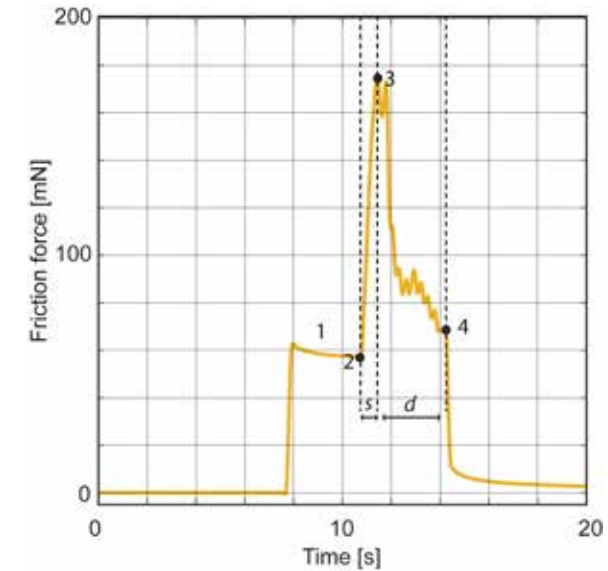


Figure 4.7. Force-time plot of the tenth repetition of a micropillar adhesive with thick bridges (B2) on a PDMS substrate. At (1), the adhesive is normally loaded, resulting in a lateral load due to crosstalk of the setup. At (2), lateral loading starts. At (3), the peak static friction force has been reached, and the adhesive starts sliding. At (4), lateral loading stops, sliding ends, and friction forces drop. The timeframe between (2) and (3), annotated with *s* in the figure, corresponds to the static friction region, and the timeframe *d* between (3) and (4) is the dynamic friction region.

Table 4.3. Mean (standard deviation in parentheses) of the transition time (in seconds) from static to dynamic friction for the three micropillar adhesives B0, B1, and B2, on glass and PDMS substrates.

	Glass	PDMS
B0	0.23 (0.07)	0.60 (0.07)
B1	0.21 (0.02)	0.63 (0.15)
B2	0.20 (0.01)	0.75 (0.13)

The effect bridging on friction stresses being smaller on glass than on PDMS substrates might be caused by mechanical coupling between neighboring pillars on glass, which reduces contact splitting effects such as defect control and inhibition of crack growth. On deformable substrates, such as PDMS, this coupling between neighboring pillars does not necessarily lead to additional loss of contact, as the substrate might conform to the buckling pillars, resulting in preservation of contact between substrate and micropillars.

Adhesion measurements

The adhesive stresses we measured for micropillars without bridging on glass substrates (in the order of 4.5 kPa) are in same order as similar adhesives tested in literature.^[14,29,30] In contrast to previous work which has shown hard core-soft shell structures are beneficial for adhesion^[18–20, 23] our B1 and B2 adhesives exhibited similar to or lower adhesion stresses than B0, both on glass and PDMS substrates. This is not surprising, as B1 and B2 did not only had a hard core and a soft shell but also bridges. The main effect of bridging is the prevention of buckling, which hardly plays a role in adhesion experiments under the (pre)loads we applied. On glass substrates, bridging of micropillars might even be disadvantageous, as effects of contact splitting such as defect control and inhibition of crack growth are reduced by bridging. Mechanical coupling of micropillars by bridging presumably introduces a local load redistribution mechanism once one micropillar detaches, resulting in locally high peak stresses, and consequent fast defect growth. This mechanical coupling increases further with increasing bridge thickness, resulting in even lower generated adhesive stresses with adhesives consisting of micropillars with thick bridges (B2). On PDMS substrates, coupling of detachment between neighboring micropillars takes place due to deformation of the substrate under local peak stresses as described by Cheung et al.,^[32] even for non-bridges micropillars.

Durability tests

Thick bridges between micropillars led to higher durability compared to non-bridged adhesives or adhesives with thin bridges. Under shear loading of micropillar adhesives, elastic forces of bridges under compressing and stretching of bridges keep connected pillars up straight. Optical microscopic images of the samples showed that bridges are still present after the durability test and no permanent collapsed pillars are visible. When collapsed, pillars adhere to neighboring pillars, resulting in irreversible collapsing.^[10] In the presence of bridges between micropillars, it is possible that bridges

are elastically stretched and compressed, resulting in recovery forces on pillars as long as they are collapsed. This assumption is supported by the fact that, in the adhesion and friction measurements, where individual adhesives were measured 5 times, with at least 10 minutes in between measurements, no history effect was visible.

Limitations and future work

A limitation of our work is that we fabricated bridges with only two different shapes. It would be useful to include more concentrations of PDMS solution for explaining the effect of bridge structures on the adhesion and friction properties of micropillar adhesives. However, precisely controlling the formation of bridge structures between micropillars remains a challenge. Spin coating on a topographically patterned substrate is affected by various factors and their combinations, such as solvent properties (e.g., evaporation speed, wettability), concentration and volume of the dispensed polymer solution, and spin speed and duration. In addition, the structural characteristics of patterned micropillars, namely diameter and height of micropillars and gaps between micropillars, also influence the coating process and resultant structures. Due to this complexity, we have not been able to create samples series in which only one parameter (e.g., the bridge thickness) differs, while the rest (e.g., bridge shape) remains the same. Instead, we opted for two distinct types of bridge structures, that is, one with thinner bridges suspended between micropillars and another with thicker bridges filling the gaps. In future work, it is undoubtedly meaningful to investigate the precise formation mechanism of bridge structures, such as concentration dependence. If future work would lead to a thorough understanding on the relation between the settings of the spincoating procedure and obtained bridge properties, the presented fabrication method could be a valuable addition to the currently available microfabrication toolbox.^[33] Combining bridges with mushroom-shaped and spatula-shaped micropillar tips could be considered as well, for enhancing friction in particular.

4.5 Conclusion

We fabricated composite soft micropillars with a stiff core, and introduced bridges between neighboring micropillars using spincoating. By varying the concentration of PDMS in the spincoated polymer solution, the geometry of the bridges, including their thickness and number density, could be varied. Friction measurements showed that bridging of micropillars has a positive

effect on generated friction, presumably due to an increase in lateral stiffness and prevention of buckling, especially when attaching to deformable substrates. We also showed that in the presence of thick bridges between micropillars, the durability of friction properties of adhesives with micropillars is improved compared to adhesives with non-bridged micropillars.

Acknowledgements

This research is supported by the Netherlands Organization for Scientific Research (NWO) Domain Applied and Engineering Sciences (TTW), (Open Technology Program, project 13353 "Secure and gentle grip of delicate biological tissues"). This work was also supported by a cohesion grant of the 3mE Faculty of Delft University of Technology between BMechE and PME departments.

References

- [1] K. Autumn, Y. A. Liang, S. T. Hsieh, W. Zesch, W. P. Chan, T. W. Kenny, R. Fearing, and R. J. Full, *Nature* **2000**, 405, 681.
- [2] W. Federle, *J. Exp. Biol.* **2006**, 209, 2611
- [3] K. Autumn, *J. Exp. Biol.* **2006**, 209, 3558.
- [4] K. Autumn, *MRS Bull.* **2007**, 32, 473
- [5] B. N. J. Persson, *MRS Bull.* **2007**, 32, 486.
- [6] M. Kamperman, E. Kroner, A. del Campo, R. M. McMeeking, and E. Arzt, *Adv. Eng. Mater.* **2010**, 12, 335
- [7] L. Afferrante and G. Carbone, *Macromol. React. Eng.* **2013**, 7, 609
- [8] S. Gorb, M. Varenberg, A. Peressadko, and J. Tuma, *J. R. Soc. Interface* **2007**, 4, 271
- [9] G. Carbone, E. Pierro, and S. N. Gorb, *Soft Matter* **2011**, 7, 5545
- [10] W. G. Bae, M. K. Kwak, H. E. Jeong, C. Pang, H. Jeong, and K. Y. Suh, *Soft Matter* **2013**, 9, 1422
- [11] B. Murarash and M. Varenberg, *Tribol. Lett.* 2011, 41, 319
- [12] A. Jagota, C. Y. Hui, N. J. Glassmaker, and T. Tang, *MRS Bull.* **2007**, 32, 492
- [13] M. Varenberg and S. Gorb, *J. R. Soc. Interface*, **2007**, 4, 721
- [14] M. Varenberg, B. Murarash, Y. Kligerman, and S. N. Gorb, *Appl. Phys. A Mater. Sci. Process.* **2011**, 103, 933
- [15] N. J. Glassmaker, A. Jagota, C.-Y. Hui, W. L. Noderer, and M. K. Chaudhury, *Proc. Natl. Acad. Sci.*, **2007**, 104, 10786
- [16] Z. He, C. Y. Hui, B. Levrard, Y. Bai, and A. Jagota, *Sci. Rep.*, **2016**, 6, 26867
- [17] Y. Tian, Z. Zhao, G. Zaghi, Y. Kim, D. Zhang, and R. Maboudian, *ACS Appl. Mater. Interfaces*, **2015**, 7, 13232
- [18] L. Xue, B. Sanz, A. Luo, K. T. Turner, X. Wang, D. Tan, R. Zhang, H. Du, M. Steinhart, C. Mijangos, M. Guttman, M. Kappl, and A. Del Campo, *ACS Nano*, **2017**, 11, 9711
- [19] H. K. Minsky and K. T. Turner, *ACS Appl. Mater. Interfaces*, **2017**, 9, 18322
- [20] S. C. L. Fischer, E. Arzt, and R. Hensel, *ACS Appl. Mater. Interfaces*, **2017**, 9, 1036
- [21] S. Gorumlu and B. Aksak, *R. Soc. Open Sci.*, **2017**, 4, 161105
- [22] B. N. J. Persson, *Tribol. Lett.* **2016**, 62, 34
- [23] H. T. Tramsen, S. N. Gorb, H. Zhang, P. Manoonpong, Z. Dai, and L. Heepe, *J. R. Soc. Interface*, **2018**, 15, 20170629
- [24] J. Y. Park, S. J. Yoo, E. J. Lee, D. H. Lee, J. Y. Kim, and S. H. Lee, *Biochip J.* **2010**, 4, 230
- [25] J. H. Koschwanetz, R. H. Carlson, and D. R. Meldrum, *PLOS ONE* 4, **2009**, e4572
- [26] P. van Assenbergh, M. Fokker, J. Langowski, J. van Esch, M. Kamperman, and D. Dodou, *Beilstein J. Nanotechnol.*, **2019**, 10, 79
- [27] B. Su, S. Wang, J. Ma, Y. Wu, X. Chen, Y. Song, and L. Jiang, *Adv. Mater.* **2012**, 24, 559
- [28] S. Roy, K. J. Ansari, S. S. K. Jampa, P. Vutukuri, and R. Mukherjee, *ACS Appl. Mater. Interfaces*, **2012**, 4, 1887
- [29] C. Greiner, A. Del Campo, and E. Arzt, *Langmuir*, **2007**, 23, 3495

- [30] D. M. Drotlef, L. Stepien, M. Kappl, W. J. P. Barnes, H. J. Butt, and A. Del Campo, *Adv. Funct. Mater.* **2013**, *23*, 1137
- [31] J. Jiang, Y. Wang, L. Jin, C. H. Hsu, S. Zhang, J. Mao, W. Yin, T. Li, B. Ni, Z. Su, J. Huang, C. Wesdemiotis, K. Yue, W. Zhang, and S. Z. D. Cheng, *ACS Appl. Nano Mater.* **2020**, *3*, 3596 (2020)
- [32] E. Cheung and M. Sitti, *Langmuir* **2009**, *25*, 6613
- [33] P. van Assenbergh, E. Meinders, J. Geraedts, and D. Dodou, *Small*, **2018**, *14*, 1703401

Chapter 5

ANISOTROPIC STIFFNESS ADHESIVES FOR HIGH SHEAR FORCES ON SOFT SUBSTRATES

This chapter has been published as:

Peter van Assenbergh*, Frank Haring*, Joshua A. Dijkman and Dimitra Dodou, *Adv. Mater. Interfaces* **2020**, 2001173, 1-9. doi: 10.1002/admi.202001173

*Both authors contributed equally to this chapter.

Abstract

Reversible attachment on soft substrates is useful in a range of applications, including soft robotics and soft-tissue surgical instrumentation. On rigid substrates, the use of micropatterned adhesives has been extensively explored. It has been shown that surface micropatterns provide conformability, thereby enabling the formation and preservation of contact with the substrate. On soft, deformable substrates, on the other hand, surface micropatterns largely lose their functionality. Alternative mechanisms have to be explored to maximize conformability and thus formation and preservation of contact on soft substrates.

We used 3D-printing to fabricate adhesives with internal cylindrical pores of various configurations leading to different combinations of high/low normal/shearing stiffness, and we measured shear forces on glass and on soft elastomeric substrates. On the glass substrate, shear forces were highest for the adhesives with the lowest normal stiffness, independently from their shear stiffness. On the soft substrates, the highest shear forces were achieved for the adhesives combining low normal stiffness, enabling contact formation, with high shear stiffness, promoting contact preservation. The beneficial effect of such anisotropic stiffness on shear forces increased with the deformability of the substrate.



5.1 Introduction

Patterned adhesives

Temporary attachment to substrates is useful in a range of applications, such as robotic devices performing pick-and-place tasks, climbing robots, biomedical applications such as skin patches, and fastening products on tilted or vertical substrates.^[1-4] Successful attachment of an adhesive on a substrate requires two phenomena to take place: contact formation between the adhesive and the substrate and preservation of the formed contact when external loads are applied.^[5,6] Consequently, for strong, yet reversible attachment, an adhesive should fulfil two contradictory properties simultaneously: high deformability in the normal direction, leading to a large contact formation, and low deformability in the loading direction, leading to preservation of the formed contact when loads are applied.^[7] The presence of such direction-dependent stiffness in a material is commonly referred to as 'anisotropic stiffness'.^[8,9]

Dry adhesives are typically patterned with repetitive microscale elements such as pillars, spatulas, or mushrooms.^[10-14] Alternatively, patterning adhesives with wrinkles has been proposed for controlling attachment.^[15-17] When attaching to hard substrates, such surface (micro)patterns are associated with high adaptability to the substrate roughness and low effective elasticity of the adhesive, leading to better contact formation than unpatterned adhesives.^[5,11,18] Additionally, surface micropatterns allow for a more uniform stress distribution than unpatterned adhesives, which contributes to better preservation of the formed contact.^[5,6,11,18] Furthermore, the contact of surface micropatterns with the substrate is split up into multiple contact points. When locally a contact point detaches, the stress is globally rebalanced over the remaining contact points, inhibiting the propagation of the defect.^[6,11,18,19] Additionally, contact split-up in multiple smaller contacts results in a drastic increase of contact line length, and thus higher separation strength.^[15]

On soft substrates, surface micropatterns might be expected to lose at least some of their advantageous properties of forming and preserving the contact over unpatterned surfaces. Contact formation between a soft substrate and an adhesive is likely to be primarily promoted by the substrate's deformability, and so the presence of a surface micropattern might not be particularly contributing to contact formation compared to an unpatterned

surface. For the preservation of contact between a soft substrate and an adhesive, the presence of a surface pattern might be even disadvantageous, because the splitting up of the contact into numerous finer elements leads to a non-uniform stress distribution at the adhesive-substrate interface, with local peak forces at the perimeter of each contact point,^[20-22] which increase the risk of crack initiation under stress. Additionally, as Cheung et al. showed, on soft polyurethane substrates with a thickness larger than 2 mm, the detachment of individual microscale cylindrical pillars led to local redistribution of stresses among neighboring pillars.^[23] Therefore, detachment of a single pillar induced detachment of the neighboring pillars and subsequent propagation of the defect throughout the whole adhesive.

Internal geometry

Beside the surface pattern of adhesives, also the internal properties of the adhesive can be designed to realize the anisotropic properties required for good grip. For example, Bartlett et al. fabricated elastomeric adhesive pads, and internally reinforced them by incorporating stiff carbon fibres, aligned with the shear direction.^[7] The presence of these fibres resulted in a drastic increase in generated shear forces compared to elastomeric pads without reinforcement, because the low stiffness in the normal direction allowed for high contact formation, and the high stiffness in the shear direction enabled efficient preservation of contact under shear loading. Micropillar reinforcement by incorporating directional stiff fibers,^[24] or by embedding hard nanoparticles in micropillars^[25] has been also shown to prevent deformations that may cause loss of contact.

Anisotropic properties in materials have also been realized without implementation of a second, reinforcing component. For example, Tramsen et al. encased granules in an elastic membrane, and showed that high friction forces are generated due to conformation of the elastic membrane to substrate irregularities, and stiffening of the adhesive due to jamming of the granular component under normal loads.^[26] Alternatively, the presence of a flat terminal layer topping a microstructure has been shown to benefit the shear performance of adhesives on hard substrates. He et al. fabricated micropillar arrays topped with a terminal layer, and attributed the higher shear forces found compared to micropillar arrays without a terminal layer to energy loss due to elastic deformations of both the sub-surface structures and the terminal layer during peeling off, reattachment of the terminal layer during sliding, and internal sliding of the sub-surface structures along each

other.^[27] The presence of multiple peeling fronts when applying load in the normal or shearing direction has been also suggested to result in a drastic increase of the peeling line length, and therefore in higher pull-off or shear forces.^[28,29]

In earlier work, we showed that, on soft substrates, micropatterned adhesives consisting of arrays of closely-packed spherical dimples, topped with a terminal layer generate higher shear forces than unpatterned adhesives as well adhesive with the same dimple micropattern but without a terminal layer.^[30] It is likely that the presence of a terminal layer results in contact formation similar to that of an unpatterned adhesive of the same dimensions. Additionally, the low stiffness of the thin terminal layer in the normal direction in combination with the high shear stiffness from the internal cavity walls allows for contact preservation during sliding.^[27,28,30] These results suggest that anisotropic stiffness enabled by a combination of an internal spherical cavity with a thin, deformable terminal layer can be beneficial for generating high shear forces.

An easy method to fabricate structures with internal geometry is 3D printing. 3D printing has been used to fabricate porous structures with anisotropic properties.^[31–34] Such anisotropic materials are applied as, for example, porous template scaffolds for tissue engineering.^[35,36] In such scaffolds, porosity has a function to maximize permeability (which is crucial for cell growth and transport of nutrients and metabolic waste), but also to match the scaffold mechanical properties with those at the implantation site.^[35,37] Duoss et al. independently varied the shear and normal stiffness of elastomeric structures by 3D printing porous architectures consisting of stacked rasters of long filaments with diameters of 100–610 μm .^[38]

Here, we use 3D printing to fabricate adhesives with porosity-induced anisotropy and use their architecture to obtain mechanical properties suitable for generating grip on hard and soft substrates. Anisotropic properties were realized by 3D printing adhesives containing internal horizontal cylindrical pores to control the stiffness in shear and normal direction. The samples were 3D-printed from a single material. We measured shear forces of 3D printed anisotropic adhesives with different architectures, resulting in various stiffness degrees, in the shear and normal direction. Shear forces were measured on rigid glass substrates as well as on deformable poly-dimethylsiloxane (PDMS) substrates.

5.2 Results

Fabricated adhesives

Fabrication

Table 5.1 shows the internal and external geometry of the four sample types fabricated using stereolithographic processing. The adhesives were $20 \times 20 \times 5 \text{ mm}^3$ in size (length \times width \times height) and contained either a single row of cylindrical pores of 2.7 mm in diameter separated by pore walls with a 0.5 mm thickness at their thinnest position, or a double row of pores of 1.28 mm in diameter separated by pore walls with a 0.15 mm thickness at their thinnest position. The adhesives with a single and double row of pores contained overhangs of 2.7 and 1.275 mm, respectively. Two types of adhesives with a single row of pores were fabricated: one with pores aligned parallel to the pulling direction x (SR-X) and another with pores aligned orthogonally to the pulling direction (SR-Y). Adhesives with a double row of pores were fabricated with pores aligned orthogonally to the pulling direction (DR-Y). Isotropic adhesives, without an internal geometry, were fabricated as reference samples (REF).

The four internal geometries were combined with three types of external (surface) geometries: unpatterned (UNP), a pattern of circular posts with a diameter of 0.5 mm and a height of 0.5 mm (PIL), and a pattern of conical pillars with a diameter of 0.5 mm at the base and 0.2 mm at the top, tilted 45° in x-direction (HKS).

Mechanical characterization

Figure 5.1 shows the adhesives with four different internal geometries, without any loading (top picture), with a normal load of 6 N (middle picture) applied via a cylindrical weight and with a shear load of 6 N (bottom picture). For each internal geometry, the structural stresses under an applied shear load of 6 N, as predicted by Finite Element Analysis (FEA), are shown. In FEA, we fixated the contact surface of the adhesives, so shear deformations occur in the bulk of the adhesives. In **Table 5.2**, the corresponding deformations of the adhesives under the applied loads, both in shear and normal direction, are reported.

Table 5.1. Photographs of 3D-printed adhesives with different internal geometries. In shear force measurements, samples were placed on the substrate with the surface pattern facing down, and pulled in the x-direction. Scale bar of internal geometries = 5 mm; scale bar of surface patterns = 1 mm.

Internal geometries		Surface patterns	
REF No internal pores		UNP Unpatterned	
SR-Y Single row of 2.7 mm diameter cylindrical pores, aligned orthogonally to the pulling direction x		PIL Circular pillars with a diameter of 0.5 mm and a height of 0.5 mm	
SR-X Single row of 2.7 mm diameter cylindrical pores, aligned parallel to the pulling direction x		HKS Conical pillars with a diameter of 0.5 mm at the base and 0.2 mm at the top, tilted 45° in x-direction	
DR-Y Double row of 1.275 mm in diameter cylindrical pores, aligned orthogonally to the pulling direction x			

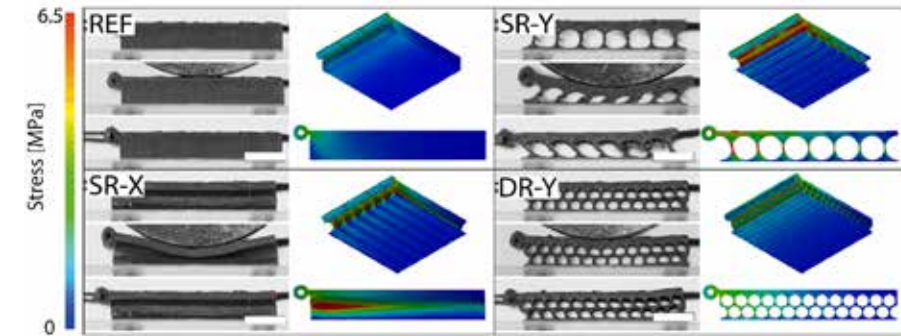


Figure 5.1. Adhesives with four internal geometries under no load, normal load, and shear load (from top to bottom), and stresses calculated with Finite Element Analysis (FEA) in bottom and side view graphical representations. The geometries with a single row of pores (SR-X and SR-Y) have the lowest normal stiffness. Scale bars are 5 mm.

Table 5.2: Experimentally determined deformations for the four internal geometries under a load of 6 N in normal and shear direction and corresponding calculated compliance k of the geometries.

	Normal direction		Shear direction	
	Deformation [mm]	k_{normal} [kN/m]	Deformation [mm]	k_{shear} [kN/m]
REF	< 0.1	>60	< 0.1	>60
SR-Y	1.5	4	1.5	4
SR-X	1.5	4	< 0.1	>60
DR-Y	0.45	13.33	0.8	7.5

FEA predicted that the adhesive with internal geometry REF distributes stresses throughout the bulk without local stress concentration. Experimental shear loading of this adhesive confirmed that it had the highest shear stiffness out of the four internal geometries.

For geometry SR-Y, FEA predicted that, under a shear force of 6 N, stresses in the internal walls are high. As it can be seen in **Figure 1**, the terminal layer experiences lower stresses in the shear direction. Stress concentra-

tions in the terminal layer are present underneath the internal pore walls. Shear loading of geometry SR-Y resulted in a shear deformation of 1.5 mm, caused by lateral tilting of the internal pore walls (**Figure 1**). Loading this geometry in the normal direction led to bending of the pore walls into an s-shape.

For geometry SR-X, FEA showed that lateral deformations under a shear force of 6 N are limited to 0.17 mm. In the terminal layer, longitudinally shaped stress concentrations were predicted, located underneath the pore walls. The corresponding empirical data showed that this geometry had the same normal stiffness but higher shear stiffness than the SR-Y geometry (**Table 5.2**).

For geometry DR-Y, FEA predicted that internal stress concentrations occur in the pore walls and are the highest closer to the point where the shear load is applied on the adhesive. At the adhesive surface, stress concentrations are longitudinally shaped, and aligned with the pore direction. Empirical testing of this geometry showed that the shear stiffness of this geometry was in between the shear stiffness of the two single-pore row internal geometries.

5 Shear forces on a glass substrate

Figure 5.2 shows the shear forces on glass for the adhesives without external geometry (UNP) as a function of internal geometry.

A two-way ANOVA for surface pattern (UNP, PIL, and HKS) and internal geometry (REF, SR-Y, SR-X, and DR-Y) showed significant main effects for both the surface pattern, $F(2,108) = 209.09$, $p < 0.001$, and the internal geometry, $F(3,36) = 62.01$, $p < 0.001$. An interaction effect of the surface pattern with the internal geometry was also found, $F(6,108) = 110.09$, $p < 0.001$.

Post-hoc analysis per external geometry group showed that, among the UNP adhesives, internal geometries SR-X and SR-Y generated significantly higher shear forces than DR-Y and REF ($p < 0.001$). Among the PIL adhesives, all three internal geometries generated higher shear forces than REF, with SR-Y resulting in significantly higher shear forces than DR-Y ($p < 0.001$). Among the HKS adhesives, no significant differences among the four internal geometries were observed.

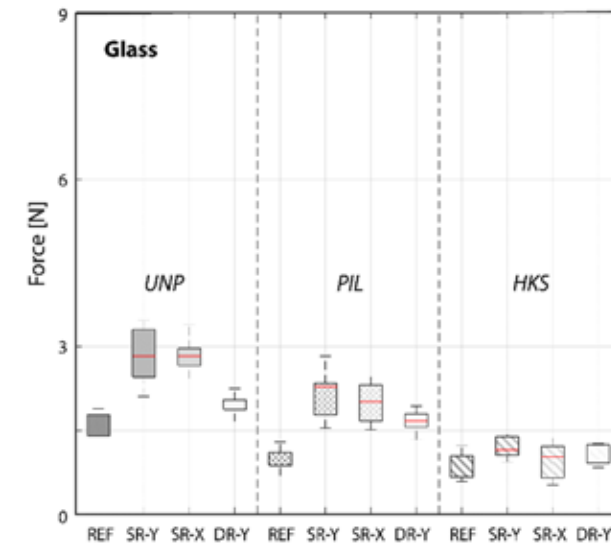


Figure 5.2. Shear forces of the four internal geometries, grouped by external surface pattern, on a glass substrate.

Post-hoc analysis per internal geometry group showed that all four internal geometries with UNP surface generated higher shear forces than the corresponding internal geometries with a HKS surface ($p < 0.001$). SR-X and SR-Y with UNP surface also generated higher shear forces than the corresponding internal geometries with surface PIL ($p < 0.001$). SR-X, SR-Y, and DR-Y with surface geometry PIL generated higher shear forces than the corresponding internal geometries with surface geometry HKS ($p < 0.001$).

5 Shear forces on PDMS substrates

Figure 5.3 shows the shear forces of adhesives with surface UNP as a function of internal geometry on PDMS substrates of three stiffness degrees.

A two-way ANOVA of shear forces of adhesives with surface UNP for substrate (PDMS-10, PDMS-20 and PDMS-30) and internal geometry (REF, SR-Y, SR-X and DR-Y) showed main effects for both the substrate, $F(2, 108) = 325.7$, $p < 0.001$, and the internal geometry, $F(3,108) = 22.31$, $p < 0.001$, as well as an interaction between substrate and internal geometry, $F(6, 108) = 8.68$, $p < 0.001$.

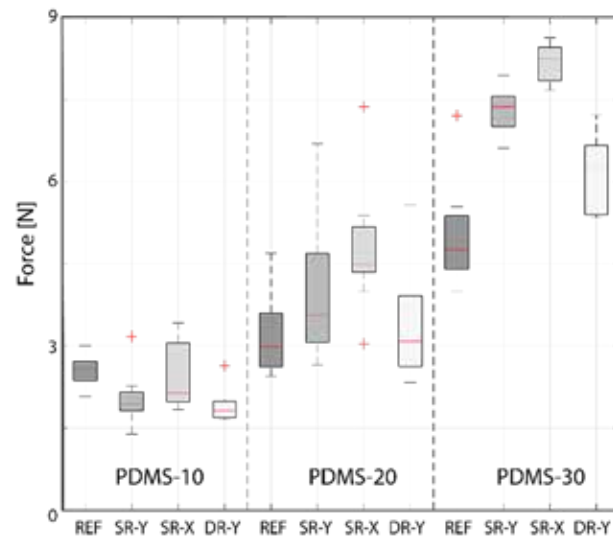


Figure 5.3. Shear forces of the four internal geometries and unpatterned surface geometry, grouped by PDMS substrate. The corresponding data for adhesives with surface patterns of pillars or hooks are presented in the supporting information (Figure I5).

Post-hoc analysis showed that significantly higher shear forces were generated on PDMS-30 than on PDMS-10 and PDMS-20 for all adhesives ($p < 0.001$), except for geometry REF, which did not generate significantly higher shear forces on PDMS-30 than both single-pore row adhesives on PDMS-20.

Geometries SR-X and SR-Y generated significantly higher shear forces on PDMS-20 than all four internal geometries on PDMS-10. Additionally, geometry DR-Y on PDMS-20 outperformed SR-Y and DR-Y on PDMS-10, and geometry REF on PDMS-20 outperformed DR-Y on PDMS-10 ($p < 0.001$).

On PDMS-10, no significant differences in shear forces were observed between the four internal geometries of adhesives. On PDMS-20 substrates, SR-X outperformed DR-Y and REF ($p < 0.001$). On PDMS-30, SR-X, SR-Y, and DR-Y outperformed REF, and both single-row geometries (SR-X and SR-Y) generating significantly higher shear forces than DR-Y ($p < 0.001$).

On all three PDMS substrates, adhesives with PIL and HKS surface patterns generated lower shear forces compared to adhesives with UNP surface with-

in each of the four groups of internal geometries ($p \leq 0.003$). Furthermore, adhesives with surface HKS were outperformed by adhesives with surface PIL ($p < 0.001$). Shear forces of adhesives with surface patterns PIL and HKS on PDMS-10, PDMS-20 and PDMS-30 are presented in the supporting information.

5.3 Discussion

Here, we used 3D printing to generate adhesives with architectures resulting in anisotropic stiffness properties to enhance gripping performance. Such anisotropic adhesives should not be confused with adhesives that generate 'anisotropic friction,' which is defined as directional grip, or grip being higher in one shearing direction than in the opposite direction.^[39–43]

Anisotropic adhesives

Fabrication

In Table 5.1, the four fabricated internal geometries and three external geometries are shown. We used 3D printing, because it is one of the few methods suitable for fabrication of overhanging features.^[44] With stereolithography, designs are printed in consecutive layers of 50 μm in thickness. We printed the adhesives in upright position (i.e., with the $5 \times 20 \text{ mm}^2$ side of the adhesive facing down). By printing the adhesives in this orientation, the mechanical stability of each cured layer is maximized, preventing printing errors that could be caused during peeling off of each cured layer from the printing bed. We fabricated adhesive with pore diameters of 1.28 mm (in DR-Y adhesives) or 2.7 mm (SR-X and SR-Y). Pore sizes were chosen because of three factors. First, for pores below 1 mm in diameter, uncured resin could not be washed out of the pores due to capillary forces after printing with the used commercial setup and resin. Second, the wall thickness between neighboring pores had to be thick enough to support the structure, and not spontaneously collapse. Third, planned adhesive dimensions had to be in the order of 1 cm^2 , resembling the length scale of soft robotic grippers or surgical grippers. Meeting these demands, we could fit 12 neighboring pore rows in a $2 \times 2 \text{ cm}^2$ adhesive, and manufactured alternative geometries with half the amount (i.e., six) of neighboring pores.

5.4 Mechanical characterization

We applied normal and shear loads of 6 N and observed the deformations of the adhesives in the corresponding loading directions. For adhesives with a single row of pores (SR-X and SR-Y), FEA predicted that it is mainly the internal pore walls that absorb the applied stress. Under the applied normal loads, we observed that pore walls took an s-shaped when buckling. In other words, normal loading, besides deformation, also led to lateral deformation. FEA also predicted that, along the surface of the adhesive, stress concentrations are present along the pores, where the terminal layer is not supported, as the surface layer thickness is lowest on these locations.

Adhesives with internal geometries SR-Y and DR-Y showed larger deformation in the shearing direction than adhesives with SR-X internal geometry. Deformation of the adhesives mostly originated from bending of the pore walls when these are aligned with the shearing direction y (Table 5.1). When pore walls are aligned with the shearing direction, as is the case in adhesives with an SR-X geometry, walls cannot deform in the direction of their alignment. Comparing a double or a single row of pores, a higher shear stiffness of DR-Y geometries compared to SR-Y adhesives originated from a lower aspect ratio and a higher accumulative length of the internal pore walls for the first geometry, reducing the bendability of the internal pore walls. Adhesives with internal geometry REF did not exhibit observable deformations under the applied shear and normal loads. The isotropic nature of this adhesive resulted in the highest geometric density of the four fabricated internal geometries, making it the stiffest adhesive. The stiffness of this adhesives is best-described by the resin's bulk tensile strength as provided by the resin manufacturer (7.7–8.5 MPa after post-curing).

Shear forces

On glass

On a glass substrate, we found that adhesives with internal pores generated higher shear forces compared to UNP adhesives, and that higher shear forces are generated with adhesives with a single row of pores than with a double row of pores. The difference in shear stiffness of internal geometries SR-X versus SR-Y did not lead to significantly different shear forces. In SR-X adhesives, bending of the pore walls is present, but this bending did not lead to deformation of the terminal layer and its subsequent detachment

from the substrate. One effect that we observed was that the variation of generated shear forces was lower for higher shear stiffness adhesives (i.e., with internal geometry SR-X) compared to adhesives with internal geometry SR-Y, pointing towards an advantage in terms of performance reliability of higher shear stiffness adhesives.

In **Figure 5.4**, bottom view images of adhesives with a UNP surface and various internal geometries are shown under a preload (PL) of 2.45 N (250 g) and under the measuring load of 0.49 N (50 g) during shearing at $t = 0$ (t_0). Additional frames of video recordings are shown in the Supporting Information. The formed contact between the adhesives and the glass substrate, appearing as light regions in the bottom view, consisted of segregated contact regions. Under the applied pre-loading, the contact points of the porous internal geometries were a vertical projection of the internal pore geometry. For adhesives with a single row of pores (SR-X, SR-Y), the thickness of contact regions were higher compared to adhesives with a double row of pores (DR-Y), suggesting that more intimate contact was formed in the former two cases. Additionally, adhesives with a single row of pores preserved more contact after the normal load was reduced to 0.49 N. These superior contact formation and preservation properties of adhesives SR-X and SR-Y likely originated from the lower average thickness of the terminal layer, and led to higher shear forces on glass substrates compared to adhesives with a double row of pores. One could reason that the splitting-up of formed contact in multiple separated contact points, leading to inhibition of crack initiation and propagation, is higher in adhesives with a double row than in adhesives with a single row of pores. Presumably, the absence of the described effects in our adhesives is because the number of contact points is too low, and the length scale of individual contact points (contact areas are on millimeter scale) is too large for such effects to manifest themselves.

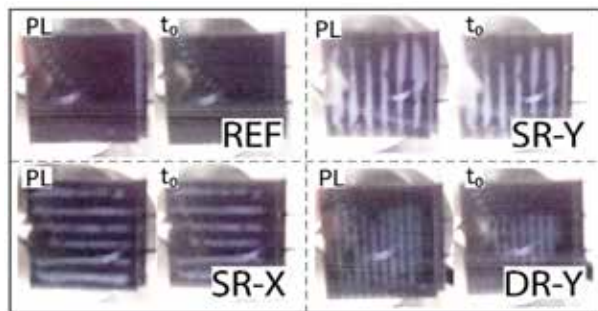


Figure 5.4. Bottom view of adhesives with the four internal geometries on glass under a preload (PL) of 2.45 N and at t_0 , where, about 3 seconds prior to sliding, the load was reduced to 0.49 N. Contact regions appear as light regions, whereas dark regions are not in contact with the substrate.

The presence of a single row of pores internal results in a 76% increase of generated shear forces on glass compared to isotropic adhesives REF, because of mentioned mechanisms.

Patterning the terminal layer with pillars (PIL) or hooks (HKS) deteriorated shear performance compared to unpatterned adhesives (REF). With the 3D printing method we used, patterns were presumably not fine enough to introduce advantageous effects of contact splitting. The spacing and the millimeter-length scale of pillars or hooks rendered a dramatic decrease in formed contact area with the substrate compared to unpatterned adhesives. A lower contact area was formed with HKS adhesives than with PIL adhesives, leading to lower shear forces. In the presence of hooks, the contact area was too low for effects of internal geometry to manifest themselves. A lower normal stiffness, introduced by bendable pore walls or terminal layers, did not compensate for the lack of contact of the HKS surface.

On PDMS

On soft PDMS substrates, the deformability of the substrate affected the mechanism with which shear forces are generated. Video recordings of shear force measurements of UNP adhesives on three PDMS substrates showed that the softer the substrate is, the more contact is formed under the applied preload (**Figure 5.5 and Supporting Information of this chapter**).

We observed that, for adhesives with a UNP surface, the formation of contact was rather similar between the four internal geometries. However, the preservation of contact after reducing the load from 2.45 N to 0.49 N was considerably higher in the presence of pores. Similar to results on glass substrates, contact preservation was largest for the adhesives with the lowest normal stiffness (SR-X and SR-Y).

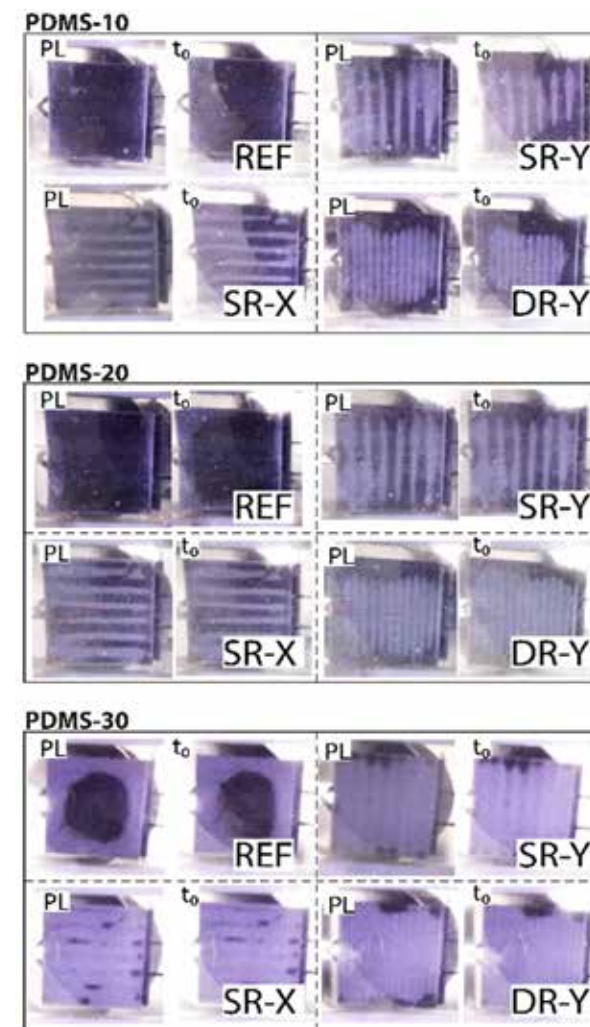


Figure 5.5. Contact area of adhesives with a surface UNP with various internal geometries under preload (PL) and the load applied during shearing (t_0). The light regions are those that are in contact with the substrate.

On PDMS-10, no effect of internal geometry was found on generated shear forces. On PDMS-20 and PDMS-30, high shear stiffness combined with low normal stiffness of adhesives led to an increase of shear forces of 49% on PDMS-20 and 63% on PDMS-30. The presence of a thin terminal layer (in SR-X and SR-Y) was increasingly beneficial for the generated shear forces on substrates with decreasing stiffness compared to a relatively thicker terminal layer (as present in DR-Y). A thin terminal layer has a higher compliance, and therefore more efficiently conforms to substrate deformations, resulting in better preservation of contact under loading compared to adhesives with a thicker terminal layer.

Similar to the results on glass, also on PDMS substrates, patterning the surface of adhesives with pillars (PIL) or hooks (HKS) resulted in systematically lower shear forces compared to unpatterned adhesives (UNP), likely due to reduced contact area when adhesives were patterned. As a result, effects of internal geometry were quenched when adhesives contained a patterned surface. Nevertheless, we did observe that surface patterns introduced a better distribution of contact over the adhesive-substrate interface compared to unpatterned adhesives, leading to lower stress concentrations (**Figure 5.6**). During sliding, the growth of defects was not continuously expanding as observed with flat adhesives, suggesting that there is less coupling between detachment of neighboring pillars or hooks. Additionally, pillars and hooks re-attached after detachment, resulting in a preservation of contact area during sliding. In the shear force measurements, these contact preservation properties were not able to compensate for the reduced total contact area with respect to unpatterned adhesives, resulting in lower shear forces. Finer surface structures (i.e., pillars or hooks with lower dimensions and spacing) might be needed to overcome the loss of contact area in patterned adhesives.

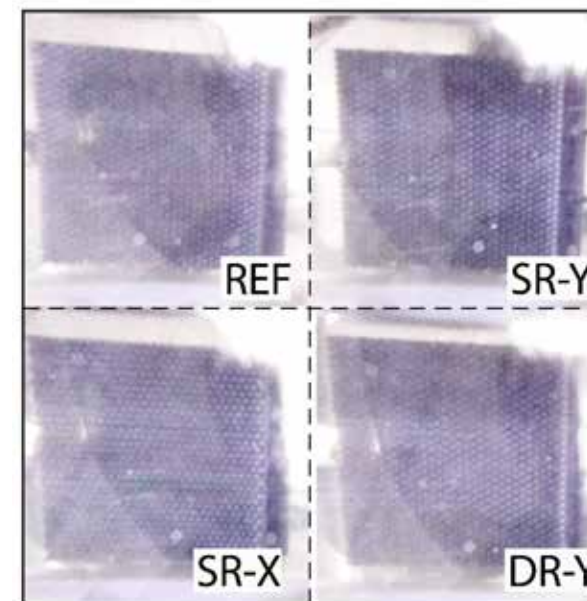


Figure 5.6. Effects of internal geometry of pillar adhesives on the formation of contact. Video images were recorded on PDMS20 substrates during sliding. Single-row pore geometries exhibited longitudinal close-contact regions aligned with the pore direction. A double row of pores resulted in a uniform distributed contact area in the center of the adhesive. Adhesives with intern geometry REF exhibited a large area of contact at the perimeter of the adhesive. The light regions are those that are in contact with the substrate.

Outlook

We showed that porous structures can be used to generate materials with direction-dependent stiffness. We varied pore size and pore wall thickness but one could also vary other parameters such as the shape of the pores and the overall porosity.^[32] With the structural variety that is offered by 3D printing, this approach could be extended to generate stiffness gradients in materials to improve the internal stress distribution when loads are applied. Furthermore, one could introduce unique stiffness profiles in additional directions of the adhesives, for example to realize high shear forces in the x-direction, but facilitate easy detachment in the y-direction, by lateral sliding.

The functionality of internal geometries of adhesives would benefit from

higher resolutions in order to fabricate smaller features and more homogeneous stiffness. Furthermore, spatially controlling direction-dependence stiff or soft regions could be improved with smaller features such as pores and pore walls, eliminating the occurrence of local stress concentrations under loading. Smaller features will also result in thinner pore walls, making the adhesives more susceptible to fatigue after multiple times of bending and elastic recovering of the geometry. Alternative 3D printing methods deserve to be explored to obtain higher resolutions, taking into account the balance between feature size and adhesive dimensions on one side, and processing time and structural strength on the other side.^[44]

Potentially, surface patterns could be optimized for attachment to rough substrates, for example, by introducing patterns that promote interlocking,^[45,46] or for attachment to wet or flooded substrates, by introducing water-draining surface patterns.^[47] Immersion brings additional viscous dissipation and associated timescales into the mechanics of these substrates which allows for further optimization of adhesion performance.

5.5 Conclusion

We showed that geometry-controlled variation of normal and shear stiffness of adhesives can be used to generate reversible grip on soft, deformable substrates, as well as on rigid glass substrates. We fabricated single-material adhesives with anisotropic properties using a stereolithographic approach. We were able to fabricate adhesives with larger deformability than expected based on the reported resin stiffness. On a rigid substrate, adhesives with the lowest normal stiffness performed best. On soft substrates, a low normal and a high shear stiffness were found to be advantageous for contact formation and preservation, respectively. In other words, decoupling of normal and shear deformations can be beneficial for contact preservation. Such anisotropy requires adhesives with rather complex adhesive architectures, which can be realized using 3D printing methods.

5.6 Experimental Section

Fabrication of Adhesives: Adhesives were fabricated using a Form2 printer (Formlabs inc., Somerville, MA, USA) with the suppliers recommended print settings and a layer thickness of 0.05 mm. Formlabs resin Flexible FLFL-GR02 (Formlabs inc., Somerville, MA, USA) was used to fabricate 20 × 20

mm² samples with a porous inner structure, a 0.5 mm high surface pattern and 0.4 mm solid back layer. Four types of internal geometries were printed (Table 1): The first geometry consisted of a row of 6 cylindrical pores, resulting in a pore diameter of 2.7 mm, positioned orthogonally to the pulling direction. The second geometry consisted of the same 2.7-mm diameter cylindrical pores, but now positioned parallel with the pulling direction. In the third geometry, two rows of 12 cylindrical pores, resulting in 1.275-mm diameter pores, positioned parallel to the pulling direction were fabricated. A fourth geometry was a reference sample, without any porosity. Each of these four internal geometries were fabricated either without surface pattern, with a pattern of 0.5 mm diameter circular pillars, or conical, 45° tilted pillars with a diameter of 0.5 mm at the base and 0.2 mm at the top, resulting in a total of 12 geometries. Each of these 12 adhesive types were printed twice, resulting in a total of 24 adhesives.

The printed samples were cleaned with compressed air (EW5601, Ewent, Geleen, Netherlands) and isopropyl alcohol (IPA, VWR Chemicals, Radnor, PA, USA) to remove uncured resin, and post-cured for 60 minutes at a temperature of 60 °C in a Form Cure oven (Formlabs Inc., Somerville, MA, USA). After post-curing, the support structures were removed and the samples were kept at room temperature for 24 hours to allow the IPA to fully evaporate.

Mechanical characterization of adhesives: Adhesives were characterized with indentation tests, performed with an Aerotech ACT115 linear motion stage, controlled with an Aerotech Soloist CP controller and a custom-built GUI in MATLAB R2016a. A FUTEK S-Beam load cell with a 10 lb capacity was mounted on the motion stage to record the forces. The load cell signal was amplified with a CPJ2S signal conditioner. The adhesives were indented using a glass lens indenter (radius of curvature = 34.5 mm, Thorlabs Inc. Newton, NJ, USA) over depth of 1.5 mm (0.5 mm for the isotropic adhesive), and forces and displacements were recorded at a frequency of 200 Hz.

FEA of adhesives: A nonlinear static analysis was performed with Inventor Nastran2020 software (Autodesk Inc., San Rafael, CA, USA). The material model was built using the resin's mechanical properties as provided by Formlabs. The elastic modulus was derived from the shore hardness using the relations from Mix and Giacomini.^[31] A mesh was generated using the

default linear elements, with an element size of 0.15 mm. The bottom of the adhesive was fixed, and a sliding constraint was applied to the central axis of the eye (where in shear force measurements, the pulling cable is connected), to ensure a pure horizontal deformation under the applied load. A bearing-load with a magnitude of 6 N was applied at the inside of the eye in the direction of pulling.

Substrate preparation: Poly-dimethoxysiloxane (PDMS, Sylgard 184, Dow Corning, Midland, MI, USA) substrates were prepared by mixing pre-polymer and curing agent mixed in 10:1, 20:1, and 30:1 weight-based ratios, obtaining substrates of 2200 kPa, 700 kPa, and 300 kPa, respectively.^[15, 23] The pre-polymer - curing agent mixtures were degassed, in measured quantities poured in 140 mm petri dishes, degassed again, and finally cured for at least 2h at 70°C to obtain substrates of 2 mm in thickness.

A glass slide was used as glass substrate.

Shear force measurements: Shear force measurements were performed using a custom-made positioning stage (ACT115, Aerotech inc, Pittsburg, PA, USA) with a 9 N load cell (LSB200, FUTEK, Irvine, CA, USA), controlled with a GUI build in MATLAB R2016a. The signal from the load cell was amplified and converted with a CPJ2S signal conditioner. Samples were connected to the load cell via a HPPE Dyneema braided wire (BBVFS25, Berkeley, Columbia, SC, USA). Before testing, samples were aligned by attaching an alignment weight to the rear end of the adhesive (see Figure I5.1 in the supporting information).

A 2.45 N (250 gr) normal pre-load was applied for 10 seconds, and a 0.49 N (50 gr) normal load during measuring, applied from 3 seconds before sliding. The sliding velocity was 1 mm s⁻¹, for a duration of 5 seconds. From the recorded force-displacement data, the peak force corresponding to the moment where the sample started sliding was extracted.

Samples were recorded in a bottom-view configuration with a webcam to monitor contact formation during preloading, and before and during sliding.

For each substrate, each adhesive sample were each measured 5 times, resulting in 10 measurements per condition.

Substrates were cleaned with ethanol every 10 measurements. PDMS substrates were replaced every 20 measurements.

Acknowledgements

This research is supported by the Netherlands Organization for Scientific Research (NWO) Domain Applied and Engineering Sciences (TTW), (Open Technology Program, project 13353 "Secure and gentle grip of delicate biological tissues"). PvA and FH contributed equally to this work. We kindly acknowledge Marta Scali and Paul Breedveld for their help in photographing the fabricated adhesives.

References

- [1] Z. Wang, Z. Wang, Z. Dai, S. Gorb, *Appl. Sci.* **2018**, *8*(1), 114.
- [2] S. Nansai, R. Mohan, *Robotics* **2016**, *5*(3), 14.
- [3] S. Song, C. Majidi, M. Sitti, in *IEEE Int. Conf. Intell. Robot. Syst.*, **2014**.
- [4] S. Baik, H. J. Lee, D. W. Kim, J. W. Kim, Y. Lee, C. Pang, *Adv. Mater.* **2019**, *31*, 1803309.
- [5] N. J. Glassmaker, A. Jagota, C. Y. Hui, J. Kim, *J. R. Soc. Interface* **2004**, *1*, 23.
- [6] C.-Y. Hui, N. J. Glassmaker, T. Tang, A. Jagota, *J. R. Soc. Interface* **2004**, *1*, 35.
- [7] M. D. Bartlett, A. B. Croll, D. R. King, B. M. Paret, D. J. Irschick, A. J. Crosby, *Adv. Mater.* **2012**, *24*, 1078.
- [8] V. A. Gorodtsov, D. S. Lisovenko, *Mech. Mater.* **2019**, *134*, 1.
- [9] R. F. S. Hearmon, *Rev. Mod. Phys.* **1946**, *18*, 409.
- [10] V. Tinnemann, E. Arzt, R. Hensel, *J. Mech. Phys. Solids* **2019**, *123*, 20-27
- [11] L. Heepe, S. N. Gorb, *Annu. Rev. Mater. Res.* **2014**, *44*, 173.
- [12] A. Del Campo, C. Greiner, E. Arzt, *Langmuir* **2007**, *23*, 10235.
- [13] L. F. Boesel, C. Cremer, E. Arzt, A. Del Campo, *Adv. Mater.* **2010**, *22*(19), 2125-2137
- [14] R. Hensel, K. Moh, E. Arzt, *Adv. Funct. Mater.* **2018**, *28*, 1800865.
- [15] E. P. Chan, E. J. Smith, R. C. Hayward, A. J. Crosby, *Adv. Mater.* **2008**, *20*, 711.
- [16] C. H. Lin, C. Y. Huang, J. Y. Ho, H. Y. Hsueh, *ACS Appl. Mater. Interfaces* **2020**, *12*, 22365.
- [17] P. C. Lin, S. Vajpayee, A. Jagota, C. Y. Hui, S. Yang, *Soft Matter* **2008**, *4*, 1830.
- [18] M. Kamperman, E. Kroner, A. del Campo, R. M. McMeeking, E. Arzt, *Adv. Eng. Mater.* **2010**, *12*, 335.
- [19] R. M. McMeeking, E. Arzt, A. G. Evans, *J. Adhes.* **2008**, *84*(7), 675-681.
- [20] A. N. Gent, *Rubber Chem. Technol.* **1974**, *47*(1), 202-212.
- [21] J. Y. Chung, M. K. Chaudhury, *J. Adhes.* **2005**, *81*(10-11), 1119-1145.
- [22] L. Heepe, L. Xue, S. N. Gorb, *Bio-Inspired Structured Adhesives: Biological Prototypes, Fabrication, Tribological Properties, Contact Mechanics, and Novel Concepts*, Springer, **2017**.
- [23] E. Cheung, M. Sitti, *Langmuir* **2009**, *25*, 6613.
- [24] L. Xue, B. Sanz, A. Luo, K. T. Turner, X. Wang, D. Tan, R. Zhang, H. Du, M. Steinhart, C. Mijangos, M. Guttman, M. Kappl, A. Del Campo, *ACS Nano* **2017**, *11*, 9711.
- [25] Y. Tian, Z. Zhao, G. Zaghi, Y. Kim, D. Zhang, R. Maboudian, *ACS Appl. Mater. Interfaces* **2015**, *7*, 13232.
- [26] H. T. Tramsen, A. E. Filippov, S. N. Gorb, L. Heepe, *Adv. Mater. Interfaces* **2020**, *7*, 1901930.
- [27] Z. He, C. Y. Hui, B. Levrard, Y. Bai, A. Jagota, *Sci. Rep.* **2016**, *6*, 26867.
- [28] M. Varenberg, B. Murarash, Y. Kligerman, S. N. Gorb, *Appl. Phys. A Mater. Sci. Process.* **2011**, *103*, 933.
- [29] K. Kendall, *J. Phys. D. Appl. Phys.* **1975**, *8*, 1449.
- [30] P. van Assenbergh, M. Fokker, J. Langowski, J. van Esch, M. Kamperman, D. Dodou, *Beilstein J. Nanotechnol.* **2019**, *10*, 79.
- [31] G. Alaimo, S. Marconi, L. Costato, F. Auricchio, *Compos. Part B Eng.* **2017**, *113*, 371.
- [32] J. Ying, L. Lu, L. Tian, X. Yan, B. Chen, *Comput. Graph.* **2018**, *70*, 157.
- [33] J. Kiendl, C. Gao, *Compos. Part B Eng.* **2020**, *180*, 107562.
- [34] T. Liu, L. Liu, C. Zeng, Y. Liu, J. Leng, *Compos. Sci. Technol.* **2020**, *186*, 107935.
- [35] D. J. Yoo, *Biomaterials* **2011**, *32*, 7741.
- [36] F. C. Fierz, F. Beckmann, M. Huser, S. H. Irsen, B. Leukers, F. Witte, Ö. Degistirici, A. Andronache, M. Thie, B. Müller, *Biomaterials* **2008**, *29*, 3799.
- [37] D. W. Huttmacher, *Biomaterials* **2000**, *21*, 2529.
- [38] E. B. Duoss, T. H. Weisgraber, K. Hearon, C. Zhu, W. Small IV, T. R. Metz, J. J. Vericella, H. D. Barth, J. D. Kuntz, R. S. Maxwell, C. M. Spadaccini, T. S. Wilson, *Adv. Funct. Mater.* **2014**, *24*, 4905.
- [39] J. Tamelier, S. Chary, K. L. Turner, *Langmuir* **2012**, *28*, 8746.
- [40] M. P. Murphy, B. Aksak, M. Sitti, *Small* **2009**, *5*, 170.
- [41] K. Jin, J. C. Cremaldi, J. S. Erickson, Y. Tian, J. N. Israelachvili, N. S. Pesika, *Adv. Funct. Mater.* **2014**, *24*, 574.
- [42] M. R. Cutkosky, *Interface Focus* **2015**, *5*, 20150015.
- [43] M. K. Kwak, H. E. Jeong, W. G. Bae, H. S. Jung, K. Y. Suh, *Small* **2011**, *7*, 2296.
- [44] P. van Assenbergh, E. Meinders, J. Geraedts, D. Dodou, *Small* **2018**, *14*, 1703401.
- [45] T. H. Büscher, S. N. Gorb, *J. Exp. Biol.* **2019**, *222*, jeb209833.
- [46] S. N. Gorb, *Philos. Trans. R. Soc. A Math. Phys. Eng. Sci.* **2008**, *366*, 1557.
- [47] A. Tsipenyuk, M. Varenberg, *J. R. Soc. Interface* **2014**, *11*, 20140113.

Chapter 6

IMPLEMENTATION OF ANISOTROPIC SOFT PADS IN A SURGICAL GRIPPER FOR SECURE AND GENTLE GRIP ON VULNERABLE TISSUES

This chapter has been published as:

Peter van Assenbergh*, Costanza Culmone*, Paul Breedveld & Dimitra Dodou. *Proceedings of the Institution of Mechanical Engineers, Part H: Journal of Engineering in Medicine*, **2020**, 0954411920971400. doi: 10.1177/0954411920971400

*Both authors contributed equally to this chapter.

Abstract

Current surgical grippers rely on friction grip, where normal loads (i.e., pinch forces) are translated into friction forces. Operating errors with surgical grippers are often force-related, including tissue slipping out of the gripper because of too low pinch forces and tissue damaging due to too high pinch forces. Here, we prototyped a modular surgical gripper with elastomeric soft pads reinforced in the shear direction with a carbon-fiber fabric. The elastomeric component provides low normal stiffness to maximize contact formation without the need of applying high normal loads (i.e., pinch forces), whereas the carbon-fiber fabric offers high shear stiffness to preserve the formed contact under the lateral loads (i.e., shear forces) that occur during tissue lifting. Additionally, we patterned the pads with a sub-surface micropattern, to further reduce the normal stiffness and increase shear stiffness. The body of the prototype gripper, including shaft, joints, and gripper tips, was fabricated in a single step using 3D printing, followed by manual attachment of the soft pads to the gripper. The gripping performance of the newly developed soft gripper on soft tissues was experimentally compared to reference grippers equipped with metal patterned pads. The soft-pad gripper generated similar gripping forces but significantly lower pinch forces than metal-pad grippers. We conclude that grippers with anisotropic-stiffness pads are promising for secure and gentle tissue grip.



6.1 Introduction

Secure and gentle soft-tissue grip is imperative in the medical domain. In almost any surgical procedure, from laparoscopy to microsurgery, soft tissues are grasped and pulled for creating space, exposing areas to be treated, or getting access to obstructed contiguous anatomical structures. The vast majority of surgical grippers used in the medical domain are equipped with patterned surfaces made of stainless steel.^[1] Such grippers employ friction grip, which relies on the translation of normal load (i.e., pinch forces) to friction forces, for grasping and pulling soft tissues.

Previous studies have shown that the majority of grasping errors with surgical grippers is force-related, with pinch forces being either too low, resulting in slipping of the tissue out of the gripper,^[2,3] or too high, resulting in possible tissue damage.^[4,5] Tissue stresses up to 800 kPa have been measured with laparoscopic grippers,^[6] which is considerably higher than the safety threshold of 200 kPa estimated for apoptosis.^[7]

Studies have shown that high pinch forces can be reduced by replacing the metal forceps of the gripper with soft pads.^[8,9] The grip of such pads on tissue is achieved thanks to their deformability in the normal direction, which enables a large contact area with the tissue. At the same time, the contact formed between the tissue and the pad is homogeneously distributed over the pad surface, eliminating the occurrence of local high peak forces on the tissue.^[8,9] A general disadvantage of a soft pad is that deformations of the pad occur not only in the normal but also in the shear direction, which might lead to tissue slipping out of the gripper during pulling. An ideal soft gripping pad would thus need to be anisotropic, fulfilling two contradictory properties: being deformable in the normal (pinching) direction, so that a large contact is formed, and stiff in the lateral (shear) direction, so that the formed contact is preserved when the tissue is being pulled.

Bartlett et al.^[10] developed such anisotropic pads for strong grip on rigid substrates. The pads consisted of a carbon-fiber fabric (CFF), part of which was embedded into an elastomeric material (poly-dimethylsiloxane, PDMS); the unembedded CFF part was served as tail via which the pad was pulled along the substrate. PDMS provided deformability in the normal direction, thereby allowing for the formation of a large contact, whereas CFF provided stiffness in the shear direction, thus allowing for the preservation

of the formed contact when pulling the pad from the CFF tail along the substrate. These authors found that, on rigid glass substrates, 100 cm² elastomeric pads without CFF had a force capacity (i.e., the maximum sustainable force) of about 10 N, whereas the addition of CFF led to a force capacity in the order of 1000 N.^[10]

Implementation of anisotropic CFF-PDMS pads in surgical grippers is a promising approach for generating secure, yet gentle, grip on biological tissue. The idea herein is to align the CFF with the shear (pulling) direction and guide the loading forces via the CFF tail into the shaft of the instrument in such a way that the elastomeric part of the soft pad is protected from undesirable shear deformations and contact loss (Figure 1).

The grip of fiber-reinforced soft pads can be further increased by patterning the otherwise plain surface of the elastomer (**Figure 6.1**). In previous work, we showed that, on soft substrates, the presence of microscale spherical voids in an elastomer, topped with a thin terminal layer, led to higher grip than an unpatterned elastomer.^[11] Thanks to its microscale thickness, the terminal layer conforms to microscale irregularities of the substrate's surface, resulting in a higher contact area compared to an unpatterned elastomer, and therefore higher shear forces. At the same time, due to bending and internal sliding of the walls that separate the internal spherical voids under shear loading, the surface structure of the elastomer stiffens in the shear direction, thereby contributing to the preservation of the formed contact during shearing.^[11,12]

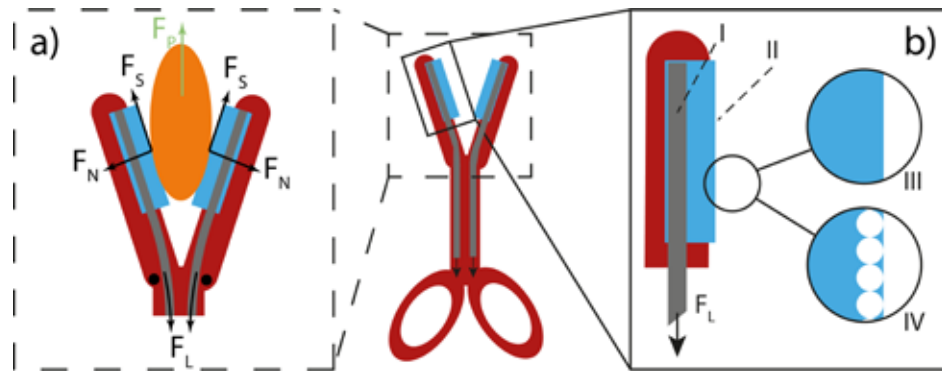


Figure 6.1. A schematic overview of a gripper pad with anisotropic properties. A) Schematic force diagram. Hinges are depicted as black dots. The gripper was closed by loading the CFF using a constant tensile load (F_t). By closing the gripper, the pinch force (F_N) acts on the tissue in the normal direction. When the tissue sample was pulled upwards using a positioning stage (F_t), a shear force (F_s) was generated at the soft pad-tissue interface. Gravitational force on the tissue is omitted from the diagram because the load cell to which the tissue was connected via a holder (not visualized here) was zeroed after the tissue was hanged to the holder. B) A stiff carbon-fiber fabric (CFF) (I) is partially embedded into a soft elastomeric material (PDMS) (II). The CFF is aligned with the shear (pulling) direction. The loading forces are guided via the unembedded CFF tail into the shaft of the instrument. The pad is fabricated either without a surface pattern (III) or with a pattern of microscale sub-surface spherical voids (IV). Under shear loading, the internal walls that separate neighboring voids collapse, resulting in lateral stiffening of the adhesive surface.

In this paper, we present the implementation of fiber-reinforced elastomeric soft pads in a modular surgical gripper instrument. We developed two types of fiber-reinforced soft pads, one with an unpatterned surface, and another with sub-surface microscale voids. Additionally, we fabricated a reference gripper by replacing the pads with stainless steel grooved plates. The performance of the three grippers on soft tissue was assessed by measuring their gripping and pinch forces applied to the tissue.

6.2 Design

Soft pads

Unpatterned soft pads were fabricated with a thickness of 0.8 mm, width of 8 mm, and length of 15 mm. A piece of polystyrene plastic foil (50 ×

50 mm²), acting as an anti-stick layer, was placed on an aluminum base plate (**Figure 6.2**, a). This anti-stick layer was covered by a 200 × 50 mm² piece of CFF (Figure 2b; 3K-200 Tex HS fibers, 200 gr/m², plain woven, purchased from www.carbonwinkel.nl, De Moer, the Netherlands), which was fixed at the short side of the baseplate using scotch tape. An 8 × 15 mm² rectangular hole was milled from an aluminum plate of 0.8 mm thickness to create a template frame (Figure 2d). Sylgard-184 (poly-dimethyl-siloxane, PDMS, purchased from Dow Corning, MI) pre-polymer (base) and crosslinker (curing agent) were mixed in a 10:1 weight-based mixing ratio and degassed in a desiccator. The template frame was placed on top of the aluminum base plate covered with CFF and filled with the pre-polymer/crosslinking mixture. The filled template frame was degassed once more to evacuate air from the CFF, allowing the pre-polymer/crosslinking mixture to fully immerse the CFF. After degassing, the filled template was cured at 70 °C for at least 2 hours, while topped with a plain glass slide to obtain a flat finish (Figure 2e). After curing, the soft pad was carefully detached from the frame, anti-stick layer, and topping glass slide. The non-immersed CFF was cut to obtain two lateral flaps and a loading tail (Figure 2).

To fabricate patterned elastomeric pads, the aforementioned plain glass slide used to top the filled template after degassing was replaced by a coated glass slide to obtain a patterned finish of the soft pad. Thereto, a plain glass slide was coated with a colloidal monolayer, prepared using a dip-coating methodology, as described in earlier work.^[11] In brief, styrene divinylbenzene beads (purchased from ThermoFisher Scientific, MA, USA) with a reported diameter of 10 μm and delivered as a 4% (w/v) dispersion in water, were re-dispersed in ethanol at 8 % (w/v) before use. The particles were transferred to the surface of a water bath, and compressed to obtain a closely packed floating monolayer of particles. In a dip-coating procedure, the monolayer was transferred to glass slides of 52 × 76 mm². An initial dipping depth of at least 40 mm was used, resulting in monolayers with at least a 52 × 40 mm² area. After curing of the soft PDMS pads, while topped with a coated glass slide, the microparticles were embedded in the pad surface. Removing the microparticles was done by dissolving them in *n*-methyl-pyrrolidone (NMP, Merck, Darmstadt, Germany). Thereto, the pads were placed horizontally, with the pattern facing up, and a droplet of NMP, large enough to fully cover the pad surface, was deposited for a duration of 10 minutes, before it was rinsed off with ethanol. This washing step was repeated two more times. Pads for reference grippers were milled

from stainless-steel with a triangular saw-tooth profile with 0.35 mm tooth height. The height of this surface pattern was chosen based on previous studies, which tested laparoscopic grippers with pattern depths varying between 0.3 and 1 mm^[13-15] and showed that a profile of 0.3 mm generated lower peak forces and thus less damage to the tissue.^[14]

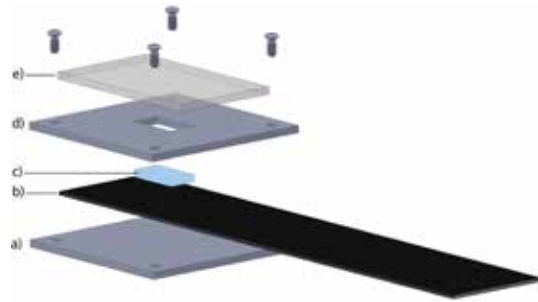


Figure 6.2. Exploded view of soft pad fabrication. An aluminum baseplate, topped with an anti-stick polystyrene foil (a) was covered with a sheet of CFF (b). A template frame in the size and thickness of the envisioned soft pad (d) was placed on the CFF and filled with uncured PDMS (c). The filled frame was covered with a plain or coated glass slide (e) to obtain unpatterned or patterned pads after curing.

3D printed gripper

Figure 6.3 shows a schematic illustration of the 3D printed gripper, consisting of a shaft, joints, and jaws. Each gripper was 3D printed as a single element, and soft pads or reference pads were implemented in a subsequent manufacturing step. The grippers were printed using a Perfactory® 4 Mini XL printer (EnvisionTEC® GmbH, Gladbeck, Germany) with a layer height in the vertical z-axis of 25 µm. The selected printer is based on vat photopolymerization technology and uses Digital Light Processing (DLP), in which the build plate moves vertically up and down into a vat of liquid polymer. When the build plate moves down, the liquid polymer is exposed to light, and, depending on the image displayed by a projector, a layer of polymer hardens. The process is repeated layer-by-layer until the object is fully printed. The grippers were printed using R5 epoxy photopolymer resin (EnvisionTEC® GmbH, Gladbeck, Germany), an acrylic resin especially developed for prototyping. The 3D printed grippers were printed in eight hours, with a vertical orientation (i.e., the shaft in a vertical position, and the jaws pointing down).



Figure 6.3. Schematic illustration of the gripper design for soft pads, and the positioning of the pads into the gripper. The shaft (a) contained a rectangular lumen, guiding the CFF to the joints. The flexural joints (b) were by default open and straightened by pulling the CFF, resulting in closing of the gripper. Each jaw contained two lateral grooves (c) for fixation of the soft pads. The lateral CFF flaps of the soft pads were folded and glued into these grooves. Underneath the soft pads' center was an open space between jaw and soft pad (d), providing some mobility in the normal direction of the soft pad. The 3D printed gripper for metal pads differed from the grippers for soft pads, in that jaws had a flat surface upon which the metal pads were glued.

The gripper shaft contained a central rectangular lumen to guide the CFF tail (Figure 6.3a). The flexural joints were based on a leaf-spring principle and printed in opened condition. The CFF tails were used to actuate the gripper; pulling them resulted in the straightening of both joints via elastic deformation, and closing of the jaws. For the fixation of the soft pads (unpatterned and patterned) to the 3D printed structure, two grooves were added on the long sides of each jaw (Figure 6.3c). The two lateral flaps of the CFFs were folded into the grooves and fixated by gluing with cyanoacrylate. The distal end was left free, and at the joint side of the pad, the CFF tail was guided into the shaft via the joint. Some open space was left between the soft pads and the jaw (Figure 6.3d) to allow for some mobility of the fibers to self-align with the shear direction.

Figure 4 shows the three printed grippers, with implemented reference. The 3D printed reference gripper had jaws with a flat surface upon which the metal pads were glued (Figure 6.4a). In order to close the reference gripper, two stripes of CFF fibers were glued at the tip of each jaw and guided into dedicated grooves positioned underneath the flat jaw surface. In soft pads, either unpatterned (Figure 6.4b) or patterned (Figure 4c, the CFF fib-

ers are embedded in the soft pads, and loaded to close the gripper. All jaws used in this work were 36 mm long, with an outer diameter of 10 mm and an opening up to 90 degrees.



Figure 6.4. The three fabricated grippers. The reference gripper (a) was equipped with a grooved stainless-steel plate. In unpatterned pads (b), the elastomeric pads appear transparent, whereas in patterned pads (c), a white haze can be seen at the pad surface. In soft pads, either patterned or unpatterned, the CFF was embedded in the elastomeric pad.

6.3 Experimental methods

Pinch force measurements

To determine the pinch forces generated on the tissue, a pressure-sensitive foil was used (5LW-2M Fujifilm Prescale, purchased from ALTHEN BV Sensors & Controls, Leidschendam, the Netherlands). This foil, consisting of a donor and acceptor sheet, colors at locations where the normal pressure exceeds 0.006 MPa. A PDMS sheet with a thickness of 5 mm was used as a representable tissue phantom in pinch force experiments. The phantom was covered on both sides with sheets of pressure-sensitive foil and placed in between the pads of an opened gripper. The gripper was closed by loading the CFF tails in the tensile direction for 5 seconds with a weight of 1.5 kg, resulting in a tensile load of 14.7 N. Coloring of the pressure foil outside of the gripper area due to deformations of the tissue phantom during grasping is included in our analysis, because these deformations are expected to be present when grasping real tissues. The obtained imprint on the pressure foil was digitalized using a scanner (Canon CanoscanLiDE 110). The digital images were analyzed using Matlab R2018b. The image was converted into black-and-white using the function *im2bw* in Matlab with a threshold of 0.8. In generated black-and-white images, colored pixels appear black, and

uncolored pixels appear white. The number of black and white pixels was counted. The gripper pad was divided into nine equally-sized segments, numbered from 1 to 9. Segments 1-3, 4-6, and 7-9 were located at the distal, middle, and proximal end (i.e., closest to the joint) of the pad, respectively.

The fraction of black pixels per segment was reported as a qualitative image of the applied pressure of different gripper pads. Per gripper type (reference, patterned, unpatterned), six imprints of pressure foil were collected, and per segment, the fraction of black pixels was averaged over these six imprints.

Gripping force measurements

Tissue substrates were prepared by cutting 50 × 50 mm² pieces from the thin end of chicken breast meat. The substrate thickness was in the order of 5 mm. Tissue substrates were preserved at -20 °C and on the day of measuring kept below 0 °C until measuring. A frozen tissue substrate was clamped in a custom-made tissue holder. The tissue holder was connected to a load cell (Futek S-Beam FLLSB 200, controlled by a custom-made LabView script), which was mounted on a positioning stage (Thorlabs PT1/M-Z8, with additional KDC101 controllers, controlled by Thorlabs Kinesis software), allowing vertical displacement of the tissue when connected to the load cell. Before measuring, the load cell was zeroed to correct for the gravitational force acting on the hanging tissue substrate. Forces were recorded at a sampling frequency of 20 Hz. The process from taking the substrate out of its cooled environment until the start of measuring took about 3-4 minutes, which was sufficient for the tissue to thaw.

The gripper was vertically placed in a holder, with the gripping jaws facing up and the shaft pointing down. The CFF tails came out of the shaft, hanging down, and were clamped together. After hanging the tissue in between the two opened gripping jaws, the gripper was closed by loading the two CFF tails using a tensile load of 14.7 N. Upon closing the gripper, we waited 5 seconds, and then the tissue, mounted on the load cell, was moved up with a speed of 1 mm/s, over a travel distance of at least 15 mm. The gripper was opened by removing the weight directly after the positioning stage came to a stop. A force-time plot was recorded from just before closing the gripper until the gripper was opened again.

A surgical gripper with soft pads

Gripping forces of all three grippers (reference, unpatterned, patterned) were each tested on three pieces of tissue, with three subsequent repetitions on each tissue piece. The peak forces obtained in the three subsequent measurements on the same tissue piece were averaged. The three obtained averages were merged into one set of three independent measurements per gripper type. Independent *t*-tests were conducted to compare the performance of the three gripper types.

6.4 Results

Pinch force measurements

Figure 6.5 shows a scan of a pressure foil after imprinting with a patterned gripper, its transfer to a black-and-white image, the segmentation of the gripper pad, and the fraction of colored pixels for each of 9 segments. It can be seen that for this particular imprint, most colored pixels can be found in segments 7, 8 and 9, indicating that pinch forces were highest at the proximal end of the gripper pad.

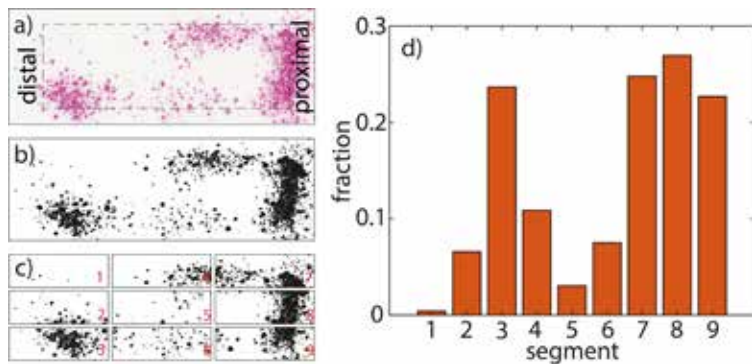


Figure 6.5. Overview of the analysis of imprinted pressure foils. (a) A scan of a pressure foil used with the patterned gripper. The dashed square indicates the outline of the gripper pad. (b) A black-and-white image of the imprint. (c) Segmentation of the imprint of the gripper pad. Segments 7-9 are at the proximal end of the pad. (d) Fraction of black pixels per segment for this particular imprint.

Results

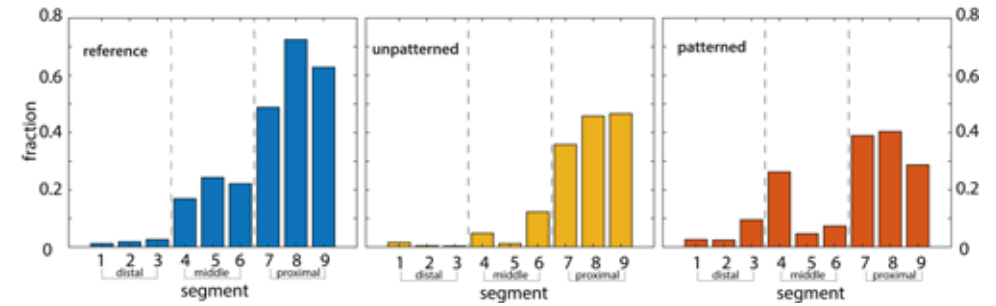


Figure 6.6. Average distribution of pinch forces for three different gripper types. Plots are the mean fraction of black pixels per segment for six imprinted pressure foils per gripper type.

Figure 6 shows the fraction of black pixels per segment for each gripper type (reference, patterned, unpatterned) averaged over the six pressure measurements that were conducted per gripper type. For all three gripper types, we found that the highest pinch forces were present at the proximal size of the pads, that is, closest to the joint (segments 7-9). Pinch forces were lowest at the distal end of the pad. Within each region (distal, middle, or proximal), we did not observe large differences in the generated stresses between the three lateral segments. Pinch forces were found to be higher for the reference gripper compared to the soft gripper pads for the proximal and middle regions.

The fraction of colored pixels throughout the full soft pad, that is, segments 1-9 summed up, was on average 0.28 (standard deviation $SD = 0.06$) for the metal reference gripper, and 0.17 ($SD = 0.03$) and 0.18 ($SD = 0.06$) for the unpatterned and patterned soft grippers, respectively. These values are the means of six pressure measurements per gripper type. *t*-tests showed that significantly higher pinch forces were generated with the reference gripper compared to the unpatterned gripper ($t(10) = -4.13$; $p = 0.002$) and the patterned gripper ($t(10) = -3.01$; $p = 0.013$). There was no significant difference in the generated pinch force between patterned and unpatterned soft pads ($t(10) = 0.35$, $p = 0.735$).

Gripping force measurements

Figure 6.7a shows a representative force-time plot of the gripping force measurements. Five stages can be distinguished. At Stage I, the gripper closed and made contact with the tissue phantom. During Stages II-IV, the tissue was moving upward. Initially, this resulted in a steep increase in forc-

es (Stage II). At Stage III, the tissue phantom started slipping. At Stage IV, this slipping reached a constant rate. At Stage V, the upward movement of the tissue phantom stopped, and the gripper opened.

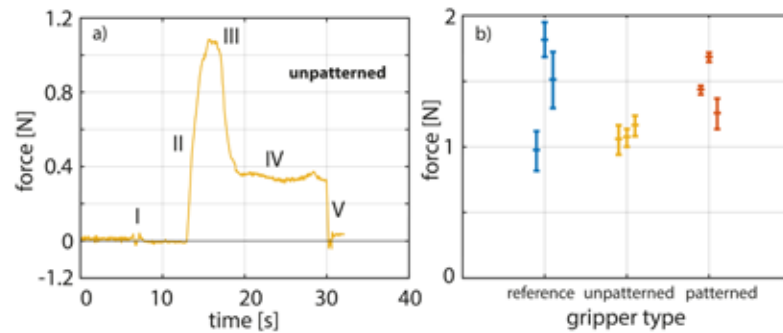


Figure 6.7. Results of shear force measurements. (a) A representative force-time plot of shear force measurements from an unpatterned gripper. First, the gripper closed (I). After around 5 seconds, the phantom was pulled upward with 1 mm/s (II-IV). The peak shear force was reached just before the phantom started sliding out of the gripper (III). The tissue was then gradually sliding out of the gripper (IV). At V, the tissue phantom stopped moving, and the gripper was opened. (b) Generated forces for each gripper type.

Significantly higher gripping forces were generated with the patterned gripper than with the unpatterned gripper ($t(4) = 2.80$, $p < 0.049$ (Figure 6.7b). The reference gripper generated gripping forces that were not significantly different from the two soft grippers.

6

6.5 Discussion

We showed that surgical grippers equipped with anisotropic pads, being soft in the normal direction and stiff in the lateral loading direction, generate comparable gripping forces but lower pinch forces than a gripper with metal pads. The gripping forces generated by the grippers were between 1 and 2 N. These forces are suitable for manipulating delicate tissues such as veins or liver tissue.^[16-18] For instance, Jia et al. generated pinch forces of 1 and 2 N and reported a pinch force threshold of 3.5 N to prevent tissue damage.^[18]

The gripper was printed in vertical orientation to fit a high number of grippers in the build platform. As a result, the applied load was orthogonal to

the plane of binding between printed layers. From a structural strength perspective, printing the grippers in a horizontal orientation would result in applied load parallel to the plane of the printed layers and therefore higher structural strength. If future designs of this gripper are meant for lifting heavier objects, changing the printing orientation of the gripper is advised to obtain stronger joints. The design of the joints is also vulnerable to torsion. We carried out preliminary tests on the mechanical properties of the gripper and found that the torsional stiffness can be increased by adding flaps laterally to the joint, as suggested by Grames et al.^[19] In the current design iteration, we decided to keep the design simple by not introducing additional elements, but in future work, it is advised to take torsion considerations into account in the gripper design.

In our measurements, the tissue substrate was used with a frozen core to prevent elastic stretching. In surgical procedures, the higher temperature of the tissue compared to the temperature in our grasping experiments will presumably result in a higher deformation of the tissue. It has to be investigated how such tissue deformation affects the gripping strength. Deformation of the soft gripper pads, on the other hand, is not expected to significantly change with expected temperature fluctuations. Moreover, oscillatory shear tests showed that PDMS with a 10:1 weight-based mixing ratio of base and curing agent exhibited linear elastic behavior up to oscillation frequencies of 10^2 rad/s, indicating elastic recovery times in the order of 10^{-2} seconds.^[20] These elastic recovery times are well below the time in between subsequent gripping actions, as reported for, for example, cholecystectomies, where Heijnsdijk et al. found a mean gripping frequency of 1.9 per minute.^[21]

Gripping forces were generated using a tensile load of 14.7 N on the CFF tails in the shaft to close the gripper. The height of this load was determined in a pilot experiment, where we found that with loads of 9.8 N or higher, significant grip on grasped tissue substrates was generated. These tensile loads are well in the range of applied handle forces in conventional surgical grippers,^[17,22,23] although the transfer of forces exerted by a gripper handle to actual pinch forces strongly depends on the closing mechanism of the gripper. We found that applied tensile loads resulted in relatively low stresses on the tissue, due to the used force transfer mechanism, and efficient distribution of pinch forces with soft pads. Due to the use of additive manufacturing, higher pinch forces can be obtained by 3D printing a gripper design in which the same

6

actuation force of 14.7 N results in higher pinch forces at the gripper jaws. 3D printing is a facile method as the instrument can be printed as one piece, and no further assembly of the platform instrument is required. Equipping of the instrument with soft pads can be done in one simple post-manufacturing step. This manufacturing approach allows for variations of the gripper design, including the length of the shaft, the opening angle of the jaws, stiffness of the joints, dimensions of the jaws and soft pads, and mechanical properties of the implemented soft pads. Moreover, pads with various surface patterns could be applied by using different templates.

A pressure-sensitive foil was used to indicate the applied pinch forces. We used this method because, with force sensors, it is complex to measure pinch forces at different locations throughout gripper pads. Between individual imprinting experiments, some variability was observed in the number of colored pixels between different distal (1 vs. 3), middle (4 vs. 6), and proximal (7 vs. 9) lateral segments. These grasping variations between different measurements were found to be random, presumably caused by misalignments of the gripper pads with the substrate. In Figure 6, a difference between segments 4 and 6 seems to be present for the patterned gripper, suggesting unequal closing of the gripper. We believe that this difference between segments 4 and 6 for the patterned gripper can be attributed to the small sample size we used, as no difference is present between segments 1 and 3 in the distal region, or between segments 7 and 9 in the proximal region of the same patterned gripper. Furthermore, in the individual imprint of a patterned gripper in Figure 5, the difference in colored-pixel count between segments 4 and 6 is small, and for the distal region (segments 1 vs. 3), the highest colored-pixel count is on the bottom side (segment 3) of the pad, supporting that differences between the lateral segments are random.

One limitation of using this foil is that our gripper pads have smaller dimensions than the applications this foil is designed for. The foil consists of microcapsules that break when a stress threshold of 0.006 MPa is exceeded, resulting in coloring of the foil. Matching the foil color shade with a reference color sample is used to obtain accurate pressures on the foil.^[24] As the dimensions of the gripper pad segments and the area of local stress concentrations are too small to determine color shades, we used a more qualitative approach of counting the number of colored pixels and refrained from reporting pinch forces generated by our grippers.

We observed in our measurements that sometimes, the tissue thickness exceeded the separation distance between the two jaws at the proximal end of the gripper. As a result, high pinch forces are present at the proximal end, and low pinch forces or no contact is present at the distal end of the pad. Such local pinch forces could be prevented by using slanted pads, or a prismatic joint movement, resulting in a parallel orientation of the two opposing pads. With parallel pads, a homogeneous distribution of pinch forces is expected, leading to higher gripping forces with lower local pinch forces.

The diameter of the gripper shaft is currently 10 mm, with the gripper tip, when closed, having a slightly larger diameter. In order to allow the use of this instrument in minimally invasive procedures, miniaturization of the instrument is necessary. Limitations of miniaturization are expected to primarily occur at the geometry of the joints of the gripper. The balance between high bendability and high recovery strength is delicate. We expect that, although the main functionality can be maintained, the exact geometry of the joints, especially the shape of the voids, will need optimization. It should be noted that the grasping performance of this gripper also strongly depends on the contact area between gripper and tissue, and thus on the area of the gripper pads. When scaling down the gripper design, the pad area can partially be maintained by using elongated the gripping jaws.

In future work, to make the gripper suitable for *in vivo* testing, to prevent exposure of the surgical area to CFF, the CFF needs to be fully embedded in the shaft of the instrument, without affecting its mechanical properties. Alternatively, it should be replaced with a fabric-like material with similar mechanical properties consisting of a single component (as opposed to numerous microscale fibers).

The lifespan of the gripper we present here is limited, as the materials the gripper is made of cannot undergo multiple sterilization cycles and joints will get fatigued after repeatable opening and closing. Therefore, we propose the use of the current gripper as a single-use instrument. From an economic perspective, single-use of the instrument is feasible, as 3D printing allows high repeatability and scaling up of manufacturing speed, and also the soft lithographic approach used for fabrication of the soft pads can be easily scaled up.^[25] Alternatively, the platform instrument could be fabricated from a material that can be equipped with disposable soft pads and can be easily sterilized.

6.6 Conclusion

Here, we replaced the conventional metal forceps of surgical grippers with gripping pads with anisotropic stiffness. We did so to prevent force-related grasping errors such as slipping of the tissue as a result of too low pinch forces, or damaging of the tissue as a result of too high pinch forces. Soft pads with anisotropic mechanical properties were fabricated, where a low normal stiffness facilitates the generation of a high contact area with tissue, even under low pinch forces, and a high lateral stiffness facilitates preservation of the formed contact when forces in the lateral direction are applied. We found that the use of soft pads in a surgical gripper prototype resulted in a decrease of generated pinch forces on the tissue, while preserving the gripping performance of conventional metal forceps. The prototype gripper, including shaft, joints, and jaws, was fabricated using 3D printing and anisotropic soft pads were post-hoc implemented in the instrument. This modular approach potentially allows for variation of the design parameters of the instrument in future design iterations, thereby enabling a facile and effective optimization of the instrument for a range of application fields.

Acknowledgements

This research is supported by the Netherlands Organization for Scientific Research (NWO) Domain Applied and Engineering Sciences (TTW), (Open Technology Program, project 13353 "Secure and gentle grip of delicate biological tissues" and project 12137 "Bio-Inspired Maneuverable Dendritic Devices for Minimally Invasive Surgery"). We kindly acknowledge Menno Lageweg, Henny van der Ster, David Jager, and Remi van Starckenburg from the Electronic and Mechanical Support Division (DEMO) of the Delft University of Technology for assistance with 3D printing, and manufacturing of parts required for fabrication of gripper pads or in the measuring setup.

References

- [1] G. Rateni, M. Cianchetti, G. Ciuti, A. Menciassi, C. Laschi, *Meccanica* **2015**, *50*, 2855.
- [2] T. R. Eubanks, R. H. Clements, D. Pohl, N. Williams, D. C. Schaad, S. Horgan, C. Pellegrini, *J. Am. Coll. Surg.* **1999**, *189*, 566.
- [3] K. R. Catchpole, A. E. B. Giddings, M. Wilkinson, G. Hirst, T. Dale, M. R. de Leval, *Surgery* **2007**, *142*, 102.
- [4] E. A. M. Heijnsdijk, A. Padeloup, A. J. Van Der Pijl, J. Dankelman, D. J. Gouma, *Surg. Endosc. Other Interv. Tech.* **2004**, *18*, 980.
- [5] H. De Visser, E. A. M. Heijnsdijk, J. L. Herder, P. V. Pistecsky, *Surg. Endosc. Other Interv. Tech.* **2002**, *16*, 1426.
- [6] J. A. Cartmill, A. J. Shakeshaft, W. R. Walsht, C. J. Martin, *Aust. N. Z. J. Surg.* **1999**, *69*, 127.
- [7] S. De, The Grasper-Tissue Interface in Minimally Invasive Surgery: Stress and Acute Indicators of Injury, Univeristy of Washington, **2008**.
- [8] J. Bos, E. W. L. J. Doornebosch, J. G. Engbers, O. Nyhuis, D. Dodou, *Proc. Inst. Mech. Eng. Part H J. Eng. Med.* **2013**, *227*, 1292.
- [9] D. D. Marucci, J. A. Cartmill, C. J. Martin, W. R. Walsh, *ANZ J. Surg.* **2002**, *72*, 476.
- [10] M. D. Bartlett, A. B. Croll, D. R. King, B. M. Paret, D. J. Irschick, A. J. Crosby, *Adv. Mater.* **2012**, *24*, 1078.
- [11] P. van Assenbergh, M. Fokker, J. Langowski, J. van Esch, M. Kamperman, D. Dodou, *Beilstein J. Nanotechnol.* **2019**, *10*, 79.
- [12] Z. He, C. Y. Hui, B. Levrard, Y. Bai, A. Jagota, *Sci. Rep.* **2016**, *6*, 26867.
- [13] J. Wang, L. Ma, W. Li, Z. Zhou, *Biosurface and Biotribology* **2018**, *4*, 50.
- [14] E. A. M. Heijnsdijk, H. DeVisser, J. Dankelman, D. J. Gouma, *Surg. Endosc. Other Interv. Tech.* **2004**, *18*, 974.
- [15] H. Chen, L. Zhang, D. Zhang, P. Zhang, Z. Han, *ACS Appl. Mater. Interfaces* **2015**, *7*, 13987.
- [16] H. Yamanaka, K. Makiyama, K. Osaka, M. Nagasaka, M. Ogata, T. Yamada, Y. Kubota, *Adv. Urol.* **2015**, 2015.
- [17] İ. M. Koç, T. Eray, B. Sümer, N. Çerçi, *Tribol. Int.* **2016**, *100*, 317.
- [18] W. Li, Z. G. Jia, J. Wang, L. Shi, Z. R. Zhou, *Tribol. Int.* **2015**, *81*, 190.
- [19] C. L. Grames, J. D. Tanner, B. D. Jensen, S. P. Magleby, J. R. Steger, L. L. Howell, in *Proc. ASME Des. Eng. Tech. Conf.*, **2015**, p. V05AT08A034.
- [20] F. Prabowo, A. L. Wing-Keung, H. H. Shen, *Adv. Mater. Res.* **2015**, *1112*, 410.
- [21] E. A. M. Heijnsdijk, J. Dankelman, D. J. Gouma, *Surg. Endosc. Other Interv. Tech.* **2002**, *16*, 1329.
- [22] J. Rosen, Ma. MacFarlane, C. Richards, B. Hannaford, M. Sinanan, in *Proc. Med. Meets Virtual Real.*, San Francisco, CA, **1999**, 1–10.
- [23] E. P. Westebring-Van Der Putten, J. J. Van Den Dobbelen, R. H. M. Goossens, J. J. Jakimowicz, J. Dankelman, *Surg. Endosc. Other Interv. Tech.* **2009**, *23*, 818.
- [24] F. Corporation, "Fujifilm's measurement film solution; Pressure Chart," **2020**.
- [25] P. van Assenbergh, E. Meinders, J. Geraedts, D. Dodou, *Small* **2018**, *14*, 1703401.

Chapter 7

Discussion



7.1 Main findings of this thesis

In this thesis, I aimed to translate grip-generating principles used by tree frogs into designs of artificial adhesives that can generate firm yet gentle grip on soft substrates.

The designs of the artificial adhesives were inspired by two important characteristics of the tree frog's attachment apparatus, namely:

- the hierarchical surface pattern present on the tree-frog toe-pad, with arrays of closely-packed pillars on both micro- and nanoscale that contribute to the establishment of a large contact area with the substrate;
- the presence of internal fibrillary structures that transmit mechanical stresses from the toe-pad surface to the internal skeleton of the tree frog to preserve the established contact when normal or shear loads are applied

In Chapter 3, we fabricated adhesives, the surface of which was patterned with arrays of densely packed either micro- or sub-microscale dimples, resembling the tree-frog toe-pad surface. In a third variation, the microscale dimple pattern was topped with a smooth thin terminal layer, in which case the dimples were transformed into sub-surface reinforcing walls.

An experimental evaluation of the dimpled adhesives showed that, on soft poly-vinylalcohol (PVA) substrates (12 and 18 kPa), adhesion and friction were higher for microscale dimples than for sub-microscale dimples. Positive effects of sub-microscale surface features described in the literature for grip on hard substrates, such as inhibition of crack growth and defect control, were not observed on soft PVA substrates. In the presence of a terminal layer, adhesion was higher compared to unpatterned reference adhesives on PVA of 12 kPa, presumably because the soft substrate got interlocked into micro-holes present on the terminal layer. The highest friction was generated by adhesives with microscale dimples without a terminal layer, likely thanks to indentation of the dimple walls into the substrate, resulting in interlocking.

In Chapter 4, micropillar adhesives laterally reinforced with bridging structures between neighbouring micropillars were fabricated. The micropillar

arrays were fabricated using a soft lithographic approach, and bridges were subsequently integrated by spin-coating a liquid precursor, forming bridges via capillary action, followed by curing. The bridge thickness was varied by varying the composition of the bridge precursor.

An experimental evaluation of the laterally reinforced micropillar adhesives showed that the micropillar adhesives with reinforcing bridges generated higher friction forces compared to micropillar adhesives without bridges. Furthermore, friction increased with bridge thickness. The possible underlying mechanism is that bridges between micropillars prevent buckling of the micropillars, which contributes to preserving contact under shear loading. Bridging of micropillars also had a positive effect on the durability of adhesives: after 100 cycles of sliding and detachment, friction properties were best preserved for the adhesives with the highest bridge thickness.

In Chapter 5, the reinforcement of adhesives on a millimeter scale is investigated. Adhesives with sub-surface cylindrical pores, separated by pore walls, were fabricated using 3D printing. Pore walls were either aligned with the shearing direction or perpendicular to the shearing direction. Pores were topped with a thin terminal layer with high deformability in the normal direction. The shear stiffness of adhesives was varied by controlling the height and direction of the internal pore walls. The normal stiffness of the adhesive was varied by controlling the thickness and number of the pore walls of the terminal layer.

An experimental evaluation of the 3D printed adhesives showed that, on a hard glass substrate, friction forces increased with decreasing normal stiffness of the adhesive, independently from their shear stiffness. The underlying mechanism presumably is that, with increasing normal stiffness, the formation of contact prior to sliding increases, resulting in higher friction forces. On soft substrates, the highest friction forces were generated by the adhesives with the lowest normal stiffness. Within this set of adhesives with the lowest normal stiffness, the highest friction forces were observed when the pores were aligned with the shearing direction. The low normal stiffness yielded high contact formation prior to sliding, whereas a high shear stiffness prevents loss of contact from the soft substrate when lateral loads are applied. The beneficial effect of such anisotropic stiffness on shear forces increased with increasing substrate softness.

In Chapter 6, soft adhesive pads internally reinforced with a stiff carbon fiber fabric were fabricated and implemented in a prototype of a novel soft surgical gripper. Two types of adhesive pads were implemented, with either an unpatterned (smooth) surface or a surface with arrays of sub-microscale dimples as presented in Chapter 3.

An experimental evaluation of the soft gripper on *ex vivo* soft tissue showed that the soft gripper generated comparable gripping force to traditional surgical grippers with forceps made of stainless steel while exerting lower normal loads on the vulnerable soft tissue, thereby reducing the risk of tissue injury.

7.2 Fabrication methods for adhesives

The different geometries of adhesives in this thesis in terms of shape, materials, and length scale required employing different fabrication methods in the experimental chapters in this thesis

Fabricating microscale features

When it comes to adhesives with microscale features (Chapters 3, 4, and 6), common challenges are the structural complexity of adhesives (e.g., overhanging features or curved surfaces) and the manufacturing speed, which is a serious obstacle to fabricating structures with dimensions in the range of centimetres.

In Chapters 3 and 6, we used the self-assembling properties of microscale colloids to form monolayers that act as molding templates. It is intrinsic to molding that the obtainable shape is a 2D pattern, extruded in the third dimension. By using a mold that is permeable for the shaped resin, and removable after curing of the resin by means of dissolving, we managed to generate overhanging features. The use of large monolayers, up to 4×4 cm², allowed us to fabricate adhesives with (sub-)microscale features with a projected contact area of 16 cm² (Figure 6). For adhesives from 10-μm microparticle templates, we also managed to remove the thin terminal layer, using a binding- and tearing approach. Directed self-assembly (DSA) is a useful approach to fabricate large-area three-dimensional molding templates without using complex micropatterning equipment. Self-assembly is directed by modifying chemical or physical properties of macromolecules such as used microparticles or modifying the physical environment (includ-

ing temperature, pH or solvent). A disadvantage of DSA is that there are limitations to the geometries one can obtain.

In Chapter 4, microscale adhesives were first fabricated by using conservative molding techniques. Inherent to molding is that only 2D patterns, extruded in the third dimension, can be fabricated, sometimes referred to as 2.5D structures. To enhance the architectural complexity and fabricate true 3D structures, including, for example, overhanging bridges (Chapter 4), or topping layers (section 7.5 of this Discussion), with molding methods, post-processing steps were used. For example, we added a second architecture directly on the fabricated architecture via spincoating and curing, or we fabricated a second architecture and combined these two via a binding process (section 1.4).

Fabricating macroscale features

For fabricating adhesives with macroscale features, 3D printing was used in Chapter 5. Despite the low resolution of this fabrication method and the mechanical properties of the resin itself, we managed to lower the effective stiffness of the printed adhesives by designing relatively thin, deformable walls and terminal layers. 3D printing at this point still has serious limitations for fabricating structures that require soft properties or high resolutions.

Chapter 6 combined a multistep approach to fabricate elastomeric pads with an embedded reinforcing carbon fibre fabric with directed self-assembly to obtain a microscale surface pattern. The dimensions of the elastomeric pad and the positioning of the carbon fibre fabric in the adhesive pad were controlled by using custom-made aluminium three-dimensional templates. To obtain a surface pattern, in Chapter 6, we placed these aluminium templates directly on a self-assembled monolayer to allow the use of a single curing step. Alternatively, adhesive pads could be fabricated first, and surface patterns could be separately fabricated and bound to the reinforced pads in a second processing step.

7.3 Form vs. function

As mentioned before, the goal of this thesis was to design adhesives that generate firm yet gentle grip on soft substrates, inspired by the tree-frog attachment apparatus.

Existing biomimetic adhesives based on the attachment system of tree frogs have been focusing on mimicking the pattern of the epidermal surface of tree frogs toe pads.^[1,2,3] The adhesive performance of these artificial adhesives is generally inferior to that of tree frogs, which can be explained by several differences between the manufactured adhesives and their biological paradigm. First, due to manufacturing limitations, features in artificial adhesives are generally larger than the hexagonal cells of the tree-frog toe-pads. However, given that for several engineering applications, the total area and payload of the artificial adhesives needs to be larger than the tree-frog toe-pads, even smaller features than those in the tree frog would actually be required. Second, the tree-frog toe-pad include a hierarchical surface patterning, which has hardly been implemented in artificial adhesives (for exceptions, see Li et al.^[4] and Liu et al.^[5]). A third limitation of existing biomimetic adhesives is that they are typically made of PDMS. PDMS is a highly hydrophobic material, whereas the surface of tree frogs toe pads has been shown to be hydrophilic. Moreover, PDMS is much stiffer than the bulk material tree-frog toe-pads consist of.^[6] Fourth, most existing biomimetic adhesives have neglected the internal fibrillary reinforcement of the toe pads (for exceptions, see Xue et al.^[2] and Bartlett et al.^[7]).

In summary, the majority of the existing tree-frog inspired adhesives primarily rely on copying the form of some of the elements of the tree-frog attachment apparatus. In this thesis, a different methodological approach was endorsed, namely by attempting to mimic the underlying function of the form rather than the form itself. Specifically, the focus of this thesis was to mimic mechanisms underlying the tree-frog attachment apparatus to satisfy two main requirements for strong grip: (1) contact formation and (2) preservation of the formed contact.

To form contact with a *hard* substrate, adhesives need to be highly deformable in the direction of normal loading in order to conform to substrate irregularities.^[8] This deformability can be maximized by varying the shape, size, or hierarchy of surface patterns.^[9,10] Alternatively, softer materials can be used for the adhesive, although this approach increases both formation as loss of contact. When approaching a *soft* substrate, a high contact area with the adhesive is readily formed by the deformation of the substrate. Surface patterning of adhesives mostly does not enhance contact formation on soft substrates. The presence of a surface pattern might even be disadvantageous for contact formation on a soft substrate because patterned adhesives have a lower effective contact area.^[11,12]

To preserve the formed contact under lateral and/or normal loads, adhesives must have sufficient mechanical strength to withstand applied loads. In tree frogs, the surface pattern of their toe pads is mechanically linked to the skeletomuscular system via keratin fibers.^[13] Due to their high tensile strength, these fibers have a strengthening function for the adhesive pad. Furthermore, tree frogs homogeneously distribute contact stresses by locally controlling the positioning of their toe pads, thereby preventing peak contact stresses and thus detachment.^[13] Similarly, internal sub-surface reinforcing components in artificial adhesives laterally strengthen adhesives to prevent loss of contact when loads are applied.^[7]

The adhesives fabricated in this thesis all contain some way of internal reinforcement. **Figure 7.1** shows the reinforcement in each of the four types of adhesives that were fabricated in this thesis, namely internal walls at various scales (Chapters 3, 5 and 6), bridges (Chapter 4), and a carbon fibre fabric (Chapter 6).

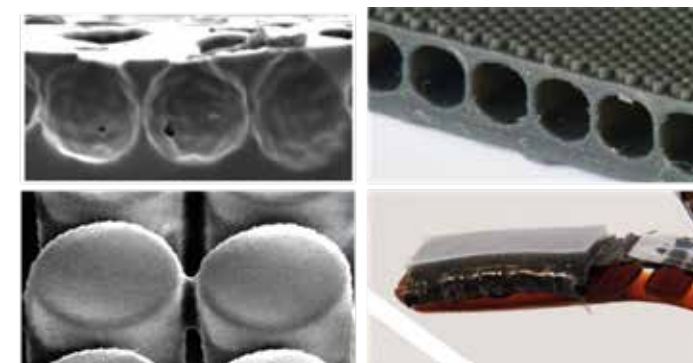


Figure 7.1. Adhesives developed in this thesis. A) Microscale dimpled adhesives topped with a terminal layer (Chapter 3). The terminal layer is soft and deformable, and sub-surface walls separating neighbouring dimples act as reinforcements in the normal direction. B) Microscale pillared adhesives with inter-pillar bridges (Chapter 4). Bridges act as sub-surface lateral reinforcements. C) 3D printed adhesives with millimetre-scale internal walls (Chapter 5). Internal walls act as lateral reinforcements. D) Adhesive pads with incorporated carbon fibres (Chapter 6). The carbon fibres act as lateral reinforcements.

Internal walls (normal or lateral reinforcement)

Sub-surface internal microscale walls provide stiffness in the normal direction to the thin terminal layer, which by itself is soft and deformable. The parts of the terminal layer in between supporting walls result in microscale soft patches in the continuous terminal layer, separated by more stiff, supported regions. This geometry introduces defect control and inhibition of crack growth—mechanisms enhanced with increasing spacing between supporting internal walls.^[14, 15]

One disadvantage of the microscale dimensions of the internal walls is that when shear loads are applied, the wall thickness is too low to significantly prevent the internal deformations of the adhesives in the lateral direction, leading to contact loss via bending of the internal walls.

The internal walls in Chapter 5 had millimeter length scale, and, due to their high bending strength, provide lateral reinforcement. Contact between adhesive and substrate is lost due to bending of the internal walls under applied shear forces. It was shown that, with increasing wall thickness, bending is reduced, preservation of contact improves, and hence, higher shear forces are generated (Chapter 5).

Bridging (Lateral reinforcement)

Bridges connecting neighboring micropillars enhance the effective lateral stiffness of micropillar adhesives. Bridging between micropillars also results in higher durability of micropillar adhesives, with the adhesives with the thickest walls exhibiting the least deterioration in friction over multiple shearing load cycles (Chapter 4).

Internal fibres (Lateral reinforcement)

Internal reinforcements in the shearing direction of adhesive pads by means of carbon fibers contributed to preserving the formed contact with soft tissue. Specifically, similar friction forces were generated by such adhesives as those generated by conventional surgical grippers, while keeping normal loads lower, resulting in more gentle grip on the vulnerable biological tissue (Chapter 6).

7.4 From experimental to real-world conditions

Testing of adhesives, both in this thesis and in the literature, is typically done on well-defined substrates such as glass, to enable a systematic evaluation of the effect of the adhesive's properties independently from the unpredictability of real-world substrates. Additionally, experimental parameters, including alignment between adhesive and substrate, and applied pre-load, load, and detachment rates, are all well-controlled to ensure high repeatability and uncontaminated data.

It remains an open question how well such adhesives perform in real-world conditions. Depending on the application field, adhesives might encounter substrates with meso- or microscale irregularities, different forms, contamination, or other unknown properties. Additionally, grasped objects can be irregularly shaped, hard to reach, vulnerable or slippery. For example, in laparoscopic surgical applications, grippers for slippery tissue have to perform pick-and-place operations of vulnerable, slippery tissue while the gripper is controlled through a trocar.

In Chapter 6, soft pads allowed gentle grasping of vulnerable tissue. The size of the pads was proportional to what can reasonably be packed in a surgical gripper, and the reinforcing fibres were elongated and guided along a shaft to match the gripper design, allowing load transmission to the gripper handle. Other applications might allow for or even require using adhesive pads with a larger area, stiffer properties, higher or lower thickness, or curved substrates. For example, in a project not presented in this thesis, we fabricated soft adhesive pads of $4 \times 4 \text{ cm}^2$ (**Figure 7.2**).^[16] We varied the surface pattern (flat, microscale dimples with or without a terminal layer), as well as the density and direction of the internal reinforcing fibres. Due to the large area of these adhesives, we managed to generate forces in the order of 1-2 N on PDMS substrates. With such large adhesives, one could think of a non-homogeneous distribution of the internal fibres, and by selectively loading of these fibres introduce folding of the soft pad to conform to curved substrates or to induce peeling-off to detach.^[16]

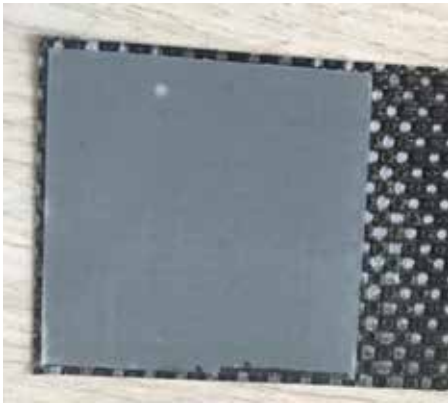


Figure 7.2. A reinforced adhesive patterned with hexagonally-packed dimples of around 8 μm in diameter. When the application allows it, scaling up the dimensions of the adhesive is a simple but effective approach of increasing the gripping force. The scale bar is 1 cm.

In a project not presented in this thesis, we found that the two-dimensional shape of adhesive pads has an effect on generated friction forces.^[17] We fabricated non-patterned, soft adhesive pads, reinforced with a carbon fiber fabric similar to the adhesives mentioned above, and varied the two-dimensional shape, as well as the thickness of the soft adhesive pad. It was found that for $2 \times 2 \text{ cm}^2$ square-shaped adhesive pads, under shear loading, peak forces are present at the four sharp corners of the adhesive. When the adhesive had an octagonal shape, these peak forces per corner were lower, and higher friction forces were generated. For adhesive pads with a thickness of 0.5 mm, circular-shaped adhesives outperformed the tested adhesives with corners (squared, octagonal). At a thickness of 2 mm, these adhesives became more vulnerable to the formation of defects along the curved contact line due to a higher normal stiffness.

7.5 Future work/Challenges ahead

Controlling the thickness, stiffness, and length of the terminal layer

The terminal layer, topping internal structures in an adhesive, is a recurring topic in this thesis. Its smooth, unpatterned surface and deformability play important roles in forming a high contact area between adhesive and substrate. In this thesis, the design of adhesives focused on the internal

reinforcing components, and not so much on the properties of the terminal layer. In the literature, terminal layers have been shown to positively affect the gripping performance of adhesives, both in normal and shearing direction.^[15,18] It remains an open question how the properties such as stiffness, thickness, or the overhang distance, i.e. the separation distance between supporting structures, of the terminal layer affect the grip-generating properties of adhesives.

Based on observations in this thesis and in the literature, we propose that:

- With decreasing thickness and stiffness of the terminal layer, the formed contact area under a given normal load increases.
- With decreasing thickness and stiffness of the terminal layer, a larger amplitude is required to make the terminal layer detach/peel off.
- With decreasing unsupported length, the reinforcing effect of the terminal layer in the lateral direction increases, resulting in higher shear force.

During this PhD project, a strategy to control the thickness and stiffness of the terminal layer was explored. Figure 2 shows the manufacturing process that was developed. In this approach, the internal structure is first fabricated via a conservative molding approach as described in Chapter 4 for non-bridged micropillar adhesives ("B0").

The terminal layer is fabricated in a separate spincoating procedure. We used uncured PDMS diluted in tert-butyl alcohol, similar to the approach of Chapter 4. Uncured PDMS was spincoated on a glass slide that was pre-coated with a release layer. The *stiffness* of the terminal layer was controlled by varying the PDMS base/linker ratio. The *thickness* of the terminal layer was controlled by the dilution of the uncured PDMS in TBA. The thickness is further controlled by varying the spincoating time and speed. Increasing spincoating times and speeds result in decreasing thickness of the terminal layer. After spincoating, the terminal layer was placed in an oven at 70°C for 15 minutes to allow partial curing of the PDMS.

Subsequently, the partially-cured terminal layer was bound to the micropillar pattern via imprinting and subsequent curing.

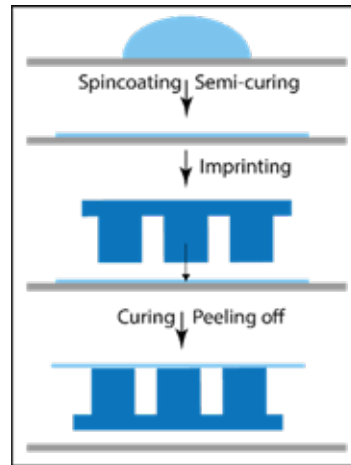


Figure 7.3. Fabrication process of a thin terminal layer via spincoating and applying it to a micropillar adhesive via imprinting.

Figure 7.4 shows the outcome of this fabrication process. We managed to fabricate micropillars with pre-defined diameter and spacing. Microscopic images of sectioned adhesives with a terminal layer show that the terminal layer is present on the pillar tips. The left image shows a partially detached terminal layer, as a result of cross-sectioning of the adhesive. Indentations of the pillar tips in the uncured terminal layer are visible. There are no perforations in the terminal layer, indicating that a flat surface finish is preserved after imprinting. The thickness of the terminal layer is about 12 μm , as was shown by profilometry measurements on fully cured spinocated PDMS layers on glass slides.

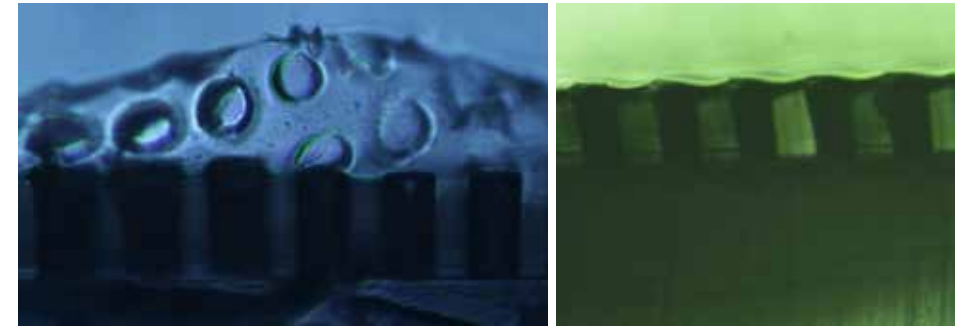


Figure 7.4. Microscopic images of fabricated adhesives. Left: A cross-section of micropillars (dark) with a terminal layer. The terminal layer partially disconnected from the pillar tips due to sectioning the adhesive. Tearing regions from the pillar tips are clearly visible. Right: The same adhesive with the terminal layer intact.

These preliminary results show that a separate preparation of the terminal layer, followed by subsequent binding to a micropatterned surface, allows for accurate control of the terminal layer properties such as its stiffness, thickness, and unsupported length. The properties of the terminal layer can be controlled by varying the PDMS base/linker ratio, the dilution of PDMS in TBA before spincoating, and the spincoating settings. Besides, the length of unsupported terminal layer in between two sub-surface micropillars can be increased with increasing pillar spacing. Such adhesives with controllable terminal layers can be used for systematically investigating the effect of the terminal layer characteristics on generating grip.

Drainage properties of micropillar adhesives on wet substrates

Adhesives in this thesis have been tested on deformable substrates that were dry or wet, but not on flooded substrates. Tree frogs, however, encounter flooded substrates in their natural habitat and do manage to adhere to them. It has been hypothesized that the particular surface pattern of tree frog toepads, containing a hexagonal network of grooves, plays a role in draining excess water at the toe pad-substrate interface to generate as much close contact as possible.^[19] This would lead to increased gripping strength, as drainage of water facilitates the formation of dry contact.

In the literature, fluid drainage from the adhesive-substrate interface is of-

ten mentioned as a mechanism contributing to grip. Gupta et al. found that, compared to unpatterned adhesives, the hydrodynamic forces for patterned adhesives are reduced at low separation distances, as a result of water flowing into the channels in between micropillars. At longer separation distances, fluid does not flow into the channels, and the micropatterned adhesive effectively acted as a smooth surface.^[20] Not much is known about how fluid moves in the microchannels when the adhesive approaches a substrate, and how dimensions and shape of micropillars and separating channels can be varied to improve the drainage properties of patterned adhesives.

In a project not presented earlier in this thesis, we investigated the drainage properties of micropillar adhesives on flooded substrates. Adhesives were fabricated similar to the micropillar adhesive B0 from Chapter 4, and the effect of channel width (20 vs. 40 μm) and pillar diameter (40 vs. 80 μm) on drainage properties and generated grip on flooded substrates was investigated.^[21]

Table 7.1. Geometrical properties of the fabricated micropatterned adhesives. "d" stands for diameter, "s" for the spacing between micropillars.

Adhesive pattern	Average pillar diameter (μm)	Average pillar spacing (μm)	Average pillar height (μm)	Surface area ^a (%)	Wall area per pillar (μm^2)	Wall area ^b (%)
d40s20	36.3	24.3	57.2	34.9	6911	52.4
d80s20	77.4	22.0	61.4	50.3	13823	62.8
d80s40	79.6	40.0	55.1	34.9	13823	52.4

^a Ratio of pillar tip area to total (pillar tip and channel) area. ^b Ratio of pillar perimeter to the perimeter of the pillar plus its spacing.

In a first experiment, using a custom-made force setup (See Chapter 3 and 4), fabricated adhesives were brought in contact with flooded glass and PDMS substrates and then detached via pulling off or sliding. Pull-off and shear forces as a result of drainage were measured and analysed. In a second experiment, the approach, attachment, and detachment cycles were repeated on a custom-made setup underneath an optical microscope to track the water flow at the adhesive-substrate interface and in the channels during and after this cycle. Water flow was visualized by immersing microparticles in the interfacial water, which could be traced under an optical microscope.^[21]

Figure 7.5 shows the pull-off forces generated by the adhesives on glass (left) and PDMS substrates (right). The pull-off measurements show that, on flooded glass substrates, water was often completely screening any interaction between substrate and adhesive, resulting in no pull-off forces (Figure 5). The strongly hydrophilic properties of the glass substrate facilitated the formation of a thin screening water layer. On smooth, unpatterned adhesives, some dry contact was formed by squeezing the water away from the adhesive-substrate interface under the applied normal loads. The presence of a surface pattern enhanced this screening effect, possibly because the pre-wetted adhesive acted like a sponge, releasing water from the channels when a normal load was applied.

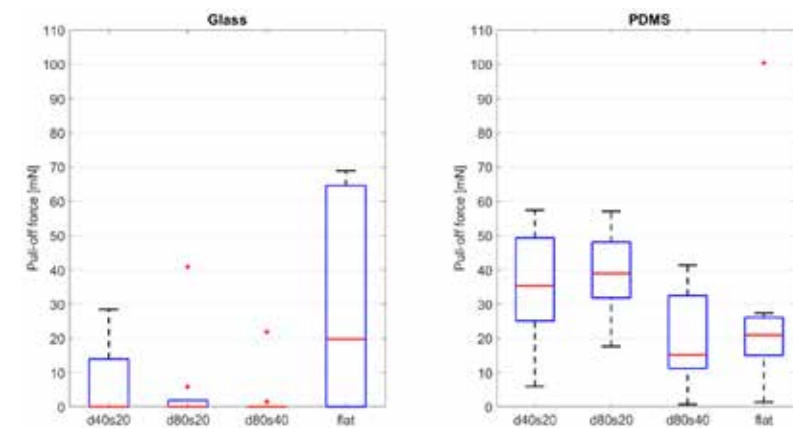


Figure 7.5. Maximum pull-off forces of adhesives with a d40s20-, d80s20-, d80s40-pattern and an unpatterned adhesive on glass (left) and PDMS (right). Ten measurements were conducted per adhesive.

On soft PDMS substrates, the above-mentioned screening effect of water was not present, because both adhesive and substrate were made of more hydrophobic PDMS. Higher pull-off forces were observed with d40s20 and d80s20 compared to adhesives d80s40 or adhesives without a surface pattern ($p < 0.05$). We presume that the channels, filled with water due to pre-wetting, act as capillary tubes. In channels with lower diameter, the travelling distance of water is higher, and air bubbles that block the flow are expelled from the channel network faster, resulting in overall higher drainage efficiency.

Figure 7.6 shows the generated friction forces on glass (left) and PDMS (right) substrates. On glass, it was found that significantly higher friction forces were generated with the two adhesive patterns with the highest channel area. There was no effect of the width of the channels or the micropillar diameter. On PDMS, no effects of channels were observed on the generated friction forces.

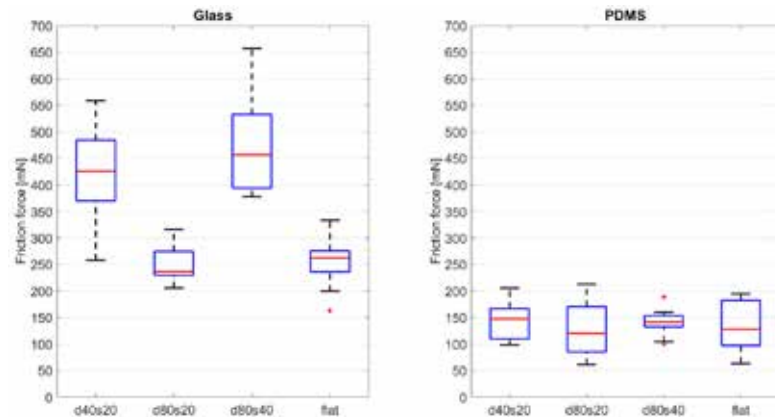


Figure 7.6. Maximum friction forces of adhesives with a d40s20-, d80s20-, d80s40-pattern and an unpatterned adhesive on glass (left) and PDMS (right). Ten measurements were conducted per adhesive.

From the biological model to designs for artificial adhesives

Figure 7.7 shows once more the outline of the research project this thesis is a part of. The chapters of this thesis primarily focused on how to translate the load-transmitting components in the tree-frog adhesive apparatus into a variety of internal reinforcements in artificial adhesives. Several other principles in the tree-frog adhesive system have been touched upon yet neither in this thesis nor in literature and deserve further investigation. Firstly, the use of reinforcing fibers to strengthen adhesives in the loading direction (Chapter 6) or to increase their cohesion has been investigated only by a small number of studies.^{[2], [7]} One might expect that adaptation of reinforcing components, for example, to the operational use of the adhesive, or to the specific object or substrate that is adhered to, can lead to a significant improvement of the gripping performance of adhesives. Secondly, active attachment control, as present in the locomotion of treefrogs, is

an interesting aspect to include in artificial adhesives. Conforming adhesive pads to irregular shaped substrates or (re)positioning the adhesive pad depending on the loading direction are powerful approaches toward optimizing gripping strength and switchable grip. Thirdly, detachment mechanisms have not been discussed in this thesis. Especially when grasped substrates are vulnerable, gentle detachment from the substrate is important. When adhesive pads are used in a pick-and-place fashion, as is the case for a surgical gripper, detachment needs to be quick and repeatable. Tree-frog toe pads are peeled off from substrates, a mechanism that is promising for artificial adhesives as well.

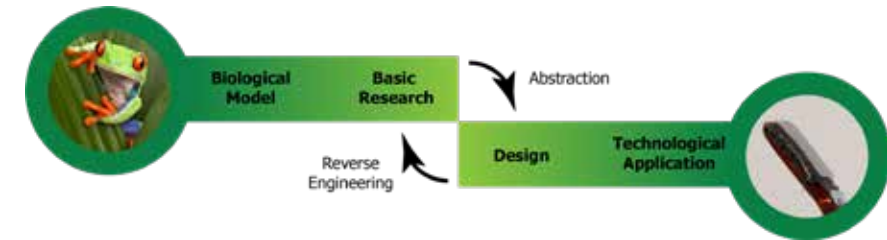


Figure 7.7. The outline of the collaborative research project this thesis is a part of, as shown in the introduction. Open questions remain both on the abstraction of our understanding of the attachment system of the tree frog to design for artificial adhesives, as on the design and implementation of a technical application.

Toward a technical application

This thesis has shown that the use of soft, reinforced pads, resembling tree frog toe pads is a good approach for, on the one hand, reducing the load-dependence of a gripper on the grasped tissue and, on the other hand, still generating a significant gripping strength (Chapter 6). We managed to reduce the load-dependence in a mechanical gripper resembling in its operation traditional surgical forceps. There are good reasons to elaborate this preliminary technical application, as working with reduced pinching forces in traditional surgical forceps has advantages for both the patients, in reducing trauma and shortening recovery times, and the surgeons, who can still use an instrument for which they are trained. The presented grasping instrument is yet a prototype, and more work is required to implement the presented soft pads in a surgical gripper suitable for clinical use (Chapter 6).

An ultimate technical solution would be a gripper for wet and slippery tis-

sue with a high load-independence, that is, a gripper tip that can adhere to tissue with only a small pre-load. Thereto, future work is required on all aspects mentioned in Figure 6. Besides optimizing the use of soft surfaces and internal reinforcements, other principles from tree frog attachment, including generating dry contact by draining interfacial water, controlling the placements and movement of pads, and switchable adhesion will have to be explored for use in the design of artificial adhesives.

References

- [1] P. Y. Isla, E. Kroner, *Adv. Funct. Mater.* **2015**, 25 (16), 2444–2450.
- [2] L. Xue, B. Sanz, A. Luo, K. T. Turner, X. Wang, D. Tan, R. Zhang, H. Du, M. Steinhart, C. Mijangos et al. *ACS Nano* **2017**, 11 (10), 9711–9719.
- [3] D. M. Drotlef, L. Stepien, M. Kappl, W. J. P. Barnes, H. J. Butt, A. Del Campo, *Adv. Funct. Mater.* **2013**, 23 (9), 1137–1146.
- [4] M. Li, W. Huang, X. Wang, *Biointerphases*, **2015**, 10(3), 031008.
- [5] Q. Liu, F. Meng, X. Wang, B. Yang, D. Tan, Q. Li, Z. Shi, K. Shi, W. Chen, S. Liu, et al., *ACS Appl Mater Interfaces* **2020**, 12, 19116–22.
- [6] J. Langowski, D. Dodou, P. van Assenbergh, J. L. van Leeuwen, *Integrative and comparative biology* **2020**, 60(4), 906–918.
- [7] M. D. Bartlett, A.B. Croll, D.R. King, B.M. Paret, D. J. Irschick, A. J. Crosby, *Advanced Materials*, **2012**, 24, 1078–1083.
- [8] L. Heepe, L. Xue, S. Gorb, *Bio-inspired Structured Adhesives; Biologically-Inspired Systems*, Vol. 9; Springer International Publishing: Cham, Switzerland, **2017**.
- [9] A. Del Campo, E. Arzt, *Macromolecular Bioscience*, **2007**, 7(2), 118–127.
- [10] M. Kamperman, E. Kroner, A. Del Campo, R.M. McMeeking, E. Arzt, *Advanced Engineering Materials*, **2010**, 12 (5), 335–348.
- [11] A. N. Gent, *Rubber Chem. Technol.* **1974**, 47(1), 202–212.
- [12] J. Y. Chung, M. K. Chaudhury, *J. Adhes.* **2005**, 81(10–11), 1119–1145.
- [13] J. Langowski, D. Dodou, M. Kamperman, J. van Leeuwen, *Frontiers in zoology*, **2018**, 15(1), 1–21.
- [14] R. V. Garg, N. Datla, *J. Adhes.*, **2019**, 95(3), 169–186.
- [15] N. J. Glassmaker, A. Jagota, C.-Y. Hui, W.L. Noderer, M. K. Chaudhury, *Proc. Natl. Acad. Sci.* **2007**, 104 (26), 10786–10791.
- [16] E. Cheung, **2019**, *Friction Forces of Micropatterned elastomer with Carbon Fibre fabric Reinforcement on soft substrates*, MSc. Thesis, Delft University of Technology, Delft.
- [17] A. Bakx, A. Hoek, O. Nekeman, M. Nieuwland, **2018**, *The effect of shape, thickness and surface area on the critical force of fiber-reinforced adhesives*, Delft University of Technology, Delft.
- [18] Z. He, C.-Y. Hui, B. Levrard, Y. Bai, Y. A. Jagota, *Sci. Rep.* **2016**, 6.
- [19] J. Barnes, J. Smith, C. Oines, M. Reinhard, *Tire Technol. Int.* **2002**, 2002, 56–60
- [20] C. Dhong, J. Frechette, *Soft Matter* **2015**, 11(10), 1901–1910
- [21] B. Haitsma Mulier, **2020**, *Grip on wet interfaces: an experimental study on the role of drainage*, MSc Thesis, Delft University of Technology, Delft

SUPPORTING INFORMATION

Supporting Information Chapter 3

SI3.1: Rheological characterization of polyvinyl alcohol (PVA) substrates (PVA-12 and PVA-18)

The storage and loss moduli of PVA subject to 2 and 3 freeze-thaw cycles were determined with a TA Instruments AR-G2 rheometer. A parallel plate geometry with diameter of 25 mm was used. Storage and loss moduli were determined at a strain of 0.05%, for a frequency range of $1 \times 10^{-1} - 1 \times 10^2$ rad/s.

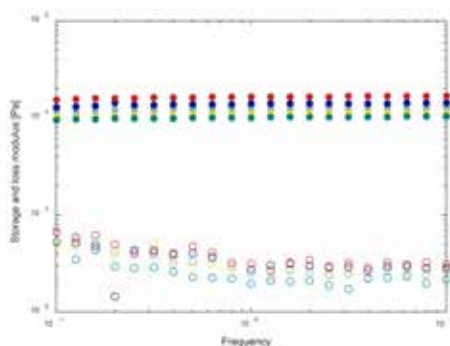


Figure SI3.1: Storage modulus (•) and loss moduli (o) as a function of angular frequency for 5 samples of PVA substrates subjected to 2 freeze-thaw cycles. The average storage modulus at 0.1 rad/s was 12.002 kPa.

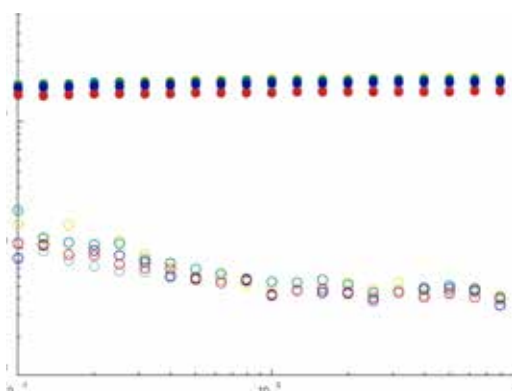


Figure SI3.2: Storage modulus (•) and loss moduli (o) as a function of angular frequency for 5 samples of PVA substrates subjected to 3 freeze-thaw cycles.

5 samples of PVA samples subjected to 3 freeze-thaw cycles. The average storage modulus at 0.1 rad/s was 18.038 kPa.

Table SI3.1: Average storage moduli for 5 PVA samples subjected to 2 freeze-thaw cycles, and 5 samples subjected to 3 freeze-thaw cycles.

	Mean (μ) at 0.1 rad/s [Pa]	Standard deviation
2 freeze-thaw cycles	12002	2.4661e+03
3 freeze-thaw cycles	18038	2.0692e+03

The mean storage moduli at 0.1 rad/s (750 μ m/s) were compared. A two-sample t-test shows that the two means significantly differed ($t(8) = 4.61$; $p = 0.0012$).

Average Tan delta (G''/G') for PVA-12 at 0.1 rad/s was 0.0517.

Average Tan delta for PVA-18 at 0.1 rad/s was 0.0724.

SI3.2: Structural characterization of sub-micrometer dimple arrays with AFM

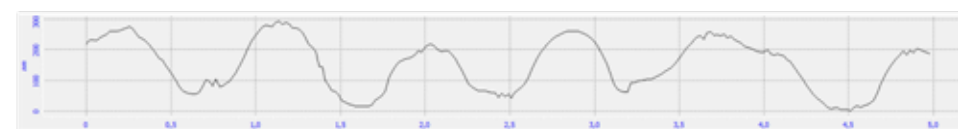


Figure SI3.3: A cross-section of a sub-micrometer dimple micropattern, recorded with atomic force microscopy (AFM). The dimple depth is about 200 nm, and the center-to-center distance between dimples is about 0.8 μ m.

SI3.3: The effect of curing at room temperature

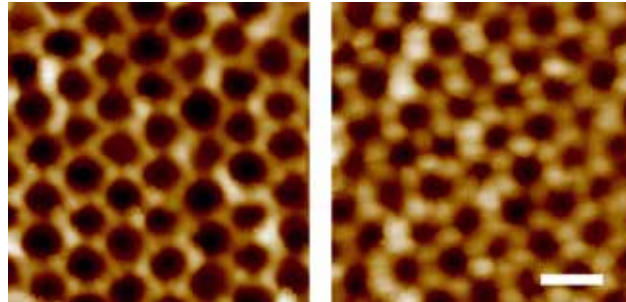


Figure SI3.4: The effect of curing the elastomer at room temperature for 48 hours (left) versus curing at 68 C for 2 hours (right). When curing at room temperature, the uncured elastomer remains in a liquid state much longer, allowing it to fully flow through the colloidal monolayer. This results in sharper edges separating neighboring dimples, and larger dimple diameters. Scale bars are 1 μm .

SI3.4: Sample fabrication and mounting

Fabrication of PDMS micropatterns

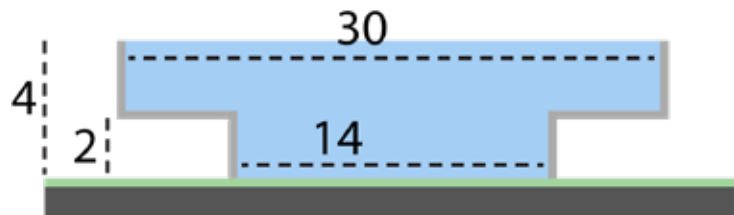


Figure SI3.5: A two-layer squared frame (light grey) was placed on a glass slide (dark grey), coated with a colloidal monolayer (green). The frame was filled with uncured PDMS and the filled frame was placed in the oven for 2 hours at 68.3° C for curing.

The dimensions of the mold are shown in mm's.

Mounting of the sample on the force platform



Figure SI3.6: The fabricated PDMS sample (blue) was placed on the force platform (light grey). A covering part from stainless steel (SS) with a squared void (dark grey) was placed on top of the sample to fixate it. Small magnets (black) were integrated in the force platform to fixate the SS covering part on the force platform.

SI3.5: Additional Data

Pull-off data

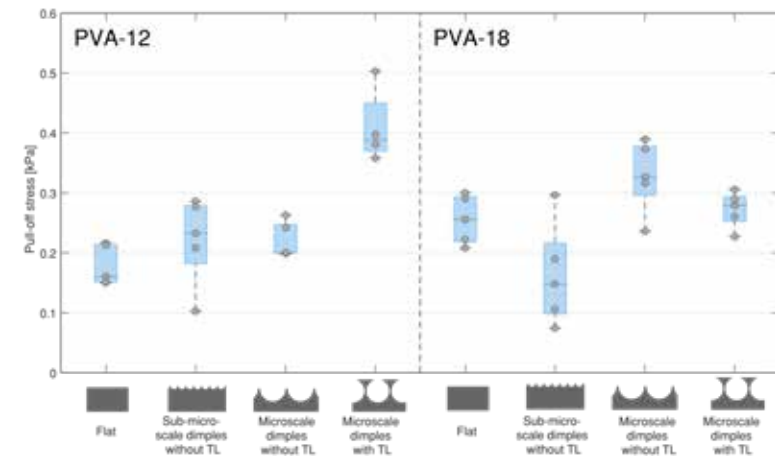


Figure SI3.7: Pull-off stress for flat samples, sub-microscale dimples without terminal layer, and microscale dimples with and without terminal layer, all from PDMS-280 on PVA-12 (left) and PVA-18 (right). Each data point represents the average of 5 consecutive measurements of one sample, and in each boxplot, 5 different samples for each geometry are included.

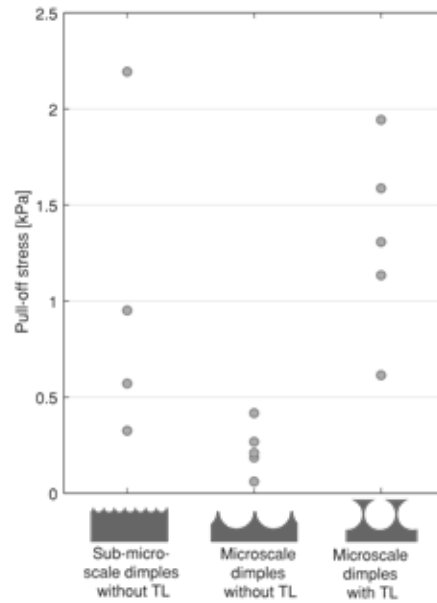


Figure SI3.8: Pull-off stress for sub-microscale dimples without terminal layer, and microscale dimples with and without terminal layer, all from PDMS-280, on glass. Each data point represents the average of 5 consecutive measurements of one sample, and in each boxplot, 5 different samples for each geometry are included.

Table SI3.2. Median and interquartile range (IQR) of pull-off forces (mN) of all fabricated micropatterns on two types of PVA.

Substrate		PVA-12				PVA-18			
Sample stiffness		PDMS-280		PDMS-580		PDMS-280		PDMS-580	
Geometry	Size	Median	IQR	Median	IQR	Median	IQR	Median	IQR
Flat	-	32.47	7.39	33.15	5.17	51.96*	16.42	57.75	9.05
Dimples without TL	Sub-microscale	45.83	19.88	45.04	26.89	28.97	21.27	56.90	16.87
Dimples without TL	Microscale	44.66	9.83	32.61**	7.36	68.19	20.31	60.83	16.35
Dimples with TL	Microscale	76.18*	17.13	63.66	13.42	57.76	15.26	44.58	21.72

TL: terminal layer
 *one missing value.
 **two missing values.

Friction data

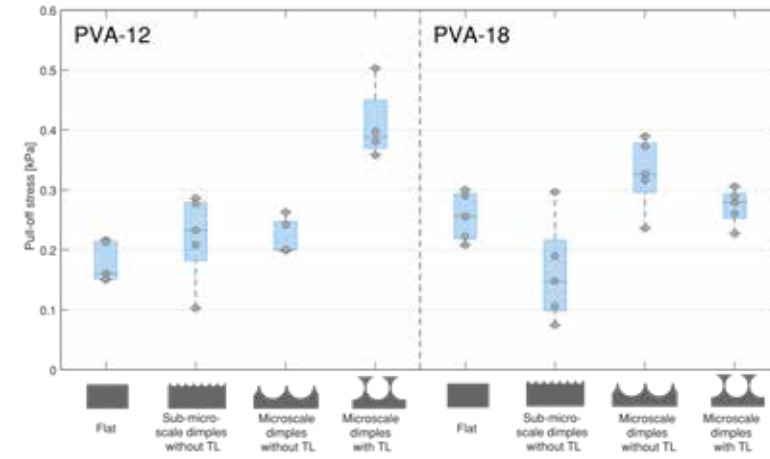


Figure SI3.9. Friction stress for PDMS-280 micropatterns of sub-microscale dimples without terminal layer, and microscale dimples with and without terminal layer, on PVA-12 (left) and PVA-18 (right). Each data point represents the average of 5 consecutive measurements of one sample, and in each boxplot, 5 different samples for each geometry are included.

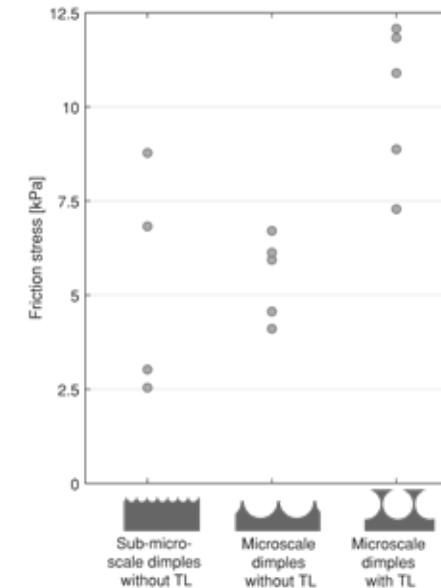


Figure SI3.10: Friction stress for sub-microscale dimples without terminal layer, and microscale dimples with and without terminal layer, all from PDMS-280, on glass. Each data point

represents the average of 5 consecutive measurements of one sample, and in each boxplot, 5 different samples for each geometry are included.

Table SI3.3: Median and interquartile range (IQR) of friction forces (mN) of all fabricated micropatterns on two types of PVA.

	Substrate	PVA-12				PVA-18			
	Sample stiffness	PDMS-280		PDMS-580		PDMS-280		PDMS-580	
Geometry	Size	Median	IQR	Median	IQR	Median	IQR	Median	IQR
Flat	-	69.03	88.84	94.02	64.12	30.53	35.49	64.18	39.19
Dimples	Sub-microscale	132.82	109.03	97.64	27.92	166.82	39.88	87.46	61.11
Dimples	Microscale	254.06	100.02	183.00	55.18	135.84	43.79	249.16	98.75
Dimples	Microscale	164.95	113.64	188.85	80.09	111.09	47.22	29.32	31.91

TL: terminal layer

Supporting Information Chapter 5

SI5.1 Measuring setup

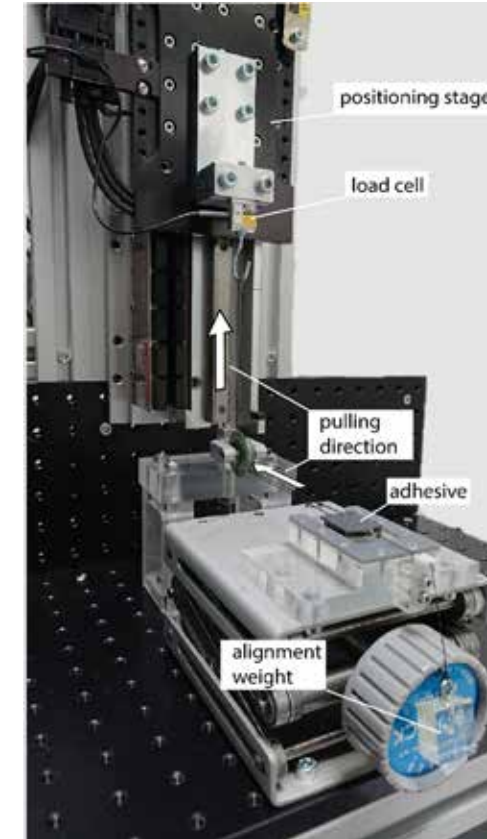


Figure SI5.1: Setup used to measure shear forces of fabricated adhesives. Before measuring, adhesives were aligned using the alignment weight. This weight was reduced before measuring.

SI5.2. Shear force measurements: Additional results

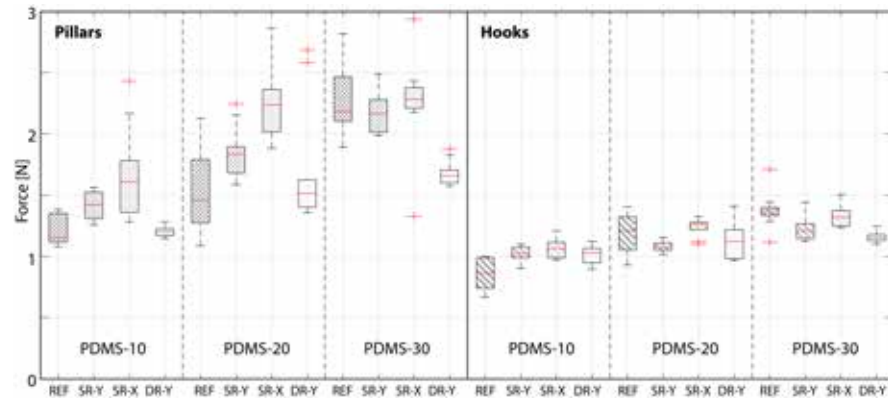


Figure SI5.2: Shear forces of adhesives patterned with pillars (left) and hooks (right) and four internal geometries on PDMS-10, PDMS-20, and PDMS-30. Note that the y-axis runs until 3 N, whereas the corresponding figure in the main text runs till 9 N.

Table SI5.1: Means and standard deviations of shear force measurements ($n = 10$).

	UNP		PIL		HKS	
	Condition	Mean \pm std	Condition	Mean \pm std	Condition	Mean \pm std
Glass	REF	1.61 \pm 0.22	REF	1.02 \pm 0.19	REF	0.86 \pm 0.23
	SR-Y	2.83 \pm 0.47	SR-Y	2.14 \pm 0.40	SR-Y	1.19 \pm 0.18
	SR-X	2.84 \pm 0.26	SR-X	2.01 \pm 0.38	SR-X	0.97 \pm 0.31
	DR-Y	1.96 \pm 0.17	DR-Y	1.65 \pm 0.18	DR-Y	1.10 \pm 0.16
PDMS-10	REF	2.54 \pm 0.26	REF	1.22 \pm 0.13	REF	0.86 \pm 0.12
	SR-Y	2.01 \pm 0.48	SR-Y	1.41 \pm 0.11	SR-Y	1.02 \pm 0.06
	SR-X	2.43 \pm 0.59	SR-X	1.68 \pm 0.37	SR-X	1.06 \pm 0.08
	DR-Y	1.90 \pm 0.301	DR-Y	1.20 \pm 0.05	DR-Y	1.01 \pm 0.08
PDMS-20	REF	3.16 \pm 0.70	REF	2.24 \pm 0.30	REF	1.19 \pm 0.16
	SR-Y	4.02 \pm 1.40	SR-Y	1.85 \pm 0.22	SR-Y	1.08 \pm 0.05
	SR-X	4.72 \pm 1.13	SR-X	2.24 \pm 0.30	SR-X	1.24 \pm 0.07
	DR-Y	3.49 \pm 1.14	DR-Y	1.71 \pm 0.50	DR-Y	1.13 \pm 0.16

PDMS-30	REF	4.99 \pm 0.91	REF	2.28 \pm 0.27	REF	1.38 \pm 0.15
	SR-Y	7.31 \pm 0.44	SR-Y	2.18 \pm 0.17	SR-Y	1.23 \pm 0.10
	SR-X	8.16 \pm 0.34	SR-X	2.26 \pm 0.39	SR-X	1.33 \pm 0.08
	DR-Y	6.20 \pm 0.74	DR-Y	1.68 \pm 0.10	DR-Y	1.16 \pm 0.05

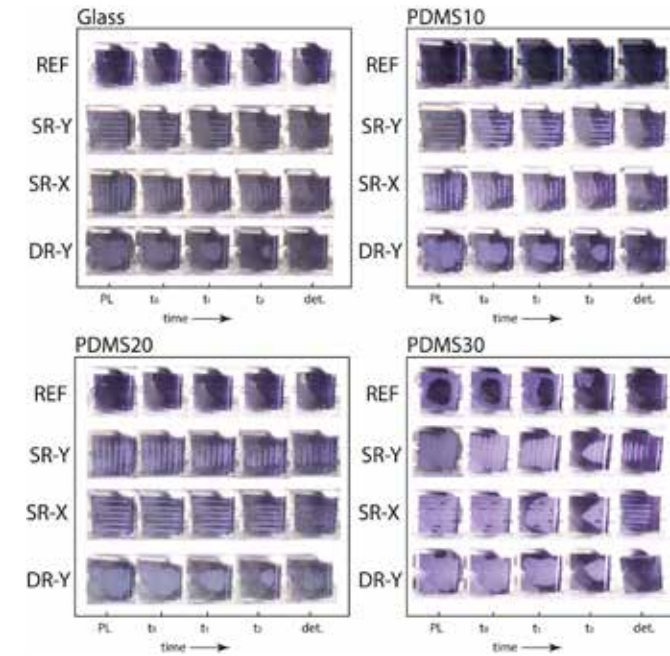


Figure SI5.3: Loss of contact of adhesives over time before, during and after shear measurements on glass and various PDMS substrates. Under PL, the contact under preload is shown, t_0 is the moment where sliding starts, t_1 is during sliding, t_2 is just for detachment, and det. shows the contact after detachment. Depending on the adhesive geometry, detachment occurred at different timescales.

ACKNOWLEDGEMENTS

Hoe vaak is het niet gebeurd, dat ik scheldend het TNW gebouw uitgelopen ben, de afgelopen waardeloze labdag verwensend, en uitkijkend naar het moment dat ik het dankwoord van mijn proefschrift kon gaan schrijven. En nu ligt er dan ook daadwerkelijk een boekje. Terugkijken waren ook deze ogenschijnlijk waardeloze labdagen nodig om tot dit proefschrift te komen. Maar veel meer is het dankzij een hele rits aan mensen dat dit proefschrift tot stand kon komen, waarvan ik in deze paragraaf er een aantal hartelijk wil bedanken.

Allereerst wil ik mijn promotoren bedanken. **Dimitra**, bedankt voor je hulp, begeleiding, je geduld, je coaching en je openheid. Ik weet nog dat toen ik op sollicitatiegesprek kwam, dat ik aangaf wel enigszins gespannen te zijn. "Nou, ik ook, hoor!" antwoorde je, en daarmee was voor mij het ijs gebroken. Je hulp bij het vormgeven van mijn experimenten en het opschrijven van mijn resultaten was absoluut onmisbaar. Na bovengenoemde waarde-loze labdagen stond jou kantoor altijd open, voor een ontvullend en hoopgevend perspectief op de dingen. Door onze samenwerking heb ik veel af- en bijgeleerd, waarvoor ik je erg dankbaar ben. **Paul**, jou enthousiasme en creativiteit werken aanstekelijk. De eerlijkheid gebied mij te zeggen dat die soms zo snel gingen, dat ik in lichte vertwijfeling je kantoor uitgelopen ben, maar na verloop van tijd vielen de stukjes op hun plek. Dank daarvoor. **Jan**, wij hebben elkaar maar weinig gesproken, maar van de kennis en kunde, alsook de labruimtes, binnen ASM heb ik dankbaar gebruik gemaakt. Ik was in het lab met mijn PDMS-creaties een vreemde eend in de bijt, maar ik heb daar desondanks met veel plezier rondgelopen. Behalve op de waardeloze labdagen dan.

Graag wil ik ook de promotiecommissie een woord van dank toedichten. Voor de bestede tijd aan het doorlezen en becommentariëren van dit proefschrift, als ook voor uw aller zitting in de commissie tijdens de verdediging wil ik u hartelijk danken.

Op deze plek wil ik ook **subsidieverstrekker TTW** noemen, dankzij wiens ondersteuning dit project mogelijk is gemaakt. De periodieke voortgangsmetingen waren altijd mooie ijkpunten, waarbij ook externe partijen hun licht over ons werk deden schijnen. Dat was vaak erg verhelderend.

Van groot belang voor het vormen van een visie voor dit proefschrift was de samenwerking met de WUR, namelijk met **Julian** en **Johan** van de Experimental Zoology Group. Julian, we zijn samen opgetrokken in de vraagstukken rondom kikkers en hoe ze plakken, en dat was erg plezierig. Discussies met jou bevestigden vaak dat we de juiste vragen stelden, en dat is al heel wat. Je werk aan de *force transducer* is vooral aan mijn experimenten besteed geweest, en voor je hulp bij de data-analyses van deze metingen wil ik je ook hartelijk bedanken. Het was prettig met je op te trekken, ook tijdens onze gezamenlijke conferentiebezoeken, en dat is heel wat waard. Ik ben blij dat jij onze inspanningen voortzet, en ik wens je daar veel succes bij.

De totstandkoming van dit proefschrift is zeker vereenvoudigd door de inspanningen van de studenten die ik heb mogen begeleiden. **Jay, Eunice, Tim, Frank en Babette**, dank voor jullie werk, geduld en doorzettingsvermogen. Het was leuk en leerzaam om samen met jullie op te trekken, en de resultaten waren zeker niet mis, wel zo leuk.

De jongens van **DEMO** wil ik ook apart noemen. Zonder jullie meedenken en maken was er van mijn proefopstellingen een stuk minder terecht gekomen. Daarnaast was het ook nog eens hartstikke gezellig. Ik noem David, Remi, Henny en Menno (dagje Force Transducer verhuizen vanuit Wageningen, jwz!), omdat ik één van hen ervan verdenk met mijn nickname "Peter-centimeter" gekomen te zijn, die verbazingwekkend snel door heel DEMO rondging.

BME Collega's, gedeelde smart is halve smart. Heerlijk om met jullie tijdens lunches, borrels, feestjes of koffiepauzes samen te zeiken, successen te delen, promoties te vieren en afleiding te zoeken. Kantoor 1, toch wel het beste kantoor, heel fijn om mijn kikkers bij jullie te mogen ontleden. Bram, Mona, Freek, Annetje, Eline, Ingrid, Marco, Martijn, Bart, Pier, superleuk dat jullie bestaan. Eline en Paul, dankzij jullie ben ik de Science Battle ingerold, en dat was een van de leukste dingen die ik tijdens mijn PhD heb gedaan. Dank ook nogmaals voor het Peter-padvinder filmpje tijdens de try-outs. Heel leuk. Over Paul gesproken, dat brengt me bij de **BITE-collega's**: Paul dus, en verder Costanza (nice and fun joint effort on the gripper-chapter), Ewout, Awaz, Juan (great fun playing football on Mondays), Aimée, het was mooi om met jullie op te trekken. Marta, thanks for your being-there over the years. Creating the epic movies for our departing colleagues was

great fun. It was a great honour to be your paranymph, and I am happy I got to know you. Ik noem verder Nadia, Elise, Jeroen (wat kan jij slecht zingen, zeg!), Bas (steeds het gevoel dat wij elkaar niet genoeg gesproken hebben), Hoda, Tonke, Roos, Nick, John, en alle anderen die aanschoven bij de lunch of de borrel. Bedankt voor de gezelligheid.

Henri, het veelvoorkomende gezamenlijke halfuurtje op de fiets naar station Zoetermeer had toch vaak een therapeutische werking. We hebben, naast hard gefietst, echt veel besproken, niet alleen PhD-gerelateerd, en daar heb ik echt onwijs goede herinneringen aan. Iedereen weet dat een PhD doen niet goed is voor je huwelijk, maar ik koester de stille hoop dat onze therapeutische praat sessies op de fiets een significante bijdrage geleverd hebben aan de instandhouding van onze beider onovertroffen huwelijken.

Een alineaatje voor alle vrienden buiten de TU misstaat ook zeker niet. Vrienden uit Gouda, dank voor jullie luisterend oor en de afleiding in de vorm van koffietjes, borrels, spelletjesavonden en potjes squash en voetbal. Sjoerd, Michelle, Kathelijne, Chris, Gernand, Jeannette, Rik, Bertina. Rik, onze walkietalkies waren vooral tijdens het schrijfproces echt fijn om te hebben. Dank daarvoor.

Benji en Moniek, mooi om jullie in ons leven te hebben. Benji, we delen prachtige jaren, en mindere jaren. We hopen op meer moois. Thomas en Paul, bedankt voor alle leuke dingen die we met elkaar doen en bespreken. Met de afronding van dit proefschrift is de supramagneet niet meer. Al vrees ik dat die in jullie harten nog wel even voort zal bestaan.

Lieve Familie, dank voor jullie volharding in het vragen hoe het nu eigenlijk gaat met mijn proefschrift. Pa en Ma, jullie plichtsbesef, doorzettingsvermogen, en ontnuchterende kijk op het leven, waarvan ik graag mag zeggen er een lepeltje van meegesnoept te hebben, hebben me erg geholpen tijdens mijn promotietraject. Daarvoor, en voor veel meer, ben ik jullie erg dankbaar. Oma Ditje, het is zover: mijn studie is af. Dank voor de gezellige koffiemomentjes met Tante Ria, vaak op weg van of naar Duitsland.

Harald, Gudrun, Marohni's und Chaborski's, vielen dank das wir immer wieder zum Besuch kommen duerfen. So ein Wochenende in Wetter ist immer wie ein kleine Urlaub, vor allem wegen euch. Und wegen das essen.

Lieve Sarah, dank voor je eindeloze geduld, ondersteuning, aanpassingen en luisterend oor en opmonterende en grappige woorden. Na waardeloze labdagen, en na alle dagen trouwens, was en is het altijd heerlijk thuis-komen bij jou. Zonder jou was dit proefschrift er misschien wel helemaal niet gekomen, en daarom draag ik dit proefschrift aan jou op. Je bent absoluut mijn lievelingsmens.

Voor al deze mooie mensen, en voor Zijn hulp in de laatste jaren wil ik tenslotte graag dhr. J. Christus bedanken. Ondanks Uw drukke agenda vond ik altijd een luisterend oor. Ik hoor nog wel eens hoe ze dat nou eigenlijk doen, die kikkers.

PERSONALIA

Curriculum Vitae

Simon Petrus (Peter) van Assenbergh was born April 20 1989 in Tricht, the Netherlands. He graduated from Gomarus Scholengemeenschap in Gorinchem in 2007. In 2013, he obtained an MSc degree in Molecular Life Sciences from Wageningen University, with a specialization in Physical Chemistry. In 2015, Peter started as a PhD researcher in the Department of BioMechanical Engineering of Delft University of Technology. During his research, a part of the work was done in the Department of Chemical Engineering from the TU Delft. The project was a close collaboration with the group of Experimental Zoology at Wageningen University & Research.

Publications

Publications part of this thesis:

- Peter van Assenbergh, Erwin Meinders, Jo Geraedts, Dimitra Dodou, *Small* **2018**, 14(20), 1703401. doi: 10.1002/smll.201703401
- Peter van Assenbergh, Marike Fokker, Julian Langowski, Jan van Esch, Marleen Kamperman and Dimitra Dodou, *Beilstein J. Nanotechnol.* **2019**, 10(1), 79-94. doi: 10.3762/bjnano.10.8
- Peter van Assenbergh, Kai Zhang, Ivan Buijnsters and Dimitra Dodou, *Appl. Phys. A* **2020**, 126, 790. doi: 10.1007/s00339-020-03947-y
- Peter van Assenbergh, Frank Haring, Joshua A. Dijkman and Dimitra Dodou, *Adv. Mater. Interfaces* **2020**, 2001173, 1-9. doi: 10.1002/admi.202001173
- Peter van Assenbergh, Costanza Culmone, Paul Breedveld & Dimitra Dodou. *Proceedings of the Institution of Mechanical Engineers, Part H: Journal of Engineering in Medicine*, **2020**, 0954411920971400. doi: 10.1177/0954411920971400

Other publications:

- Rossow, T., Hackelbusch, S., **Assenbergh, P. Van**, Seiffert, S., A Modular Construction Kit for Supramolecular Polymer Gels. *Polym. Chem.* **2013**, 4, 2515-2527. doi: 10.1039/C3PY00104K
- Hackelbusch, S., Rossow, T., **Assenbergh, P. Van**, Seiffert, S., Chain Dynamics in Supramolecular Polymer Networks. *Macromolecules* **2013**, 46(15), 6273-6286. doi:10.1021/ma4003648

